UNIVERSIDAD DE GRANADA

DOCTORAL THESIS

Experimental and analytical study of the hydrodynamics of swell and sea waves with partially reflective structures

Author

Andrea M. Lira Loarca

Supervisors

Asunción Baquerizo Azofra

Sandro Longo

Doctoral Programme in Biogeochemical Fluid Dynamics and their Applications
University of Granada, Spain

and

Doctoral School in Engineering and Architecture
University of Parma, Italy

Editor: Universidad de Granada. Tesis Doctorales
Autor: Andrea Lira Loarca
ISBN: 978-84-1306-327-0
URI: http://hdl.handle.net/10481/57414

UNIVERSIDAD
DE GRANADA

DOCTORAL THESIS

Experimental and analytical study of the hydrodynamics of swell and sea waves with partially reflective structures

Author:
Andrea M. LIRA LOARCA

Supervisors:
Asunción BAQUERIZO AZOFRA, PhD
Sandro LONGO, PhD

A thesis submitted in fulfillment of the requirements for the Dual Doctoral degree

in the

Doctoral Programme in Biogeochemical Fluid Dynamics and their Applications
University of Granada, Spain

and

Doctoral School in Engineering and Architecture
University of Parma, Italy

June 4, 2019

"Lo bello del arte es el experimento, la aventura, la búsqueda"

Augusto Monterroso

EXPERIMENTAL AND ANALYTICAL STUDY OF THE HYDRODYNAMICS OF SWELL AND SEA WAVES WITH PARTIALLY REFLECTIVE STRUCTURES

Abstract

The modeling of the interactions of different forcing agents, such as wind and waves, and maritime structures is a challenging problem with significant applications in coastal engineering leading to a usual implementation of complex numerical models. However, at the predesign stages of a project, there is need for fast, efficient and accurate analytical models that allow the search of the optimal configurations according to different design criteria. Furthermore, the studies regarding structural optimization, analytical and experimental, often do not consider the effect of wind forcing on the incident and reflected swell wave trains and the interaction with local wind-driven waves due to the complexity of the nonlinear interactions taking place.

Therefore, this thesis focuses on the study and modeling of wave-structure interactions of partially reflective maritime structures under swell and sea waves at different time scales, for which different methodologies are proposed and analyzed. Firstly, an analytical model for the oblique wave interaction of irregular waves with a maritime structure is proposed. The structure is delimited by a semi-submerged plate and a back wall enclosing a chamber. Then, a laboratory study of the same structure is carried out with experimental tests under paddle-generated regular and irregular waves in combination with wind–sea waves for different wind speeds (wind tunnel) to account for the interaction of swell and sea waves. The analytical and experimental analyses focus on the effect of the geometry of the system characterized in terms of its relative submergence d/h and relative width B/L and the effects of wind-driven waves superimposed on swell on the overall behavior of the system. Finally, a methodology for the long-term simulation of extreme events is derived and used as forcing conditions impinging on the structure. Simulations using Monte Carlo techniques are performed to assess the uncertainty of the results.

The analytical model provides a simple and efficient engineering tool to search for an optimal design (trade-off between performance and structural design) towards the goals of harbor tranquility in the far field region of the reflector, wave energy extraction in the inner chamber and structural safety analysis of the loads acting on the plate. It considers linear wave theory, taking into account the head loss due to the constriction of the flow. The results are compared to those obtained with computational fluid dynamics models, revealing that the proposed model is capable to efficiently describe the performance of these systems for weakly nonlinear incident waves.

The performance of the system is studied by means of the reflection and capture coefficients and the structural component is dealt with by analyzing the maximum loads on the plate. The results showed that the behavior of the system varies with a periodicity at $B\cos\theta/L = 0.5$. When dealing with irregular waves, the spectra at the seaward region and inside the chamber show a nodal and antinodal structure that varies with the distance to the reflector. This structure, as well as the phase lag between the free surface elevations at both sides of the plate, affects the total loads over the plate.

The experimental tests involving the combination of paddle-generated regular and irregular waves with wind–sea waves (wind tunnel) provide an added value to the research as there are not many research facilities where it is possible to have controlled conditions of wind and paddle-generated waves. For the experiments involving incident regular wave with a wave period similar to the 1^{st} natural period of the chamber, an amplification of wave energy in the seaward region is measured in the case of a relative submergence of $d/h = 0.58$, in agreement with the analytical model results. Wind–sea waves have a higher influence on the variation of the wave period of the waves seaward and leeward of the plate, and more so for the experiments with $T_{z_0}/T_1 \geq 1.5$. The influence of wind-driven waves on the overall performance of the system depends on the wave period of the swell wave.

In order to analyze the behavior of the system in its useful life and under extreme conditions, a methodology for the long-term simulation of extreme events including the temporal evolution is developed. Extreme events are defined in combination of the threshold, the minimum storm duration and interarrival times by means of goodness-of-fit testing. The multivariate statistical characterization of the different maritime variables and their temporal dependence is studied by a combination of mixed probability distribution functions, vector autoregressive and copula models proving to be an efficient and accurate model to simulate long time series of extreme events. By means of Monte Carlo techniques, a large number of simulations were performed and applied to the analytical model to analyze the long-term performance of the structure and the uncertainty associated with the analysis.

EXPERIMENTAL AND ANALYTICAL STUDY OF THE HYDRODYNAMICS OF SWELL AND SEA WAVES WITH PARTIALLY REFLECTIVE STRUCTURES

Resumen

El modelado de las interacciones entre diferentes agentes climáticos, como el viento y el oleaje, con diferentes estructuras marítimas, es un desafío con aplicaciones muy importantes en ingeniería costera que normalmente conlleva el uso de modelos numéricos complejos. Sin embargo, en las etapas de prediseño de un proyecto, se necesitan modelos analíticos rápidos, eficientes y precisos que permitan la búsqueda de las configuraciones óptimas de acuerdo con diferentes criterios de diseño. Además, los estudios de interacción oleaje–estructura, analíticos y experimentales, a menudo no consideran el efecto del forzamiento del viento en el oleaje incidente y reflejado ni la interacción con mar de viento local debido a la complejidad de las interacciones no lineales de los procesos físicos.

Por ello, esta tesis se centra en el estudio y modelado de la interacción oleaje–estructura en el caso de estructuras marítimas parcialmente reflejantes bajo la acción de mar de fondo (oleaje tipo *swell*) y mar de viento (oleaje tipo *sea*) a diferentes escalas temporales, para lo cual se proponen y estudian diferentes metodologías. En primer lugar, se define un modelo analítico para la interacción de oleaje irregular oblicuo con una estructura marítima. La estructura está delimitada por una placa semi–sumergida y una pared vertical impermeable. En segundo lugar, se lleva a cabo un estudio experimental de la misma estructura bajo la influencia de oleaje swell regular e irregular generado con palas (canal de oleaje) en combinación con oleaje sea para distintas velocidades de viento (túnel de viento). El análisis de los resultados obtenidos con el modelo analítico y el análisis experimental se centra en el efecto de la geometría del sistema caracterizado en términos de la sumergencia relativa d/h y el ancho relativo B/L del sistema, así como los efectos del oleaje tipo sea superpuesto al oleaje swell a una escala de ola individual y estado de mar. Finalmente, para el estudio de la estructura en su vida útil, se propone una metodología para la simulación a largo plazo de eventos extremos de clima marítimo que incluyen como condiciones de forzamiento en el análisis de la estructura. Se realizan simulaciones utilizando técnicas de Monte Carlo para evaluar la incertidumbre de los resultados.

El modelo analítico proporciona una herramienta de ingeniería simple y eficiente para la búsqueda de un diseño óptimo (compromiso entre rendimiento y diseño estructural) en términos de actividad portuaria (disminución de la agitación) en la región de campo lejano del reflector, extracción de energía undimotriz en la cámara interior y seguridad estructural del sistema por medio del análisis de las cargas que actúan sobre la placa. El modelo considera teoría de

onda lineal, teniendo en cuenta la pérdida de carga debida a la constricción del flujo. Los resultados se comparan con los obtenidos mediante modelos de dinámica de fluidos computacional, validando que el modelo propuesto es capaz de describir de manera eficiente el rendimiento del sistema para oleaje incidente débilmente no lineal.

El comportamiento del sistema se analiza por medio de los coeficientes de reflexión y captura y la componente estructural se estudia con las cargas máximas actuando en la placa. Los resultados mostraron que el comportamiento del sistema varía con una periodicidad en $B\cos\theta/L = 0.5$. En el caso de oleaje irregular, los espectros en la región a barlomar y sotamar muestran una estructura nodal y antinodal que varía con la distancia al reflector. Esta estructura, así como el desfase entre las elevaciones de la superficie libre a ambos lados de la placa, afectan las cargas totales actuando sobre la placa.

Los ensayos experimentales realizados con oleaje regular e irregular en combinación con oleaje sea (túnel de viento) proporcionaron un valor agregado a este trabajo, ya que no existen muchas instalaciones de laboratorio donde sea posible tener condiciones controladas de viento y oleaje. En el caso de los ensayos con oleaje regular con un período similar al primer período natural de la cámara, se obtiene una amplificación de la energía de onda en la región a barlomar para una sumergencia relativa de $d/h = 0.58$, en concordancia con los resultados obtenidos con el modelo analítico. El oleaje tipo sea tiene una mayor influencia en la variación del período de las olas a barlomar y sotamar de la placa, y más aún en los experimentos en los que $T_{z_0}/T_1 \geq 1.5$. La influencia del oleaje tipo sea en el rendimiento general del sistema depende del período de onda periódica.

Con el fin de analizar el comportamiento de la estructura durante toda su vida útil y en condiciones de régimen extremal, se desarrolla una metodología para la simulación a largo plazo de eventos de tormenta, incluyendo su evolución temporal. Los eventos extremos se definen considerando conjuntamente el umbral, la duración mínima de la tormenta y los tiempos de calma entre tormentas, mediante análisis de bondad del ajuste. La caracterización estadística multivariada de las diferentes variables marítimas y su dependencia temporal se estudia mediante una combinación de funciones de distribución de probabilidad mixtas, modelos vectoriales autorregresivos y modelos de cópula. Los resultados demuestran que se obtiene un modelo eficiente y preciso para la simulación de series temporales largas de eventos extremos. Mediante el uso de técnicas de Monte Carlo, se realizan una gran cantidad de simulaciones y se utilizan como condiciones de forzamiento al modelo analítico para analizar el rendimiento a largo plazo de la estructura y la incertidumbre asociada con el análisis.

Acknowledgements

I would like to express my deep gratitude to Profs. Asunción Baquerizo Azofra and Sandro Longo, my thesis supervisors, for their direction, encouragement and useful critiques. Without your trust, guidance and long hours of discussion, this thesis would have never been possible. Thank you, Asunción, for your empathy and respect and for the opportunity to work with you and develop myself as a scientist and researcher. I appreciate you always finding the time to assist me and encourage me in this work. Thank you, Sandro for the warm welcome and hospitality during my research stay at Parma and for bearing with me on the long research discussions.

I would like to offer my very great appreciation to Prof. Miguel Losada Rodríguez for welcoming me into his research group and passing on his knowledge and passion for the coastal engineering. Thank you, Miguel for your patience and for all the time you have spent giving me advice and scientific direction. It has been an honor to work with you, learn with you and I hope to continue doing so for many years to come.

I am grateful to Prof. Miguel Ortega Sánchez for introducing me to the research world back when I was finishing my Civil Engineering degree and for his encouragement to follow this line of work. My grateful thanks are also extended to Dr. María Clavero Gilabert for showing the world of laboratory experiments and allowing me to 'play' countless hours in the CIAO. This thesis was born from the excitement that the whole lab team passed on to me while doing my Masters' thesis.

A very special gratitude goes out to all the members (past and present) of the Fluid Dynamics Group of the University of Granada and the Department of Engineering and Architecture of the University of Parma. It was fantastic to have the opportunity to meet you and work with you. Special thanks for the, much needed, talks and laughs, that have seen me through long hours of work.

This thesis would have not been possible without the funding provided by the research group TEP-209 (Junta de Andalucía) and project AQUACLEW, part of ERA4CS, an ERA-NET initiative by JPI Climate co-funded by the European Union (Grant 690462). I wish to acknowledge the mobility grants given by the University of Granada PhD International Mobility Programme 2016/17, the Erasmus+ Programme KA1 (2017/18 – 2018/19) and the Campus of International Excellence of the Sea (CEIMAR).

And finally, last but by no means least, I am forever grateful to my family and friends, for being there for me. To my parents, you have encouraged me to work hard and press on, never doubting that I could accomplish anything I set my mind to. I can honestly say that this thesis would not exist if it weren't for your support and love in all the different stages of my life.

A mis padres

Contents

List of Figures

List of Tables

Introduction

State of the art review

The modeling of the interactions between maritime structures and forcing agents, such as waves and wind, is a challenging problem with important applications in coastal engineering (Sawaragi, 1995; Goda, 2000). In the last decades, environmentally friendly coastal structures, like partially submerged barriers, have become of great interest for environmental protection, recreation or wave energy extraction facilities. This type of barriers can reduce the wave energy inside a harbor or a marina while allowing sediment and water exchanges (Koutandos et al., 2005; Liu and Al-Banaa, 2004), with more research being done towards the design optimization regarding space limitations and the need to control wave reflection and incident sea wave dissipation (Liu and Faraci, 2014; Faraci et al., 2015). At the same time, these structures can be designed towards wave energy extraction when considering an oscillating water column (OWC) wave energy converter (WEC) therefore combining the the design of breakwaters capable of hosting power generation structures (Mustapa et al., 2017; Pawitan et al., 2019). With that purpose, many experimental and theoretical studies have been performed to evaluate the efficiency and hydrodynamic behavior of partially reflective structures under different forcing conditions.

Analytical and experimental modeling of partially reflective structures

The complexity of the processes taking place on the interaction of oblique incident waves with partially reflective maritime structures often leads to the adoption of complex numerical models. However, due to their high computational cost, these codes are not practical during the decision-making or the first stages of the project where different alternatives need to be considered. Therefore, the use of accurate, fast and efficient analytical models is essential to assess the optimal parameters of the system during the predesign phase (Liu and Li, 2013; Monk et al., 2013).

Different researchers have analyzed the hydrodynamical behavior of various marine structures using analytical models. In general, these models consider the

velocity potential problem and search for solutions based on the method of eigenfunctions expansion with the main differences between them found in the wave type and matching conditions.

Dean, 1945; Ursell and Dean, 1947 first studied the wave reflection of incident progressive waves on a fully and partially submerged vertical barrier. Losada et al., 1992; Losada et al., 1993b studied the modeling of vertical thin barriers as breakwaters by means of an analytical model. Losada et al., 1992 studied the linear theory for periodic waves impinging obliquely on a vertical thin barrier, using the eigenfunction expansion method. This study was then extended to analyze oblique modulated waves (Losada et al., 1993b). Linear theory was also applied to analyze the scattering of irregular waves impinging on fixed vertical thin barriers, with a good agreement between the analytical model and experimental data by other authors (Losada et al., 1994).

Other type of energy dissipation structures are slotted walls, in which it is necessary to consider the energy dissipation mechanism in the matching conditions. This is the case of a Jarlan-type breakwater that consists of a perforated front wall and a vertical impermeable back wall (Jarlan, 1961). Bennett et al., 1992 developed a theory for calculating the reflection coefficient based on the study of energy dissipation by Mei et al., 1974; Mei, 1989 which used a semi-empirical description of eddy-shedding at the perforated front wall. Isaacson et al., 1998 analyzed the wave interactions with a thin vertical slotted barrier, taking into account the energy dissipation according to Sollitt and Cross, 1972. More recently, Liu et al., 2007 analyzed an infinite array of partially perforated caissons with transverse sidewalls following the work by Yu, 1995 to define the boundary conditions along the perforated front walls. They obtained the values of the main influencing factors for which the hydrodynamic performance was optimum. Liu and Faraci, 2014 suggested a sloped rock-filled core between a rigid vertical barrier with an open window and an impermeable wall. A semi-analytical solution for normal incidence was proposed and validated using the results from physical model tests (Faraci et al., 2012), obtaining an excellent agreement between the two models.

These type of structures have a versatile character and can be aimed at protecting a harbor or as wave energy converters as studied by Boccotti, 2012; Falcão, 2000; Torre-Enciso et al., 2009. Therefore, there is still need for an efficient tool which allows to search for an optimal configuration concerning different design criteria such as harbor tranquility, wave energy extraction and structural safety that usually implies a trade-off between performance and structural design. This work proposes an analytical model for the interaction of regular and irregular waves with a simple maritime structure of a chamber delimited by a thin vertical semi-submerged barrier and an impermeable back wall.

Regarding the experimental studies on semi-submerged barriers, Kriebel et al., 1999 studied their efficiency under regular and irregular waves in terms of the transmission and reflection coefficients, while Liu and Al-Banaa, 2004 carried out experiments under solitary waves focusing on the wave forces acting on the barrier. Koutandos et al., 2005 presented an experimental study of waves acting on a partially submerged breakwater with four different configurations, including a single fixed barrier under regular and irregular waves in shallow and intermediate water. The results showed the effect of the various configurations on transmission, reflection and energy dissipation, highlighting that the main governing design parameter could change depending on forcing conditions (for short waves the main parameter was the submergence of the barrier, for long waves it was the width of the chamber). Due to the limitations of the laboratory facilities, most of the experimental studies on wave interaction with maritime structures such as the ones mentioned, are limited to paddle–generated regular or irregular waves.

However, in nature we find swell waves coexisting with wind-driven waves. Swell waves are described as long-period waves that have been traveling for long distances and in absence of wind can be locally analyzed by means of standard wave spectra. Wind–sea waves are actively growing due to the forcing action from the local wind, and are characterized as non-regular waves consisting of a spectrum in continuous evolution. The wave growth mechanism forced by local wind has been a very debated subject among researchers with different analysis performed to study the vertical momentum transfer in wind–sea waves under different conditions (Addona et al., 2018). This transfer is quite important to describe the flow field and to quantify all the exchanges inside the water column and at the interface with the air, but its analysis is quite difficult due to the complexity of field measurements or the reproducibility of the conditions in laboratory facilities.

This is the reason why most of the experimental studies on wave interaction with maritime structures do not consider the effect of wind forcing on both the incident and reflected swell wave trains, the interaction of the driven sea waves with the structure and the nonlinear interaction between the different wave field components. Therefore, there is still need for further research on the wave-structure interaction under wind driven waves superimposed on swell, taking into account their intrinsic irregular and random complex nature.

Simulation of extreme events and their evolution

The design of coastal and port infrastructures usually considers wave height as one of the main maritime variables that triggers successive stress states affecting their operationality, serviceability and reliability. Most of the time, the focus is

on the ultimate limit state failure modes, which produce the collapse of the structure and/or on the operational stoppage modes. For the first ones, the classical approach fits an extreme probabilistic model to the extreme conditions such as annual maximum significant wave height or POT (Peaks–Over–Threshold), and the design values are then obtained for a certain return period. The selection of this value is aimed at ensuring the safety of the structure in regards of its main failure depending on the admissible consequences from it. The 'mean' regime is sometimes used to assess the operational stoppage modes. In more modern approaches, there is also the need to assess the loss of functionality of the structure, required to analyze the progression of damage which is closely related to the storm evolution and duration (Borgman, 1969).

In coastal and maritime engineering, storms are customarily defined as independent events during which the significant wave height exceeds a certain threshold $H_{s,u}$ which is related to the minimum admissible damage of a sea state. The traditional POT analysis is based on the definition of this threshold and also on the minimum time span between consecutive events, δ_0, required to guarantee their independence. The selection of the threshold is subjective, requiring a balance between sample selection bias and variance. That is, a high enough value is required to guarantee the independence of consecutive events and the validity of the model, but a too high threshold will lead to few events resulting in large variance (Méndez et al., 2006). The definition of the minimum interarrival time varies in the literature from hours to days depending on the region and is always considered a constant value, i.e. is independent from the selected threshold (Méndez et al., 2006; Li et al., 2014). However, there are several ($H_{s,u}$, δ_0) combinations capable of ensuring, with a reasonable reliability, storm independence and the validity of the model. There is still need to study the selection of suitable threshold and interarrival time values and their relation (Solari et al., 2017).

The study of damage progression models of maritime structures requires not only a definition of the storm in terms of its duration and peak value but a characterization of its evolution in time. Several authors have used an idealized "storm shape" such as a triangular geometry to characterize the storm evolution, and searched for its equivalence with a real storm by comparing their magnitude, power or duration (Boccotti, 2000; Corbella and Stretch, 2012). However, the storm history evolution of the sea states in sea and swell waves is not adequately reproduced by these theoretical models and is not enough for applications where the features and evolution of the metocean time series are relevant (Martín-Soldevilla et al., 2015; Jäger et al., 2018).

Other works propose different methodologies for simulating time-dependent series for meteorological and oceanic variables based on: (i) theoretical Poisson processes; (ii) multidimensional copulas; and/or (iii) vectorial autoregressive models (VAR). Payo et al., 2008 proposed a methodology to randomly simulate

the sequence of storms and calms based on historical climate data, assuming that the occurrence of sea states over a relatively high significant wave height threshold is a Poisson process and, accordingly, the interarrival time between consecutive storms follows an exponential distribution. They simulated the peaks and duration of the storms by means of their joint distribution function and the shapes using empirical orthogonal functions. Copulas models have been widely used for multivariate simulations of metocean variables, for a detailed review and comparison between the different families, the reader is referred to Li et al., 2018.

Recently there has been more research towards the analysis and simulation of multivariate storm events and long-term time series of climate data with different statistical approaches. However, due to the interdependency and random character between variables, to provide a multivariate statistical model still proves a challenging task (Li et al., 2018). The modeling of complete time series increases the computational cost but allows for the characterization of the evolution of metocean variables (Jäger et al., 2018). Solari and Gelder, 2011 used non-stationary mixture distributions and a VAR model to simulate multivariate time series met-ocean variables.

In some of the previous works, the wave direction was not included in the multivariate analysis or was studied independently justified by (i) limitations in dataset availability, (ii) waves impinging from a limited range of directions, (ii) weak correlation between significant wave height and wave direction (Li et al., 2014; Corbella and Stretch, 2013). However, for the study of certain processes, the wave direction cannot be disregarded, e.g. when wave reflection has a key role as in the study of breakwaters damage (Vílchez et al., 2016; Folgueras et al., 2016).

Objectives

This PhD thesis was devised in light of the need of an increased understanding and better modeling of maritime structures taking into account the forces exerted by highly nonlinear waves and the kinematics and dynamics under wind–driven waves at different time scales. These vary from the individual waves and the sea state, to full storm events and up to the useful life of the structure on a long-term basis. For this purpose, a series of specific goals were addressed:

I. Set-up and validation of an analytical model for the optimization of maritime structures under regular and irregular waves forcings.

II. Analysis of the hydrodynamics of the interaction of swell and sea waves with partially reflective structures by laboratory experiments.

III. Study of the suitable and rigorous selection of the parameters that define extreme events.

IV. Development of a methodology for the analysis and simulation of multivariate long-term time series of extreme events for its application, e.g., in damage evolution models of maritime structures.

Thesis outline

This thesis is structured in two main parts,

- Part I describes the methodologies developed and used in the thesis
- Part II presents the validation and main results of application.

In Part I, Chapter 1 introduces an analytical model for the interaction of oblique incident regular waves with a maritime structure and its extension to irregular waves. Chapter 2 describes the experimental set-up and protocol for the laboratory experiments including paddle-generated regular and irregular waves in combination with wind–sea waves. Finally, Chapter 3, introduces the statistical methodology for long-term simulation of extreme events and their temporal evolution.

In Part II, Chapter 4 presents the validation of the analytical model in comparison with numerical model results and the comparison between the analytical and experimental studies. Chapter 5 describes the results of the analytical model under regular and irregular waves for the optimization of the system. Chapter 6 analyzes the experimental results for wind–sea waves with and without the combination of paddle-generated regular and irregular waves. Chapter 7 includes an example of application for the design of a maritime structure under extreme events.

The main conclusions of the thesis and some future lines of work are presented in the last chapter and finally, some additional experimental results are included in Appendix A.

Publications

The work done throughout this thesis has resulted in the following publications:

Journal Papers

- M.L. Jalón, **A. Lira-Loarca**, A. Baquerizo, and M.A. Losada (2019). "An analytical model for oblique wave interaction with a partially reflective harbor structure". In: *Coastal Engineering* 143, pp. 38 –49. ISSN: 0378-3839. DOI: https://doi.org/10.1016/j.coastaleng.2018.10.015

- **A. Lira-Loarca**, A. Baquerizo, and S. Longo (2019a). "Interaction of Swell and Sea Waves with Partially Reflective Structures for Possible Engineering Applications". In: *Journal of Marine Science and Engineering* 7.2. ISSN: 2077-1312. DOI: 10.3390/jmse7020031

International Conferences

- **A. Lira-Loarca**, M. Cobos, A. Baquerizo, and M.A. Losada (2018a). "A multivariate statistical model to simulate storm evolution". In: *Proceedings of the 36th International Conference on Coastal Engineering (ICCE18)*. Baltimore, Maryland, USA

- **A. Lira-Loarca**, M. Cobos, A. Baquerizo, and M.A. Losada (2018b). "Multivariate forecasting of extreme wave climate and storm evolution". In: *Proceedings of the International Conference on Time Series and Forecasting (ITISE18)*. Granada, Spain

- **A. Lira-Loarca**, A. Baquerizo, and S. Longo (2018c). "Wind-wave interaction with a vertical semi-immersed barrier". In: *Proceedings of the 7th International Conference on the Application of Physical Modelling in Coastal and Port Engineering and Science (Coastlab18)*. Santander, Spain

Spanish Conferences

- **A. Lira-Loarca**, A. Baquerizo, and M.A. Losada (2019b). "Un estudio sobre el control de la agitación en la dársena de Guadiaro en el Puerto de Málaga". In: *XV Jornadas Españolas de Ingeniería de Costas y Puertos*. Málaga, Spain

Part I

Methods

Chapter 1

Analytical model for regular and irregular swell waves

Note

The present chapter presents the theoretical model published on:

M.L. Jalón, **A. Lira-Loarca**, A. Baquerizo, and M.A. Losada (2019). "An analytical model for oblique wave interaction with a partially reflective harbor structure". In: *Coastal Engineering* 143, pp. 38 –49. ISSN: 0378-3839. DOI: `https://doi.org/10.1016/j.coastaleng.2018.10.015`

This chapter presents an analytical model for the study of the interaction of oblique incident regular waves with a maritime structure considering linear wave theory and taking into account the head loss due to the constriction of the flow. The theoretical formulation is presented on §1.1 and the main hydrodynamic performance on §1.2. The extension of the model to study irregular waves is introduced on §1.3.

1.1 Theoretical formulation

The theoretical formulation for regular waves with and without head loss consideration was presented in detail in Jalón, 2016. For clarity, this chapter includes an overview of the general formulation.

This model considers the interaction of a monochromatic wave train impinging on a maritime structure on a horizontal bed. The structure is composed by a fixed thin vertical barrier with a submergence d and at a distance B from a solid

and vertical back wall (Figure 1.1). As observed in the Figure 1.1, the origin of the coordinate system is located on the barrier at the still water level (SWL). The x–axis is positive in the leeward direction (towards the back wall), the y–axis is the horizontal axis lying on the plate and the z–axis is pointing up. The incident wave has an amplitude A_0, an angular frequency ω and is propagating with an incident wave angle θ. For simplicity of the model, it is considered that the barrier has an infinite width (y-axis).

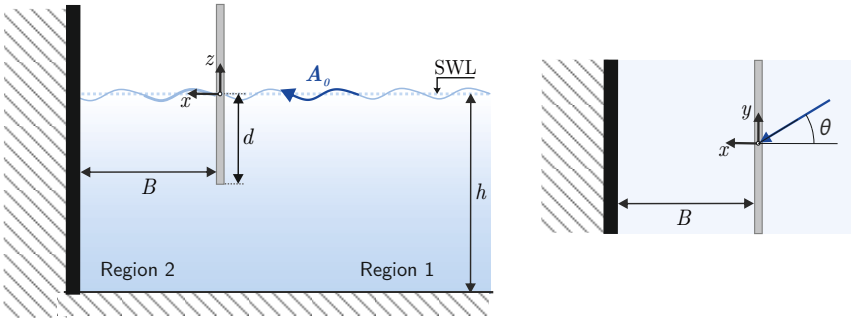

FIGURE 1.1: Definition sketch of the maritime structure and coordinate system.

The problem is formulated in terms of the velocity potential satisfying the Laplace equation in the fluid, the mixed boundary condition on the free surface and the kinematic conditions at the boundaries, by assuming non-viscous and incompressible fluid and irrotational flow. The plate divides the domain into two regions: (1) the seaward region ($x < 0$) with velocity potential Φ_1 and (2) the leeward region ($0 < x < B$) with velocity potential Φ_2. The velocity potential Φ_n is defined as follows,

$$\Phi_n(x, y, z, t) = \Re\{\phi_n(x, z)e^{i(\lambda y - \omega t)}\}, \tag{1.1}$$

where $n = 1, 2$ (seaward and leeward region), $\Re\{.\}$ depicts the real part, t is the time, and $\lambda = k_0 \sin\theta$ with k_0 being the incident wavenumber corresponding to the real solution k of the dispersion equation,

$$\frac{\omega^2}{g} = k \tanh(kh). \tag{1.2}$$

The velocity potential Φ_n, results from superposing a partial standing wave and a set of evanescent modes N_l (Losada et al., 1993a). This modes contain the terms that decay far from the plate and far from the wall, respectively and correspond to the eigenfunctions of the problem in z derived from the method of separation of variables associated to the pure imaginary roots of the dispersion

equation ($k_l = ik'_l, l > 0$ with k'_l a positive real number). $\phi_n(x,z)$ is then expressed as:

$$\begin{aligned}\phi_1(x,z) &= A_0 I_0(z) e^{i\Gamma_0 x} + \sum_{l=0}^{\infty} D_l I_l(z)\, e^{-i\Gamma_l x} \qquad \text{for } x < 0,\\ \phi_2(x,z) &= \sum_{l=0}^{\infty} C_l I_l(z) \left(e^{i\Gamma_l x} + e^{-i\Gamma_l (x-2B)}\right) \quad \text{for } 0 < x < B,\end{aligned} \tag{1.3}$$

where,

$$I_l(z) = \frac{-ig}{\omega} \frac{\cosh(k_l(h+z))}{\cosh(k_l h)}, \tag{1.4}$$

$$\Gamma_l = \sqrt{k_l^2 - \lambda^2}. \tag{1.5}$$

In Equation 1.3 I_0 is the depth dependent function and Γ_0 is the component in the x–axis of the wavenumber vector of the propagating modes of the incident and reflected wave ($\Gamma_0 = k_0 \cos\theta$). Regarding the wave amplitudes in the seaward region, D_0 is the complex amplitude of the reflected wave and D_l ($l > 0$) denotes the evanescent modes. In the leeward region, the solution includes the complex amplitude of the propagating mode C_0 and a series of evanescent modes given by C_l ($l > 0$). Φ_2 already meets the flux condition at the wall ($x = B$).

Considering that the solutions in both regions must be equal at the common interface, the velocity potentials must satisfy the following boundary conditions:

(a) The horizontal speeds must coincide in the aperture ($-h < z < -d$).

(b) There is no flow going through the plate ($-d < z < 0$).

(c) The surface elevations η at both sides of the barrier differ in a term representing the momentum loss.

The momentum loss is considered as a quadratic head loss following the model by Mei et al., 1974:

$$\eta_1(x,z,t) - \eta_2(x,z,t) = \frac{\xi}{2g} u_2(x,z,t)|u_2(x,z,t)| + \frac{\Upsilon_i}{g} \frac{\partial u_2(x,z,t)}{\partial t}, \tag{1.6}$$

where u_2 is the horizontal velocity at the gap, ξ is the friction coefficient depending primarily on the geometry of the hole, and Υ_i is an inertia coefficient that can be empirically obtained. Equation (1.6) is obtained from the momentum balance and the continuity equation in a control volume centered at the plate. The terms in the left side of the equation are, therefore, proportional to the pressure terms

in the Bernoulli equation. The first term in the right side derives from the convective terms while the second one is linked to the local acceleration and is small compared to the convective term. This model has been successfully applied to other analogous problems (Roldán, A.J. and Losada, M.A. and Losada, I.J., 1992; Baquerizo et al., 2002).

ξ is formulated using an empirical expression valid for sharp-edged orifices (Mei et al., 2005):

$$\xi = \left(\frac{1}{C\epsilon} - 1\right)^2, \tag{1.7}$$

where $C = 0.6 + 0.4\epsilon^3$ and $\epsilon = \frac{h-d}{h}$ is the relative aperture.

The friction term can be linearized by introducing an equivalent friction coefficient ζ_e related to the velocity at the aperture u_2. The linearized term must give the same energy loss per period than the quadratic one. An error e, introduced by the linearization process, can be defined as:

$$e = \frac{\xi}{2g} u_2|u_2| - \zeta_e u_2. \tag{1.8}$$

ζ_e is chosen so that the mean square of the error is minumum. Following Mei et al., 2005, time-averaging e^2 gives,

$$\overline{e^2} = \overline{\left(\frac{\xi}{2g} u_2|u_2|\right)^2} - \frac{\xi}{g}\zeta_e \overline{u_2^2|u_2|} + \zeta_e^2 \overline{u_2^2}, \tag{1.9}$$

where the overbar indicates the average over one wave period.

The minimum value of Equation 1.9 is found by equating $\frac{\partial \overline{e^2}}{\partial \zeta_e} = 0$ and by approximating u_2 by a simple harmonic, which leads to the following expression for ζ_e:

$$\zeta_e(x,z) = \frac{4\xi}{3\pi}|u_2(x,z)|. \tag{1.10}$$

In Equation 1.10, $|u_2(x,z)| \approx |C_0 I_0(z) i\Gamma_0 (e^{i\Gamma_0 x} - e^{-i\Gamma_0(x-2B)})|$ obtained from the velocity potential ϕ. ζ_e depends on the amplitude of the oscillation and, given

that u_2 varies with depth, it also depends on the coordinate z. Finally, the matching conditions at the plate, $x = 0$, are:

$$\frac{\partial \phi_1}{\partial x} = \frac{\partial \phi_2}{\partial x} \qquad -h < z < -d \tag{1.11a}$$

$$\frac{\partial \phi_1}{\partial x} = \frac{\partial \phi_2}{\partial x} = 0 \qquad -d < z < 0 \tag{1.11b}$$

$$\phi_1(x,z) - \phi_2(x,z) = -\frac{i}{\omega}\zeta_e(x,z)\phi_{2,x}(x,z) \qquad -h < z < -d \tag{1.11c}$$

Following Losada et al., 1992 and given the fact that $\{I_l(z)\}_{l=1}^{\infty}$ is a set of orthogonal functions, the condition of equal speeds at the gap is met if $D_l = A_0 - C_l(1 - e^{i2B\Gamma_l})$, $l = 0$ and $D_l = -C_l(1 - e^{i2B\Gamma_l})$, $l > 0$. In order to simultaneously solve the other two matching conditions linked to the impermeability of the plate and the head loss at the gap, their left hand terms are truncated to N_l terms and combined into the following piecewise function $G(z)$:

$$G(z) = \begin{cases} -2A_0 I_0(z) + \sum_{l=0}^{N_l} C_l I_l(z) \left[2 + \Gamma_l \frac{\zeta_e}{\omega}(1 - e^{i2B\Gamma_l})\right] & \text{for } -h < z < -d \\ \sum_{l=0}^{N_l} C_l I_l(z) i\Gamma_l \left(1 - e^{i2B\Gamma_l}\right) & \text{for } -d < z < 0 \end{cases} \tag{1.12}$$

In order to have a null value of the modulus of the complex function $G(z)$, the coefficients C_l that minimize the following integral are searched:

$$\int_{-h}^{0} |G(z)|^2 dz. \tag{1.13}$$

Equation (1.13) leads to the following set of equations:

$$\int_{-h}^{0} G(z)^* \frac{\partial G(z)}{\partial C_l} dz = 0 \quad \text{for } l = 0, 1, ..., N_l, \tag{1.14}$$

where * indicates the complex conjugate.

An iterative procedure is required to solve the problem (Eq. 1.14) given that $\zeta_e(z)$ depends on the amplitude of the horizontal velocity $|u_2(x = 0, z)|$ and that this is an unknown variable of the problem.

1.2 Hydrodynamic performance

Different kinematic and dynamic properties of the system (see Figure 1.2) can be obtained from the velocity potential and the C_l coefficients.

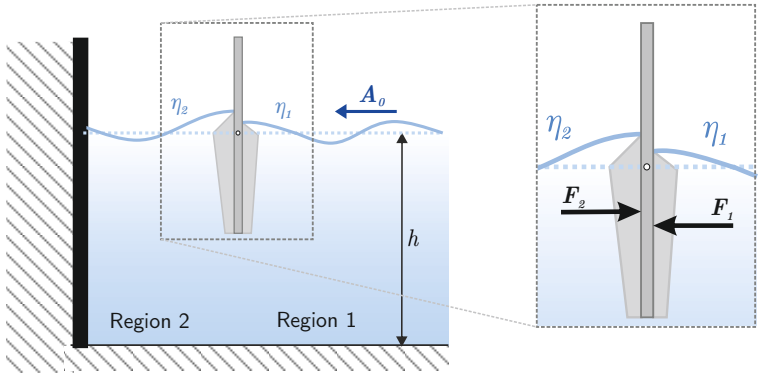

FIGURE 1.2: Definition sketch of free surface elevation, pressures and forces on the structure.

The equations of the free surface elevation for region 1 ($x < 0$) and region 2 ($0 < x < B$) read,

$$\begin{aligned}\eta_1(x,y,t) &= \Re\left\{\left[A_0(e^{i\Gamma_0 x} + e^{-i\Gamma_0 x}) - \sum_{l=0}^{N_l} C_l(1 - e^{i2B\Gamma_l})e^{-i\Gamma_l x}\right] e^{i(\lambda y - \omega t)}\right\} \\ \eta_2(x,y,t) &= \Re\left\{\sum_{l=0}^{N_l} C_l\left(e^{i\Gamma_l x} + e^{-i\Gamma_l(x-2B)}\right) e^{i(\lambda y - \omega t)}\right\}\end{aligned} \tag{1.15}$$

The complex reflection coefficient $\mathbb{K}_\mathbb{R}$ and the complex capture coefficient $\mathbb{K}_\mathbb{C}$, can be defined with respect to incident wave amplitude A_0 and the complex amplitude C_0 of the propagating wave inside the chamber.

The modulus of the reflection coefficient, K_R, is defined as,

$$K_R = |\mathbb{K}_\mathbb{R}| = \frac{|A_0 - C_0(1 - e^{i2B\Gamma_0})|}{|A_0|}, \tag{1.16}$$

and its phase is given by

$$\varphi_R = \mathrm{Arg}(\mathbb{K}_\mathbb{R}) = \mathrm{atan2}(\Im\{\mathbb{K}_\mathbb{R}\}, \Re\{\mathbb{K}_\mathbb{R}\}). \tag{1.17}$$

The modulus of the capture coefficient, K_C, reads,

$$K_C = \frac{|C_0|}{|A_0|}, \tag{1.18}$$

and the phase is defined as

$$\varphi_C = \mathrm{Arg}(\mathbb{K}_\mathbf{C}) = \mathrm{atan2}(\Im\{\mathbb{K}_\mathbf{C}\}, \Re\{\mathbb{K}_\mathbf{C}\}). \tag{1.19}$$

The ratio between the mean wave amplitude inside the chamber and the incident wave amplitude, defines an amplification factor Q,

$$Q = \frac{1}{B|A_0|}\int_0^B |\eta_2| dx. \tag{1.20}$$

The phase lag Ψ is defined as

$$\Psi = \omega t_{max}, \tag{1.21}$$

where t_{max} is the time difference of the maximum surface elevation at $x = 0$.

The pressure field associated with the surface elevation in each region (Figure 1.2) can be defined as:

$$P_n(z,t) = \begin{cases} \rho_w g\left(\frac{cosh(k(h+z))}{cosh(kh)}\eta_n - z\right) & z \leq 0 \\ \rho_w g\left(\eta_n - z\right) & z > 0 \end{cases} \quad n = 1,2 \tag{1.22}$$

where ρ_w is the water density and η_n is the free surface elevation at the plate for each region.

By integrating the pressure over depth per unit width of plate, the instantaneous force exerted on the plate can be obtained,

$$F_t(t) = F_1(t) - F_2(t) = \int_{-d}^{\eta_1} P_1(z,t)dz - \int_{-d}^{\eta_2} P_2(z,t)dz. \tag{1.23}$$

Leeward-acting forces F_l (forces exerted towards the chamber) correspond to positive values of the total force ($F_1 > F_2$) whereas negative values ($F_2 > F_1$) correspond to seaward-acting forces F_s. The peak forces are obtained as the maximum and minimum values of the total force in a wave period T and correlate to the maximum values of the leeward-acting and seaward-acting forces, respectively.

1.3 Extension to irregular waves

There are several ways to calculate the characteristics of the hydrodynamics for irregular waves using regular wave models (Huang et al., 2011). In this case, since linear wave theory has been used, it can be assumed that the irregular sea state is the result of the superposition of a number of harmonic components. For an incident spectrum $S(\omega)$, the range of angular frequencies of interest is divided into N_j bands $(\omega_{j-1}, \omega_j], j = 1, ..., N_j$ of equal width $\Delta\omega = \omega_j - \omega_{j-1}$ with potential

functions $\Phi_{n,j}$ that satisfy the governing equations, the boundary conditions and the matching conditions as explained in sections 1.1-1.2. The resulting velocity potential Φ_n then reads,

$$\Phi_n(x,y,z,t) = \sum_{j=1}^{N_j} \Phi_{n,j}(x,y,z,t) = \Re\left\{ \sum_{j=1}^{N_j} \phi_{n,j}(x,z) e^{i(\lambda_j y - \omega_j t)} \right\} \quad n = 1,2. \tag{1.24}$$

The incident irregular wave train is the superposition of regular wave components of angular frequencies ω_j and complex amplitudes A_0^j given by

$$A_{0,j} = |A_{0,j}| e^{i\varphi_j} = \sqrt{2S(\omega_j)\Delta\omega_j} e^{i\varphi_j}, \quad j = 1,2,...,N_j, \tag{1.25}$$

where the phases φ_j are randomly obtained from a uniform distribution over $[0, 2\pi]$.

It is assumed that the incident wave energy is distributed in a range of frequencies (ω_L, ω_H) therefore neglecting a percentage of energy in the lowest and highest frequencies (Liu et al., 2008). The corresponding surface elevation and wave forces time series for each region can be obtained by solving the equations of sections 1.1-1.2 for each component and then considering the superposition of them to obtain the total values.

Chapter 2

Experimental study for swell and sea waves

Note

This chapter presents the experimental methodology published on:

A. Lira-Loarca, A. Baquerizo, and S. Longo (2018c). "Wind-wave interaction with a vertical semi-immersed barrier". In: *Proceedings of the 7th International Conference on the Application of Physical Modelling in Coastal and Port Engineering and Science (Coastlab18)*. Santander, Spain

A. Lira-Loarca, A. Baquerizo, and S. Longo (2019a). "Interaction of Swell and Sea Waves with Partially Reflective Structures for Possible Engineering Applications". In: *Journal of Marine Science and Engineering* 7.2. ISSN: 2077-1312. DOI: 10.3390/jmse7020031

This chapter presents the experimental study of the interaction of a paddle-generated regular and irregular waves in combination wind–sea waves generated with the wind tunnel with a maritime structure. The laboratory facility and the experimental set-up are presented on §2.1 while the experimental protocol is introduced on §2.2. The methodology for data analysis and definition of the main variables are presented on §2.3.

2.1 Experimental Facility

An experimental study was carried out in the Atmosphere-Ocean Interaction Flume (CIAO) of the Andalusian Institute for Earth System Research, Granada, Spain (Figure 2.1). This facility is dedicated to the study of the coupling of processes between the ocean and the atmosphere focusing on the air-sea exchange

of energy, mass and momentum. These processes are particularly important and of interest to many scientific disciplines such as climate forecast, wave breaking, cloud formation, hurricane forecast and statistical wave forecast, among others (Nieto et al., 2015).

The flume is 16 m long, 1 m wide and designed for a water depth of $\approx$ 70 cm. This facility is equipped with different systems that allow the generation of the following processes:

- Waves
  - Through wind generation
  - Through wave paddles (upwind or downwind)
- Wind
- Currents
- Rain

The wave generation through wave paddle consists of two piston-type wavemakers, one at each end of the flume and equipped with an active wave absorption system. Therefore, unwanted re-reflections of waves at the generating paddle can be avoided as the secondary paddle compensates for the reflected waves according to simultaneous wave measurements (for a detailed description of the active absorption system, the reader is referred to Lykke Andersen et al., 2016). The system allows the generation of regular up to second order and irregular waves, parametric or user-defined spectra, solitary waves and user-defined time series with wave periods in the range of 1-5 seconds and wave heights up to 25 cm.

The wind generation system is a 24 m long closed-circuit wind tunnel with mean wind speed at start of the test section —representative of U_{10} conditions in prototype— up to 12 m/s, which can generate waves with an effective fetch length of up to 12 m. The two wavemakers allow the generation of waves following or opposing the wind direction.

The current-generation system is composed by two external pumps which can create longitudinal currents of up to 0.75 m/s in both directions of the flume. Lastly, the facility is equipped with a rain generator at the mid–section of the flume and allowing for the generation of rain with intensity of 75-300 mm/h.

To carry out the experiments presented in this study, we used the wave and wind generation systems allowing the combination of regular, irregular and wind-driven waves. The current and rain generation systems were kept off during the duration of the experiments.

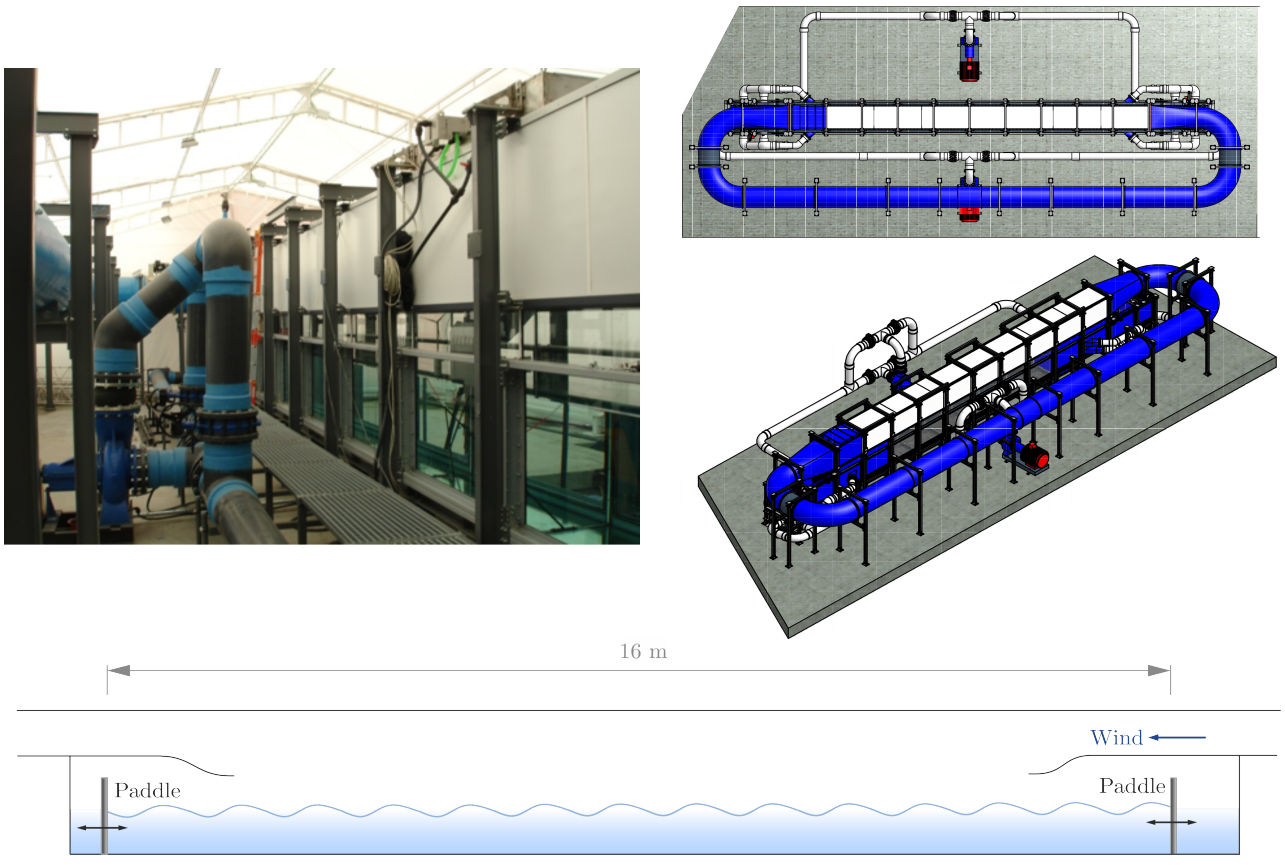

FIGURE 2.1: Atmosphere-Ocean Interaction Flume (CIAO)

2.1.1 Atmosphere-Ocean Interaction Flume (CIAO) calibration

Wave generation

Prior to the installation of the OWC device, in order to analyze the behavior of the system and the reflection performance of the active absorption system, a calibration of the CIAO was done using four wave gauges (Figure 2.2).

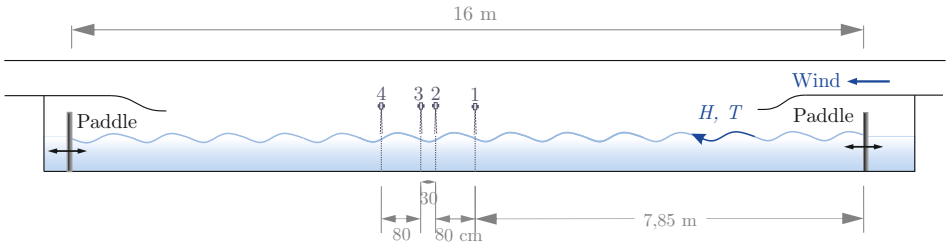

FIGURE 2.2: Side view of CIAO and calibration setup

The tests were done under paddle-generated regular waves with active absorption with different wave periods T ranging from 1 to 5 seconds. The tested wave heights H were obtained according to Biesel equation for the cases $S_0/h =$ 0.1 and 0.2,

$$\frac{H}{S_0} = \frac{4\sinh^2(k_0 h)}{\sinh(2k_0 h) + 2k_0 h}, \tag{2.1}$$

where S_0 is the wavemaker stroke and k_0 is the wavenumber. Figure 2.3 presents the results of the reflection coefficient and the flume calibration. It can be observed that the reflection coefficient is under 10% with minimum values of $\approx$ 5%. The experimental results show a good agreement with the theoretical values. For more details on the flume calibration, the reader is referred to Nieto et al., 2015; Lira-Loarca et al., 2016.

Wind generation

Measurements of wind speed were collected using a Pitot tube for different rotation rates (RPM=40, 60, 80, 100%) of the wind turbine, at a section located $\approx$ 10 m from the wind tunnel exit. Measurements were taken for different z–points in the air column for $\approx$ 60 s with a data rate of 1 kHz. Figure 2.4 presents the wind profile for the different wind speed tests where a log-profile can be observed up to a certain height from where it becomes constant. The wind speed for which the profile becomes constant is then defined as the representative wind speed U_{ref} of the experiments —representative of U_{10} conditions in prototype—.

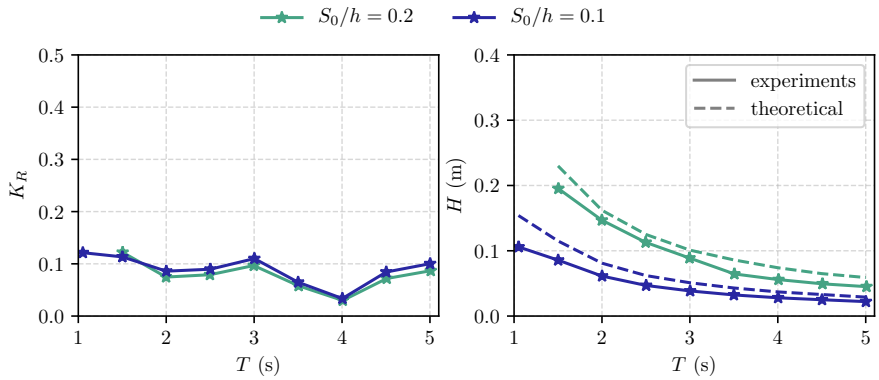

FIGURE 2.3: Reflection coefficients and flume calibration

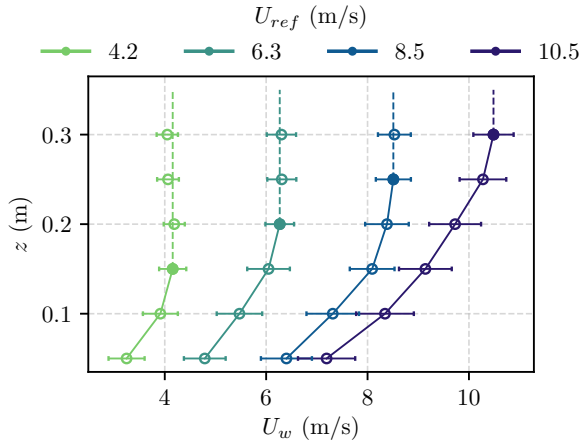

FIGURE 2.4: Wind speed profiles (symbols and error bars) for different rotation rates of the wind turbine (colors). The filled symbol indicates the z–position where the profile becomes constant (dashed line). The origin of the z-axis is at the SWL.

The friction velocity u_* can be estimated as,

$$u_* = \sqrt{C_D} U_w, \tag{2.2}$$

where C_D is the drag coefficient, approximated by the linear relation $C_D \approx (0.8 + 0.065U_w) \cdot 10^{-3}$ (Massel, 1996). For the representative wind speeds obtained in Figure 2.4, $U_{ref} = 4.2, 6.3, 8.5, 10.5$ m/s, values of $u_* = 0.14, 0.22, 0.31, 0.40$ m/s are obtained.

Smooth flow is characterized by $\mathrm{Re} \lessapprox 0.13$ whereas fully rough turbulent flow has values $\mathrm{Re} \gtrapprox 2.5$ (Kraus and Businger, 1995). The roughness Reynolds number (Massel, 1996) is defined as,

$$\mathrm{Re}_{z_0} = z_0 \frac{u_*}{\nu_a}, \tag{2.3}$$

where ν_a is the kinematic viscosity and z_0 is the roughness length given by Charnock's formula,

$$z_0 = m \frac{u_*^2}{g}, \tag{2.4}$$

with m in the range of $0.3 \cdot 10^{-2} - 0.3 \cdot 10^{-2}$. Considering $m = 0.021$ (Massel, 1996), $z_0 = 4.05 \cdot 10^{-5}$ is obtained for the lowest $u_* = 0.14$ m/s and $z_0 = 3.5 \cdot 10^{-4}$ is obtained for $u_* = 0.4$ m/s. This values give Reynolds numbers in the range $\mathrm{Re}_{z_0} = 0.38 - 9.6$.

Figures 2.5 and 2.6 present the energy spectra at two z–positions and for the different angular speeds of the fan used in the tests. The spectra depicted in Figure 2.5 are nondimensionalized following the von Kármán dimensionless spectrum as $S^* = fS/\sigma^2$ and $f^* = fL/\bar{u}$, where f is the frequency, S is the spectral density function, σ^2 is the variance, $\bar{u}$ is the mean and L is the integral length scale. Regarding Figure 2.6 it can be observed that the energy increases with the wind speed R_{ref} and corresponds to frequencies ≤ 2 Hz with peaks at $0.2 - 0.4$ Hz. The spectra show a qualitatively good agreement with other experimental work in wind tunnels with short test sections and with the von Kármán spectrum (see e.g. Pires et al., 2013).

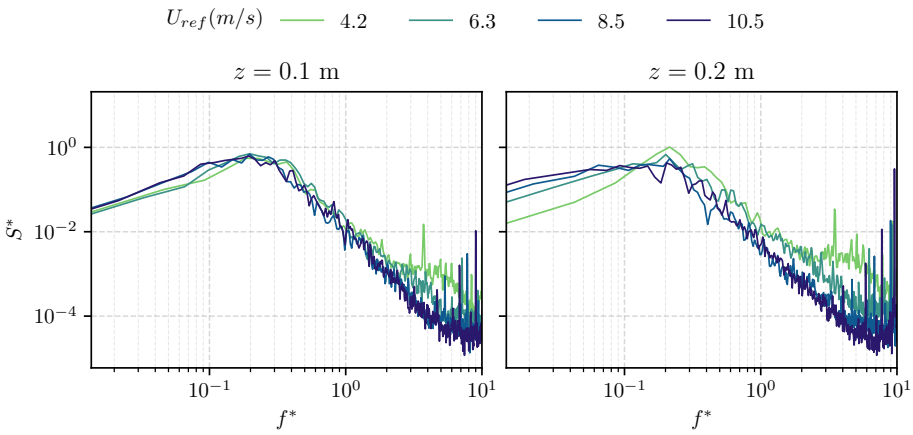

FIGURE 2.5: Dimensionless wind speed log-spectra at different z-positions and for different reference wind speeds U_{ref}

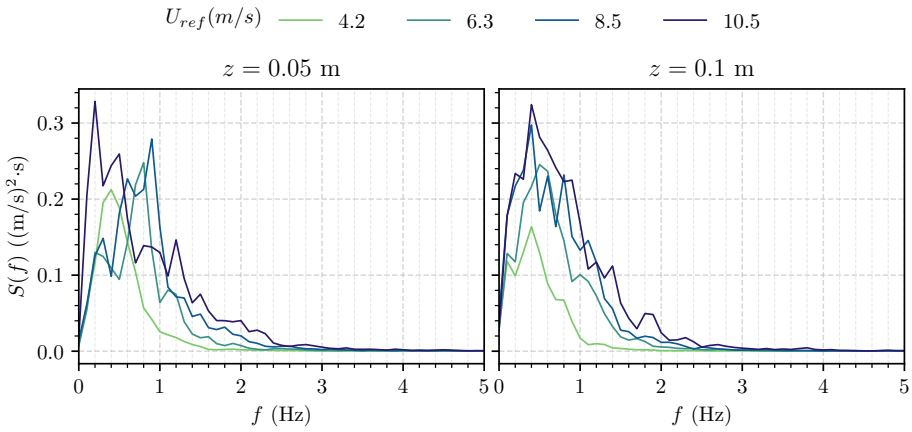

FIGURE 2.6: Wind speed spectra at different z-positions and for different reference wind speeds U_{ref}

2.1.2 Maritime structure model setup

A rigid thin barrier, with a thickness of 1.9 cm and a submergence d was installed vertically in the CIAO (Figure 2.7) with a water depth of $h = 0.7$ m. This barrier was located at 11 m from the generating wavemaker and spaced a distance $B = 2.5$ m from a vertical and impermeable back wall (B is the chamber width). The $x-$ and $z-$ axis refer to the stream-wise and vertical direction, respectively, with the origin at the mean water level at the section where the vertical thin plate is located.

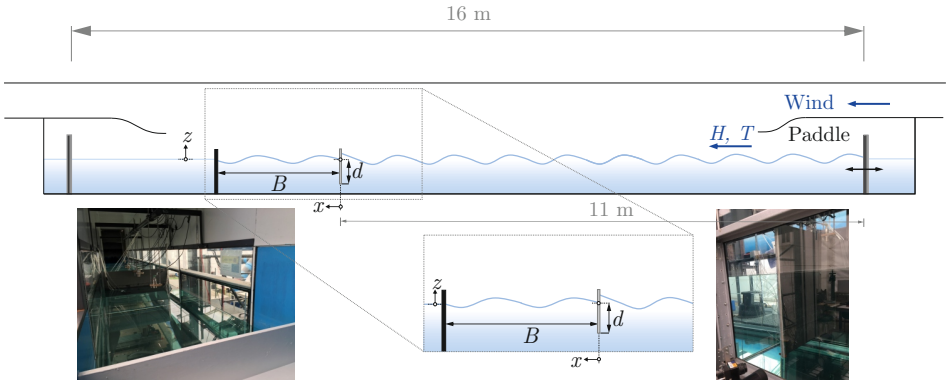

FIGURE 2.7: Side view of CIAO and definition sketch of experimental maritime structure

The natural oscillation periods of the flume and chamber were approximated using Merian's formula,

$$T_{N,M} = \frac{2}{\sqrt{gh}} \left[\left(\frac{N}{a} \right)^2 + \left(\frac{M}{b} \right)^2 \right]^{-1/2}, \tag{2.5}$$

with $N, M = 0, 1, 2, ...$ and a and b the length and width of the given chamber. Considering the wave flume (length between the two wavemakers), with $a = 16$ m and $b = 1$ m, the first and second main modes are $T_{1,0} = 12.21$ s and $T_{2,0} = 6.11$ s, respectively. Given the position of the plate and the back wall, the length of the flume is reduced to $a = 11$ m with $T_{1,0} = 8.4$ s and $T_{2,0} = 4.2$ s. Considering the length up to the back wall, $a = 13.5$ m, $T_{1,0} = 10.3$ s and $T_{2,0} = 5.15$ s are obtained. The cross-modes give similar values in all cases with $T_{1,1} \approx T_{2,1} \approx 0.76$ s and $T_{1,2} \approx T_{2,2} \approx 0.38$ s.

Regarding the chamber with $a = 2.5$ m, the first and second modes are $T_{1,0} = 1.9$ s and $T_{2,0} = 0.95$ s, respectively.

2.2 Experimental Protocol

Table 2.1 presents the different parameters of wind intensity U_{ref} and downwind paddle-generated incident waves characterized by (H^{input}, T^{input}). In the case of regular waves experiments, (H^{input}, T^{input}) correspond, respectively, to the wave height and period for regular waves. For the irregular waves cases, the parameters stand for the significant wave height and peak period of the given spectrum.

TABLE 2.1: Experimental forcing conditions for wave and wind generation. H^{input} and T^{input} are the input setup values of the wave generation software and U_{ref} represents the reference wind speed. *R*: regular waves. *JW*: JONSWAP incident wave spectrum ($\gamma = 3.3$). *PM*: Pierson-Moskowitz ($U_w = 20$ m/s). *W*: wind-generated waves.

Test	H^{input} (m)	T^{input} (s)
Regular waves - *R*1	0.07	1.85, 2.8, 4.76
Regular waves - *R*2	0.06	1.65; 3.0; 4.7
JONSWAP - *JW*1	0.075	1.4; 1.8; 2.6; 4.7
JONSWAP - *JW*2	0.06	1.65; 3.0; 4.7
Pierson-Moskowitz - *PM*	0.08	1.65; 3.0; 4.7

Test	U_{ref} (m/s)
*W*0	0
*W*1	4.2
*W*2	6.3
*W*3	8.5
*W*4	10.5

Given the different combinations of forcing conditions and geometrical configurations, experiments are identified with the following nomenclature *AAx_Ty_Wz* where:

- *AA* denotes the regular/irregular wave experiment:
  - *R*1: regular waves with $H^{input} = 0.07$ m
  - *R*2: regular waves with $H^{input} = 0.06$ m
  - *JW*1: JONSWAP incident wave spectrum with $H^{input} = 0.075$ m
  - *JW*2: JONSWAP incident wave spectrum with $H^{input} = 0.06$ m
  - *PM*: Pierson-Moskowitz incident wave spectrum with $H^{input} = 0.08$ m
  - *W*: wind–generated waves
- *x* denotes the relative submergence characteristic:
  - *a*: $d/h = 0.33$
  - *b*: $d/h = 0.58$
  - *c*: $d/h = 0.71$

- *Ty* denotes the wave period characteristic depending on each regular/irregular wave experiment (Table 2.1)
- *Wz* denotes the wind–sea waves characteristics:

  *W*0: $U_{ref} = 0$ m/s

  *W*1: $U_{ref} = 4.2$ m/s

  *W*2: $U_{ref} = 6.3$ m/s

  *W*3: $U_{ref} = 8.5$ m/s

  *W*4: $U_{ref} = 10.5$ m/s

Table 2.2 summarizes the nomenclature and parameters of the tests. For the sake of simplicity and readability, the nomenclature for paddle-generated waves in combination with wind–sea waves is broken down only for the experiment *R*1*a*_*T*1 as an example.

Water level measurements were obtained using seven ultrasound acoustic wave gauges (UltraLab ULS 80D) installed at different sections along the flume (Figure 2.8) with a maximum repetition rate equal to 75 Hz, a nominal resolution of 0.18 mm and a reproducibility of ±0.15%.The overall accuracy is 0.5 mm.

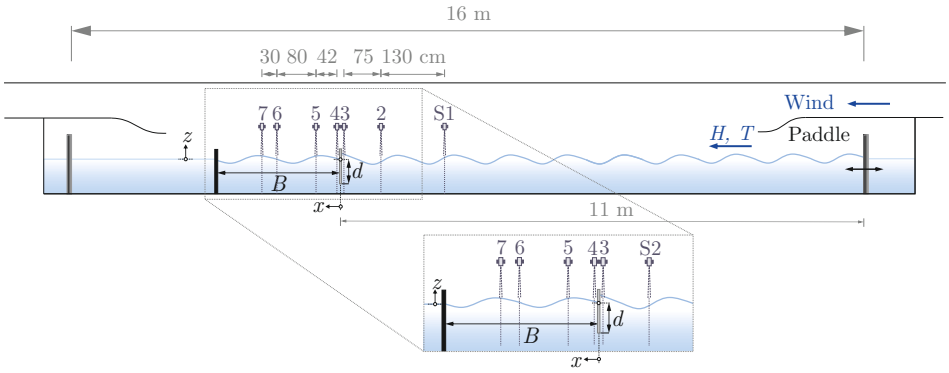

FIGURE 2.8: Experimental setup. *B* is the chamber width and *d* is the plate submergence. S1–S7 are wage gauges for surface elevation measurements.

Figure 2.9 presents the time–averaged free surface signal against the measuring time for the test *R*1*c*_*T*1 and different wind conditions. The signal was acquired for 185 seconds, for which the signal convergence was satisfactory.

TABLE 2.2: Nomenclature and parameters of all the experiments of regular and irregular waves (paddle-generated) with/without the combination of wind-driven waves. H^{input} and T^{input} are the input setup values of to the wave generation software, d/h is the relative submergence and U_{ref} represents the reference wind speed[1].

Test	H^{input} (m)	T^{input} (s)	d/h	U_{ref} (m/s)
Wind–sea waves				
*W*1*a*	–	–	0.33	4.2
*W*1*b*	–	–	0.58	4.2
*W*1*c*	–	–	0.71	4.2
*W*2*a*	–	–	0.33	6.3
*W*2*b*	–	–	0.58	6.3
*W*2*c*	–	–	0.71	6.3
*W*3*a*	–	–	0.33	8.5
*W*3*b*	–	–	0.58	8.5
*W*3*c*	–	–	0.71	8.5
*W*4*a*	–	–	0.33	10.5
*W*4*b*	–	–	0.58	10.5
*W*4*c*	–	–	0.71	10.5
Regular waves (paddle-generated) with/without wind–sea waves				
*R*1*a*_*T*1	0.07	1.85	0.33	
• *R*1*a*_*T*1_*W*0				0
• *R*1*a*_*T*1_*W*1				4.2
• *R*1*a*_*T*1_*W*2	0.07	1.85	0.33	6.3
• *R*1*a*_*T*1_*W*3				8.5
• *R*1*a*_*T*1_*W*4				10.5
*R*1*b*_*T*1	0.07	1.85	0.58	0, 4.2, 6.3, 8.5, 10.5
*R*1*c*_*T*1	0.07	1.85	0.71	0, 4.2, 6.3, 8.5, 10.5
*R*1*b*_*T*2	0.07	2.78	0.58	0, 4.2, 6.3, 8.5, 10.5
*R*1*b*_*T*3	0.07	4.76	0.58	0, 4.2, 6.3, 8.5, 10.5
*R*2*a*_*T*1	0.06	1.65	0.33	0, 4.2, 6.3, 8.5, 10.5
*R*2*b*_*T*1	0.06	1.65	0.58	0, 4.2, 6.3, 8.5, 10.5
*R*2*c*_*T*1	0.06	1.65	0.71	0, 4.2, 6.3, 8.5, 10.5
*R*2*b*_*T*2	0.06	3	0.58	0, 4.2, 6.3, 8.5, 10.5
*R*2*b*_*T*3	0.06	4.7	0.58	0, 4.2, 6.3, 8.5, 10.5
Irregular waves (paddle-generated) with/without wind–sea waves				
*JW*1*a*_*T*1	0.075	1.4	0.33	0, 4.2, 6.3, 8.5, 10.5
*JW*1*b*_*T*1	0.075	1.4	0.58	0, 4.2, 6.3, 8.5, 10.5
*JW*1*c*_*T*1	0.075	1.4	0.71	0, 4.2, 6.3, 8.5, 10.5
*JW*1*b*_*T*2	0.075	1.8	0.58	0, 4.2, 6.3, 8.5, 10.5
*JW*1*b*_*T*3	0.075	2.6	0.58	0, 4.2, 6.3, 8.5, 10.5
*JW*1*b*_*T*4	0.075	4.7	0.58	0, 4.2, 6.3, 8.5, 10.5
*JW*2*a*_*T*1	0.06	1.65	0.33	0, 4.2, 6.3, 8.5, 10.5
*JW*2*b*_*T*1	0.06	1.65	0.58	0, 4.2, 6.3, 8.5, 10.5
*JW*2*b*_*T*2	0.06	3.0	0.58	0, 4.2, 6.3, 8.5, 10.5
*JW*2*b*_*T*3	0.06	4.7	0.58	0, 4.2, 6.3, 8.5, 10.5
*PMa*_*T*1	0.08	1.65	0.33	0, 4.2, 6.3, 8.5, 10.5
*PMb*_*T*1	0.08	1.65	0.58	0, 4.2, 6.3, 8.5, 10.5
*PMc*_*T*1	0.08	1.65	0.71	0, 4.2, 6.3, 8.5, 10.5
*PMb*_*T*2	0.08	3.0	0.58	0, 4.2, 6.3, 8.5, 10.5
*PMb*_*T*3	0.08	4.7	0.58	0, 4.2, 6.3, 8.5, 10.5

[1] For simplicity, the nomenclature for experiments involving wind is presented only for experiment *R*1*a*_*T*1.

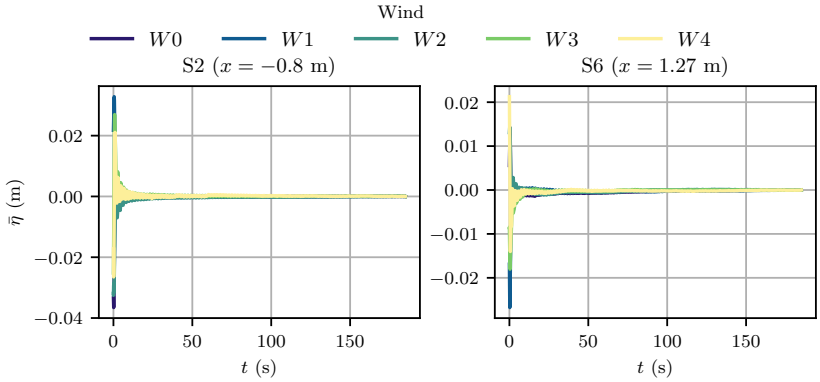

FIGURE 2.9: Time-averaged surface level as a function of measuring time for the test $R1c\_T1$ and different wind conditions.

Scaling

The model investigated in this work can be replicated in real-world applications guaranteeing Froude similarity, commonly adopted for the design of maritime structures. We notice that using a Froude-based similarity and working with the same fluid viscosity for both model and prototype, inevitably violates the Reynolds number scaling and lower values in the model than in prototype are obtained. This is a known problem of scale effects where air flows in transition regime are obtained in the laboratory whereas turbulent flows are obtained in field conditions.

In this case, a partial dynamic similarity is achieved using Froude scaling, neglecting the Reynolds number, the Weber number in hypothesis that the air-water curvature is limited (limited wave steepness), and the Mach number considering that aerated breaking does not occur. A length scale of λ_l is adopted with a velocity and time scale of $\sqrt{\lambda_l}$. Assuming a geometrical scale of $1/14$, experiment $R1a\_T1\_W0$, e.g., scales to an incident wave height of $H^{input} = 1$ m, $T^{input} = 7$ s, $L = 59$ m in water depths of $h = 10$ m.

2.3 Data analysis

The surface elevation data from the different wave gauges was analyzed using the python NumPy and SciPy packages.

Pre-processing

Acoustic wave gauges were used to obtain free surface elevation data at different positions along the flume (§2.2). The signal can contain spike noise due to experimental conditions, therefore the quality of the raw signals can be improved by means of preprocessing techniques. In this study, the outliers in each raw signal were removed with the phase-space despiking method by Mori et al., 2007 based on the concept and method of Goring and Nikora, 2002 and a moving average to smooth out fluctuations.

Reflection analysis

Reflection parameters of the experimental data are estimated using the three–gauge method presented on Baquerizo et al., 1997; Baquerizo, 1995 as an extension of the work of Mansard and Funke, 1980. The Fourier coefficients of the incident and reflected waves for each frequency are obtained by the minimization of the square sum of the errors at the three gauges. Then, the incident S_I and reflected wave spectra S_R are estimated at each gauge position. The modulus of the reflection coefficient K_R is obtained so that K_R^2 is the ratio of the wave energy components propagating in both directions (Baquerizo et al., 1997). The global reflection coefficient can be approximated using the zeroth-order moments of each spectra as,

$$K_R = \sqrt{\frac{m_{0_R}}{m_{0_I}}}. \tag{2.6}$$

A representative value of the phase of the reflection coefficient φ_R is obtained by means of Equation 1.17 for the peak frequency of the incident spectrum. In this study the analysis was restricted to the range $0.5 < f/f_p < 3$ in which the spectral moments of the periodic (regular and irregular) wave component was not negligible and with f_p being the peak frequency of the regular or irregular wave (paddle-generated).

The root mean square (r.m.s.) incident wave height is calculated by means of the zeroth-order moment of the incident spectra m_{0I} as follows:

$$H_{rms_I} = \sqrt{8m_{0_I}}. \tag{2.7}$$

The corresponding incident wave amplitude is defined as,

$$A_0 = A_{rms_I} = H_{rms_I}/2. \tag{2.8}$$

The envelope of the free surface elevation at each x–location for a partial standing wave can be calculated as (Baquerizo, 1995),

$$H_{rms_T} = H_{rms_I} TF, \tag{2.9}$$

where TF is the modulus of the complex transfer function $\mathbb{TF}$ which depends on the reflection coefficient (Baquerizo, 1995; Losada et al., 1997) and can be calculated as,

$$TF = \left[1 + K_R^2 + 2K_R \cos(2kx - \varphi_R)\right]^{1/2}. \tag{2.10}$$

Statistical analysis

The statistical analysis consists on applying the zero-upcrossing technique to the surface elevation time series obtaining the individual wave heights and periods of the signal.

Spectral analysis

Spectral analysis was also performed to the different surface elevation data. The spectra are obtained with the Welch method, using a Hanning window with 50% overlap resulting in 17 degrees of freedom and a spectral resolution of 0.039 Hz.

Phase lag

The phase lag is defined, as in the case of the analytical model (Eq. 1.21), as $\Phi = \omega t_{max}$, with ω being the angular frequency. t_{max} represents the time difference of the maximum surface elevation position between the signal of sensors S3 and S4 within a wave period. For its calculation, the signal of each sensor is divided into waves of period T^{input} and the position of the maximum surface elevation is found.

Phase-averaging

The free surface elevation can be decomposed as follows:

$$\eta = \overline{\eta} + \widetilde{\eta} + \eta', \tag{2.11}$$

where $\bar{\eta}$, $\tilde{\eta}$ and η' denote the mean, periodic and turbulent components of the free surface time series. Phase-averaging extracts $\tilde{\eta}$ using

$$\widetilde{\eta} = \frac{1}{N} \sum_{n=0}^{N-1} \eta, \tag{2.12}$$

over sufficient ensembles N. Therefore, all signals within a certain interval or window are averaged depending on an oscillating period which can be determined following diverse methodologies (Sonnenberger et al., 2000; Ostermann et al., 2014). In this work, the signal is divided into waves of period T^{input} (Table 2.2).

Chapter 3

Long-term simulation of extreme events

Note

This chapter introduces the methodology presented on:

A. Lira-Loarca, M. Cobos, A. Baquerizo, and M.A. Losada (2018a). "A multivariate statistical model to simulate storm evolution". In: *Proceedings of the 36th International Conference on Coastal Engineering (ICCE18)*. Baltimore, Maryland, USA

A. Lira-Loarca, M. Cobos, A. Baquerizo, and M.A. Losada (2018b). "Multivariate forecasting of extreme wave climate and storm evolution". In: *Proceedings of the International Conference on Time Series and Forecasting (ITISE18)*. Granada, Spain

This chapter presents the methodology to simulate long-term time series of maritime storm events and their evolution as presented on Figure 3.1. Firstly, the extreme events are defined in §3.1 by the combined selection of the threshold, the minimum storm duration and the minimum interarrival time. §3.2 presents the stochastic characterization of the distribution functions of the main maritime variables and their dependence and finally, §3.3 depicts the simulation methodology of long time series of wave climate under storm conditions.

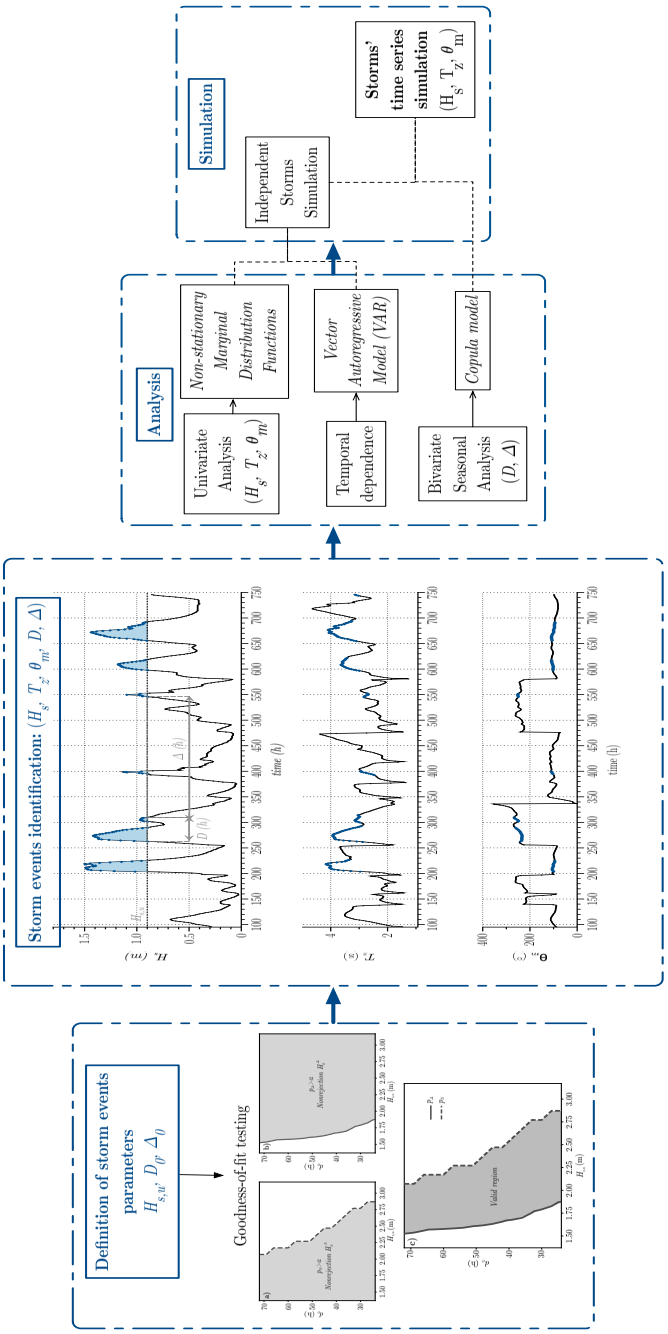

FIGURE 3.1: Flow diagram for the methodology of long-term storm simulation

3.1 Definition of storm events

Sea storms are generally defined as a rare event that occurs when the significant wave height H_s exceeds a certain threshold $H_{s,u}$ (Figure 3.2). The selection of the threshold has to guarantee that the events are independent so that the counting process, N, describing the number of occurrences in a certain time interval follows a Poisson distribution or, equivalently, the time lapse between storms — interarrival time—, Δ, follows an exponential distribution. Taking the year as a reference, the parameter of the Poisson distribution, λ_N, is the mean annual number of storms, that coincides with the inverse of the expected value of the corresponding exponential, $\bar{\delta}$, and it is usually estimated from available sea state data.

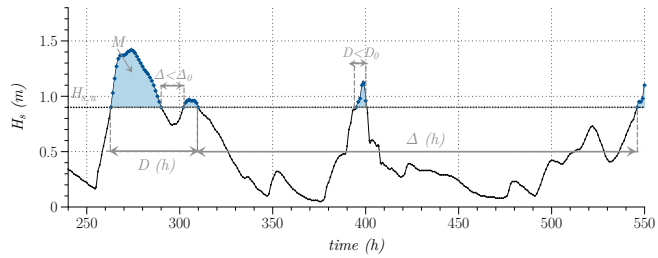

FIGURE 3.2: Definition of a storm event and the associated variables

In practice, for a given selected threshold, $H_{s,u}$, the identification of individual storms also requires to define a minimum value of the storm duration, $d_{s,0}$, to avoid interpreting relatively small and short exceedances of the wave height as storms, and a minimum interarrival time between successive events, δ_0, so that the independence assumption is fulfilled. Both values depend on the threshold and cannot be set arbitrarily. A too low δ_0 or $d_{s,0}$ results in an overestimation of the number of storms, while a too high δ_0 leads to an overestimation of the storms duration. Moreover the selection of these parameters is site–specific given their dependence to physical atmospheric phenomena. Taking this into account, we propose a criterion for the joint selection of $H_{s,u}$, $d_{s,0}$ and δ_0 based on two hypothesis testing.

For a given set of selected ($H_{s,u}$, δ_0, $d_{s,0}$) values, we test simultaneously the following hypotheses:

- For the distribution of the number of events, N:

  H_0^N: N follows a Poisson distribution (null hypothesis) *against*

  H_1^N: N does not follow a Poisson distribution

- For the interarrival times, Δ:

  H_0^{Δ}: Δ follows an Exponential distribution (null hypothesis) *against*

  H_1^{Δ}: Δ does not follow an Exponential distribution

To evaluate the goodness-of-fit of the number of events N distribution, a χ^2 non parametric test is performed with data samples obtained from sea states maritime data: $n_1, n_2, ...n_M$ with M being the number of years available in the dataset. In the case of the interarrival times Δ, a Kolmogorov-Smirnov (KS) test is used, with $\delta_1, \delta_2, ..., \delta_K$, $K = \sum_{m=1}^{M} n_m - 1$, the number of interarrival times between events. We then choose a significance level α to define the critical values for the rejection of the null hypotheses and obtain the corresponding p-values, p_N and p_Δ.

Mapping, for a given value of δ_0, the isolines of α for both tests over a selected band of $H_{s,u}$ and $d_{s,0}$, we obtain the nonrejection region of the null hypothesis as the intersection between the region where $p_N > \alpha$ and $p_\Delta > \alpha$ (Figure 3.3).

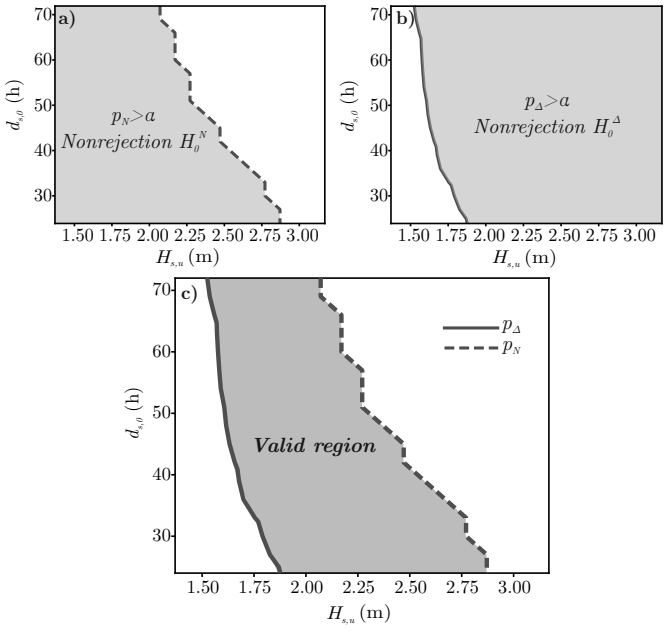

FIGURE 3.3: c) Limits of the valid region of significant wave height thresholds $H_{s,u}$ and events durations $d_{s,0}$ as the intersection between: a) the nonrejection region of the null hypothesis of the number of events $p_N > \alpha$ and b) the nonrejection region of the null hypothesis of the interarrival times $p_\Delta > \alpha$.

Additionally, due to the equivalence of the null hypothesis H_0^N and H_0^Δ, it should be checked that λ_N and $\bar{\delta}$, indicating the estimated mean values of N and Δ, respectively, are related so that $\lambda_N \approx 1/\bar{\delta}$.

3.2 Stochastic characterization of the main maritime variables and their temporal dependence

Once the values $H_{s,u}$, δ_0, $d_{s,0}$ are set, the following information is obtained from the historical climate data:

- records of the annual number of storms N, storms duration, D_s, and interarrival times, Δ
- multivariate time series during storm conditions of the significant wave height, $H_s(t)$, peak period $T_p(t)$ and mean incoming wave direction $\theta_m(t)$

Interdependence of storm events

The storm duration, D_s, and the interarrival time between consecutive storm events, Δ, have a strong degree of dependency between them (Li et al., 2018) and storm events show a strong seasonal variation in mid-latitudes (ROM 0.0-01, 2001). Therefore, the interdependence of storm events is analyzed seasonly by fitting a copula model to (D_s, Δ).

For each season, the coupling between the storm duration D_s and the following calm period Δ was characterized by their joint distribution function, $F(D_s, \Delta) = C(F_{D_s}(d_s), F_\Delta(\delta))$ where F_{D_s} and F_Δ are the marginal Cumulative Distribution Functions (CDFs) of the duration and interarrival time, respectively, and C is a copula function. The Archimedean copulas have been widely used in for bivariate simulations in hydrology and coastal engineering (Li et al., 2018) and were the selected model in this work.

Univariate distributions

The time series of significant wave height under storm conditions ($H_s(t) \geq H_{s,u}$) and the concomitant values of peak wave period (T_p) and mean wave direction (θ_m) are fitted to univariate distributions functions. Note that both random variables, H_s and T_p, are non-negative, unbounded above, and have asymptotic probability functions showing heavy upper tails.

Intra-dependence of storm events

The temporal dependence and interdependence of the maritime variables under consideration was characterized by means of a Vector Autoregressive model of order q —VAR(q) model— following Solari and Gelder, 2011; Lütkepohl, 2005. The fitted univariate distribution functions of each variable are used to transform the time series of $H_s(t)$, $T_p(t)$ and $\theta_m(t)$ into stationary normalized multivariate time series $Z_{H_s}(t)$, $Z_{T_p}(t)$ and $Z_{\theta_m}(t)$ as,

$$Z_X(t) = \Phi^{-1}(F_X(x(t))) \text{ for } X = H_s,\ T_p \text{ and } \theta_m, \tag{3.1}$$

where Φ^{-1} is the inverse function of the CDF of the Normal distribution, and $F_X(x(t))$ is the CDF of the random variable X evaluated at $x(t)$. In this work, a VAR(q) model is used given by (Lütkepohl, 2005),

$$\boldsymbol{x_t} = \boldsymbol{\nu} + \sum_{j=1}^{q} A_j \boldsymbol{x_{t-j}} + \boldsymbol{e_t}, \tag{3.2}$$

where $\boldsymbol{x_t} = (x_{1_t}, x_{2_t}, \ldots, x_{k_t})$ is a vector with the values of the k variables at t-time; $\boldsymbol{\nu}$ is a vector that allows for a nonzero mean; q is the number of past x values used in the prediction; $e_t = (e_{1_t}, e_{2_t}, \ldots, e_{k_t})$ is a white noise matrix or error and A_j is a autoregressive coefficient matrix given by

$$A_j = \begin{bmatrix} a^j_{1,1} & a^j_{1,2} & \cdots & a^j_{1,k} \\ a^j_{2,1} & \cdots & \cdots & a^j_{2,k} \\ & \cdots\cdots\cdots & & \\ a^j_{k,1} & \cdots & \cdots & a^j_{k,k} \end{bmatrix}. \tag{3.3}$$

The parameters of the model at order q are obtained by means of least square errors and the order q of the model was chosen from a range up to 20 as the one that gave the best Bayesian Information Criterion.

3.3 Time series simulation of storm events

The simulation process comprises the following steps:

- With the use of Monte Carlo techniques and the results of the fitted CDFs and VAR model, a simulation of a continuous series of maritime variables (H_s, T_p, θ_m) under storm conditions $H_s \geq H_{s,u}$ is done.
- A new threshold $H'_{s,u}$ must be set in order to define independent storms while keeping the selected δ_0 and d_0 in each case. The selection $H'_{s,u}$ is done by maintaining the similarity between the CDF of the storms duration of

the historical and simulated H_s data. A record of independent storm events (H_s, T_p, θ_m) and their duration (D) is obtained.

- The independent storms are then distributed in time by simulating the duration of the interarrival time, δ, from the corresponding season copula function $F(D_s, \Delta)$ for each given storm duration, D_s.

During the simulation process a limiting wave steepness is set, to avoid arbitrarily steep waves, using the following formulation valid for irregular wave trains (ROM 1.0-09, 2009) $s_s = H_{m0}/\overline{L_0}$ where s_s is the significant wave steepness bounded by $0.045 \geq s_s \geq 0.055$ in the North Atlantic Ocean and $0.055 \geq s_s \geq 0.065$ in the Mediterranean Sea (ROM 1.0-09, 2009) and L_0 is the mean incident wavelength.

Part II

Results

Chapter 4

Validation of the analytical and experimental results

This chapter presents the validation of both the analytical model and the experimental results. §4.1 introduces the comparison of the analytical model results under regular waves with CFD models whereas §4.2 presents the results of the experimental study fo regular waves without wind–sea waves along with the results of the analytical model.

4.1 Numerical simulations

Note

This section presents some of the results published on:

M.L. Jalón, **A. Lira-Loarca**, A. Baquerizo, and M.A. Losada (2019). "An analytical model for oblique wave interaction with a partially reflective harbor structure". In: *Coastal Engineering* 143, pp. 38 –49. ISSN: 0378-3839. DOI: `https://doi.org/10.1016/j.coastaleng.2018.10.015`

The analytical model presented on Chapter 1 was verified by:

- The degree of fulfillment of the boundary conditions
- The comparison of the results with Computational Fluid Dynamics (CFD) models

Firstly, in order to analyze the order of magnitude for the error of the calculations when truncating the series for intermediate water depths, the analytical model was run for different values of the number of evanescent modes, N_l and

for $h = 10.0$ m, $d/h = 0.5$, $B/h = 1$ and a normal incident regular wave with $A_0 = 0.5$ m and $kh = 1.717$. The two main geometrical variables used for the interpretation of the results are the relative submergence d/h and the relative width B/L.

Figure 4.1 represents the horizontal velocity component $|u|$ at $x = 0$ and $z = 0$ on the seaward side the plate, where the impermeability condition is imposed. As observed, the solution converges as N_l increases and the order of magnitude for the error is $\approx O(10^{-2})$ for $N_l \geq 50$ and under $O(10^{-3})$ for $N_l \geq 200$.

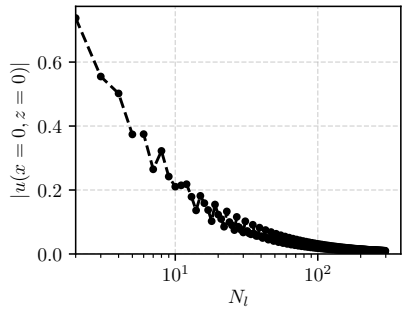

FIGURE 4.1: Amplitude of the horizontal velocity component $|u|$ (m/s) in $x = 0$ and $z = 0$, with respect to the number of evanescent modes N_l.

The analysis depth dependent function $G(z)$ is used to measure the goodness of the model to fulfill the boundary conditions not only locally but uniformly in the z–axis which, according to its definition (Eq. 1.12-1.14), should be approximately zero in the water column. Figure 4.2 presents $G(z)$ for different values of relative width B/L with L being the wavelength at the front of the structure for a depth h ($L = 2\pi/k_0$). It can be observed that, except at the discontinuity ($z = -d$), the error is of the order of magnitude of 10^{-2} for the case $B/L = 0.56$ and lower for the rest. The behavior of the solution at the discontinuity, $z = -d$, is due to the Gibbs phenomenon of a truncated Fourier series expansion of a piece-wise function.

4.1.1 Importance of head loss consideration

The amplification factor Q and the phase lag Ψ defined in §1.2 were calculated with and without the consideration of head loss, and compared with the numerical solutions obtained by Teixeira et al., 2013 for different wave periods ($T = 5 - 18$ s) and the results are presented in Figure 4.3. It can be observed that the analytical model presents a similar behavior in agreement with the numerical models when considering head loss ($\zeta_e \neq 0$) for both the amplification factor

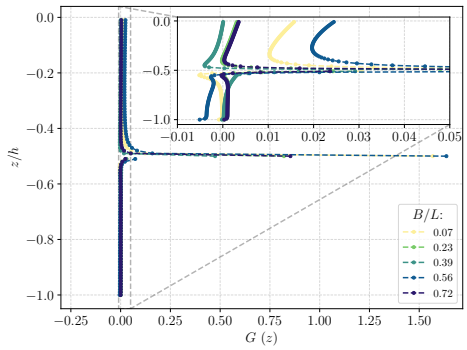

FIGURE 4.2: Piece-wise function G(z) for different values of relative width B/L.

(with mean square errors $R^2 = 0.95$ for Fluent and $R^2 = 0.92$ for Fluinco) and the phase lag (with corresponding values $R^2 = 0.98$ and $R^2 = 0.9$). It is observed that when the analytical models does not take head loss into account ($\zeta_e = 0$), there is a very sudden change in the phase lag values from 0° to 180° coinciding with an amplification ($Q \approx 2.5$) for $B/L = 0.13$. However, the with the consideration of friction there is a more gradual variation in the phase lag values and the peak in Q is eliminated.

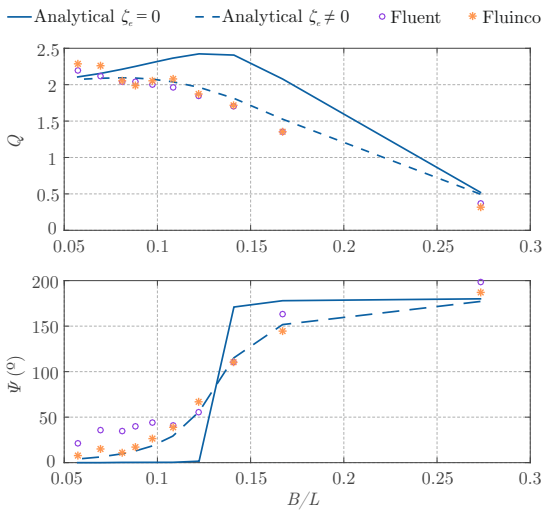

FIGURE 4.3: Amplification factor Q and phase lag Ψ with respect to the relative width B/L. Numerical models: Fluent (o), Fluinco (*). Analytical model: $\zeta_e = 0$ (solid line), $\zeta_e \neq 0$ (dashed line)

4.2 Laboratory experiments

The analytical model presented in §1 was run for the prototype values of the experiments presented in the Table 2.1 for normal wave incidence $\theta = 0°$ with $\lambda_l = 1/14$ as introduced in §2.2. This section is intended to give an overview of the agreement between analytical and experimental results for the regular waves experiments without wind. A more in-depth analysis of the analytical model results and the discussion of its implications for the design optimization of maritime structures is presented on Chapter 5. The experimental results are further analyzed including the experiment with wind–sea waves on Chapter 6.

Figure 4.4 presents the experimental and analytical modulus K_R and phase φ_R of the reflection coefficient with respect to the relative submergence d/h and the relative width of the system B/L. The analytical results (contours) are derived from Equations 1.16 and 1.17 whereas the experimental results (points) are obtained following the reflection analysis of §2.3 for all the regular wave experiments –$R1$ and $R2$– without the presence of wind $W0$. The wavelength used for the calculation of B/L corresponds to the wavelength of the input period of the wave generation software ($L_{0_{W0}}$). Figure 4.5 depicts the same results but with a different representation in order to better appreciate the order of magnitude of the difference between analytical and experimental results.

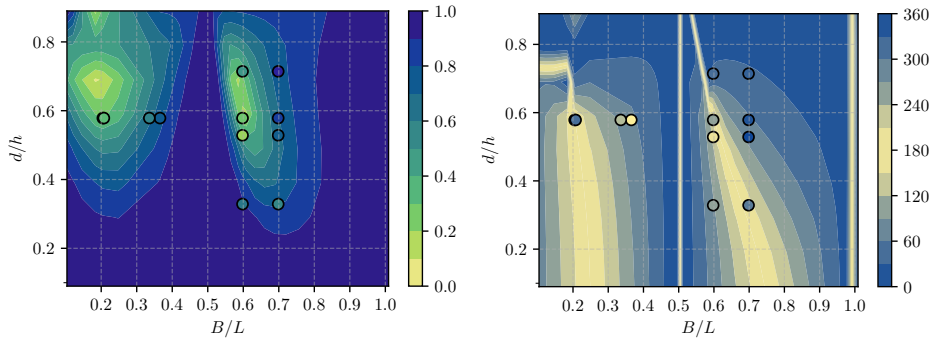

(A) K_R (B) φ_R (°)

FIGURE 4.4: Modulus (K_R) and phase (φ_R) of the reflection coefficient with respect to the relative submergence d/h and the relative width of the system B/L. Comparison between analytical (contours) and experimental (points) results.

In can be observed that the experimental and analytical results present a good agreement with a mean absolute error (MAE) of 0.18 in the case of K_R (Figures 4.4a and 4.5–left). For B/L close to 0.6, the reflection coefficient decreases with

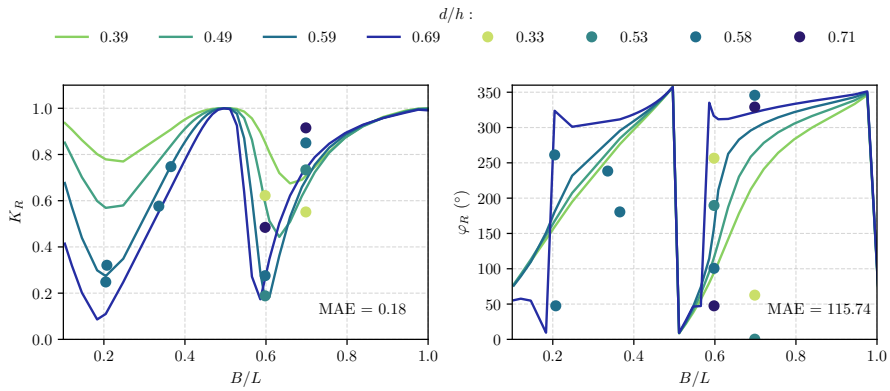

FIGURE 4.5: Modulus K_R (left) and phase φ_R (right) of the reflection coefficient with respect to the relative width of the system B/L and for different relative submergences d/h (colors). Comparison between analytical (lines) and experimental (points) results. MAE: mean absolute error.

increasing d/h up to values of $d/h \approx 0.7$ when it starts increasing again. It can be observed that for $d/h = 0.58$ –corresponding to experiments $R1b$ and $R2b$– and $B/L \leq 0.6$ the values of the reflection coefficient differ in approximately 0.02 whereas in the case of $B/L = 0.7$ the difference reaches values of 0.1 with the experimental and analytical results giving $K_R \approx 0.86$ and 0.76 respectively. The worst agreement is obtained for the $R1a$ and $R2a$ cases with $d/h = 0.33$ where there is a difference of K_R of about 0.2 for the case $B/L = 0.6$. This difference can also be attributed to the high dependence of the results on the B/L values as observed in the figures. In the case of the experimental results, the wavelength value is affected by the long wave and harmonics created by the physical constraints of a closed flume and its subdivision by the back wall and the plate. In the case of φ_R (Figure 4.4b and 4.5–right) the experimental results maintain the trend of the analytical results. Nonetheless, a lower agreement is obtained due to the spectral analysis of the phase depending highly on the selected frequency in the case of the experimental results.

Figures 4.6 and 4.8 present at the seaward and leeward region, respectively, the experimental and analytical maximum dimensionless amplitude $\max \eta(t)/A_0$ with respect to the relative submergence d/h and the relative width of the system B/L at different x–locations. A_0 is the amplitude of the incident wave and equals $H_{rmsI}/2$ for the experimental results and the theoretical incident wave amplitude for the analytical results. The contours correspond to the analytical model results and the points correspond to the $R1$ and $R2$–experiments without wind. The x–locations are $x = 0$ and the corresponding to the different positions of the wave

gauges used in the experiments. Figures 4.7 and 4.9 depict the same results but with a different representation in order to better appreciate the order of magnitude of the difference between analytical and experimental results.

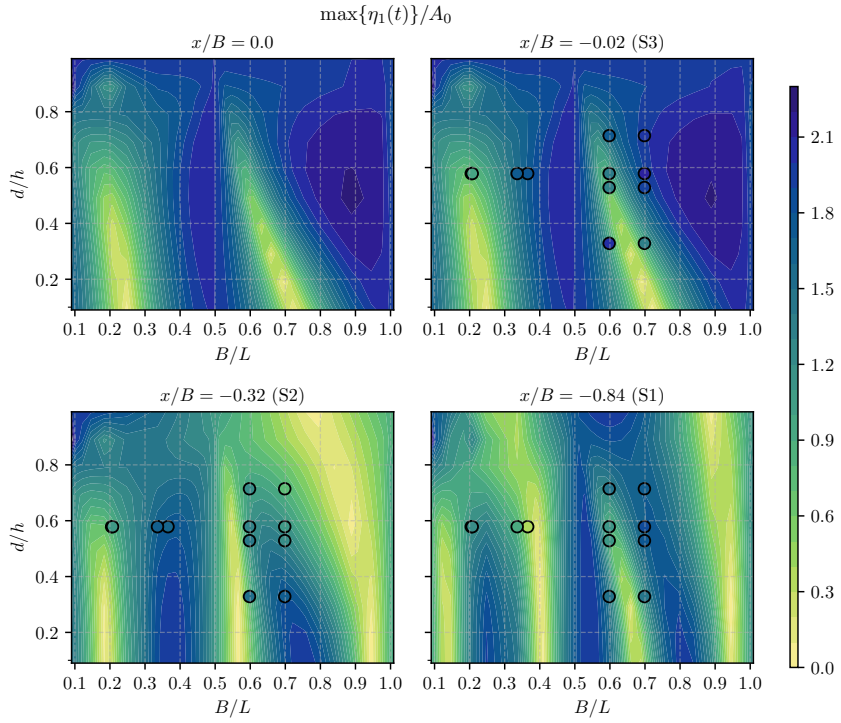

FIGURE 4.6: Maximum dimensionless amplitude for regular waves in the seaward region at different x–positions, with respect to the relative submergence d/h and the relative width of the system B/L. Comparison between analytical (contours) and experimental (points) results.

In the case of the seaward region (Figures 4.6 and 4.7), the experimental results follow the same quasi-nodal and quasi-antinodal behavior presented by the analytical results.

It can be observed that the analytical results are the same for $x/B = 0, -0.02$, as the wave gauge S3 was intended to represent the conditions at the face of the plate but needed to be slightly separated from it for the physical set-up. As in the case of the reflection coefficient, the results for $d/h > 0.4$ show a good agreement between analytical and experimental. In the case of $x/B = -0.02$, the experimental results give slightly higher values than the analytical results

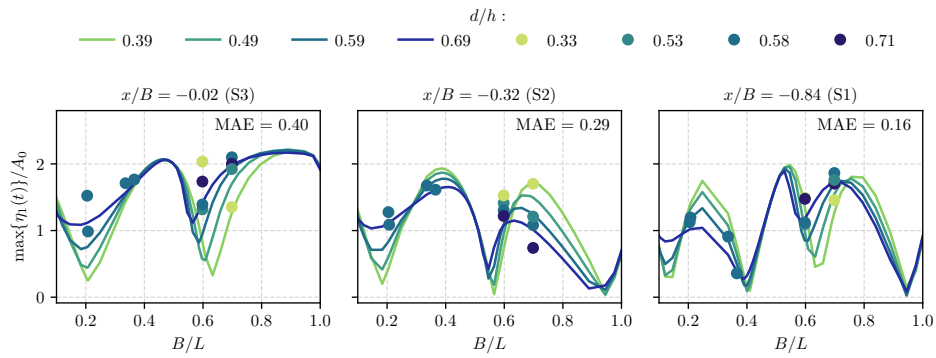

FIGURE 4.7: Dimensionless amplitude for regular waves in the seaward region at different x–positions, with respect to the relative width B/L and for different relative submergences d/h. Comparison between analytical (lines) and experimental (points) results. MAE: mean absolute error.

with differences of the order of magnitude of 0.1-0.5 and a MAE=0.4; the highest difference is obtained for the case $R1a\_T1$ with $d/h = 0.33$ and $B/L \approx 0.6$. In this case, it can be observed that for slightly lower values of B/L, similar $\max \eta_1$ are obtained. For the other two x–positions, $x/B = -0.32$ and -0.84 there is a good agreement with MAE of 0.29 and 0.16, respectively.

The leeward region (Figures 4.8 and 4.9) follows the same behavior as the seaward region for all the x–positions showing a good agreement between the analytical and experimental results with the MAE taking values of $0.3 - 0.46$ except for the case $x/B = 0.51$ with a value of 0.78. In the case of the position closest to the plate ($x/B = 0.02$), the experimental values are higher than the analytical of the order of $0.5 - 1.1$. The highest differences are obtained for the cases with $d/h = 0.58$ and $B/L = 0.37 (R1b\_T2)$ and $B/L = 0.7$ ($R2b\_T1$) with a difference of $\max \eta_2/A_0 \approx 1$ between the analytical and experimental results. In the case of wave gauge S5 and S7 the experimental results are higher when $B/L \approx$ 0.35-0.4 and give a good agreement for the rest of the B/L and d/h cases with MAE$\approx$ 0.3.

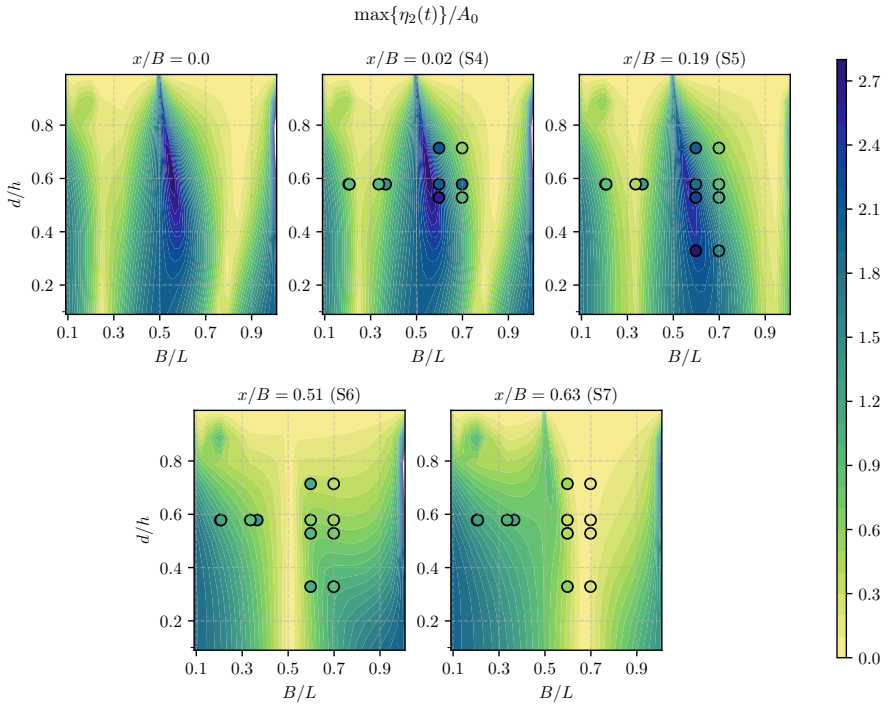

FIGURE 4.8: Dimensionless amplitude for regular waves in the leeward region at different x–positions, with respect to the relative submergence d/h and the relative width of the system B/L. Comparison between analytical (contours) and experimental (points) results.

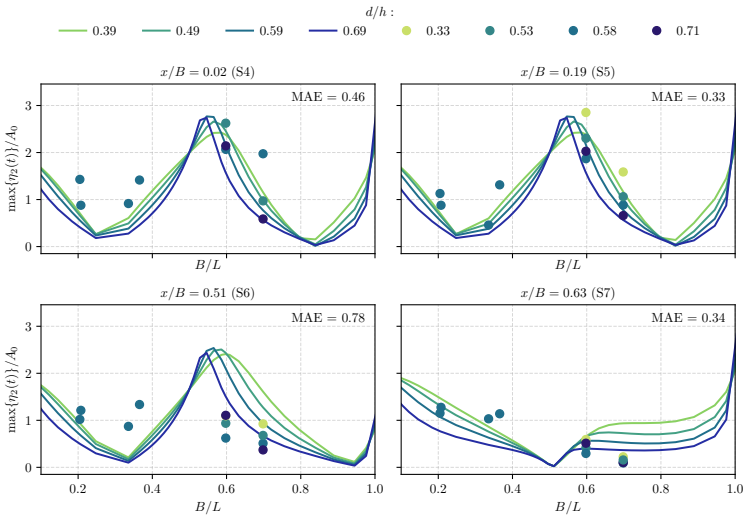

FIGURE 4.9: Dimensionless amplitude for regular waves in the leeward region at different x–positions, with respect to the relative width B/L and for different relative submergences d/h. Comparison between analytical (lines) and experimental (points) results.

4.3 Conclusions

The proposed analytical model presents a good performance when compared to the results of CFD models (Teixeira et al., 2013), proving its capacity to efficiently evaluate the hydrodynamic performance of the system when considering weakly nonlinear incident waves.

The results show that the solution converges as the number of evanescent modes N_l increases when the series is truncated, with errors of less than $O(10^{-3})$ for $N_l \geq 200$.

The comparison between the analytical model results and the numerical models highlights the importance of the head loss consideration into the analytical model. When head loss is not taken into account, there is an amplification, coinciding with a sudden change in the phase lag for a given value of the relative width. However, the inclusion of friction eliminates the peak in the amplification factor and the phase lag presents a more gradual variation. Therefore, an accurate representation of the phase lag and the general hydrodynamic behavior of the system depends on the correct mathematical representation of the head loss at the gap.

The analytical and experimental results present a good agreement for the reflection coefficient K_R with a mean absolute error (MAE) of 0.18. Regarding the phase of the reflection coefficient φ_R, the fit between experimental and analytical results is not as good which could be due to the fact that the phase is highly dependent on the frequency resolution and value of the incident spectrum.

Regarding the maximum surface elevation in both the seaward and leeward region, a good agreement is obtained with values of the MAE of $0.16 - 0.4$ in the seaward region and $0.33 - 0.78$ in the leeward region. This difference can also be attributed to the fact that this values vary depending on the B/L value so a displacement on the experimental results can be expected due to the physical limitations of the flume and chamber and their effects on the total wavelength and surface elevations.

Chapter 5

Design optimization for regular and irregular swell waves

Note

This chapter presents some of the results published on:

M.L. Jalón, **A. Lira-Loarca**, A. Baquerizo, and M.A. Losada (2019). "An analytical model for oblique wave interaction with a partially reflective harbor structure". In: *Coastal Engineering* 143, pp. 38 –49. ISSN: 0378-3839. DOI: `https://doi.org/10.1016/j.coastaleng.2018.10.015`

The analytical model presented in Chapter 1 was implemented for different wave and geometrical configurations in order to analyze the influence of the main geometrical parameters on the behavior of the system. According to the convergence results presented on §4.1, the model was run for a fixed number of evanescent modes $N_l = 200$.

This chapter presents the results of said model for the interaction of oblique incident regular and irregular waves. The influence of fundamental design parameters, such as geometric and wave characteristics, on the hydrodynamic behavior and the loadings on the plate is analyzed. §5.1 presents the results under regular waves with normal and oblique incidence whereas §5.2 anayzes the influence of irregular waves. Finally, §5.3 gives the main conclusions of the study.

5.1 Regular Waves

The first step was to analyze the results under regular swell waves. Therefore the model was implemented for an incident regular wave with an incident wave

amplitude $A_0 = 0.5$ m, wave period $T = 7$ s, for a water depth $h = 10$ m and different values of submergence d and chamber width B.

Figures 5.1 and 5.2 present the modulus and phase, respectively, of (a) the reflection and (b) the capture coefficients calculated as presented on §1.2 (Eq. 1.16-1.19) for different values of relative submergence d/h and relative width B/L. As observed the response of both K_R and K_C is periodic at $B/L = 0.5$.

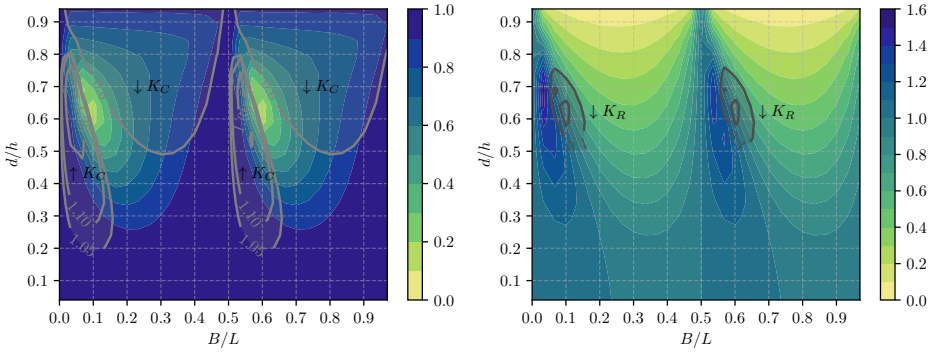

(A) K_R (B) K_C

FIGURE 5.1: Modulus of the reflection K_R and capture K_C coefficients with respect to the relative submergence (d/h) and the relative width (B/L) of the system, for normally incident regular waves $\theta = 0°$. Solid lines represent the isolines of (a) the maximum/minimum values of K_C and (b) minimum values of K_R.

A maximum value of the modulus of the reflection coefficient ($K_R = 1$) is obtained for the lowest relative submergences ($d/h \lesssim 0.25$), corresponding to a perfect reflection from the impermeable back wall and maximum wave transmission through the gap with values of φ_C in phase with the incident wave ($\varphi_I = 0°$) as observed in Figure 5.2b. For values of d/h over 0.25 approximately, the maximum reflection in region 1 (seaward) is obtained for very small values of B/L and for B/L slightly larger than 0.5 highlighting the periodic behavior of the system. In these cases, maximum values of K_C can also be observed.

In general, maximum capture coefficients ($K_C > 1.1$) coincide with higher reflections ($K_R > 0.8$) as observed in Figure 5.1a and with φ_R close to quadrature values with respect to the incident wave ($60° < \varphi_R < 120°$) as observed in Figure 5.2a and according to the definitions of both the complex reflection and capture coefficients given on Equations 1.16-1.19, there is a phase lag between the two depending on the chamber width as observed in Figures 5.1-5.2.

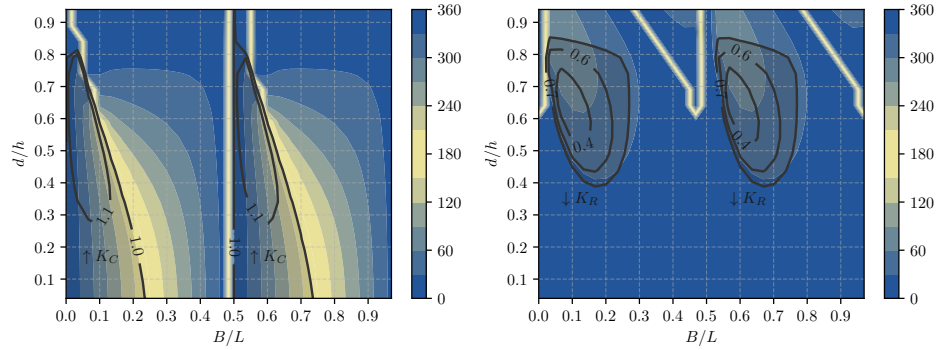

(A) φ_R (°) (B) φ_C (°)

FIGURE 5.2: Phase of the reflection φ_R and capture φ_C coefficients with respect to the relative submergence (d/h) and the relative width (B/L) of the system, for normally incident regular waves $\theta = 0°$. Solid lines represent the isolines of (a) the maximum values of K_C and (b) minimum values of K_R (Figure 5.1)

At d/h close to 0.60, the minimum reflection is found at $B/L = 0.1$ and 0.6 (periodicity at $B/L = 0.5$, as in Sahoo et al., 2000). The efficiency of the system in regard to energy capture is minimum for B/L close to 0.3 and 0.8 with bandwidths depending on the relative submergence (Figure 5.1b).

Figure 5.3 presents the reflection and capture coefficients for oblique wave incidence. A similar periodic behavior as in the normal incidence case can be observed at $B/L' = 0.5$, with $L' = L/\cos\theta$.

As expected, there is a slight variation from the results corresponding to normal incidence $\theta = 0°$, but the general behavior of the system remains the same. Maximum values of K_C are obtained for low values of B/L' and close to 0.6 for which a high K_R is also obtained. Figure 5.4 depicts the modulus of the reflection and caption coefficients versus incident wave angle θ for the case $d/h = 0.64$ and different B/L. The incident wave angle for which the capture coefficient is maximum K_C varies depending on the value of B/L and seems to reach the best performance for B/L close to 0.6 and $\theta \approx 25°$. For those values, K_R is also close to its maximum 1.

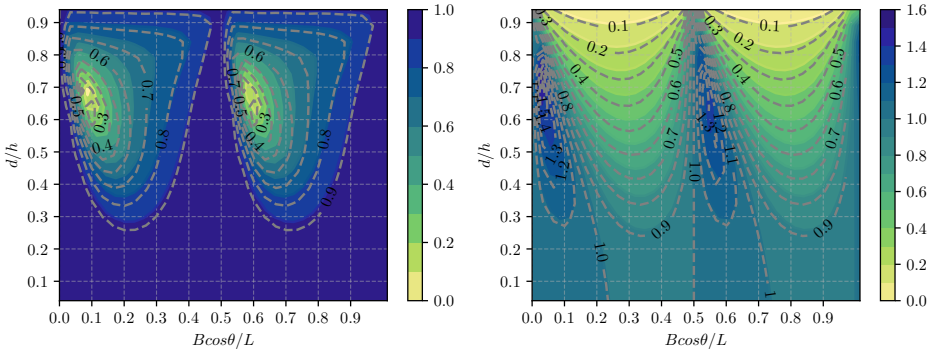

(A) K_R (B) K_C

FIGURE 5.3: Modulus of the reflection coefficient K_R and the capture coefficient K_C with respect to the relative submergence (d/h) and the relative width (B/L') with $L' = L/cos\theta$, for obliquely incident regular waves. The dashed lines correspond to the the case $\theta = 0°$ (Figure 5.1)

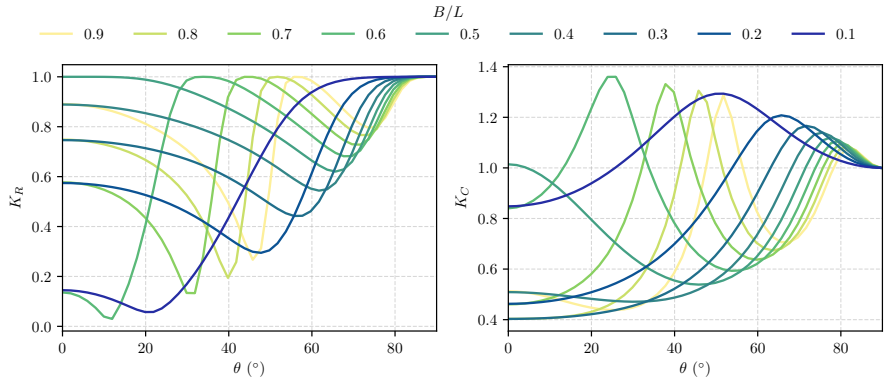

FIGURE 5.4: Modulus of the reflection K_R and capture K_C coefficients with respect to the incident angle (θ) of regular waves and the relative width B/L for the case $d/h = 0.64$.

Figure 5.5 presents the maximum dimensionless amplitudes at both sides of the barrier ($x = 0$) in terms of the relative submergence d/h and the relative width B/L with A_0 being the incident wave amplitude.

It can be observed that depending on the phase and modulus of the reflection coefficient (Figure 5.1a-5.2a), $x = 0$ presents a quasi-nodal or quasi-antinodal

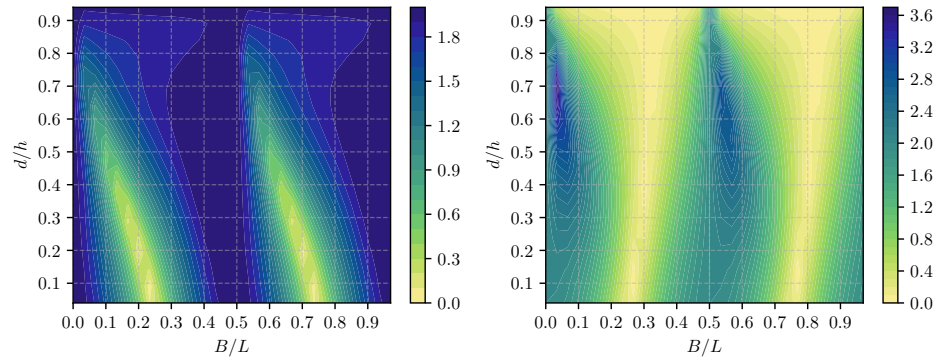

(A) $\max\{\eta_1(x=0,t)\}/A_0$ (B) $\max\{\eta_2(x=0,t)\}/A_0$

FIGURE 5.5: Maximum dimensionless amplitude in the seaward and leeward regions at $x = 0$ with respect to the relative submergence d/h and the relative width B/L of the system, for normally incident regular waves $\theta = 0°$.

behavior at the seaward face of the plate (Figure 5.5a). Values of $\max\{\eta_1(x = 0,t)\}/A_0$ close to zero are observed when $K_R = 1$ and φ_R presents values in phase opposition with respect to the incident wave. Quasi-antinodes ($\max\{\eta_1(x = 0,t)\}/A_0 \approx 2$) are present when φ_R is in phase with the incident wave. Similarly, different d/h and B/L combinations lead to a quasi-node or quasi-antinode behavior at the leeward side of the plate related to the modulus and phase of the transmission coefficient (Figure 5.5b). The presence of quasi-nodes or quasi-antinodes at both faces of the plate is crucial for the calculations of the stability of the structure given that the forces acting on it are directly proportional to the free surface elevations.

Figures 5.6 to 5.8 present the maximum dimensionless amplitudes at different x–locations in the seaward and leeward side in order to understand the nodal and antinodal behavior around the maritime structure. This is a key factor for the design of harbor protection structures as certain d/h and B/L combinations will lead to lower forces acting on the plate. Additionally, depending on the d/h and B/L configuration there will be certain x–positions away from the structure with reduced or amplified total wave energy.

As observed in Figure 5.6 quasi-nodes are found on the seaward side of the plate $\max\{\eta_1(x = 0,t)\}/A_0 \approx 0$ for $d/h \leq 0.3$ and B/L close to 0.7. The value of $\max\{\eta_1(t)\}/A_0$ starts to increase as we move away from the plate in the seawards direction as observed in Figure 5.6 where at $x/B \approx -0.3$ a quasi-antinode is visible for it to start decreasing again until it reaches a quasi-node

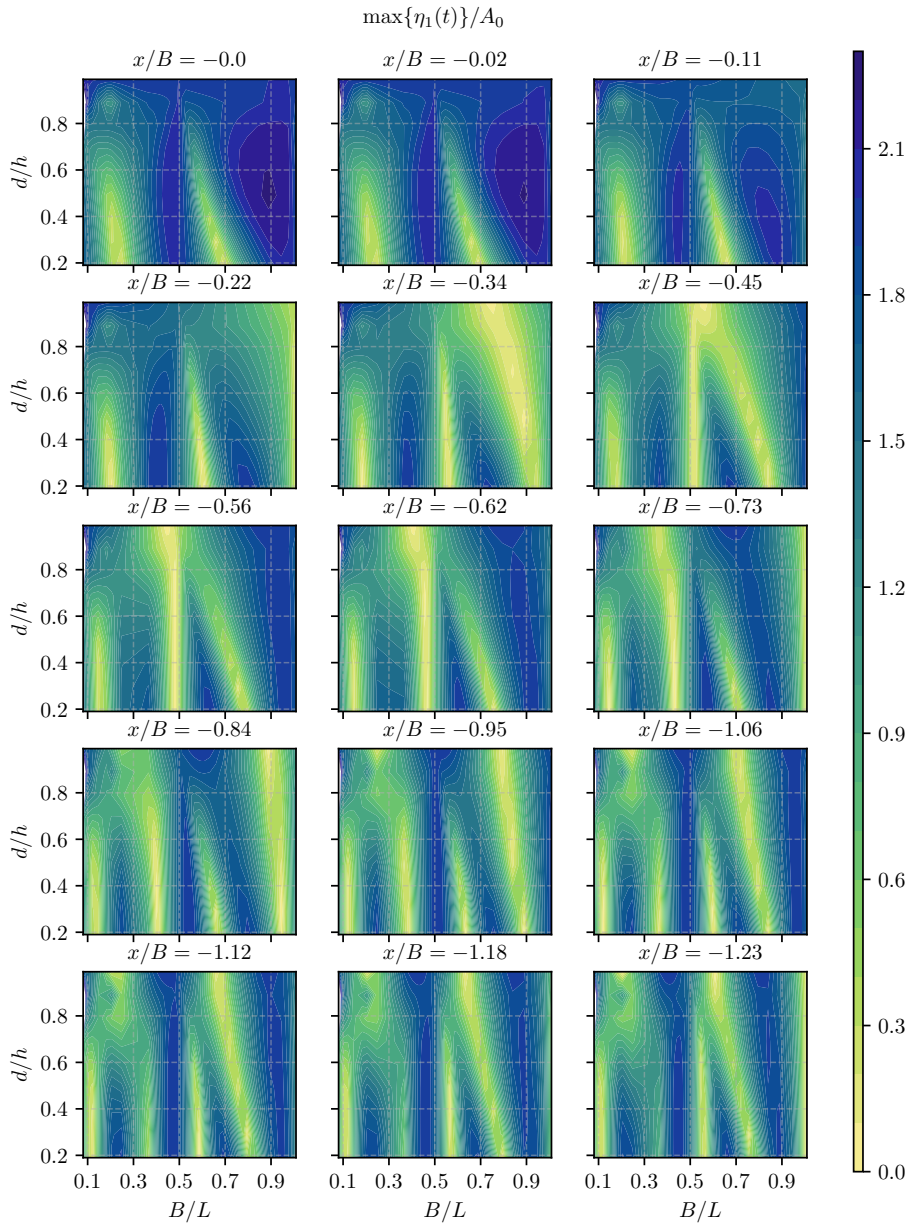

FIGURE 5.6: Maximum dimensionless amplitude in the seaward region (region 1) at different x–locations with respect to the relative submergence d/h and the relative width B/L of the system, for normally incident regular waves $\theta = 0°$.

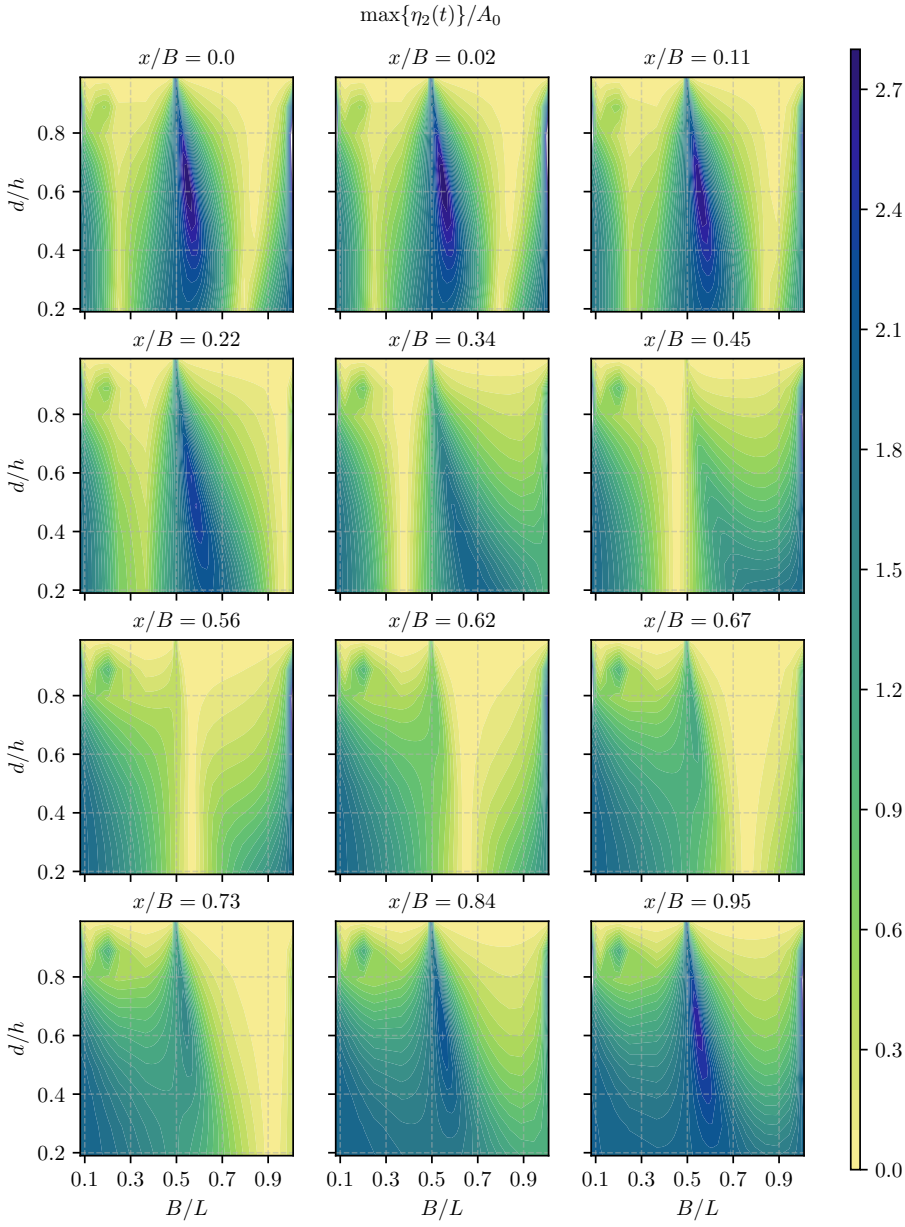

FIGURE 5.7: Maximum dimensionless amplitude in the leeward region (region 2) at different x–locations with respect to the relative submergence d/h and the relative width B/L of the system, for normally incident regular waves $\theta = 0°$.

at $x/B \approx -0.6$. Therefore for a certain d/h and B/L configuration, a periodic behavior can be observed in the maximum surface elevations with respect to the x–axis (Figure 5.8). This behavior is also present in the leeward region (Figure 5.7 and 5.8) although with a phase lag due to the influence of the plate. Therefore, for the given $d/h \leq 0.3$ and $B/L \approx 0.7$, quasi-antinodes are observed at $x/B \approx 0.3$ and quasi-nodes at $x/B \approx 0.65$. At $x/B \approx -0.5$ for $B/L = 0.51$ quasi-nodes are present for all the d/h cases. This is also the case where maximum K_C were found for values $0.5 < B/L < 0.6$ and $0.3 < d/h > 0.6$ as explained in Figure 5.1b.

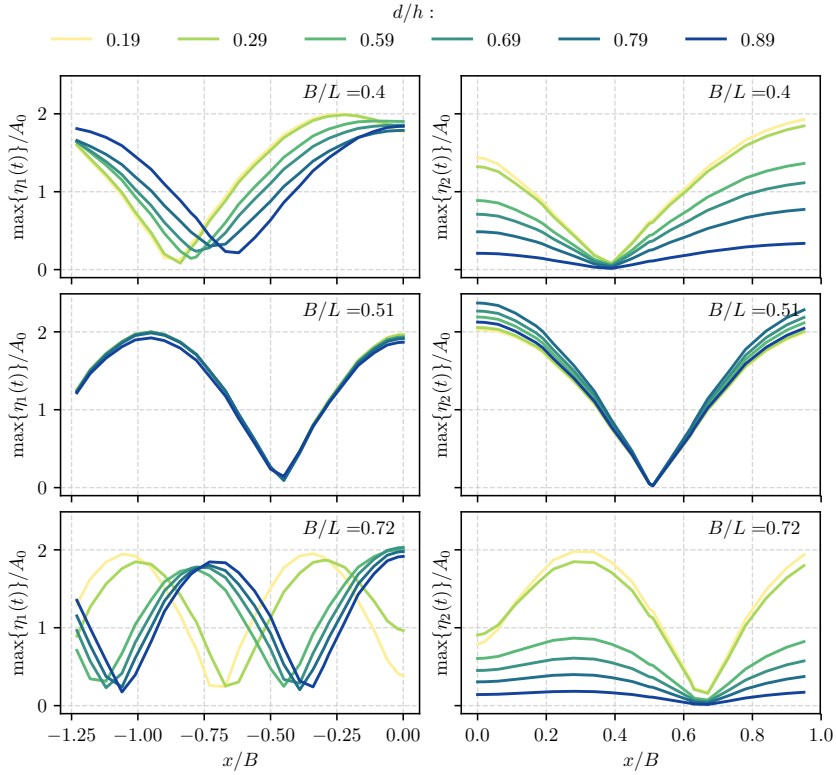

FIGURE 5.8: Maximum dimensionless amplitude in the seaward (left) and leeward (right) regions with respect to the x–axis for different values of relative submergence d/h and relative width B/L of the system, for normal regular wave incidence $\theta = 0°$.

5.1.1 Peak forces

Values of the phase of the reflection coefficient φ_C close to 180° indicate the presence of quasi-nodes in the seaward region ($\max\{\eta_1(x=0,t)\} \approx 0$) as observed in Figures 5.2a and 5.5a that would therefore generate lower loads acting on the plate towards land (F_l). At the same time, the presence of a quasi-node on the leeward side gives minimum forces acting towards sea (F_s). Therefore, these variables are considered to be decisive factors to obtain the maximum/minimum loads at both sides of the plate; however, the total load on the plate also depends on the relative phase lag between the surface elevations in both regions. Figure 5.9 presents the phase lag between the surface elevations at both sides of the plate (Equation 1.21). Critical total loads in both directions would be obtained when the surface elevations are approximately in phase opposition ($\Psi \approx 180°$) which corresponds to $B/L \lessapprox 0.3$ (periodic at $B/L = 0.5$) and high values of d/h.

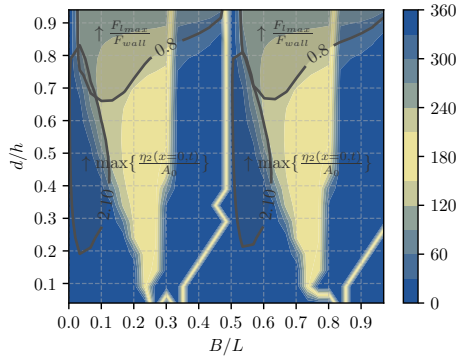

FIGURE 5.9: Phase lag Ψ (°) between the surface elevation at both sides of the plate with respect to the relative submergence d/h and the relative width B/L, for normally incident regular waves. The isolines indicate the areas with the highest values of $\max\{\eta_2(x=0,t)\}/A_0$ (Figure 5.5b) and $F_{l_{max}}/F_{wall}$ (Figure 5.10a).

Taking into account equations 1.22 and 1.23, the time variation of the total force on the plate largely depends on the head loss. Indeed, the larger the difference between the free surface elevations, the larger the absolute value of the force, with a sign depending on the sign of $\eta_1 - \eta_2$. The dimensionless peak forces F_{max}/F_{wall} are presented in Figure 5.10 where F_{wall} is the maximum force per unit width exerted by an incident wave train on a wall ($d/h = 1$) (Dalrymple and Dean, 1991).

As observed, for values around $B/L \approx 0.5$, and despite the maximum reflection and the relatively large amplitudes at the seaward side $\max\{\eta_1(x=0,t)\}$, forces are in balance due to the fact that the oscillations are almost in phase

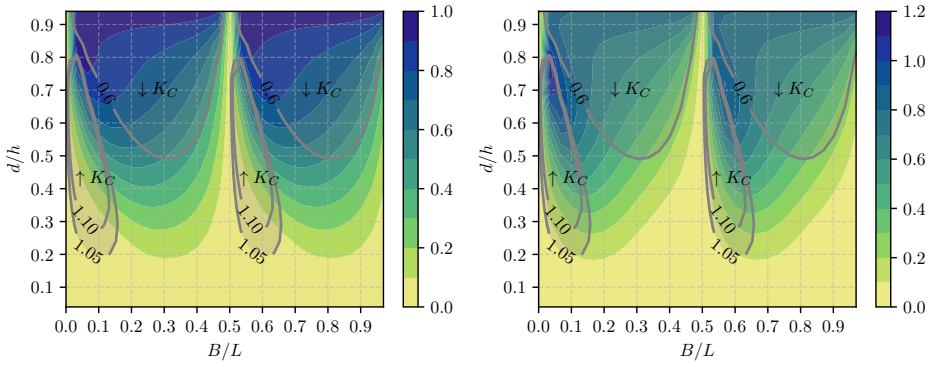

(A) $F_{l_{max}}/F_{wall}$ (B) $F_{s_{max}}/F_{wall}$

FIGURE 5.10: Dimensionless leeward-acting peak forces $F_{l_{max}}/F_{wall}$ and seaward-acting peak forces $F_{s_{max}}/F_{wall}$ on the plate ($x = 0$) with respect to the relative submergence d/h and the relative width B/L, for normally incident regular waves. The isolines indicate maximum ($\uparrow K_C$) and minimum ($\downarrow K_C$) capture coefficient as estimated in Fig. 5.1b

($\Psi \approx 0°$) and the most favorable conditions regarding the loads on the plate are obtained ($F_{max} \approx 0$).

In relation to the combination of the maximum/minimum loads on the plate and the capture coefficient inside the chamber, the regions around $0.5 < d/h < 0.7$ and $0.2 < B/L < 0.4$ (with periodicity at $B/L = 0.5$) seem to provide a balance of relatively low forces acting on the plate and low capture coefficients, an ideal situation e.g. for harbor design where lower wave heights are required. On the other hand, when studying the maximum wave energy inside the chamber (i.e. the design of wave energy converters), values around $B/L \approx 0.5$ and $0.3 < d/h < 0.6$ provide an optimum balance of low loads acting on the plate and high capture coefficients. In this case, it is also possible to find locations the seaward region where a quasi-node is present and therefore lower wave heights as observed for $x/B \approx -0.5$ on Figure 5.8.

5.2 Irregular Waves

Given that in nature, irregular waves are found with the combined action of different frequency components, it is necessary to analyze the structure when forced by irregular waves according to the methodology presented on §1.3. The model

was implemented for a TMA wave spectrum, commonly used in maritime engineering, with a peak wave period $T_p = 7$ s, significant wave height $H_s = 1.8$ m and peakedness parameter $\gamma = 1$ for the incident wave train. The frequency range was considered so that it included 90% of the total energy of the incident wave spectrum. The nondimensionalization of results was done using the peak frequency ($f_p = 1/T_p$), its associated wavelength L_p and the root mean square (r.m.s) characteristics of the theoretical incident wave spectrum: $H_{rms_I} = \sqrt{8m_0}$ and the incident wave amplitude value A_0 defined as $A_0 = A_{rms_I} = H_{rms_I}/2$.

Figure 5.11 presents the time series of η at both sides of the plate for different values of B/L_p and d/h.

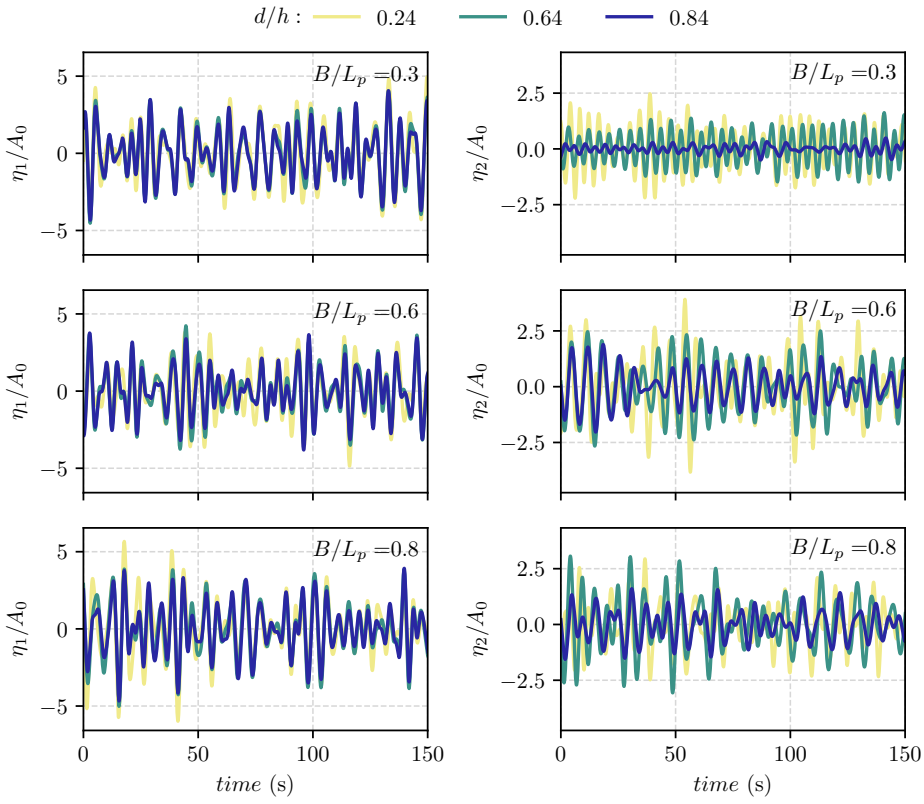

FIGURE 5.11: Dimensionless surface elevation (η/A_0) time series at $x = 0$ in the seaward (left) and leeward (right) regions for different values of the relative submergence d/h and relative width B/L_p and normally incident irregular waves.

It can be observed that the presence of the plate, in addition to modify the wave energy content inside the chamber, produces a phase lag between the surface elevations at both regions following the same behavior as in the case of regular waves (Figure 5.9). The highest values of free surface elevations in the leeward region (η_2/A_{m_0}) are obtained for $B/L_p = 0.5 - 0.6$ as expected by the results of Figure 5.5b.

In order to analyze the influence of the geometry of the system on the different wave frequencies present in nature, Figure 5.12 depicts the dimensionless total spectra of η in both regions for different values d/h and B/L_p with $S^* = S(f) * f_p/m_0$.

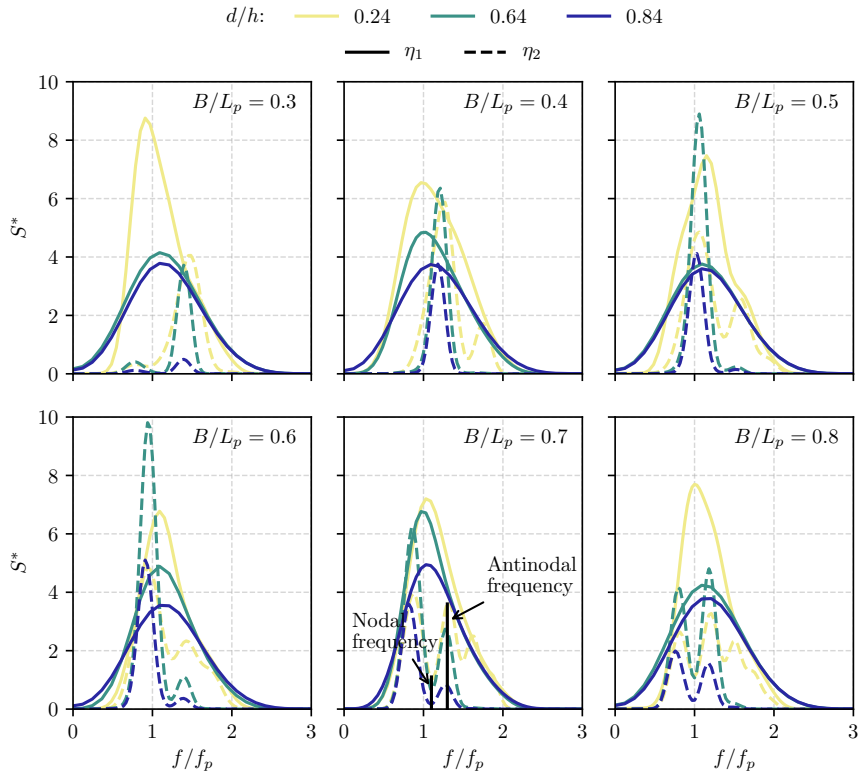

FIGURE 5.12: Dimensionless spectrum S^* of surface elevations at $x = 0$ in the seaward (solid lines) and leeward (dashed lines) regions for different values of relative submergence d/h and relative width B/L_p and normally incident irregular waves.

The results show a nodal and antinodal frequency structure for the total spectrum in the leeward region due to the superposition of the incident and reflected components. The number of antinodal frequencies and the distance between them vary with the relative width, while the energy for a given B/L_p value varies with the relative submergence.

Figure 5.13 presents the spectra for the case $B/L_p = 0.6$ and $d/h = 0.64$ at different values of x in the seaward region. It can be observed that the nodal and antinodal structure changes with the distance from the plate as expected by the results of Figures 5.6 and 5.8. This behavior has to be accounted if for e.g. one of the targets of the design is to obtain the best configuration towards harbor tranquility.

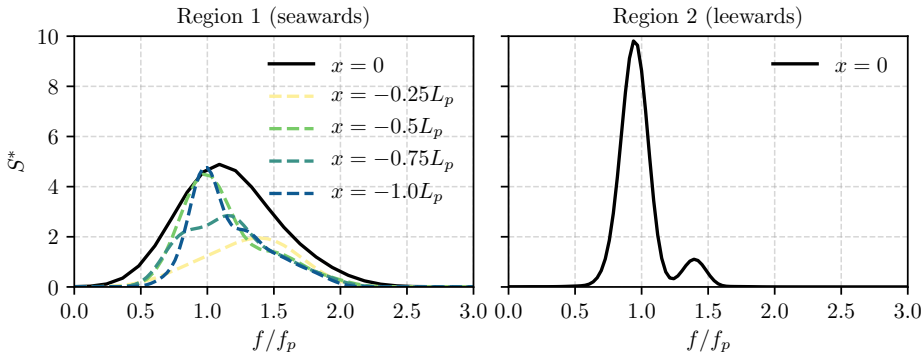

FIGURE 5.13: Dimensionless spectrum S^* of simulated surface elevation in the seaward region (left) at different x–locations and in the leeward region at $x = 0$ for normally incident irregular waves. These results correspond to the case $B/L_p = 0.6$ and $d/h = 0.64$.

The dynamic loads over the plate when forced by irregular sea states also need to be evaluated in order to have an overall picture of the performance of the structure. This includes the analysis of the forces and moments acting on the structure. In this case, for simplicity only the forces were analyzed by means of the total force F_t on acting the plate as shown in Figure 5.14 for different values of d/h and B/L_p. The superposition of the loads from both regions, lagged at some frequencies, produces an oscillation of the total force that changes its intensity as well as its direction. Due to the superposition of the incident and reflected components, the leeward surface spectrum presents nodal and antinodal frequencies depending on the geometry of the system.

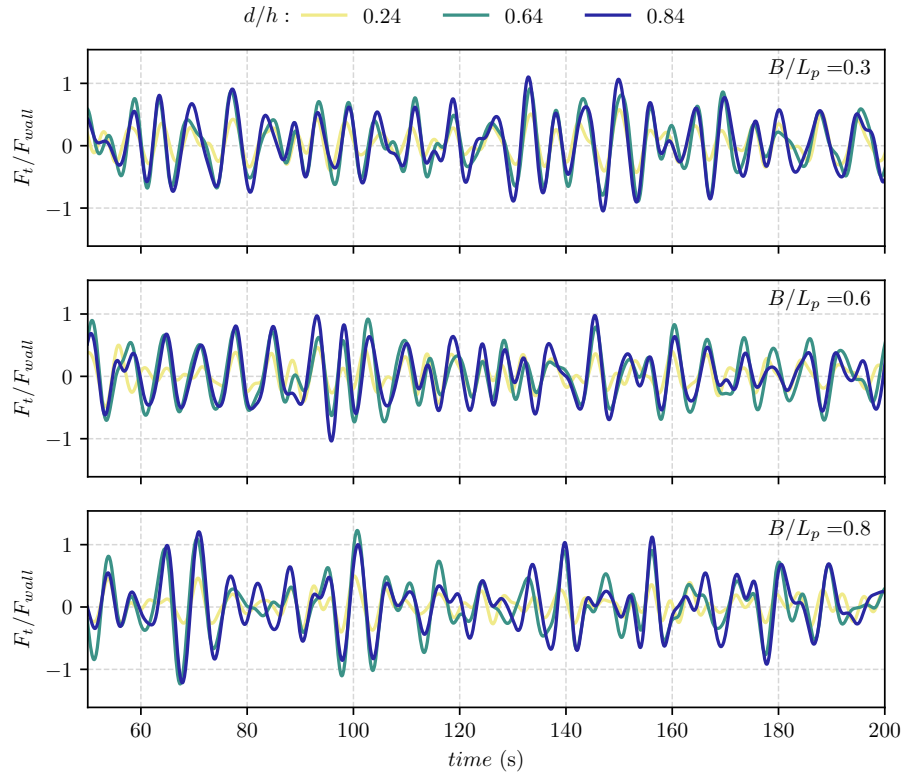

FIGURE 5.14: Time series of the dimensionless total wave forces F_t/F_{wall} acting on the plate ($x = 0$) for different values of the relative submergence d/h and relative width B/L_p and normally incident irregular waves.

It can be observed in Figure 5.14 that the lowest forces are obtained for the case $d/h = 0.24$ in all the considered cases of B/L_p. For higher relative submergences, the cases $B/L_p = 0.3$ and 0.8 present a few higher peaks than $B/L_p = 0.6$ although the general trend remains the same as in the case of regular waves.

The results of the wave forces in combination with the surface elevations are of great interest since these would be the predominant governing variables for the design of a wave energy converter device (η amplification) and/or harbor protection (η reduction) as well as the structural analysis. For example, in the cases of a wave energy converter design, it might be of interest to design a system with $B/L = 0.6$ and $d/h = 0.64$ given that it provides a higher surface elevation amplification and lower forces acting on the plate. This can be observed in Figure

5.12 in which, for $B/L_p = 0.6$ the amplitude of the oscillations inside the chamber and the energy content at some frequencies is higher than in the seaward region giving, as a result, values of the ratio between forces $F_t/F_{wall} < 1$ in Figure 5.14.

Figure 5.15 presents the empirical cumulative distribution function (ECDF) and the Normal distribution fit of the surface elevation in the leeward and seaward regions for $B/L_p = 0.6$ and different values of relative submergence d/h.

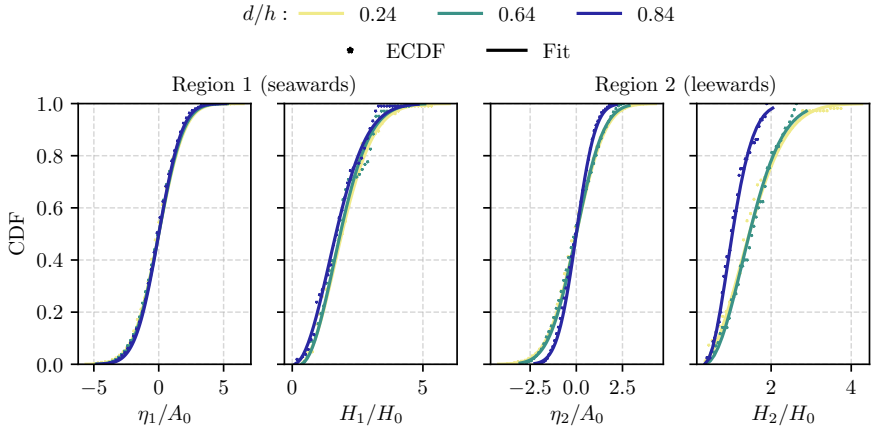

FIGURE 5.15: Empirical Cumulative Distribution Function (ECDF) and theoretical fit of the dimensionless surface elevation and wave heights in the leeward and seaward regions at $x = 0$ for $B/L_p = 0.6$ and different values of relative submergence d/h and normally incident irregular waves.

It can be observed that the CDF of the surface elevation in the seaward region is almost the same regardless of d/h for $x = 0$. However, inside the chamber it shows a change in variance. Applying the zero-crossing technique to the surface elevation time series, it is possible to obtain the individual wave heights of each signal and their distribution also presented on Figure 5.15. The wave heights in each region were fitted to Rayleigh distributions. As in the case of the surface elevation, the wave heights in the seaward region present the same distribution regardless of the relative submergence whilst in the leeward region the wave height varies with d/h.

Following the same procedure with the total force time series we obtained the leeward-acting forces F_l (crests) and seaward-acting forces F_s (throughs) and their distributions. Figure 5.16 presents the ECDF and the Normal fit of the total forces F_t and the Weibull fit of F_l and F_s. As expected, the case with the lowest

relative submergence presents the lowest forces while the cases $d/h = 0.64$ and 0.84 present similar distributions.

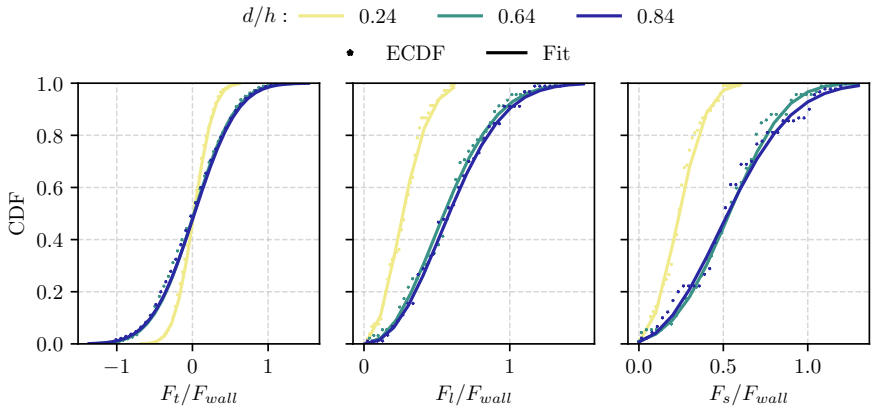

FIGURE 5.16: Empirical Cumulative Distribution Function (ECDF) and theoretical fit of the dimensionless total force F_t (left), leeward-acting forces F_l (middle) and seaward-acting forces F_s (right) on the plate ($x = 0$) for $B/L_p = 0.6$ and different values of relative submergence d/h and normally incident irregular waves.

5.3 Conclusions

The results of the implementation of an analytical model to study the effect of obliquely incident regular and irregular waves on a maritime structure are presented. The model works under the assumptions of linearized wave theory and taking into account the head loss due to the constriction of the flow.

The behavior of the system is analyzed through the reflection and capture coefficients and the structural component of the system is dealt by means of the maximum loads acting on the plate proving to be a simple and efficient methodology for the optimization of the design of maritime structures (trade-off between performance and structural design) for (i) controlled wave agitation for harbor tranquility, (ii) energy extraction in the leeward region and (iii) loads acting on the structure.

The more relevant conclusions are:

- Due to the wave-structure interaction, the spectra in both regions contains nodal and antinodal frequencies depending on the geometrical configuration of the system, water depth and the incident wave characteristics (H, T, θ).
- At $x = 0$ the spectrum presents one peak outside the chamber and several peaks inside the chamber. The number of peaks and the distance between them depends on the geometric characteristics. In the seaward region far from the reflector the spectrum presents a nodal structure applicable for controlled harbor agitation.
- The accurate representation of the phase lag and the general hydrodynamic behavior of the system depends on the correct mathematical representation of the head loss at the gap.
- For increasing wave incidence, the behavior of the system varies with a periodicity at $B/L' = 0.5$ where $L' = L/\cos\theta$.

Chapter 6

Interaction of swell and wind–sea waves

Note

Some of the results of the regular swell waves in combination with wind–sea waves presented in this chapter were published on:

A. Lira-Loarca, A. Baquerizo, and S. Longo (2018c). "Wind-wave interaction with a vertical semi-immersed barrier". In: *Proceedings of the 7th International Conference on the Application of Physical Modelling in Coastal and Port Engineering and Science (Coastlab18)*. Santander, Spain

A. Lira-Loarca, A. Baquerizo, and S. Longo (2019a). "Interaction of Swell and Sea Waves with Partially Reflective Structures for Possible Engineering Applications". In: *Journal of Marine Science and Engineering* 7.2. ISSN: 2077-1312. DOI: 10.3390/jmse7020031

This chapter presents the results of the experimental study carried out in the CIAO flume as described in Chapter 2. Tests involved the combination of paddle-generated swell waves and wind-driven sea waves and were divided into three groups and presented on independent sections:

- §6.1. *Wind-driven sea waves* generated by different wind speeds of the wind-tunnel without paddle-generated waves.
- §6.2. Paddle-generated *regular swell waves* with/without *wind–sea waves*
- §6.3. Paddle-generated *irregular swell waves* with/without *wind–sea waves*

Therefore, for clarity in all the results presented henceforth when talking about paddle-generated swell waves the corresponding *regular waves* or *irregular waves*

term will be used, whereas when referring to local wind–sea waves generated by the wind tunnel the term *wind–sea waves* or *wind-driven waves* will be used. The final part (§6.4) presents the main conclusions of the experimental study.

The analysis aims for a better understanding of the hydrodynamic behavior of the system when the structure interacts with swell and sea waves. Therefore, we analyzed the experimental data with respect to the geometry of the chamber and under different wind conditions U_{ref}.

During the experiments, the relative submergence d/h was modified by varying the submergence of the plate d whereas the water depth $h = 0.7$ m was kept constant. To test different values of the relative width B/L, the chamber width B remained fixed and different configurations of wave periods, with and without the combination of wind, were tested, therefore changing the wavelength of the incident wave.

With the system configuration presented on §2.1 the first two natural oscillation periods of the chamber ($B = 2.5$ m) are close to $T_1 = 1.9$ s and $T_2 = 0.95$ s approximated using Merian's formula (Equation 2.5). Given the position of the plate and the back wall, the length of the flume is reduced to 11 m with $T_{1,0} = 8.4$ s and $T_{2,0} = 4.2$ s. Considering the length up to the back wall, 13.5 m, $T_{1,0} = 10.3$ s and $T_{2,0} = 5.15$ s are obtained. The cross-modes give similar values in both cases with $T_{1,1} \approx T_{2,1} \approx 0.76$ s and $T_{1,2} \approx T_{2,2} \approx 0.38$ s.

6.1 Wind–sea waves

Table 6.1 presents the nomenclature and the values of the S1–gauge parameters of the experiments with wind-driven waves. T_{z0} and T_p are the mean and peak wave period obtained by the statistical and spectral analysis, respectively, of the surface elevation data of the wave gauge S1 ($x = -2.1$ m).

It can be observed that the mean period of the waves T_{z0} in the seaward region (S1) is not affected by the plate submergence d/h as it remains almost constant for a same wind speed configuration e.g. tests $W1a$–$W1c$ with $T_z0 \approx 0.2$ regardless of the different d/h. As expected, the mean wave period increases with the increase of wind speed reaching values of $\approx$ 0.4 for the highest wind speed $W4$ as the waves are developing. Regarding the peak period T_p, a higher deviation can be found regarding the different submergences and it starts having values similar to the mean period as the wind speed increases. This is due to the fact that for higher winds, the wind-driven waves are grouped together and the spectrum takes a narrower shape and therefore the mean and peak periods are more alike.

Figure 6.1 presents the surface elevation time series of the wave gauges S1 and S2 in the seaward region for the different wind–sea waves experiments. A

TABLE 6.1: Nomenclature and S1–gauge parameters of the wind–sea waves experiments. T_{z0} and T_p represent the mean and peak wave period, respectively of the surface elevation data of S1. T_1 is the first natural period of the chamber. Each column depicts the mean value $\pm$ the difference —when applicable— between the values of repetitions of the same test.

Test	d/h	U_{ref} (m/s)	T_{z0} (s)	T_p (S)	T_{z0}/T_1
$W1a$	0.33	4.2	0.22	1.58	0.11
$W1b$	0.58	4.2	0.21	1.72 ± 0.14	0.11
$W1c$	0.71	4.2	0.22	0.89 ± 0.69	0.11
$W2a$	0.33	6.3	0.27	0.29	0.14
$W2b$	0.58	6.3	0.27	0.29	0.14
$W2c$	0.71	6.3	0.27	0.29 ± 0.01	0.14
$W3a$	0.33	8.5	0.31	0.35	0.16
$W3b$	0.58	8.5	0.30	0.33	0.16
$W3c$	0.71	8.5	0.31	0.34	0.16
$W4a$	0.33	10.5	0.39	0.45	0.20
$W4b$	0.58	10.5	0.38	0.42 ± 0.03	0.20
$W4c$	0.71	10.5	0.40	0.44 ± 0.04	0.21

more random behavior is obtained for lower wind speeds whereas developed and grouped waves can be found for the highest wind $W4$ and almost double the height for S2. Test $W4$ presents similar $T_{z0} \approx 0.39$ s for all the different submergences which yield values of $L_{z0} \approx 0.24$ m. According to the analytical model results and taking account the periodical behavior of the system, for $B/L \approx 0.5$, high values of the reflection coefficient are obtained and for S1, a quasi-antinode can be found and slightly higher values of η_1 are obtained as the submergence decrease. For S2 a quasi-node is present and higher η_1 values are obtained for the highest submergences. Figure 6.2 presents the time series in the leeward region for wave gauges S5 and S6. It can be observed that the wave height is of the same order of magnitude for both wave gauges and it does not vary as much between configurations Wa–Wc as it does in the seaward region. The surface elevation data presents lower values $\eta_2 \approx 0.01$ with respect to those in the seaward region $\eta_1 \approx 0.05$ which will lead to low energy inside the chamber.

Figure 6.3 presents the power spectrum of the surface elevation data for the wind–sea W–experiments, different wind speeds and sensors S1 and S2 in the seaward regions and S5 and S6 in the leeward region. For the lowest wind speed $W1$ and in the seaward region, two different energy regions can be found at frequencies $f \lessapprox 2$ Hz and $4 \lessapprox f \lessapprox 6$ Hz. The first region corresponds to the frequencies of the wind (Figure 2.6) which indicates the presence of the wind acting on the water surface without wave developments. With the increase of the wind speed,

the energy at the lower frequencies becomes negligible as the waves start to develop in the higher frequencies. It can also be observed that the spectral density increases, takes a narrower shape and the peak frequency decreases. In the leeward region (S5 and S6), the spectrum does not present a definite shape or peak frequency showing peaks for frequencies around the first natural frequency of the chamber $f_1 = 1/T_1 \approx 0.5$ and its harmonics and in general lower frequencies than in the seaward region as the dominating mechanism is the excitations of the natural oscillations modes of the chamber and not the short-crested wind-driven waves, with energy of two orders of magnitude lower than in the seaward region.

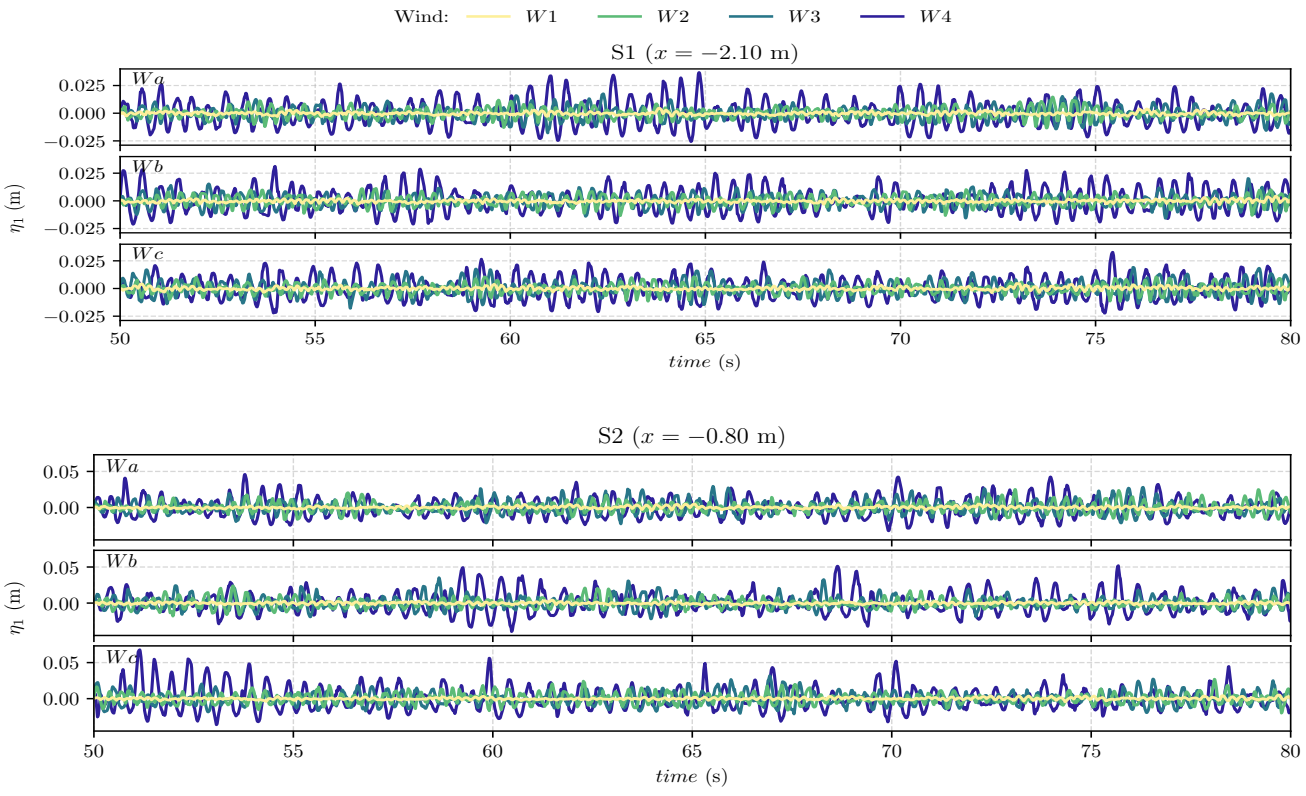

FIGURE 6.1: Surface elevation time series in the seaward region (η_1) for the wind–sea waves *W*–experiments (rows) and different wind speeds (colors). The top and bottom plots represent the surface elevation data of S1 and S2, respectively.

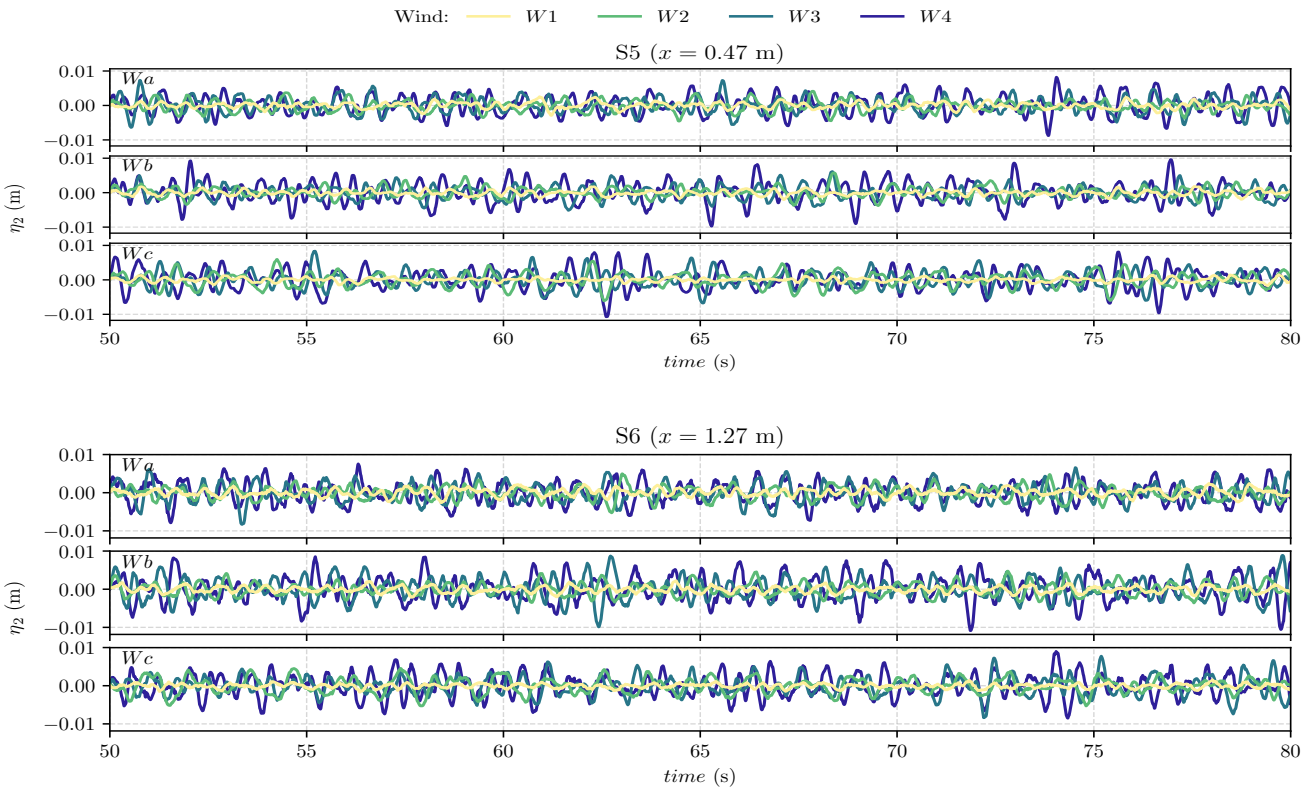

FIGURE 6.2: Surface elevation time series in the leeward region (η_2) for the wind–sea waves *W*–experiments (rows) and different wind speeds (colors). The top and bottom plots represent the surface elevation data of S5 and S6, respectively.

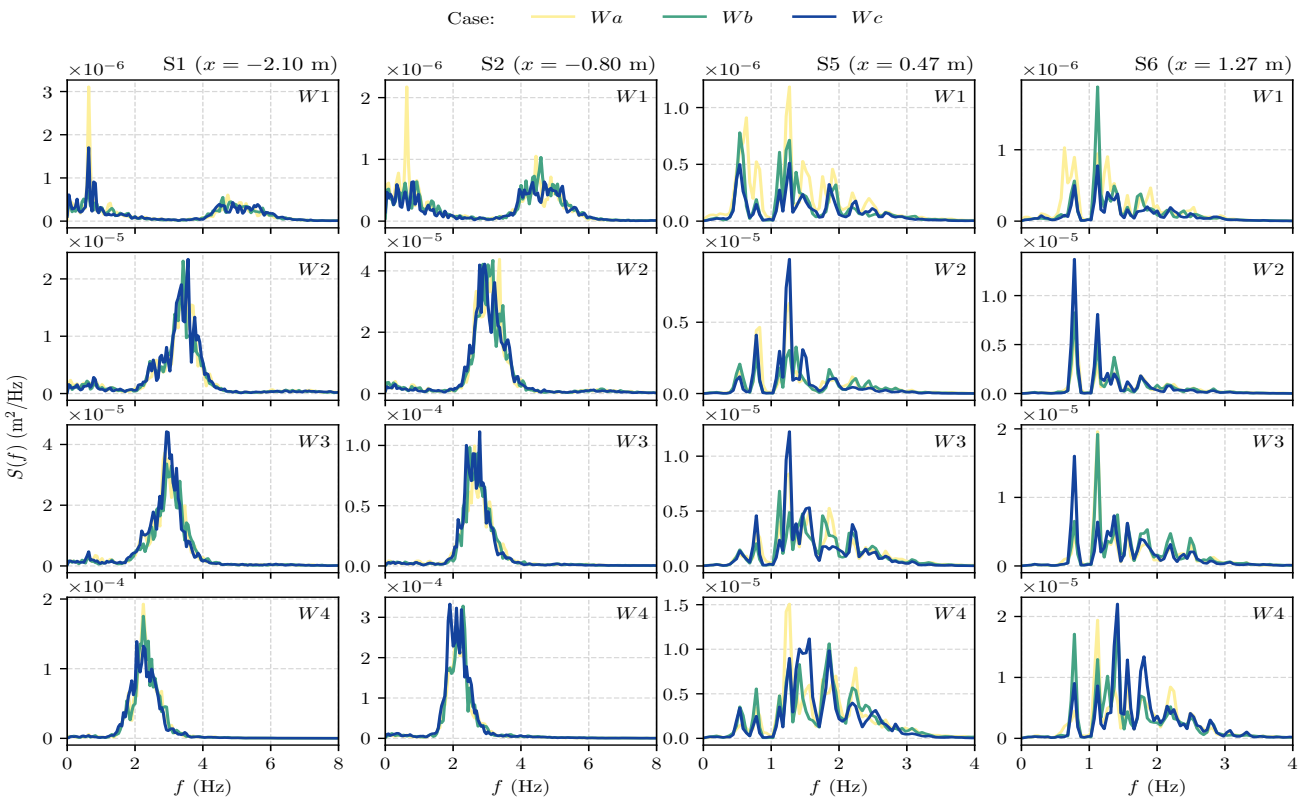

FIGURE 6.3: Power spectrum (S) of η for the wind–sea waves W–experiments (colors), different wave gauges (columns) and wind speeds (rows).

Figure 6.4 presents the power spectrum of the surface elevation data in the seaward region (S1 and S2) for the *Wb*–experiment and different wind speeds. It can be observed that the spectra at both positions follows the shape given in literature of wave spectrum with increasing fetch under steady wind conditions (Phillips, 1967) where the spectral density increases with wind/fetch and the peak frequency decreases and the saturation range can be clearly observed. In the Figures different limits have been drawn. Phillips, 1967 defined the saturation ranges as the range of frequencies over which the spectrum is saturated and close to its upper limit imposed by dissipation processes. This saturation range can be defined as,

$$S(f) = \beta g^2 f^{-5} \tag{6.1}$$

where β is a numerical constant. Massel, 1996 extended the definition with β being a function of external growth conditions,

$$S(f) = 4b^4 \delta^2 g^2 f^{-5} \tag{6.2}$$

with $\delta = \frac{\sigma_\eta f_p^2}{g}$ being a characteristic slope in deep water, σ_η^2 is the variance and b is obtained from a normalization condition,

$$\sigma_\eta^2 = \int_0^\infty S(f) df \tag{6.3}$$

It can be observed in Figure 6.4 that for S1, the saturation range is clearly defined with Equation 6.1 for $\beta = 0.8 \times 10^{-4}$ where waves are still growing. In the case of S2, for a longer fetch the spectral density is higher, waves are developed and moved away from the saturation range defined by Massel, 1996.

Figures 6.5 and 6.6 present the power spectrum of the surface elevation data in the seaward and leeward regions, respectively, for the *Wb*–experiment, different wind speeds and temporal subsets. The results for the *Wa* and *Wc* experiments are presented on the Appendix A.1. Each temporal subsets takes a 15 s time series of data and are intended to represent the different characteristics as the waves are being developed. It can be observed in the seaward region that for the first temporal subsets, the spectrum is not clearly defined and starts taking a more narrow-band shape as the waves are more developed. The spectrum from the full time series $t = 185$ s presents a lower energy content than the spectra for the last temporal subsets. This is the same for the leeward region where the spectral density is of two orders of magnitude lower than in the seaward region and a great variation can be found when taking different temporal subsets.

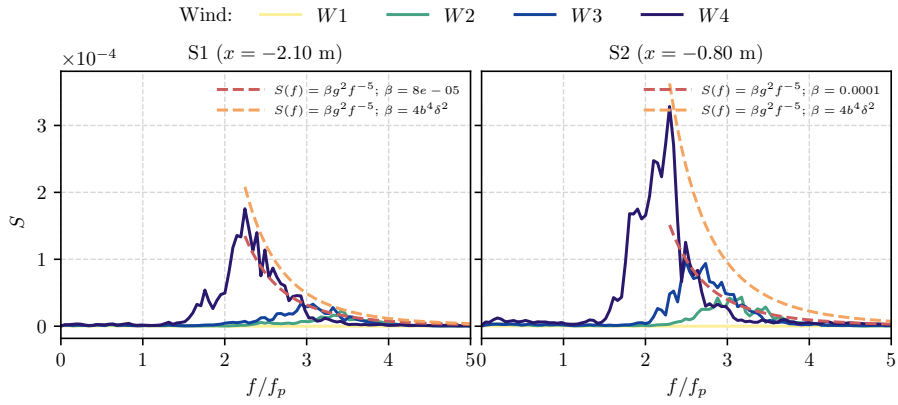

FIGURE 6.4: Power spectrum of η_1 for the wind–sea waves experiment *Wb*, different wind speeds (rows) and temporal subsets (colors). The left and right plots represent the surface elevation data of S1 and S2, respectively.

In the case of the seaward region and the lowest wind speed *W*1, the energy is dispersed over a large range of frequencies $f \approx 0 - 6$ Hz with a higher variation depending on the selected temporal series. For higher wind speeds the spectral density presents peaks of order of magnitude $O(10^{-4})$ and between frequencies of 2.5–4.5 Hz for *W*1, 2–4 Hz for *W*2 and 1.5–3.5 Hz for *W*4 for S1 and slightly lower for S2. Regarding the leeward region, lowest frequencies moving towards the resonant frequencies of the chamber with lower energy $O(10^{-5})$. It can be highlighted that the energy content at the resonant frequencies varies from gauges S5 and S6 depending on the location of the quasi-nodes and quasi-antinodes.

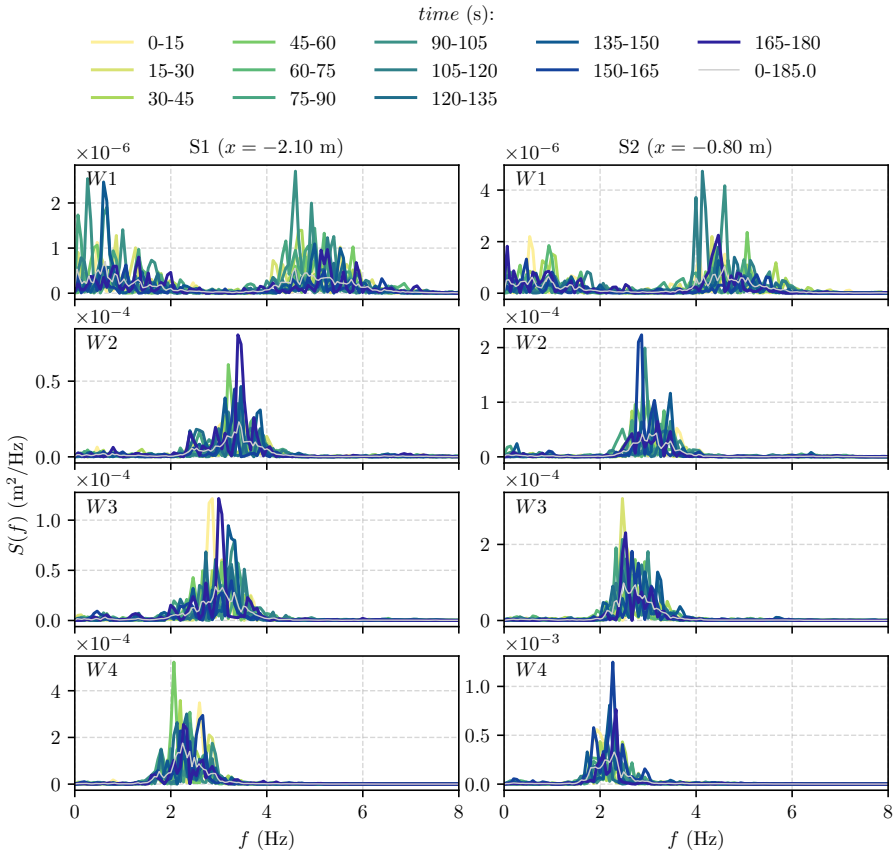

FIGURE 6.5: Power spectrum of η_1 for the wind–sea waves experiment *Wb*, different wind speeds (rows) and temporal subsets (colors). The left and right plots represent the surface elevation data of S1 and S2, respectively.

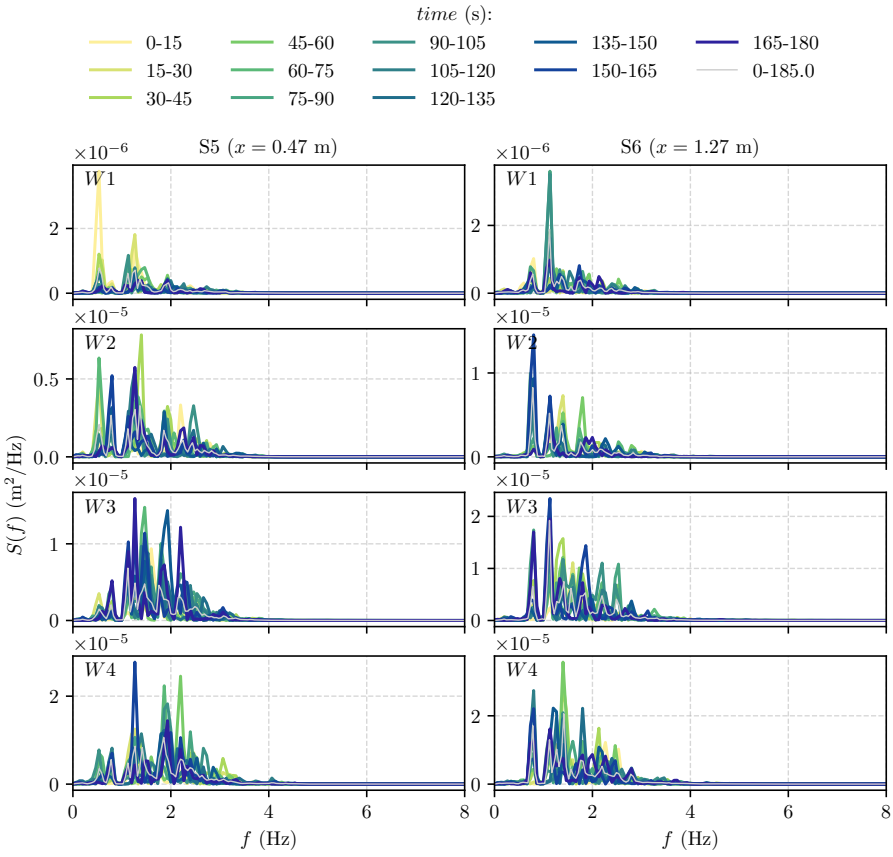

FIGURE 6.6: Power spectrum of η_2 for the wind–sea waves experiment *Wb*, different wind speeds (rows) and temporal subsets (colors). The left and right plots represent the surface elevation data of S5 and S6, respectively.

6.2 Regular waves

The next group of experiments was done under paddle–generated *regular waves* with/without the combination of *wind–sea waves* (generated by the wind tunnel). The nomenclature and input parameters are presented on Table 6.2.

TABLE 6.2: Nomenclature and parameters of the regular and wind–sea waves experiments. H^{input} and T^{input} are the input setup values of the wave generation software, d/h is the relative submergence and U_{ref} represents the reference wind speed.

Test	d/h	H^{input} (m)	T^{input} (s)	U_{ref} (m/s)
$R1a\_T1$	0.33	0.07	1.85	
• $R1a\_T1\_W0$				0
• $R1a\_T1\_W1$				4.2
• $R1a\_T1\_W2$	0.33	0.07	1.85	6.3
• $R1a\_T1\_W3$				8.5
• $R1a\_T1\_W4$				10.5
$R1b\_T1$	0.58	0.07	1.85	0, 4.2, 6.3, 8.5, 10.5
$R1c\_T1$	0.71	0.07	1.85	0, 4.2, 6.3, 8.5, 10.5
$R1b\_T2$	0.58	0.07	2.78	0, 4.2, 6.3, 8.5, 10.5
$R1b\_T3$	0.58	0.07	4.76	0, 4.2, 6.3, 8.5, 10.5
$R2a\_T1$	0.33	0.06	1.65	0, 4.2, 6.3, 8.5, 10.5
$R2b\_T1$	0.58	0.06	1.65	0, 4.2, 6.3, 8.5, 10.5
$R2c\_T1$	0.71	0.06	1.65	0, 4.2, 6.3, 8.5, 10.5
$R2b\_T2$	0.58	0.06	3	0, 4.2, 6.3, 8.5, 10.5
$R2b\_T3$	0.58	0.06	4.7	0, 4.2, 6.3, 8.5, 10.5

[1] For simplicity, the nomenclature for experiments involving wind is presented only for experiment $R1a\_T1$.

Table 6.3 lists the values obtained from the statistical analysis of the surface elevation data of the S1–gauge and the reflection analysis as explained in §2.3 (reflection coefficient K_R and incident wave height H_{rms_I}) for the regular wave experiments without wind. $T_{z0_{W0}}$ is the mean wave period and is always coincident with the input period T^{input}, whereas H_{rms_I} is not coincident with the imposed value H^{input}. $L_{0_{W0}}$ represents the wavelength obtained by means of the linear dispersion equation (Eq. 1.2) for the experiment without wind. Table 6.4 lists the parameters for all the regular and wind–sea waves experiments.

Regarding the experiments without wind (Table 6.3) it can be observed that the lowest reflection coefficients are obtained for experiments $R1b\_T1\_W0$ and $R1b\_T3\_W0$ corresponding to the higher values of capture coefficient according

to the analytical model results. This will be further investigated when analyzing the data of the leeward sensors.

TABLE 6.3: Incident and S1–gauge parameters of the regular wave experiments without wind–sea waves. H_{rms_I} is the incident wave height. $T_{z0_{W0}}$ and $L_{0_{W0}}$ are mean wave period and wavelength, respectively, of the S1-data for the experiment without wind. Each column depicts the mean value $\pm$ the difference —when applicable— between the values of repetitions of the same test.

Test	d/h	H^{input} (m)	H_{rms_I} (cm)	K_R	$T^{input} = T_{z0_{W0}}$ (s)	$B/L_{0_{W0}}$	$T_{z0_{W0}}/T_1$
R1a_T1_W0	0.33	0.07	5.7	0.65	1.85	0.6	0.97
R1b_T1_W0	0.58	0.07	5.5	0.27	1.85	0.6	0.97
R1c_T1_W0	0.71	0.07	7.2 ± 0.09	0.45	1.85	0.6	0.97
R1b_T2_W0	0.58	0.07	9.1	0.76	2.78	0.37	1.46
R1b_T3_W0	0.58	0.07	6.7 ± 0.9	0.26	4.76	0.21	2.5
R2a_T1_W0	0.33	0.06	4	0.52	1.65	0.7	0.87
R2b_T1_W0	0.58	0.06	4 ± 0.04	0.82 ± 0.03	1.65	0.7	0.87
R2c_T1_W0	0.71	0.06	4.2 ± 0.05	0.89 ± 0.02	1.65	0.7	0.87
R2b_T2_W0	0.58	0.06	3.6 ± 0.19	0.68 ± 0.11	3	0.34	1.58
R2b_T3_W0	0.58	0.06	5.3 ± 0.53	0.29 ± 0.03	4.7	0.21	2.47

For clarity, all the results presented henceforth are dimensionless with respect to the corresponding incident values of the experiments without wind given on Table 6.3.

TABLE 6.4: Incident and S1–gauge parameters of the regular and wind–sea waves experiments. H_{rms_I} is the incident wave height. T_{z0} is the mean wave period of the S1–data. Each column depicts the mean value $\pm$ the difference —when applicable— between the values of repetitions of the same test.

Test	d/h	H^{input} (cm)	H_{rms_I} (cm)	K_R	T^{input} (s)	T_{z0} (s)
*R*1*a*_*T*1_*W*0			5.7	0.65		1.85
*R*1*a*_*T*1_*W*1			5.4	0.66		1.85
*R*1*a*_*T*1_*W*2	0.33	7	5.4	0.68	1.85	1.67 ± 0.14
*R*1*a*_*T*1_*W*3			5.1	0.75		1.49 ± 0.1
*R*1*a*_*T*1_*W*4			5.1	0.66		1.35 ± 0.3
*R*1*b*_*T*1_*W*0			5.5	0.27		1.85
*R*1*b*_*T*1_*W*1			5.6 ± 0.04	0.33		1.84
*R*1*b*_*T*1_*W*2	0.58	7	6.6 ± 0.20	0.85 ± 0.08	1.85	1.61 ± 0.04
*R*1*b*_*T*1_*W*3			5.6 ± 0.06	0.38 ± 0.01		1.52 ± 0.03
*R*1*b*_*T*1_*W*4			5.7 ± 0.04	0.30 ± 0.01		1.22 ± 0.05
*R*1*c*_*T*1_*W*0			7.2 ± 0.09	0.45		1.85
*R*1*c*_*T*1_*W*1			7.2 ± 0.03	0.45		1.85
*R*1*c*_*T*1_*W*2	0.71	7	7.5 ± 0.07	0.48	1.85	1.84
*R*1*c*_*T*1_*W*3			7.4 ± 0.02	0.56		1.83
*R*1*c*_*T*1_*W*4			7.9	0.47		1.72 ± 0.04
*R*1*b*_*T*2_*W*0			9.1	0.76		2.78
*R*1*b*_*T*2_*W*1			8.9 ± 0.13	0.78		1.66 ± 0.15
*R*1*b*_*T*2_*W*2	0.58	7	9.0 ± 0.11	0.78	2.78	0.73
*R*1*b*_*T*2_*W*3			9.1 ± 0.12	0.77		0.66 ± 0.04
*R*1*b*_*T*2_*W*4			9.3 ± 0.17	0.77		0.52
*R*1*b*_*T*3_*W*0			6.7 ± 0.9	0.26		4.76
*R*1*b*_*T*3_*W*1			6.6 ± 0.96	0.26		4.48 ± 0.04
*R*1*b*_*T*3_*W*2	0.58	7	6.6 ± 0.94	0.26	4.76	2.41
*R*1*b*_*T*3_*W*3			6.6 ± 0.90	0.25		2.7 ± 0.41
*R*1*b*_*T*3_*W*4			6.7 ± 0.83	0.25		1.79 ± 0.47
*R*2*a*_*T*1_*W*0			4	0.52		1.65
*R*2*a*_*T*1_*W*1			4.0	0.5		1.65
*R*2*a*_*T*1_*W*2	0.33	6	3.9	0.54	1.65	1.46
*R*2*a*_*T*1_*W*3			3.9	0.53		1.17
*R*2*a*_*T*1_*W*4			4.4	0.54		0.94
*R*2*b*_*T*1_*W*0			4 ± 0.04	0.82 ± 0.03		1.65
*R*2*b*_*T*1_*W*1			4.0 ± 0.02	0.79		1.65
*R*2*b*_*T*1_*W*2	0.58	6	4.0 ± 0.02	0.82 ± 0.01	1.65	1.52 ± 0.02
*R*2*b*_*T*1_*W*3			4.2 ± 0.01	0.80		1.39 ± 0.08
*R*2*b*_*T*1_*W*4			4.7 ± 0.06	0.79		1.2
*R*2*c*_*T*1_*W*0			4.2 ± 0.05	0.89 ± 0.02		1.65
*R*2*c*_*T*1_*W*1			4.2 ± 0.02	0.90 ± 0.02		1.65
*R*2*c*_*T*1_*W*2	0.71	6	4.3 ± 0.02	0.94 ± 0.02	1.65	1.52 ± 0.02
*R*2*c*_*T*1_*W*3			4.6 ± 0.06	0.91 ± 0.03		1.5
*R*2*c*_*T*1_*W*4			5.0	0.92		1.3
*R*2*b*_*T*2_*W*0			3.6 ± 0.19	0.68 ± 0.11		3
*R*2*b*_*T*2_*W*1			3.6 ± 0.20	0.69 ± 0.10		2.25 ± 0.12
*R*2*b*_*T*2_*W*2	0.58	6	3.6 ± 0.19	0.69 ± 0.10	3	0.96 ± 0.07
*R*2*b*_*T*2_*W*3			3.6 ± 0.18	0.68 ± 0.10		0.83 ± 0.03
*R*2*b*_*T*2_*W*4			3.0	0.78		0.55 ± 0.03
*R*2*b*_*T*3_*W*0			5.3 ± 0.53	0.29 ± 0.03		4.7
*R*2*b*_*T*3_*W*1			5.3 ± 0.5	0.29 ± 0.03		4.42 ± 0.16
*R*2*b*_*T*3_*W*2	0.58	6	5.3 ± 0.53	0.28 ± 0.02	4.7	2.24 ± 0.34
*R*2*b*_*T*3_*W*3			5.3 ± 0.47	0.28 ± 0.03		2.03 ± 0.38
*R*2*b*_*T*3_*W*4			5.4 ± 0.45	0.29 ± 0.02		1.44 ± 0.39

Figures 6.7 and 6.8 depict the dimensionless surface elevation η/A_0 for the $R1$– and $R2$–experiments, respectively, in the seaward region. A_0 is incident wave amplitude obtained from the reflection analysis of the S1–data in the absence of wind as explained on §2.3. Figures 6.9 and 6.10 present the case of the leeward region experiments.

Regarding the seaward region, it can be observed that the highest relative amplitudes are obtained for the tests with wave periods $T1$ where the incident wave period is close to the value of the first natural period of the chamber in which the B/L configuration gives place to quasi-antinodes for the positions of $S1$ and $S2$. In this case the wind speed enhances the peaks and the troughs of the regular waves, possibly due to the coupling of wind oscillations present in the wind spectrum in the band $f < 2$ Hz with peaks around 0.5–1 Hz. It also superimposes shorter waves that are greater for the chamber configurations with higher reflection coefficients. In the case of the experiments with $d/h = 0.58$ (b–configuration) and higher wave periods $T2$ (longer waves), the relative wave height is reduced with values around $\eta/A_0 \leq 1$ for the $S1$–position which almost coincides with a quasi-node. The wind speed seems to have a lesser influence on the long wave oscillation as it is more difficult for the shorter wind–sea waves to alter the behavior of the periodical component of the energetic long wave. This is of special interest when designing a maritime structure for harbor protection where the location of quasi-nodes is wanted.

In the case of the leeward region, it can be observed that the highest relative amplitude inside the chamber is given for the $R1$–tests with $d/h = 0.33 - 0.58$, with almost double of the incident wave amplitude at the section S5 (which is very close to a quasi-antinode), for all wind speeds. Despite the fact that in the seaward region, the $R2$–test showed a similar behavior of wave amplification, in the leeward region the behavior changes proving the influence of the T_z/T_1 ration of wave amplification inside the chamber. The deformation of the regular wave induced by wind action in the seaward region is transmitted inside the chamber, where an asymmetry between crests and troughs is observed. This could be due to the amplification modes of the system and to the re-reflection, both controlled by geometry. In passing, we notice that free surface oscillations are strongly affected by the forcing term and by the damping, the latter mainly due to dissipation Longo et al., 2013. For limited dissipation, a blow up of the oscillations is expected for multiple harmonic in the forcing term. In this respect, the free surface oscillations in the chamber can vary significantly if energy is extracted.

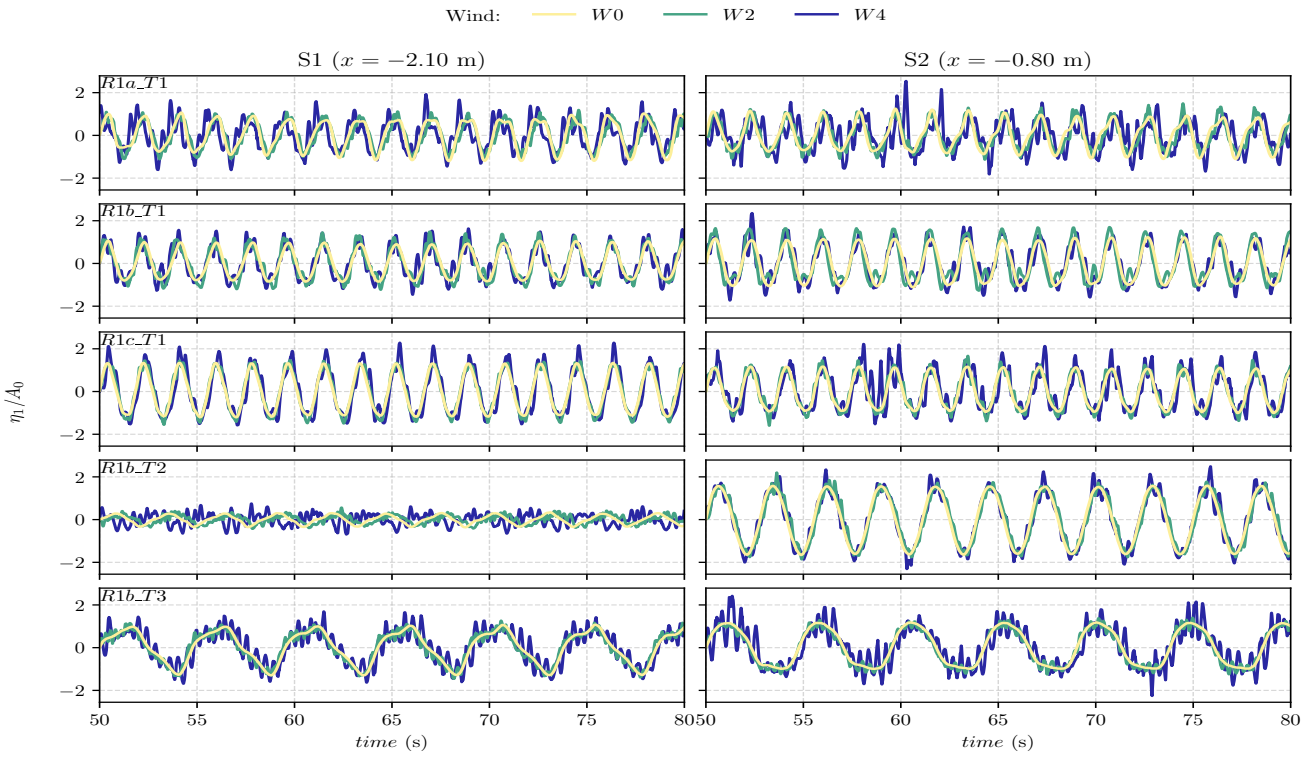

FIGURE 6.7: Dimensionless surface elevation time series in the seaward region (η_1 / A_0) for the regular waves *R*1– experiments (rows) and different wind speeds (colors). The left and right columns represent the surface elevation data of S1 and S2, respectively.

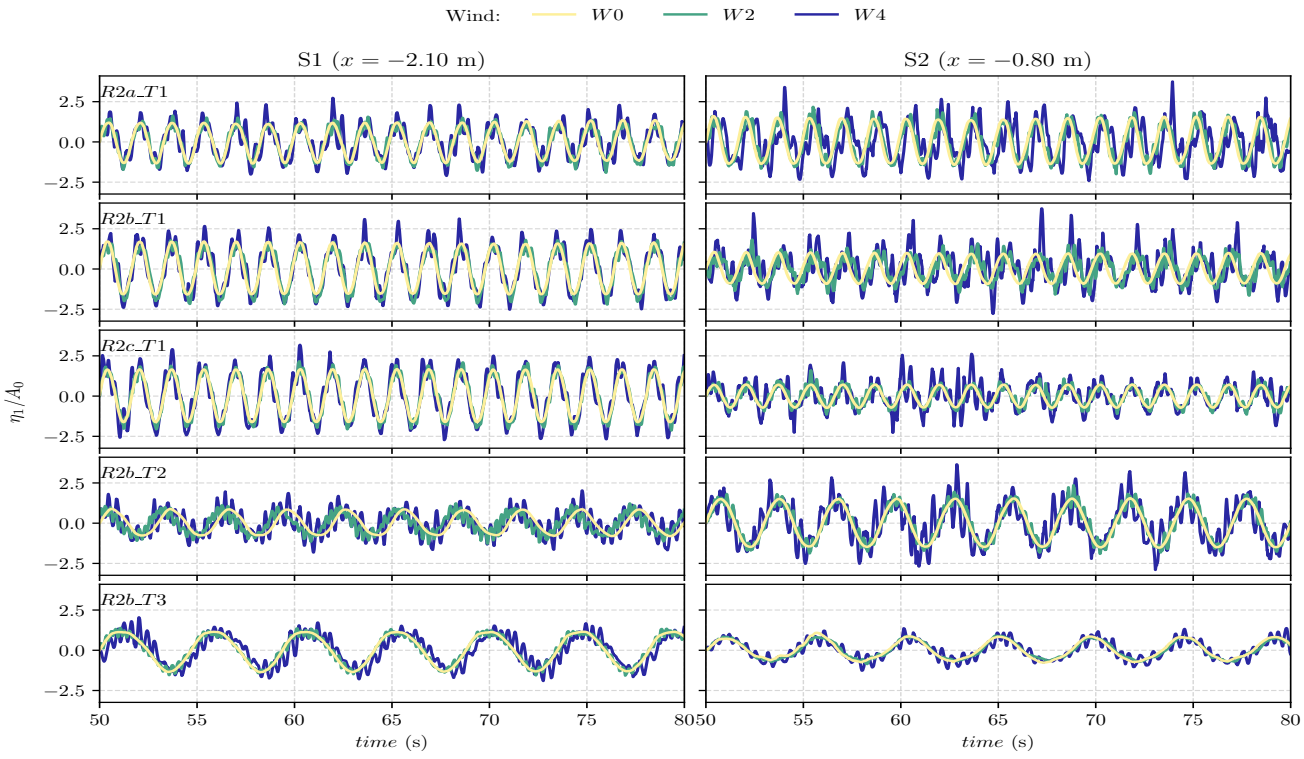

FIGURE 6.8: Dimensionless surface elevation time series in the seaward region (η_1/A_0) for the regular waves *R*2– experiments (rows) and different wind speeds (colors). The left and right columns represent the surface elevation data of S1 and S2, respectively.

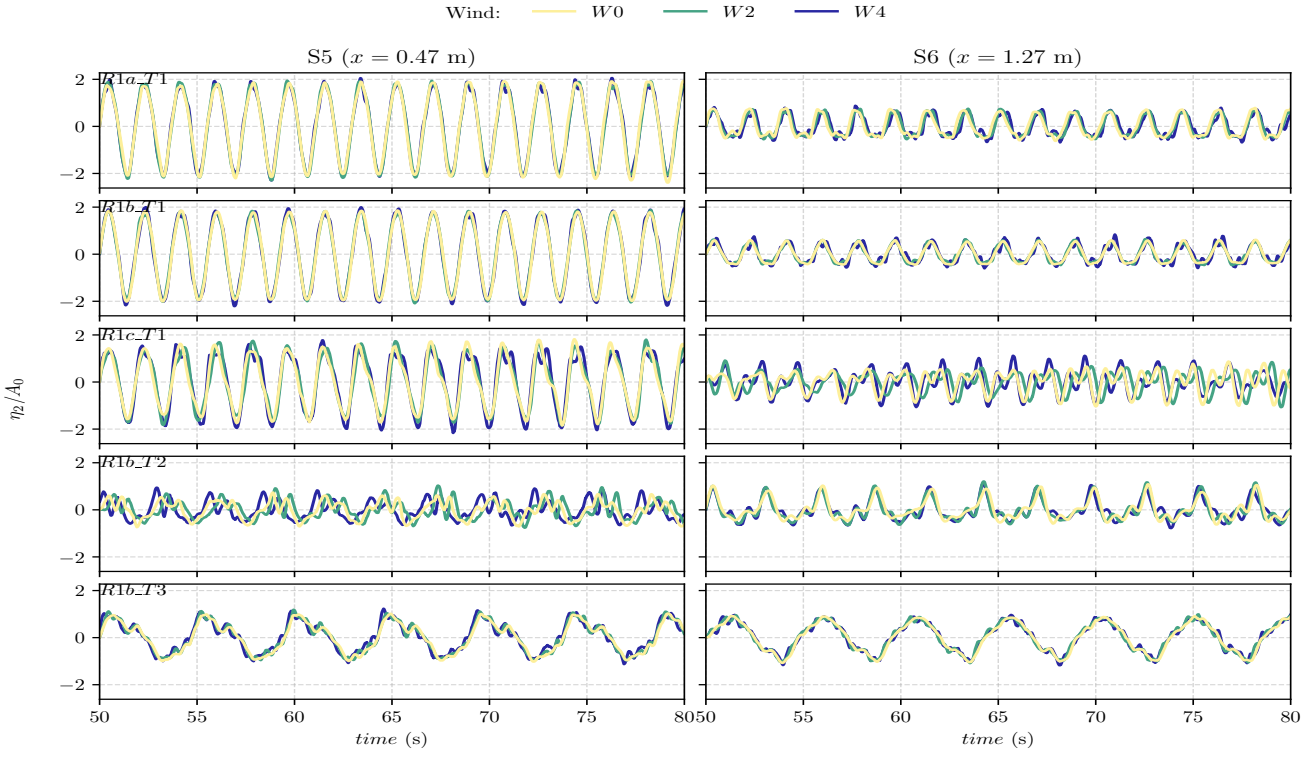

FIGURE 6.9: Dimensionless surface elevation time series in the leeward region (η_2/A_0) for the regular waves *R*1– experiments (rows) and different wind speeds (colors). The left and right columns represent the surface elevation data of S5 and S6, respectively

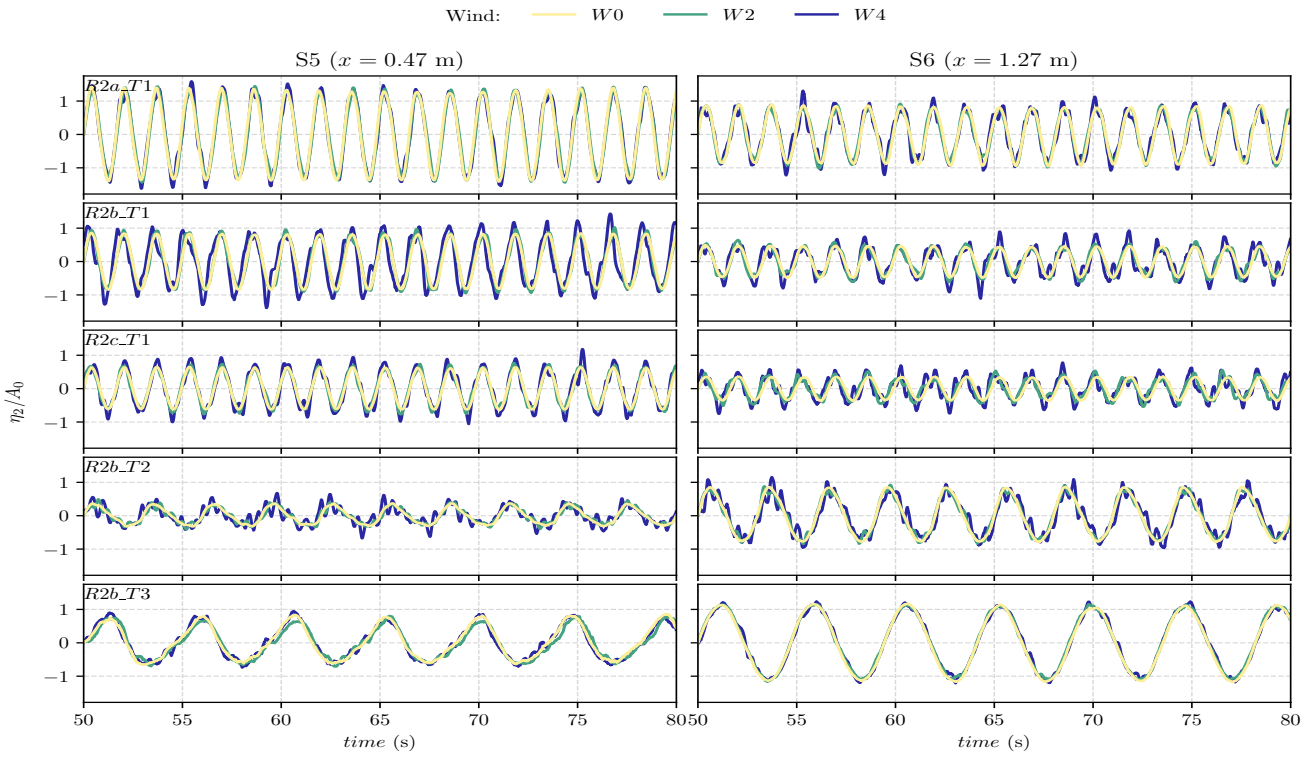

FIGURE 6.10: Dimensionless surface elevation time series in the leeward region (η_2/A_0) for the regular waves *R*2–experiments (rows) and different wind speeds (colors). The left and right columns represent the surface elevation data of S5 and S6, respectively

Figure 6.11 depicts, the dimensionless r.m.s. wave height, wave period and wavelength with respect to x/B for the $R1$–experiments and different wind speeds. In the leeward region, the ratio H_{rms}/H_I is related to the transmission coefficient. It also depicts in the first row (H_{rms}/H_I) and seaward region, the envelope of wave heights for a partial standing wave calculated as presented on Equation 2.9. Figure 6.12 presents the same results for the $R2$–experiments.

It can be observed that for each individual test the wave height remains almost constant for a given x/B–location, regardless of the wind speed. Therefore, wind-driven waves have almost no influence in the amplification or reduction of the periodic wave inside the chamber. In the case of the highest plate submergence, $d/h = 0.71$ ($R1c\_T1$ and $R2c\_T1$), higher values of wave height are present in the seaward region (region 1) and lower values in the leeward region. This result was expected, given the high reflection of the incident wave and the low energy transmitted inside the chamber. The highest values inside the chamber are obtained for the experiment $R1b\_T1$ with $d/h = 0.58$. In this case, S5 gives a value of $H_{rms}/H_I \approx 2$, showing a resonant behavior inside the chamber. However, a high variation between the sensors inside the chamber is observed in this test, with values in the range $0.5 - 2$ between S7 and S5. It can be attributed to the partial standing pattern inside the chamber that exhibits a spatial variation of the total wave amplitude with values depending on the relative distance of each gauge to quasi-nodes and quasi-antinodes. The maximum values of the transmission coefficient, with the presence of quasi-antinodes, are obtained for experiments with wave period $T1$ where the ratio $T_{z0_{W0}}$ is close to 1.

The main influence of wind-driven waves is observed in the estimations of $T_z/T_{z0_{W0}}$ and $L/L_{0_{W0}}$ which present a similar behavior. As observed, $L/L_{0_{W0}}$ decreases for increasing wind speeds and is more evident for section S2, where the wind is expected to have a higher influence as the wind-driven waves have had a longer fetch to be developed. This reduction is higher in the $R1a\_T1$ with the lowest relative submergence. This can be attributed to the fact that higher reflections are likely to be associated to higher submergences showing partial standing oscillations. Therefore, a reduction of the nonlinear interaction between wind–sea waves and the periodic component is expected in these cases. In the seaward region, there is an almost fivefold reduction of the wavelength with the highest wind. In the leeward region, this influence changes depending on $T_{z0_{W0}}/T_1$, e.g., for experiments $T4$ there is a negligible change of the wavelength with wind speed.

In the case of the $R2\_T1$ experiments, a similar behavior to $R1$–experiments is observed with slightly higher wave heights obtained in the seaward region. When there is an increase of the regular-wave period (experiments $T2$ and $T3$)

a significant reduction in the wave heights inside the chamber is observed highlighting the importance of the ratio between the mean period and the first natural period of the chamber.

As presented on Table 6.3, the experiments $R1b\_T1$ and $R2b\_T1$ present values of $T_{z0_{W0}} \approx 1$, experiments $R1b\_T2$ and $R2b\_T2$ present $T_{z0_{W0}} \approx 1.5$ and $R1b\_T3$ and $R2b\_T3$ give $T_{z0_{W0}} \approx 2.5$. In the cases with $T2$ and $T3$ the lowest values of wave height inside the chamber are presented. In the seaward region significant higher values are presented for experiments $T2$ than $T3$. In these cases with higher wave periods of the regular wave ($T2$ and $T3$), the wave period and wavelength is reduced up to values of 0.25 with the highest wind. This could be attributed to the statistical zero-crossing analysis where shorter waves are traveling along the longer waves and therefore the mean wave period is significantly affected by these short individual waves detected by the analysis.

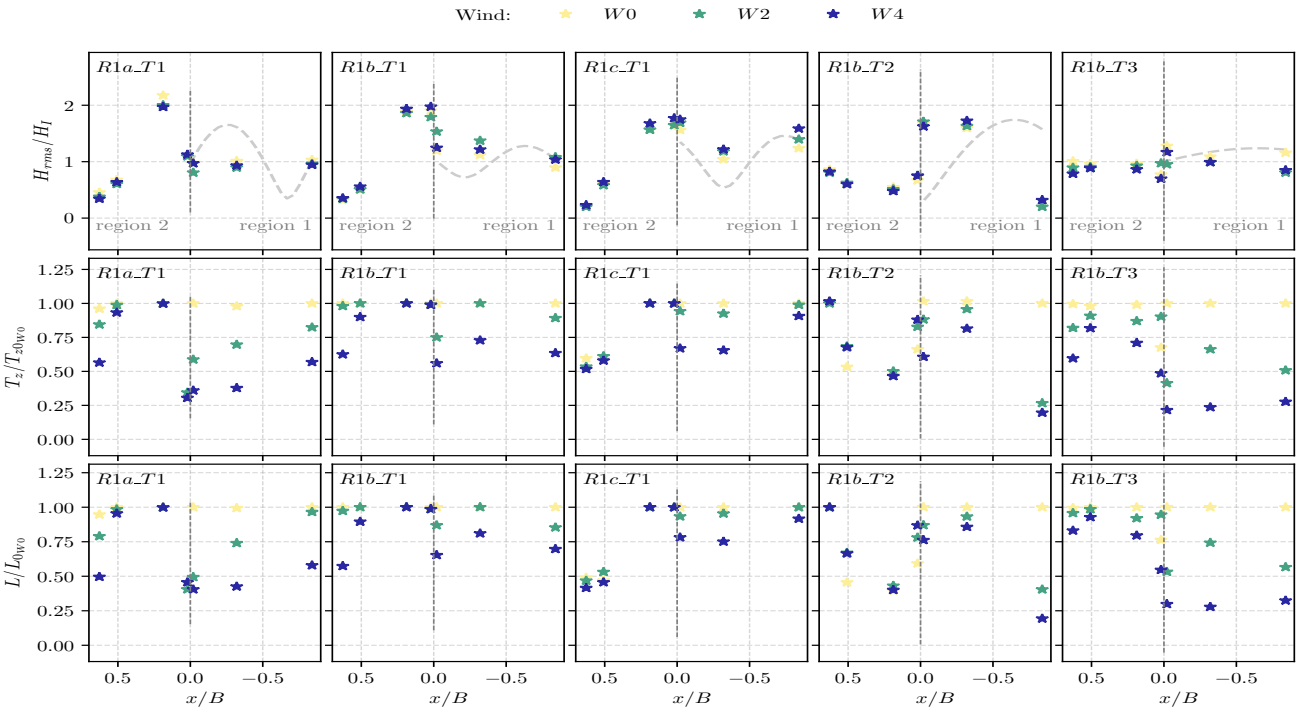

FIGURE 6.11: Dimensionless statistical parameters with respect to x/B for the regular waves $R1$–experiments (columns) and different wind speeds (colors). The rows (top to bottom) depict the dimensionless r.m.s. wave height (H_{rms}/H_I), mean wave period ($T_z/T_{z0_{W0}}$) and mean wavelength $L/L_{0_{W0}}$). The first row presents the dimensionless envelope of wave heights calculated by means of the transfer function (gray dashed line).

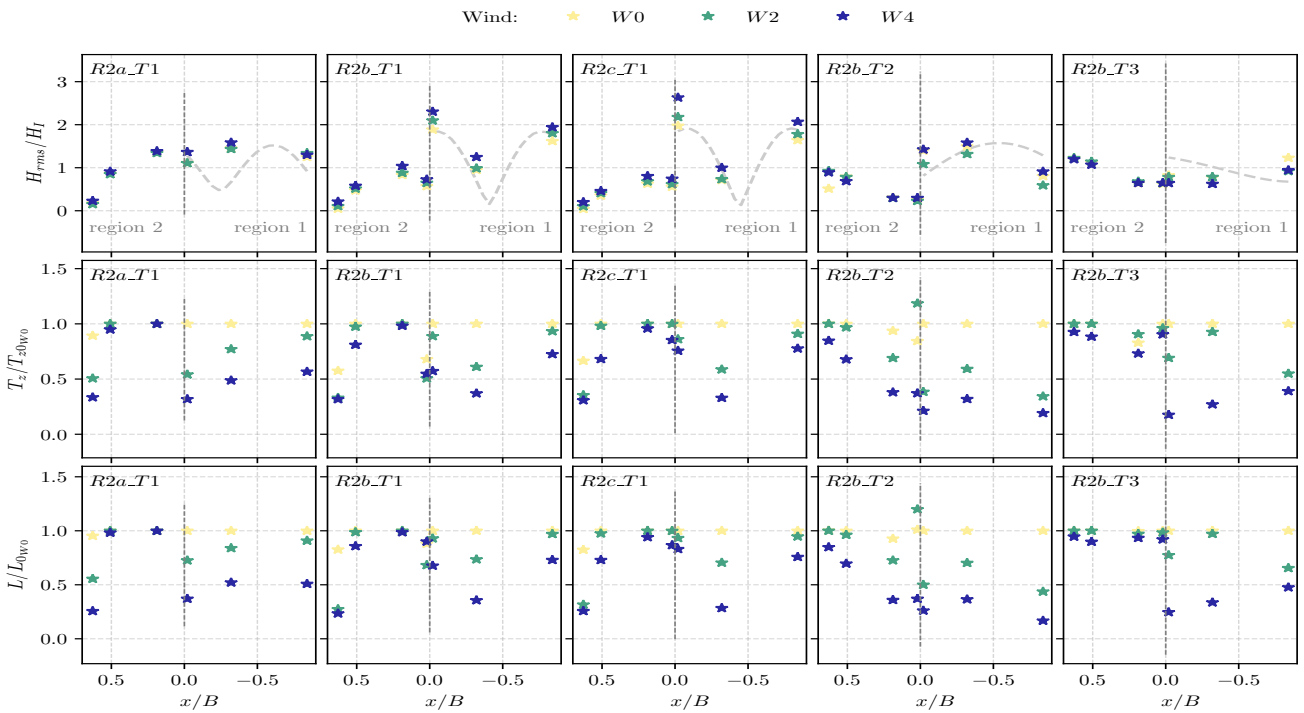

FIGURE 6.12: Dimensionless statistical parameters with respect to x/B for the regular waves $R2$–experiments (columns) and different wind speeds (colors). The rows (top to bottom) depict the dimensionless r.m.s. wave height (H_{rms}/H_I), mean wave period ($T_z/T_{z0_{W0}}$) and mean wavelength $L/L_{0_{W0}}$). The first row presents the dimensionless envelope of wave heights calculated by means of the transfer function (gray dashed line).

The analysis of the surface elevation data for wind-driven waves varies greatly from one temporal subset to another as previously explained in §6.1 (Figures 6.5 and 6.6). Therefore, given the higher influence of wind on the mean wave period estimation, Figures 6.13 and 6.14 present the temporal evolution of the wave period dimensionless mean period for $R1$ and $R2$–experiments, respetively, for different wave gauges and wind speeds.

It can be observed that in the leeward region, there is change with the temporal subset of the estimated mean period for the case without wind, mainly for the $T2$ giving the nonlinear interactions of the incident wave with the chamber. In the leeward region a similar change can be observed for higher wind speeds. In the rest of the cases a higher influence, as expected, is presented in the seaward region with differences in the mean period of the order of $O(0.2)$–$O(0.5)$ due to the fact that wind-driven waves are constantly changing and developing.

These results are mirrored in the power spectrum $S^* = S(f)f_{p_I}/m_{0_I}$ shown in Figure 6.15 and 6.16 for the $R1$ and $R2$–experiments, respectively. The results are dimensionless with respect to the peak frequency f_{p_I} and the zeroth-order moment m_{0_I} of the incident wave spectra for the experiment in the absence of wind. At high frequencies the scenario is controlled by wind-driven waves, energy increases and the resonant frequencies become less noticeable for the experiments with the lower regular wave period. In the case of the highest wave period $T3$ the harmonics are still noticeable even with the highest wind speeds where the periodic orbital motion of the energetic long wave convects the shorter wind-driven waves.

Inside the chamber the peak frequency in all sections almost corresponds to the frequency of the regular waves, which is very close to the natural period of the chamber, $T_{z0_{W0}}/T_1 \approx 1$ for the $T1$ cases and the harmonics become more important in the $T2$–$T3$ cases. The energy is higher for sensor S5 closest to the plate and the energy in the chamber increases with respect to the seaward region for the lowest wave period cases for the main frequency; whereas there is an energy decrease at higher frequencies with respect to the seaward side. This is attributed to nonlinear interaction between wind-driven waves, periodic waves and resonant waves controlled by the geometry of the system and also to the filtering effect of the screen, more efficient for high frequency components. For clear cut results, it will be necessary to further explore the wave profile and its variation with different geometrical configurations and with different forcing conditions.

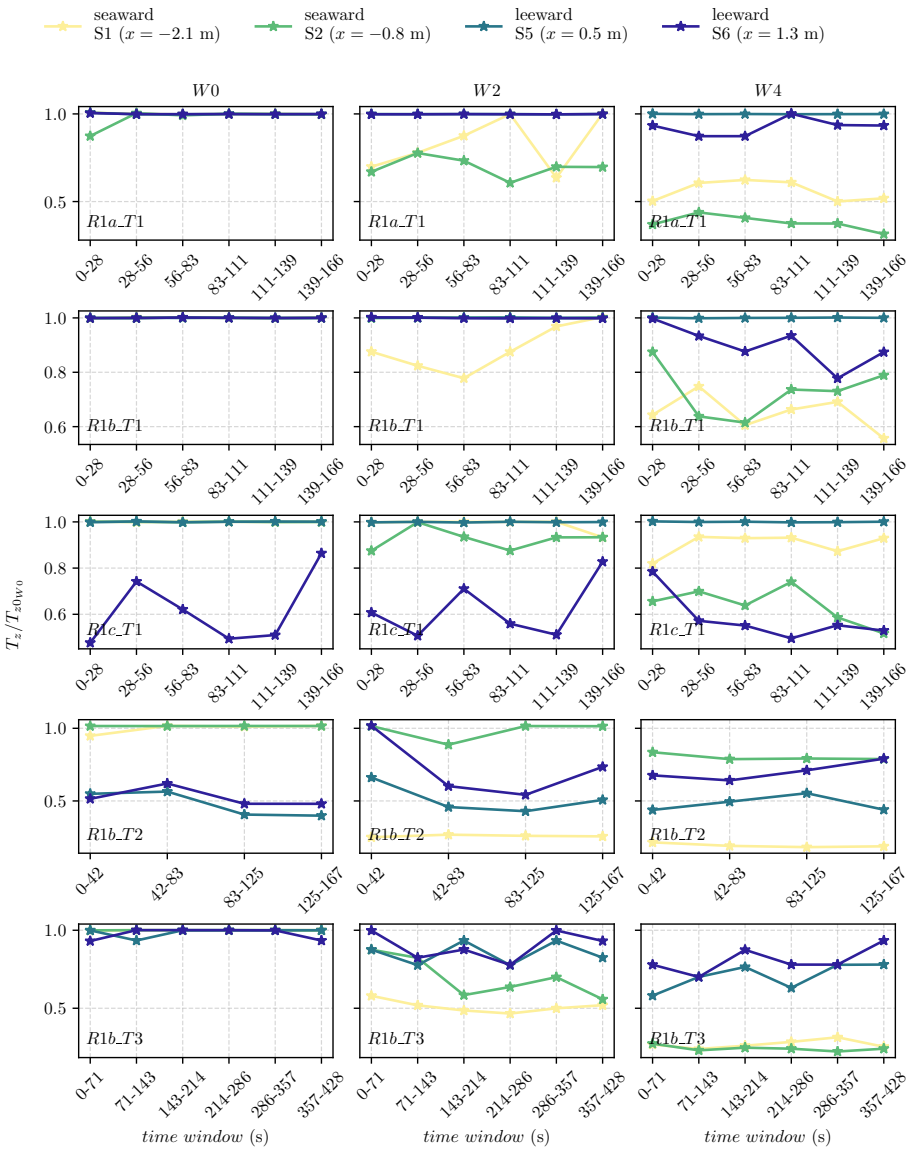

FIGURE 6.13: Dimensionless mean wave period $T_z/T_{z0_{W0}}$ for the regular waves *R*1–experiments (rows), different wind speeds (columns), wave gauges (colors) and temporal subsets (x–axis).

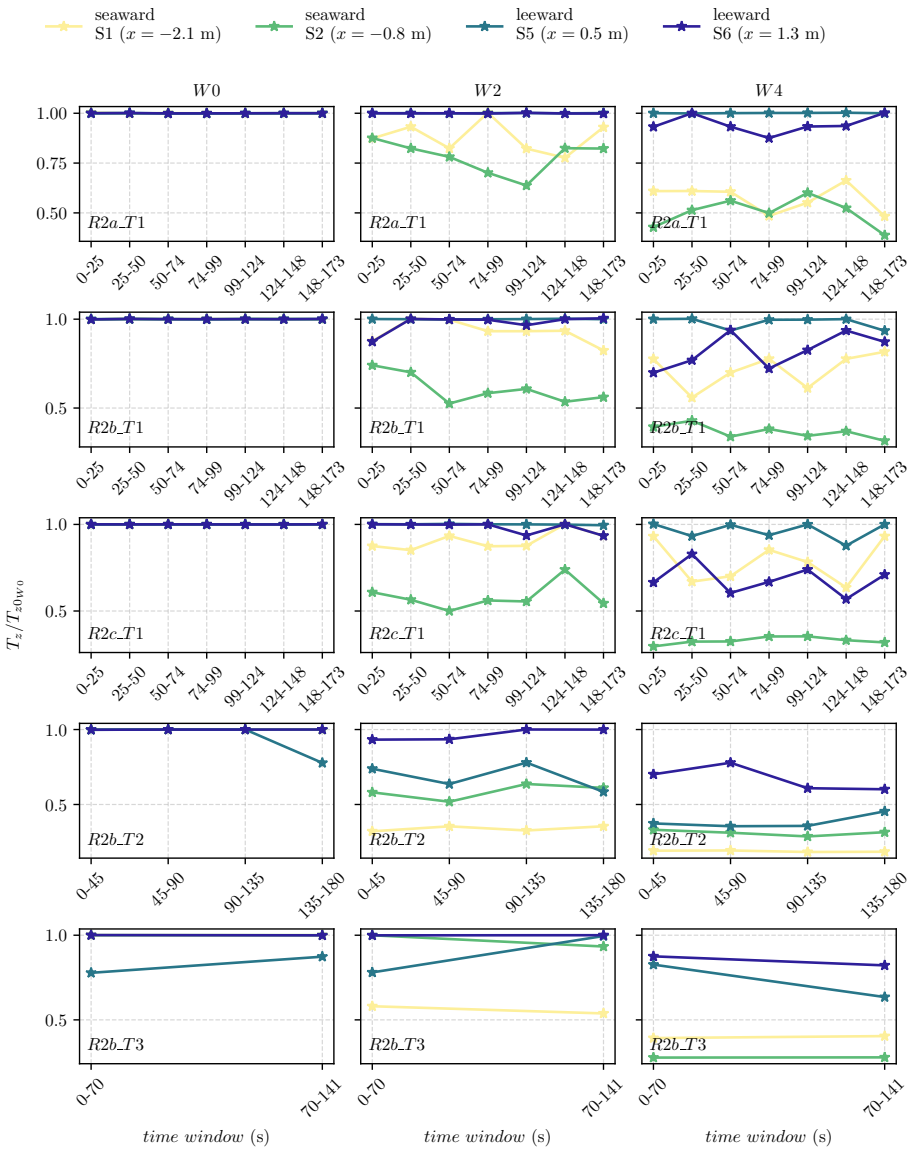

FIGURE 6.14: Dimensionless mean wave period $T_z / T_{z0_{W0}}$ for the regular waves *R*2–experiments (rows), different wind speeds (columns), wave gauges (colors) and temporal subsets (x–axis).

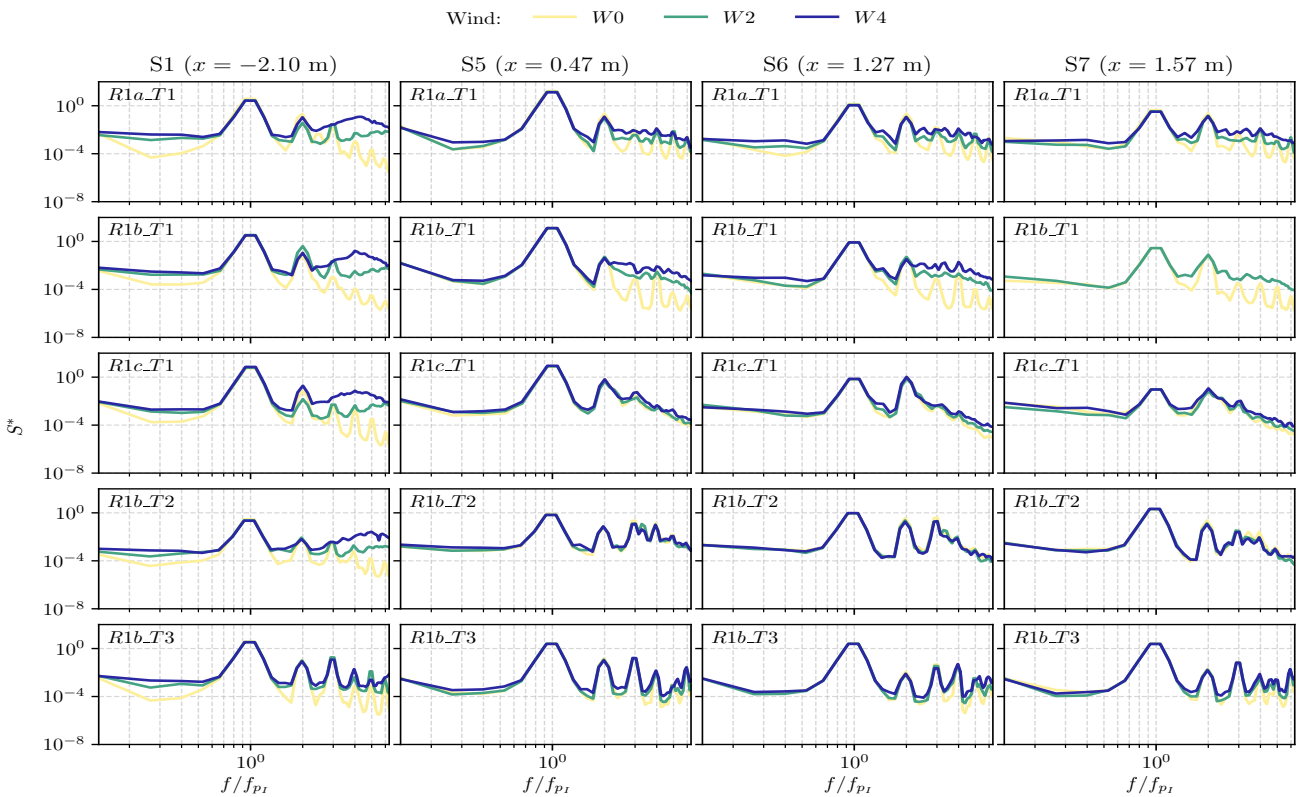

FIGURE 6.15: Dimensionless power spectrum (S^*) of η for the regular waves $R1$–experiments (rows), different wave gauges (columns) and wind speeds (colors).

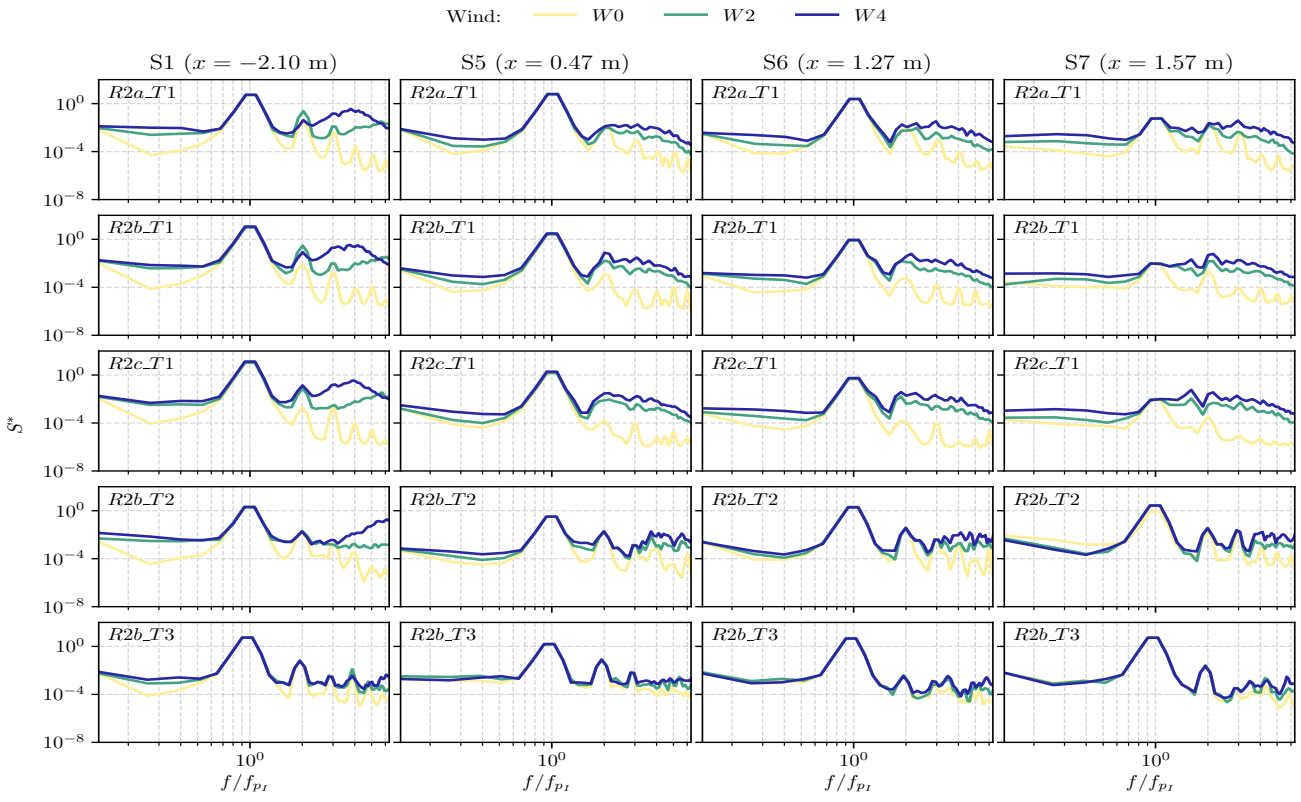

FIGURE 6.16: Dimensionless power spectrum (S^*) of η for the regular waves *R*2–experiments (rows), different wave gauges (columns) and wind speeds (colors).

Figure 6.17 presents the dimensionless spectra for experiment $R1a\_T1$ for different temporal subsets. Each temporal subsets takes a temporal slice of data and are intended to represent the different characteristics as the waves are being developed and coupled with wind-driven waves. The results of this analysis for the remaining $R1$– and $R2$–experiments are presented on the Appendix A.2. In this case given that the start of the test was done once enough time has passed since the activation of the wave and wind generation systems, not noticeable changes can be observed for the peak frequencies corresponding to the regular wave. A slight difference between temporal subsets can be observed for higher frequencies where the wind–sea waves dominate and the wave characteristics are expected to change as these are being developed and coupled with the periodic wave and its harmonics.

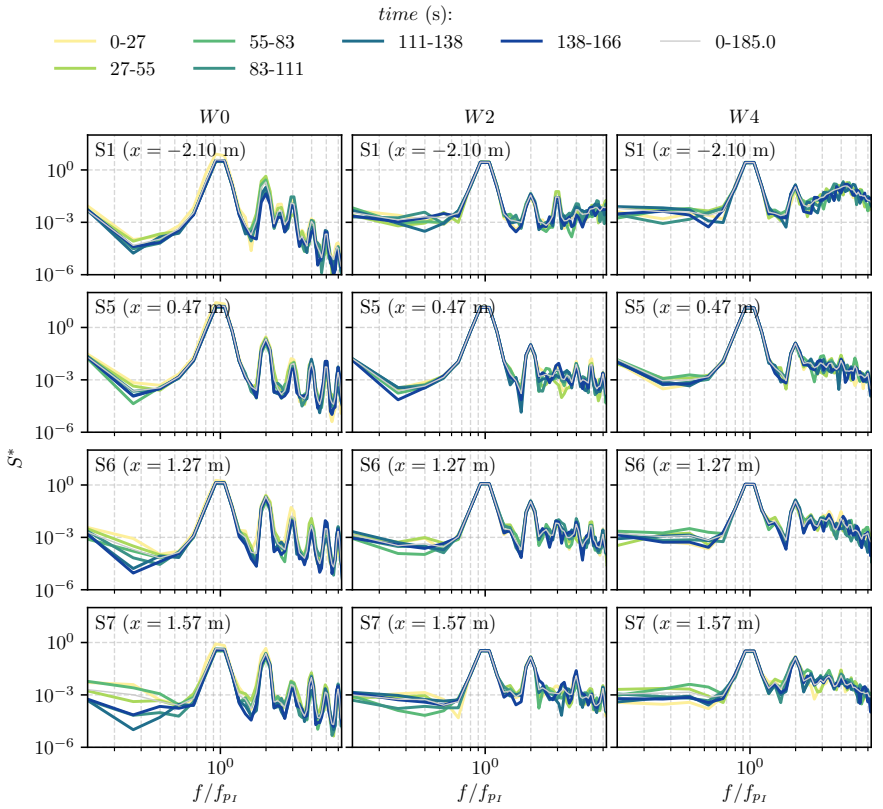

FIGURE 6.17: Dimensionless power spectrum (S^*) of η for the regular wave experiment $R1a\_T1$, different wind speeds and different temporal subsets.

Figures 6.18 and 6.19 present the dimensionless phase-averaged surface level for the $R1$ and $R2$–experiments, for different sensors and wind speeds. It can be observed that both the predominant regular wave phase, and the wave profile, change from the seaward to the leeward region. In the case of the highest relative submergence $d/h = 0.71$ ($R1c$), the transmission of the longer periodic wave is expected to be lower, and the changes could be due to the wind acting on the free surface. Sensor 5, shows a wave profile similar to the incident wave, with an increment in wave height due to its position in a quasi-antinode in the $R1$–experiments. S6 shows a reduction of the wave height and some changes in wave profile. As expected, due to the shading effect of the plate, the influence of wind-driven waves is limited to the seaward region, with a more evident variation of the wave profile for the case of $d/h = 0.58$ ($R1b$) and the highest wind speeds.

Figure 6.20 shows H_{max} and H_{rms} of sensors S5, S6 and S7 for the experiments with the same relative submergence $R1b$ and $R2b$. Each point represents a different configuration of regular wave (paddle-generated) and wind speed and they were ordered according to the relation $T_{z0_{W0}}/T_1$ (x–axis) where $T_{z0_{W0}}$ is the mean wave period of the experiment without wind and T_1 the 1st order natural period of the chamber. An amplification of wave energy is observed for values T_z/T_1 close to 1 for all wind speeds in the case of S5. For most of the experiments in the absence of wind, the same values of H_{max} and H_{rms} are obtained while in tests with wind, H_{max}/H_{rms0} presents higher values than H_{rms}/H_{rms0}. This is expected and due to the fact that the r.m.s. is a statistic that takes into account all the wave heights in the signal, therefore, taking into account the shorter wind-driven waves, its value is expected to be lower than H_{max}.

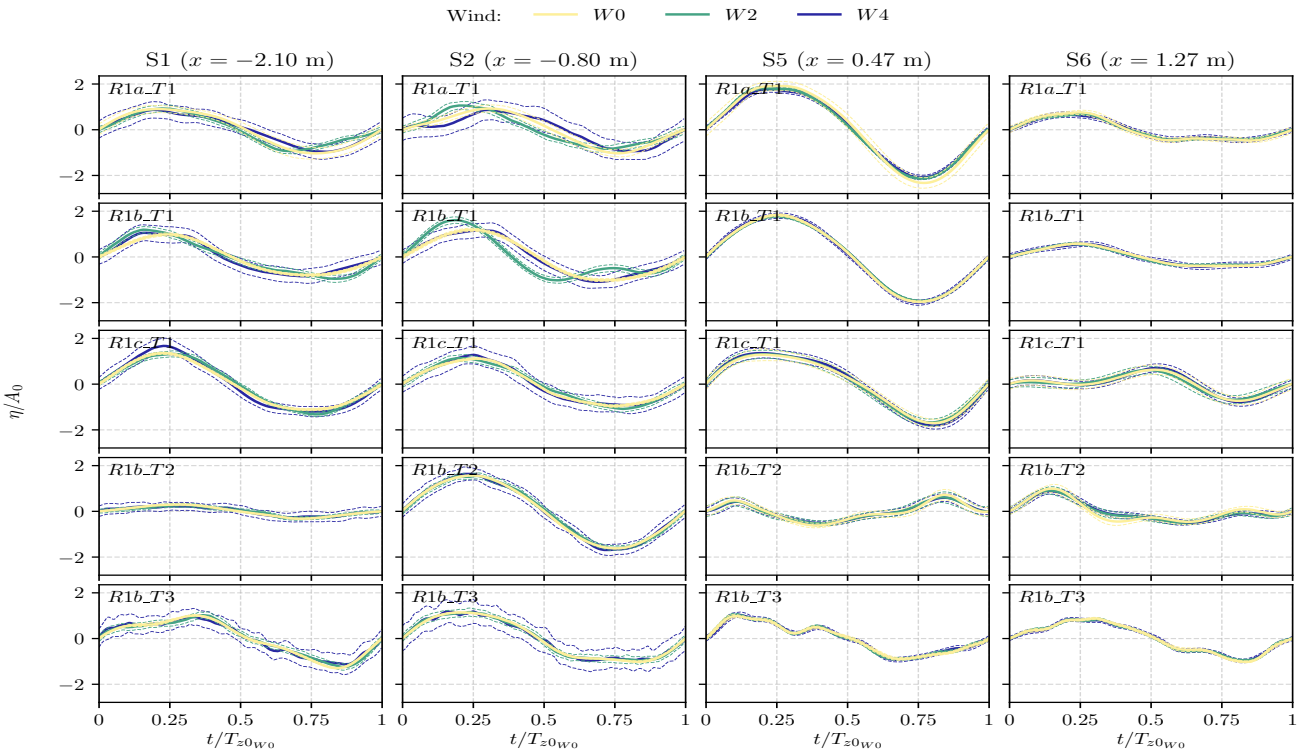

FIGURE 6.18: Phase-averaged dimensionless free surface elevations (η / A_0) for the regular waves $R1$–experiments (rows), different wave gauges (columns) and wind speeds (colors). The dashed lines correspond to the phased-averaged value $\pm$ one standard deviation.

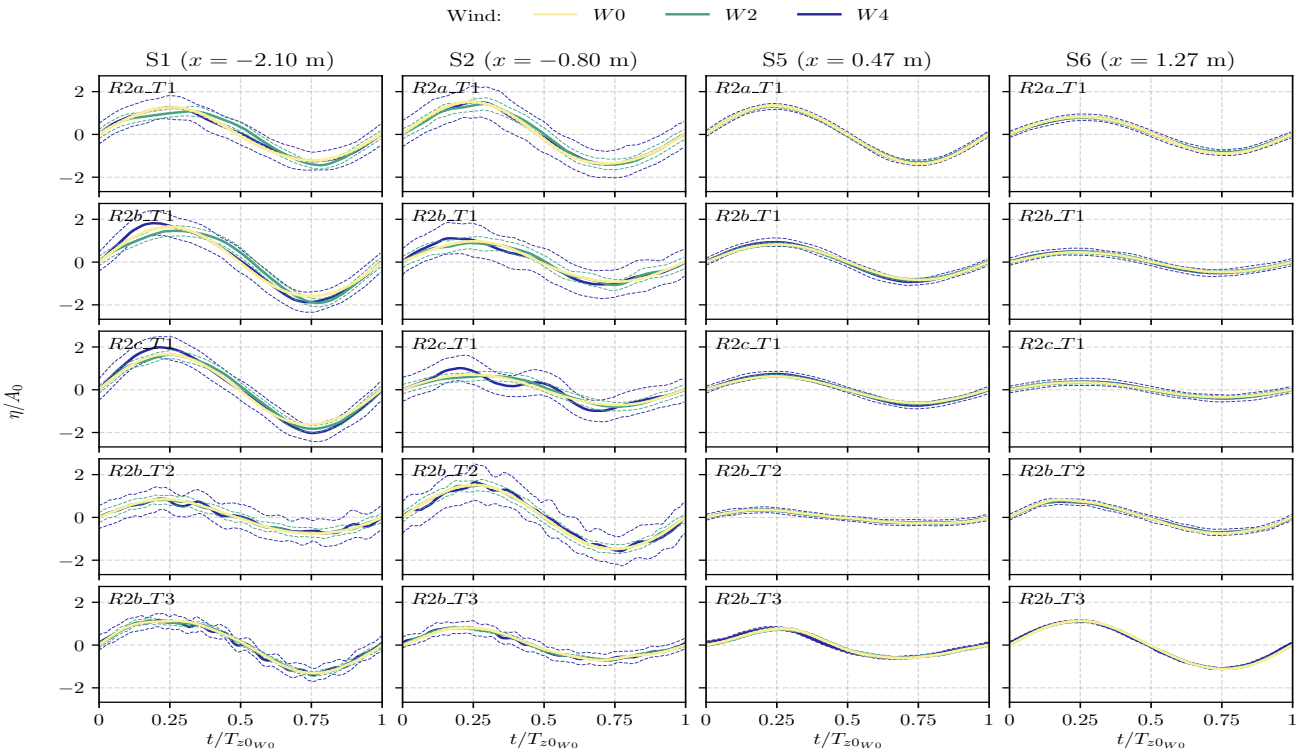

FIGURE 6.19: Phase-averaged dimensionless free surface elevations (η / A_0) for the regular waves *R*2–experiments (rows), different wave gauges (columns) and wind speeds (colors). The dashed lines correspond to the phased-averaged value $\pm$ one standard deviation.

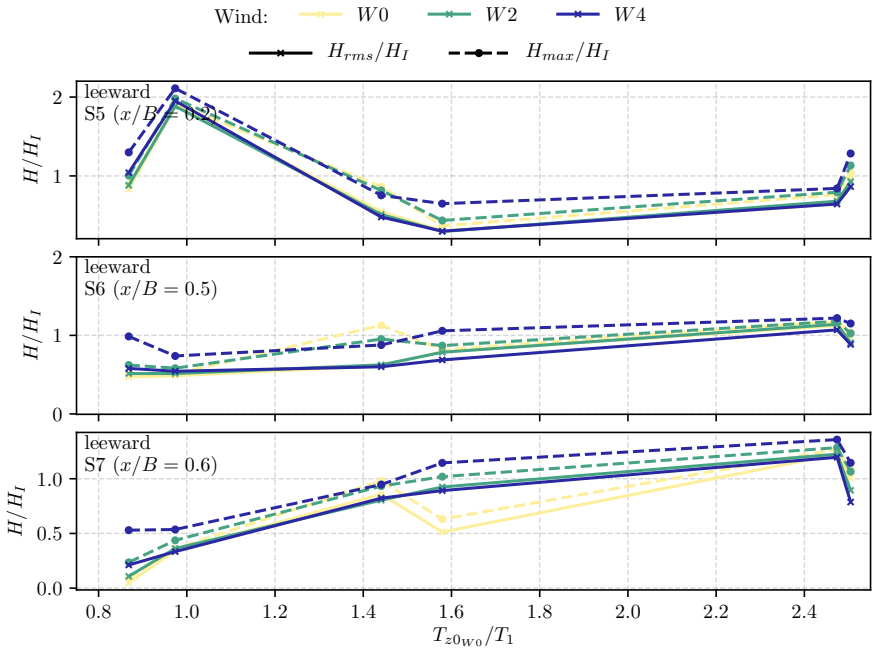

FIGURE 6.20: Dimensionless maximum and r.m.s. wave heights for different wave gauges (rows) and wind speeds (colors). The x–axis represents the ratio between the mean period without wind $T_{z0_{W0}}$ and the first natural period of the chamber T_1. In each panel, the different points correspond to the experiments with the same relative submergence d/h and different configurations of regular waves experiments with and without the combination of wind–sea waves.

6.3 Irregular waves

This section includes an initial analysis of the experimental data under paddle-generated irregular waves and wind-driven waves. Initially, the experimental design included the use of Particle Image Velocimetry (PIV) device to study the velocity field below the plate and pressure sensors to obtain the wave forces acting on the plate fundamental for the understanding of the interactions of a highly non-linear system. Unfortunately, the data from both systems had to be discarded due to technical errors and unsuitability of the devices to be employed in a windy environment. Therefore the analysis under irregular waves includes only the main parameters and the spectral analysis as presented for regular waves. Further experiments are deemed necessary for the complete understanding of the system when coupling paddle-generated irregular waves and wind–sea waves.

Table 6.5 presents the nomenclature and parameters of all the experiments involving irregular waves with/without the combination of wind–sea waves.

Table 6.6 lists the values of the incident and S1–gauge parameters of the irregular wave experiments without wind $W0$. H_{rms_I} is the incident wave height and K_R is the reflection coefficient obtained by reflection analysis (§2.3). $T_{z0_{W0}}$ and T_p are the mean and peak wave period obtained by the statistical and spectral analysis, respectively. L_0 represents the wavelength obtained by means of the linear dispersion equation (Eq. 1.2) for the experiment without wind. T_1 is the first natural oscillating period of the chamber ($B = 2.5$ m). Tables 6.7 and 6.8 list the parameters for all irregular and wind–sea waves experiments with JONSWAP and Pierson-Moskowitz incident spectrum, respectively.

It can be observed that the reflection coefficient increases with the plate submergence for experiments $JW1\_T1$ and decreases as the peak period of the irregular wave increases for a given plate submergence. This is the same for experiments $JW2$ and PM. In general the reflection coefficient decreases when wind-driven waves are coupled along with the mean period of wave gauge S1.

Figures 6.21 to 6.23 present the dimensionless power spectrum of the free surface elevations for the experiments $JW1$, $JW2$ and PM. It is noticeable that in all cases the wind–sea waves seemed not to have a noticeable impact on the energy behavior of the system as the main energetic frequencies correspond to the peak frequency of the paddle-generated irregular waves and the resonant periods of the chamber. The resonant periods are more noticeable for longer wave periods of the irregular wave with two distinguished peaks on the spectra. Further analysis needs to be made to understand the non-linear interactions of irregular swell waves and wind–sea waves including the use of other experimental devices such as LDV, PIV and pressure sensors.

Figure 6.24 presents the dimensionless spectra for experiment $JW1a\_T1$ for different temporal subsets. Each temporal subsets takes a temporal slice of data

TABLE 6.5: Nomenclature and parameters of the irregular and wind–sea waves experiments. H^{input} and T^{input} are the input setup values of to the wave generation software, d/h is the relative submergence and U_{ref} represents the reference wind speed.

Test	d/h	H^{input} (m)	T^{input} (s)	U_{ref} (m/s)
$JW1a\_T1$	0.33	0.075	1.4	
• $JW1a\_T1\_W0$				0
• $JW1a\_T1\_W1$				4.2
• $JW1a\_T1\_W2$	0.33	0.075	1.4	6.3
• $JW1a\_T1\_W3$				8.5
• $JW1a\_T1\_W4$				10.5
$JW1b\_T1$	0.58	0.075	1.4	0, 4.2, 6.3, 8.5, 10.5
$JW1c\_T1$	0.71	0.075	1.4	0, 4.2, 6.3, 8.5, 10.5
$JW1b\_T2$	0.58	0.075	1.8	0, 4.2, 6.3, 8.5, 10.5
$JW1b\_T3$	0.58	0.075	2.6	0, 4.2, 6.3, 8.5, 10.5
$JW1b\_T4$	0.58	0.075	4.7	0, 4.2, 6.3, 8.5, 10.5
$JW2a\_T1$	0.33	0.06	1.65	0, 4.2, 6.3, 8.5, 10.5
$JW2b\_T1$	0.58	0.06	1.65	0, 4.2, 6.3, 8.5, 10.5
$JW2b\_T2$	0.58	0.06	3.0	0, 4.2, 6.3, 8.5, 10.5
$JW2b\_T3$	0.58	0.06	4.7	0, 4.2, 6.3, 8.5, 10.5
PMa_T1	0.33	0.08	1.65	0, 4.2, 6.3, 8.5, 10.5
PMb_T1	0.58	0.08	1.65	0, 4.2, 6.3, 8.5, 10.5
PMc_T1	0.71	0.08	1.65	0, 4.2, 6.3, 8.5, 10.5
PMb_T2	0.58	0.08	3.0	0, 4.2, 6.3, 8.5, 10.5
PMb_T3	0.58	0.08	4.7	0, 4.2, 6.3, 8.5, 10.5

[1] For simplicity, the nomenclature for experiments involving wind is presented only for experiment $JW1a\_T1$.

TABLE 6.6: Incident and S1–gauge parameters of the irregular waves experiments without wind–sea waves. H_{rms_I} is the incident wave height. $H_{rms_{S1}}$, T_{z0} and L_0 represent the r.m.s. wave height, mean wave period and wavelength, respectively, of the surface elevation data of S1 for the experiment without wind. Each column depicts the mean value ± the difference —when applicable— between the values of repetitions of the same test[1].

Test	d/h	H^{input} (m)	H_{rms_I} (cm)	K_R	T^{input} (s)	T_p (s)	$T_{z0_{W0}}$ (s)	$B/L_{0_{W0}}$	$T_{z0_{W0}}/T_1$
*JW*1*a*_*T*1_*W*0	0.33	0.075	7.7	0.87	1.4	1.37	1.13	1.29	0.59
*JW*1*b*_*T*1_*W*0	0.58	0.075	8.0	0.90	1.4	1.29 ± 0.08	1.04	1.51	0.54
*JW*1*c*_*T*1_*W*0	0.71	0.075	9.0	1.0	1.4	1.32 ± 0.04	1.06	1.47	0.56
*JW*1*b*_*T*2_*W*0	0.58	0.075	6.5 ± 0.27	0.81 ± 0.04	1.8	1.95 ± 0.09	1.27	1.05	0.67
*JW*1*b*_*T*3_*W*0	0.58	0.075	5.0	0.69	2.6	2.28	1.58	0.74	0.83
*JW*1*b*_*T*4_*W*0	0.58	0.075	4.9 ± 0.33	0.41 ± 0.07	4.7	5.12	2.79	0.36	1.47
*JW*2*a*_*T*1_*W*0	0.33	0.06	5.8	0.76	1.65	1.58	1.23	1.10	0.65
*JW*2*b*_*T*1_*W*0	0.58	0.06	6.4 ± 0.58	0.88 ± 0.02	1.65	1.58	1.25	1.09	0.66
*JW*2*b*_*T*2_*W*0	0.58	0.06	4.1 ± 0.04	0.69 ± 0.04	3.0	3.41	1.67	0.69	0.88
*JW*2*b*_*T*3_*W*0	0.58	0.06	4.5 ± 0.37	0.52 ± 0.18	4.7	3.75 ± 0.34	2.29	0.50	1.2
*PMa*_*T*1_*W*0	0.33	0.08	–	–	1.65	1.58	1.13	1.29	0.59
*PMb*_*T*1_*W*0	0.58	0.08	7.5 ± 0.06	0.89	1.65	1.93 ± 0.35	1.22	1.13	0.64
*PMc*_*T*1_*W*0	0.71	0.08	7.4 ± 0.02	0.90 ± 0.02	1.65	1.46 ± 0.25	1.17	1.21	0.61
*PMb*_*T*2_*W*0	0.58	0.08	5.8 ± 0.20	0.68 ± 0.04	3.0	2.84 ± 0.57	1.57 ± 0.05	0.75	0.83
*PMb*_*T*3_*W*0	0.58	0.08	5.6 ± 0.12	0.37 ± 0.01	4.7	4.10	2.53	0.41	1.33

[1] The values missing from the columns H_{rms_I} and K_R correspond to tests where the reflection analysis was not possible due to faulty wave gauge data.

and are intended to represent the different characteristics as the waves are being developed and coupled with wind-driven waves. The results of this analysis for the remaining *JW*1–, *JW*2– and *PM*–experiments are presented on the Appendix A.3. As in the case of the regular waves experiments, not noticeable changes can be observed for the peak frequencies corresponding to the irregular wave. A slight difference between temporal subsets can be observed for higher frequencies where the wind–sea waves dominate and the wave characteristics are expected to change as these are being developed and coupled with the periodic wave and its harmonics.

TABLE 6.7: Incident and S1–gauge parameters of the Jonswap irregular and wind–sea waves experiments. H_{rms_I} is the incident wave height. $H_{rms_{S1}}$ and T_{z0} represent the r.m.s. wave height and mean wave period of the surface elevation data of S1. Each column depicts the mean value ± the difference —when applicable— between the values of repetitions of the same test[1].

Test	d/h	H^{input} (m)	H_{rms_I} (cm)	K_R	T^{input} (s)	T_p (s)	T_{z0} (s)
JW1a_T1_W0			7.7	0.87		1.37	1.13
JW1a_T1_W1			6.9	0.88		1.37	0.91
JW1a_T1_W2	0.33	0.075	9.4	0.83	1.4	1.37	1.00
JW1a_T1_W3			7.3	0.80		1.28	0.92
JW1a_T1_W4			–	–		1.46	0.77
JW1b_T1_W0			8.0	0.90		1.29 ± 0.08	1.04 ± 0.02
JW1b_T1_W1	0.58	0.075	8.8 ± 0.35	0.91 ± 0.02	1.4	1.24 ± 0.04	1.03
JW1b_T1_W2			7.3 ± 0.30	0.92 ± 0.03		1.20	0.94 ± 0.03
JW1c_T1_W0			9.0	1.0		1.32 ± 0.04	1.06 ± 0.06
JW1c_T1_W1			10.6 ± 1.46	0.96 ± 0.02		1.32 ± 0.04	1.01 ± 0.03
JW1c_T1_W2	0.71	0.075	9.3 ± 0.14	0.96 ± 0.01	1.4	1.32 ± 0.04	1.01
JW1c_T1_W3			8.0	0.92		1.24 ± 0.04	0.94 ± 0.04
JW1c_T1_W4			8.0	0.88		1.28	0.9 ± 0.02
JW1b_T2_W0			6.5 ± 0.27	0.81 ± 0.04		1.95 ± 0.09	1.27 ± 0.02
JW1b_T2_W1			6.3 ± 0.07	0.80 ± 0.05		1.72 ± 0.14	1.22 ± 0.07
JW1b_T2_W2	0.58	0.075	6.4 ± 0.16	0.81	1.8	1.86	1.12 ± 0.05
JW1b_T2_W3			7.0 ± 0.17	0.75 ± 0.02		1.78 ± 0.08	1.05 ± 0.07
JW1b_T2_W4			6.7 ± 0.28	0.74 ± 0.02		1.78 ± 0.08	0.93 ± 0.05
JW1b_T3_W0			5.0	0.69		2.28	1.58 ± 0.03
JW1b_T3_W1			5.6 ± 0.35	0.73 ± 0.02		2.28	1.38 ± 0.14
JW1b_T3_W2	0.58	0.075	5.6 ± 0.52	0.75 ± 0.01	2.6	2.28	1.05 ± 0.02
JW1b_T3_W3			6.8 ± 0.26	0.71		2.28	1.00 ± 0.04
JW1b_T3_W4			5.9 ± 0.38	0.71 ± 0.03		2.28	0.80 ± 0.03
JW1b_T4_W0			4.9 ± 0.33	0.41 ± 0.07		5.12	2.79 ± 0.03
JW1b_T4_W1			5.2 ± 0.29	0.35 ± 0.01		4.61 ± 0.51	2.16 ± 0.12
JW1b_T4_W2	0.58	0.075	4.8 ± 0.39	0.39 ± 0.01	4.7	5.12	1.10 ± 0.04
JW1b_T4_W3			4.8 ± 0.07	0.37 ± 0.01		4.61 ± 0.51	0.96 ± 0.05
JW1b_T4_W4			5.0	0.37		5.12	0.75 ± 0.02
JW2a_T1_W0			5.8	0.76		1.58	1.23
JW2a_T1_W1			5.4	0.73		1.58	1.18
JW2a_T1_W2	0.33	0.06	5.8	0.76	1.65	1.58	1.02
JW2a_T1_W3			5.2	0.69		1.58	0.9
JW2a_T1_W4			5.1	0.77		1.58	0.72
JW2b_T1_W0			6.4 ± 0.58	0.88 ± 0.02		1.58	1.25 ± 0.08
JW2b_T1_W1			6.0 ± 0.54	0.89		1.58	1.16
JW2b_T1_W2	0.58	0.06	5.7 ± 0.32	0.87 ± 0.01	1.65	1.58	1.03 ± 0.03
JW2b_T1_W3			5.5 ± 0.16	0.86		1.64 ± 0.07	0.91 ± 0.01
JW2b_T1_W4			6.2 ± 0.16	0.82 ± 0.02		1.58	0.92 ± 0.04
JW2b_T2_W0			4.1 ± 0.04	0.69 ± 0.04		3.41	1.67 ± 0.03
JW2b_T2_W1			4.5 ± 0.26	0.70 ± 0.05		2.84 ± 0.57	1.44 ± 0.08
JW2b_T2_W2	0.58	0.06	4.4 ± 0.32	0.71 ± 0.03	3	2.84 ± 0.57	1.02 ± 0.12
JW2b_T2_W3			4.3 ± 0.13	0.70 ± 0.03		2.84 ± 0.57	0.78 ± 0.01
JW2b_T2_W4			4.6 ± 0.05	0.69 ± 0.05		2.60 ± 0.33	0.65
JW2b_T3_W0			4.5 ± 0.37	0.52 ± 0.18		3.75 ± 0.34	2.29 ± 0.53
JW2b_T3_W1			3.8 ± 0.11	0.50 ± 0.18		4.27 ± 0.85	1.55 ± 0.10
JW2b_T3_W2	0.58	0.06	3.9 ± 0.08	0.56 ± 0.18	4.7	3.70 ± 1.42	0.89 ± 0.05
JW2b_T3_W3			4.0 ± 0.33	0.53 ± 0.18		4.27 ± 0.85	0.73 ± 0.05
JW2b_T3_W4			4.2 ± 0.58	0.58 ± 0.15		3.70 ± 1.42	0.66 ± 0.04

[1] The values missing from the columns H_{rms_I} and K_R correspond to tests where the reflection analysis was not possible due to faulty wave gauge data.

TABLE 6.8: Incident and S1–gauge parameters of the Pierson-Moskowitz irregular and wind–sea waves experiments. H_{rms_I} is the incident wave height. $H_{rms_{S1}}$ and T_{z0} represent the r.m.s. wave height and mean wave period of the surface elevation data of S1. Each column depicts the mean value $\pm$ the difference —when applicable— between the values of repetitions of the same test.

Test	d/h	H^{input} (m)	H_{rms_I} (cm)	K_R	T^{input} (s)	T_p (s)	T_{z0} (s)
PMa_T1_W0			–	–		1.58	1.13
PMa_T1_W1			7.3	0.79		1.58	1.10
PMa_T1_W2	0.33	0.08	–	–	1.65	2.05	1.08
PMa_T1_W3			–	–		1.58	1.04
PMa_T1_W4			–	–		1.58	0.96
PMb_T1_W0			7.5 ± 0.06	0.89		1.93 ± 0.35	1.22 ± 0.04
PMb_T1_W1			7.0	0.85		1.2	1.12 ± 0.03
PMb_T1_W2	0.58	0.08	7.7 ± 0.40	0.89 ± 0.02	1.65	1.39 ± 0.19	1.07 ± 0.02
PMb_T1_W3			7.4 ± 0.23	0.83 ± 0.01		1.24 ± 0.04	0.97 ± 0.01
PMb_T1_W4			7.4 ± 0.17	0.81		1.20	0.94 ± 0.02
PMc_T1_W0			7.4 ± 0.02	0.90 ± 0.02		1.46 ± 0.25	1.17 ± 0.01
PMc_T1_W1			–	–		1.24 ± 0.04	1.16 ± 0.06
PMc_T1_W2	0.71	0.08	8.4 ± 0.16	0.88 ± 0.01	1.65	1.39 ± 0.19	1.09 ± 0.04
PMc_T1_W3			8.0 ± 0.29	0.88 ± 0.01		1.20	1.04 ± 0.02
PMc_T1_W4			–	–		1.71	0.88 ± 0.05
PMb_T2_W0			5.8 ± 0.20	0.68 ± 0.04		2.84 ± 0.57	1.57 ± 0.05
PMb_T2_W1			6.3 ± 0.18	0.68 ± 0.01		2.28	1.43 ± 0.03
PMb_T2_W2	0.58	0.08	5.9 ± 0.19	0.69 ± 0.01	3.0	2.84 ± 0.57	1.09
PMb_T2_W3			5.8 ± 0.05	0.67 ± 0.02		2.84 ± 0.57	1.04
PMb_T2_W4			6.2 ± 0.06	0.67 ± 0.02		3.41	0.88 ± 0.06
PMb_T3_W0			5.6 ± 0.12	0.37 ± 0.01		4.10	2.53 ± 0.13
PMb_T3_W1			5.3 ± 0.06	0.42 ± 0.03		4.61 ± 0.51	2.02 ± 0.02
PMb_T3_W2	0.58	0.08	5.5 ± 0.05	0.40 ± 0.01	4.7	3.75 ± 0.34	1.41 ± 0.10
PMb_T3_W3			5.2 ± 0.10	0.40 ± 0.02		4.10	0.99 ± 0.05
PMb_T3_W4			5.4 ± 0.06	0.40 ± 0.01		4.10	0.83 ± 0.01

[1] The values missing from the columns H_{rms_I} and K_R correspond to tests where the reflection analysis was not possible due to faulty wave gauge data.

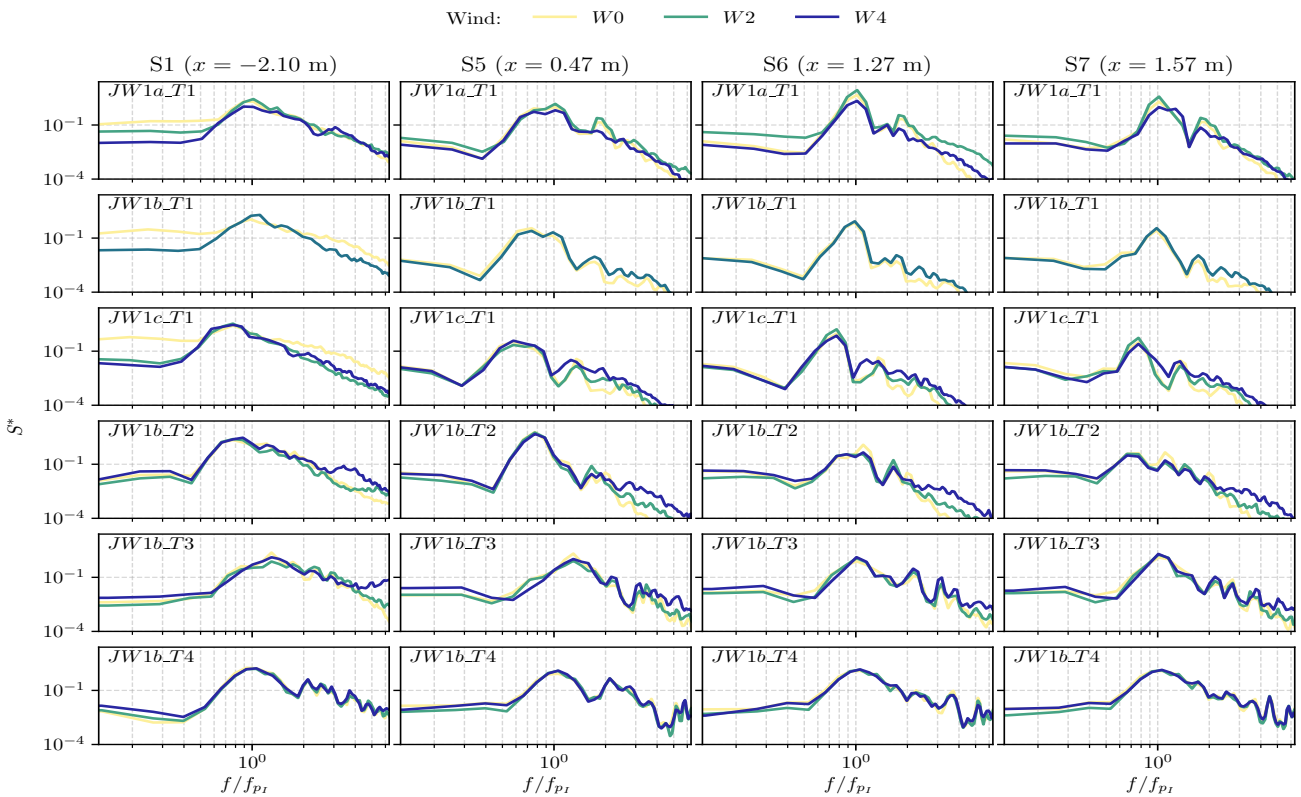

FIGURE 6.21: Dimensionless power spectrum (S^*) of η for the Jonswap irregular waves *JW*1–experiments (rows), different wave gauges (columns) and wind speeds (colors).

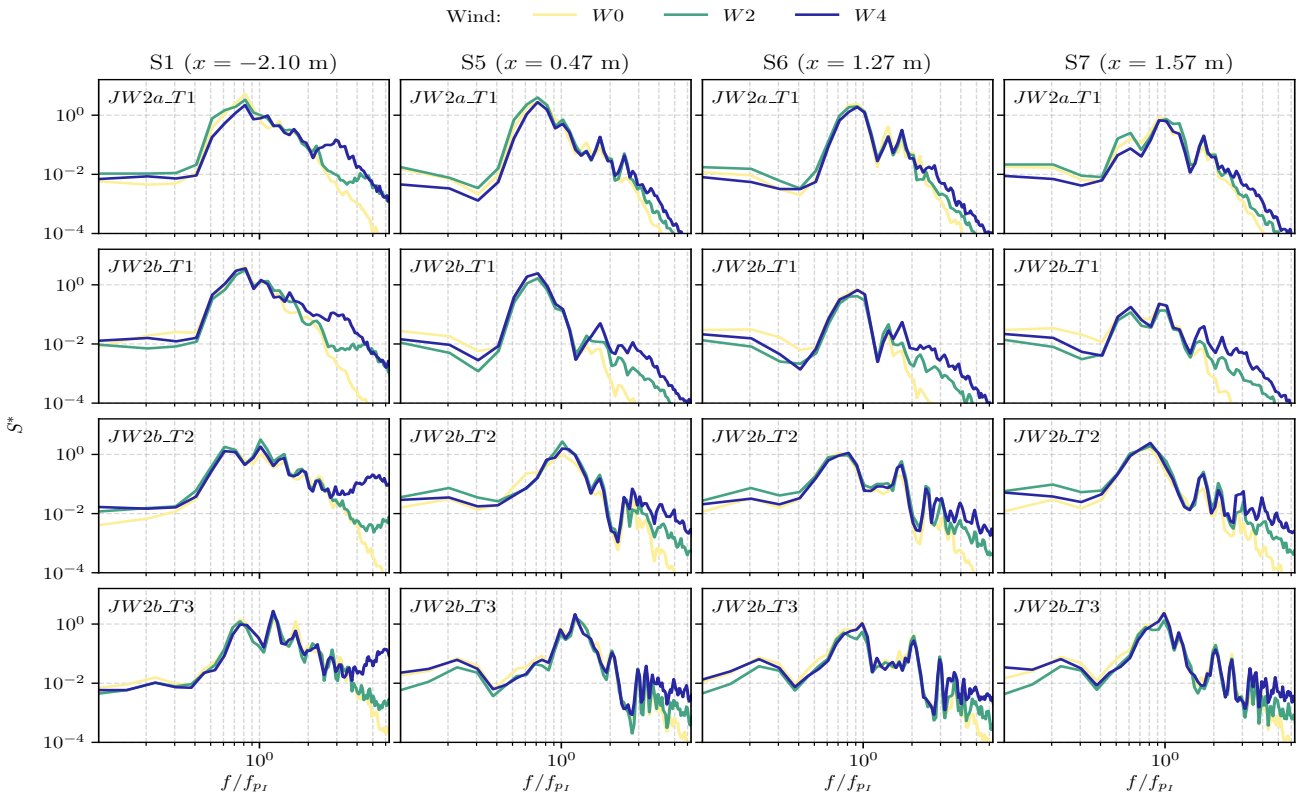

FIGURE 6.22: Dimensionless power spectrum (S^*) of η for the Jonswap irregular waves *JW*2–experiments (rows), different wave gauges (columns) and wind speeds (colors).

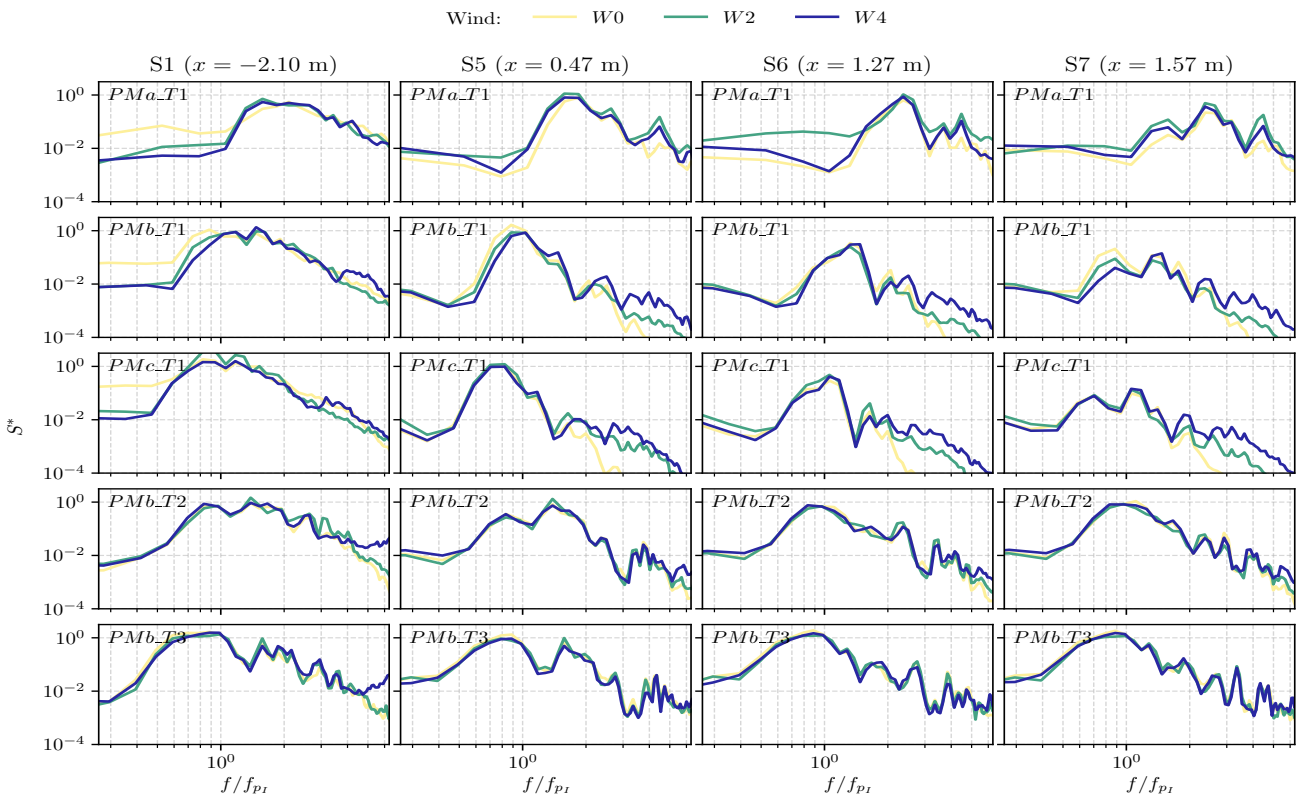

FIGURE 6.23: Dimensionless power spectrum (S^*) of η for the Pierson-Moskowitz irregular waves *PM*–experiments (rows), different wave gauges (columns) and wind speeds (colors).

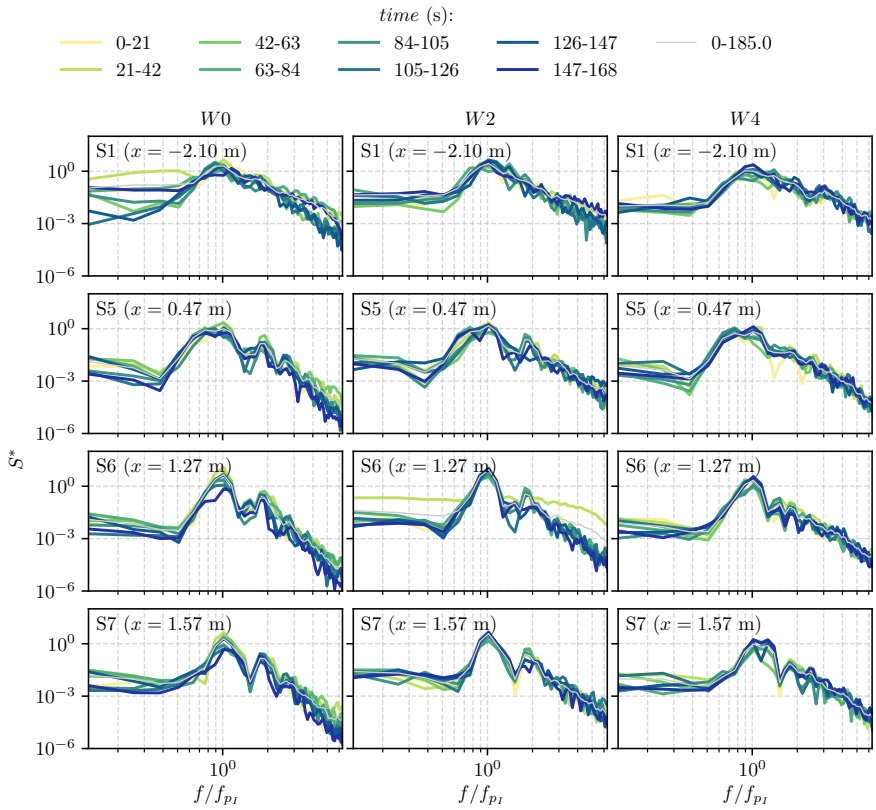

FIGURE 6.24: Dimensionless power spectrum (S^*) of η for the Jonswap irregular wave wave experiment *JW1a_T1*, different wind speeds and different temporal subsets.

6.4 Conclusions

The experimental results of the hydrodynamic interaction of regular and irregular waves, in combination with short wind-driven waves, with a vertical fixed semi-submerged barrier are presented. The analysis focused on the seaward wave characteristics and the submergence on the plate, with special attention on the role of wind–sea waves providing new insight of the influence of wind-driven waves on the incident wave characteristics and in the wave field inside the chamber as it still remains a topic to be further investigated in maritime and coastal engineering. Initially, the experimental design included the use of Particle Image Velocimetry (PIV) device to study the velocity field below the plate and pressure sensors to obtain the wave forces acting on the plate. Unfortunately, the data from both systems had to be discarded due to technical errors and unsuitability of the devices to be employed in a windy environment. The analyses of the experimental data are mainly descriptive due to the lack of sufficient data to extract information of a highly non-linear system.

For the experiments involving incident regular wave configuration with a wave period similar to the 1st natural period of the chamber, an amplification of wave energy in the seaward region is measured for a relative submergence of $d/h = 0.58$, in agreement with the analytical model results. In the case of higher submergences, the fixed plate operates in a highly reflective manner and a reduction of the wave energy inside the chamber can be observed. Therefore, the submergence of the plate is a key parameter for the design of these types of structures, either for harbor protection (energy reduction), or WEC devices (energy amplification).

Wind-driven waves have a high influence on the total wave period and symmetry of the waves. The influence of wind–sea waves is more noticeable for the experiments where $T_{z0}/T_1 \geq 1.5$, in which the short-crested waves proved to have a higher influence on the resulting wave periods and heights in the seaward region. Therefore, the influence of wind–sea waves on the behavior of the structure depends greatly on the period of the predominant periodic component (swell).

The spectrum involving swell and sea waves presents different resonant peaks. At high frequencies the scenario is controlled by wind-driven waves and the resonant frequencies of the flume become less evident. Inside the chamber the peak frequencies in all sections correspond to the swell waves, closer in period to the natural period of the chamber. At higher frequencies the energy decreases with respect to the seaward side. This is attributed to nonlinear interaction between wind-driven waves, periodic waves and resonant waves controlled by the geometry of the system and also to the filtering effect of the screen, more efficient for high frequency components. The overall behavior of the system depends on the

relative values of periodic waves, wind–sea waves, and resonant periods of the chamber.

Chapter 7

Example of application

Note

This chapter compiles some of the results presented on:

M.L. Jalón, **A. Lira-Loarca**, A. Baquerizo, and M.A. Losada (2019). "An analytical model for oblique wave interaction with a partially reflective harbor structure". In: *Coastal Engineering* 143, pp. 38 –49. ISSN: 0378-3839. DOI: `https://doi.org/10.1016/j.coastaleng.2018.10.015`

A. Lira-Loarca, M. Cobos, A. Baquerizo, and M.A. Losada (2018a). "A multivariate statistical model to simulate storm evolution". In: *Proceedings of the 36th International Conference on Coastal Engineering (ICCE18)*. Baltimore, Maryland, USA

In maritime engineering design, it must be studied if a structure meets the safety requirements in each and every one of the sea states to which it is subjected in the useful life. In general, a sea state is the temporal scale at which the verification equation is formulated for the different failure modes of the structure (ROM 0.0-01, 2001; ROM 1.1-18, 2018). The verification equation is formed by the balance between favorable and unfavorable terms and applied considering that, during the sea state, all the parameters and variables remain stationary from a statistical point of view (Solari and Losada, 2014).

Using a safety margin format for the analysis, the verification equation can be written as the difference between favorable and unfavorable terms, $SM = F_c - F_t$ with F_c defined as a critical stress value and failure occurs when $SM < 0$. Simulation techniques can used to obtain the safety margin and to asses its uncertainty.

To this end, the methodology presented on Chapter 3 for the time series simulation of storm events is used to generate 100 equally probable 50-year time series of storm events and are presented and discussed on §7.1. The corresponding free surface elevations and wave forces time series are found by means the analytical model introduced on Chapter 1 and the results are presented on §7.2. The main conclusions are presented on §7.3.

7.1 Time series simulation of storm events

The methodology presented on Chapter 3 is applied to simulate a 50-year time series of storm events using the historical hindcast data provided by Puertos del Estado, Spanish Ministry of Public Works of SIMAR 2041080 (3.58°W, 36.67°N) with hourly sea states data from 1958 to 2006. Figure 7.1 presents the time series of the significant wave height H_s, peak period T_p and mean wave direction θ_m corresponding to SIMAR 2041080.

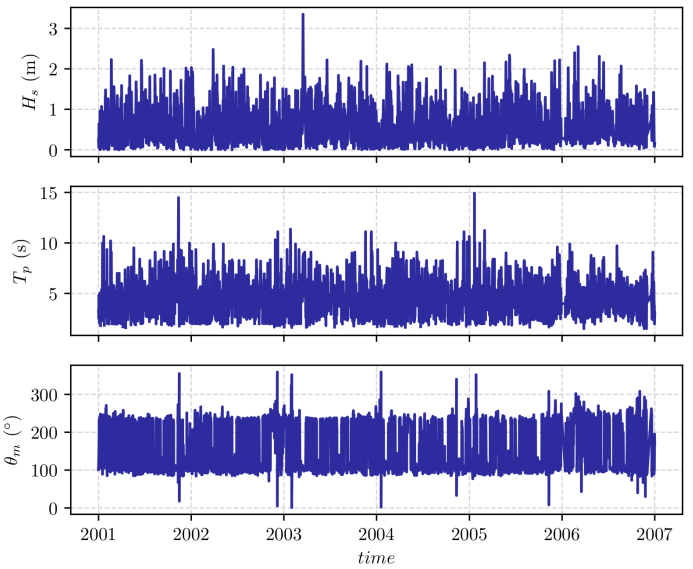

FIGURE 7.1: Historical wave climate data from SIMAR 2041080. H_s, T_p and θ_m are the significant wave height, peak period and mean direction, respectively.

Definition of storm events

The selection of the threshold $H_{s,u}$, minimum storm duration $d_{s,0}$ and minimum interarrival time δ_0 was done with the hypotheses testing presented in §3.1. Different values of $H_{s,u}$ were tested ranging from the 90$^{\text{th}}$–99.9$^{\text{th}}$ percentiles whereas the tested values of $d_{s,0}$ varied from 12–170 hours and δ_0 varied from 12–60 hours. Figure 7.2 presents the valid region of $H_{s,u}$ and $d_{s,0}$ values for different δ_0. A similar behavior can be observed for all the different δ_0 cases with a slight deviation for the highest minimum storm durations $d_{s,0}$. For $\delta_0 = 12$ hours, the valid region is set for $H_{s,u} \lessapprox 1.5$ (97.5$^{\text{th}}$ percentile), for the highest $d_{s,0}$ and $H_{s,u} \lessapprox 2.1$ (99.7$^{\text{th}}$ percentile) for $d_{s,0} \approx 20$ h. In the case of $\delta_0 = 60$ h the valid region comprises $H_{s,u} \lessapprox 1.7$ (98.8$^{\text{th}}$ percentile), for the highest $d_{s,0}$ and $H_{s,u} \lessapprox 2.2$ (99.8$^{\text{th}}$ percentile) for $d_{s,0} \approx 20$ h.

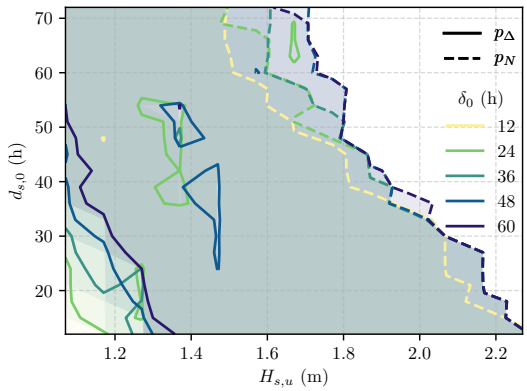

FIGURE 7.2: Valid regions of $H_{s,u}$ (x–axis), $d_{s,0}$ (y–axis) and δ_0 (colors) for SIMAR 2041080. Each region is defined as the intersection between the nonrejection regions of the null hypotheses of the interarrival times $p_\Delta > \alpha$ (solid lines) and the number of events $p_N > \alpha$ (dashed lines).

The selected ($H_{s,u}$, δ_0, $d_{s,0}$) must fulfill the hypotheses tests, $\lambda_N \approx 1/\bar{\delta}$ and provide an adequate number of events allowing for the statistical multivariate characterization of the storm events. Based on empirical grounds and other studies in the area a value of $\delta_0 = 24$ h was selected. Figure 7.3 depicts the valid region for $\delta_0 = 24$ h as well as the contours of $|\lambda_N - 1/\bar{\delta}|$ and the mean annual number of storm events, λ_N.

Taking into consideration the different conditions we have chosen the values of $H_{s,u} = 1.5$ m and $d_0 = 30$ h obtaining a series of 165 storm events comprising a total of 8610 hourly sea states of H_s, T_p, θ_m (Figure 7.4).

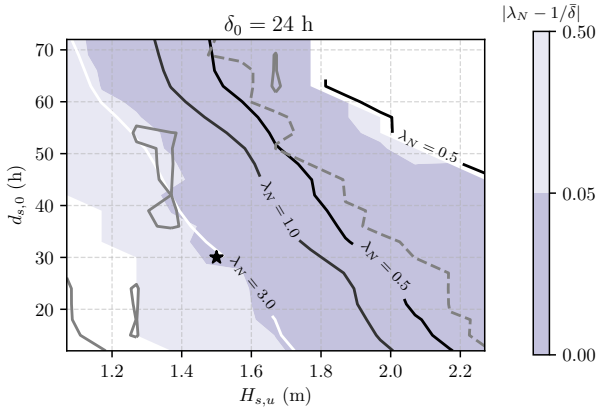

FIGURE 7.3: Valid region of $H_{s,u}$, $d_{s,0}$ and $\delta_0 = 24$ h as the intersection between the nonrejection regions of $p_\Delta > \alpha$ (solid gray line) and $p_N > \alpha$ (dashed gray line). Contour of $|\lambda - 1/\bar{\delta}|$ and the annual mean of the number of storm events, λ_N. The star symbol indicates the chosen $(H_{s,u}, d_{s,0})$.

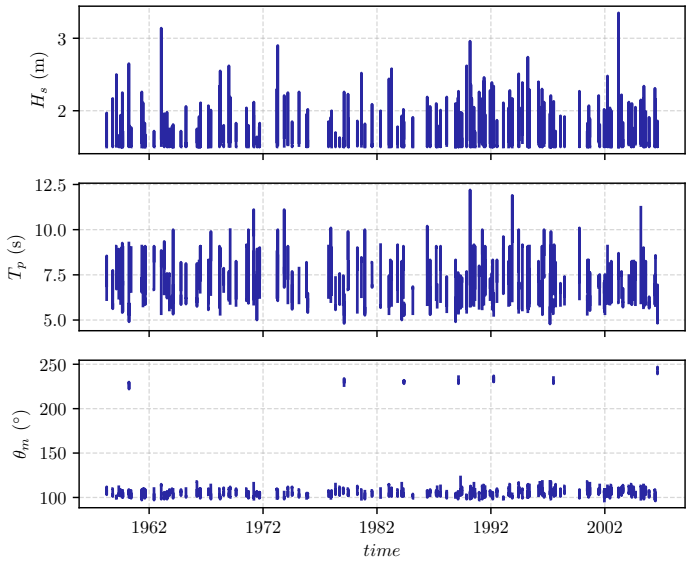

FIGURE 7.4: Historical storm events from SIMAR 2041080 for $H_{s,u} = 1.5$ m, $d_0 = 30$ h and $\delta_0 = 24$ h.

Interdependence of (D_S, Δ) via Archimedean copulas

Figure 7.5 presents the scatter plots of (d_s, δ). The longest storm events are found during Spring and Winter with the more extreme ones being in the latter. Therefore a bivariate distribution for (D_s, Δ) was estimated for each season.

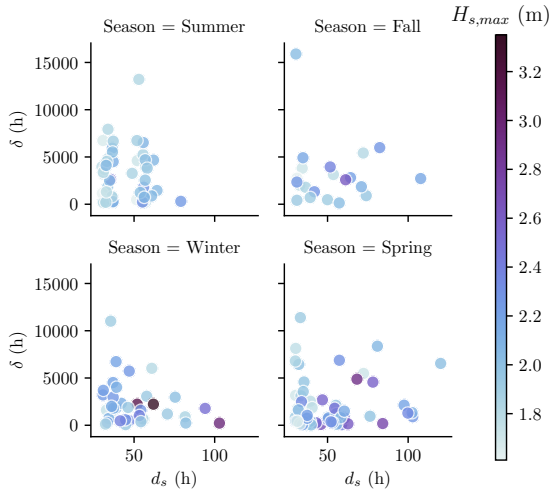

FIGURE 7.5: Scatter plots of storm duration d_s and interarrival time δ of storm events for the different seasons. The colors represent the $H_{s,max}$ of each event.

Among the Archimedean copulas, frequently used in coastal engineering (Li et al., 2018), the Clayton copula for Fall, Winter and Spring and the Frank copula for Summer, provided the best fit. Figure 7.6 presents the bivariate density estimate of D_s, Δ as well as the simulated values using the corresponding copula model.

The Clayton and Frank copula are defined as,

$$C_{\theta_c}(d_s, \delta) = \left(d_s^{-\theta_c} + \delta^{-\theta_c} - 1\right)^{-\frac{1}{\theta_c}} \tag{7.1}$$

$$C_{\theta_c}(d_s, \delta) = \frac{1}{ln\theta_c} ln\left(1 + \frac{(\theta_c^{d_s} - 1)(\theta_c^{\delta} - 1)}{\theta_c - 1}\right) \tag{7.2}$$

where θ_c is the dependence obtained from the Kendall rank correlation coefficient (τ_k) (Salvadori et al., 2007). The seasonal, marginal ECDFs of D and Δ were calculated from the historical data via Kernel Density Estimation (KDE) and the value of θ_c was found with a Canonical Maximum Likelihood (CML) method (Li

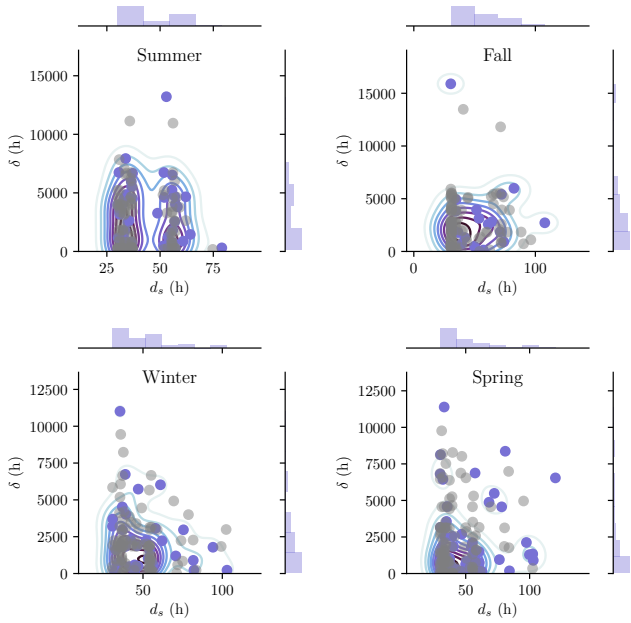

FIGURE 7.6: Empirical joint density functions of historical D_s and Δ for the different seasons and scatterplot of simulated values (gray points).

et al., 2014)). Table 7.1 presents the dependency parameters, Kendall's τ_K and Spearman's ρ_s.

Season	Family	θ_c	τ	ρ_s
Summer	Frank	0.00012	0.0	-0.006
Fall	Clayton	0.039	0.019	0.048
Winter	Clayton	-0.232	-0.131	-0.186
Spring	Clayton	-0.027	-0.014	-0.031

TABLE 7.1: Parameters of the copula fit θ_c, Kendall's τ_K and Spearman's ρ_s

Marginal distributions of maritime climate (H_s, T_p, θ_m)

The empirical distribution of the significant wave height values that exceed the given threshold and their concomitant peak periods and mean wave directions

are fitted to the univariate extremal distribution models with Maximum Likelihood Estimate (MLE) of the parameters by means of the *scipy.stats* Python library. Figure 7.7 presents the results of fitting a Generalized Pareto distribution for H_s, 2-Lognormal distributions for T_p and 2-Truncated-Normal distributions for θ_m.

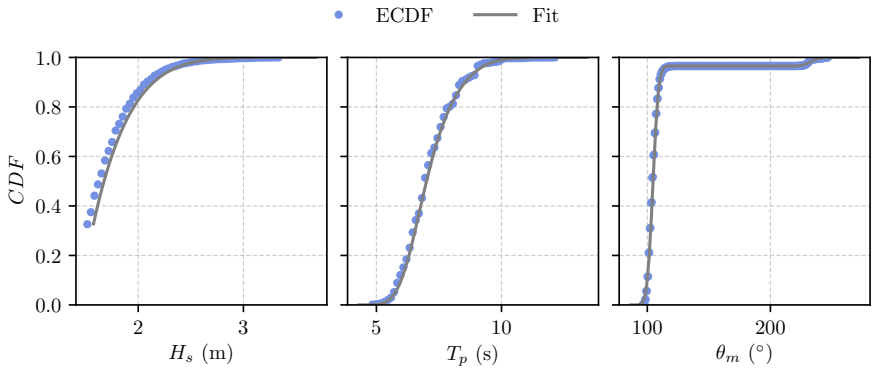

FIGURE 7.7: Empirical Cumulative Distribution Function —ECDF— (blue) and theoretical fit (gray) of the significant wave height H_s, peak wave period T_p and mean wave direction θ_m.

Simulation of storm events

The fitted univariate distribution functions and the VAR(q)-model parameters were used to simulate a continuous time series of storm variables of H_s, T_p, and θ_m whose CDFs present a good fit with the historical storm events data as observed on Figure 7.8.

A new threshold $H'_{s,u}$ must be set in order to define independent storms while keeping the selected δ_0 and d_0 in each case. The selection $H'_{s,u}$ is done by maintaining the similarity between the CDF of the storms duration. Figure 7.9 shows the storms duration ECDF for the historical data and the simulated storms for several thresholds.

Independent storm events are obtained with $H'_{s,u} = 2.16$ m and are then distributed in time by adding the corresponding succeeding interarrival time via copula model. Figure 7.10 presents a simulated 50-year time series of storm events.

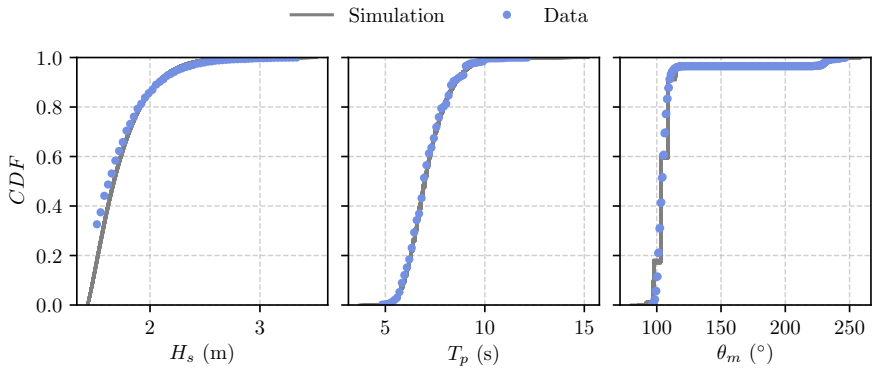

FIGURE 7.8: Cumulative Distribution Function —CDF— of the historical (blue) and simulated (gray) data of significant wave height H_s, peak wave period T_p and mean wave direction θ_m.

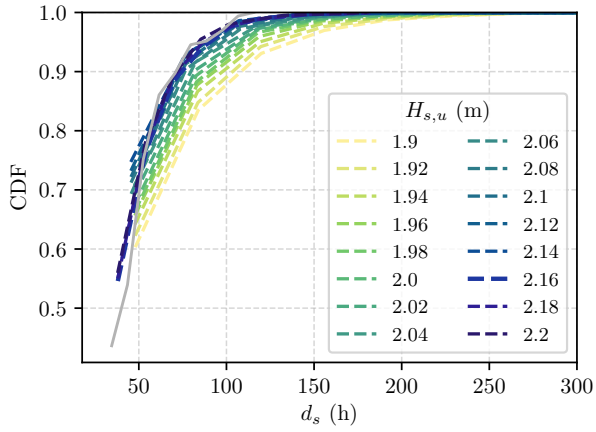

FIGURE 7.9: Selection of the H_s'–threshold to compatibilize the storm durations. Empirical CDF of historical (gray) and simulated data for several thresholds (dashed colors).

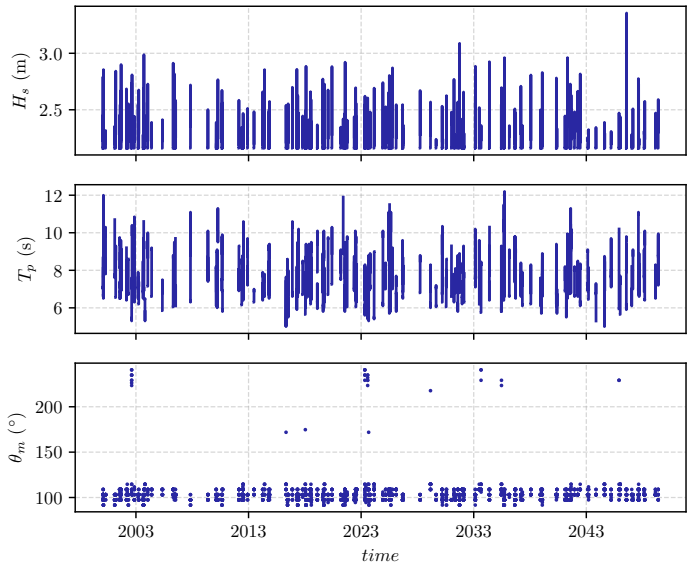

FIGURE 7.10: Simulated storm events from SIMAR 2041080

Verification of storm shape, magnitude, potential damage and occurrence

Figure 7.11 presents the normalized historical and simulated storms. The normalized time is with respect to the total storm duration d_s and the variables are normalized regarding the maximum significant wave height $H_{s,max}$ and the corresponding concomitant values $T_{p|H_{s,max}}$ and $\theta_{m|H_{s,max}}$, therefore $H_s^* = H_s/H_{s,max}$, $T_p^* = T_p/T_{p|H_{s,max}}$ and $\theta_m^* = \theta_m/\theta_{m|H_{s,max}}$. It can be observed that several types of storms are registered and adequately reproduced with the model highlighting that the methodology accurately reproduces sea and swell storms as well as other shapes of storms that diverge from the triangular or trapezoidal traditional shapes.

Figures 7.12 and 7.13 present the 2D scatter plots of the most relevant variable to check the suitability of the simulations. Figures 7.12 presents the historical and simulated H_s, T_p and θ_m and $H_{s,max}$ and d_s. As observed, the simulations yield very similar results to the historical data.

Figure 7.13 presents the relation between the storm magnitude M, peak wave power P_w and the storm duration d_s. The magnitude M takes into account the interdependence of the significant wave height H_s and the storm duration d_s and is defined area describing the storm history above the given threshold,

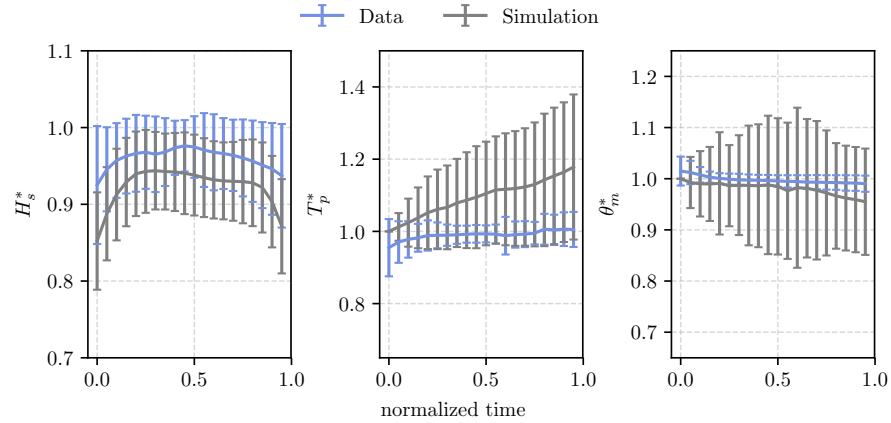

FIGURE 7.11: Normalized storm shapes and concomitants values including confidence intervals for historical (gray) and simulated (blue) events.

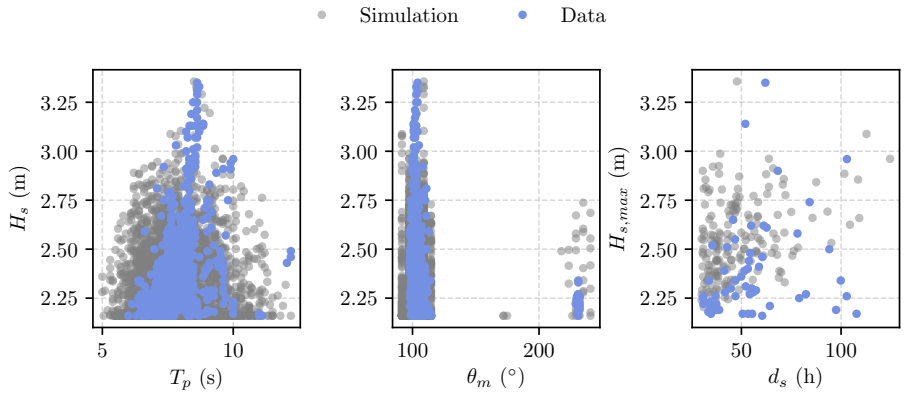

FIGURE 7.12: Scatter plots of historical (blue) and simulated (gray) data for H_s, T_p, θ, $H_{s,max}$ and d_s

$$M = \int_0^{d_s} (H_s(t) - H'_{s,u}(t))dt \tag{7.3}$$

The wave peak power P_w is an instantaneous measure of the storm and therefore quantifies the interdependence of H_s with T_p and is defined as,

$$P_w = E \cdot c_g = \left(\frac{1}{16}\rho_w g H_s(t)^2\right)\frac{gT_p(t)}{4\pi} \tag{7.4}$$

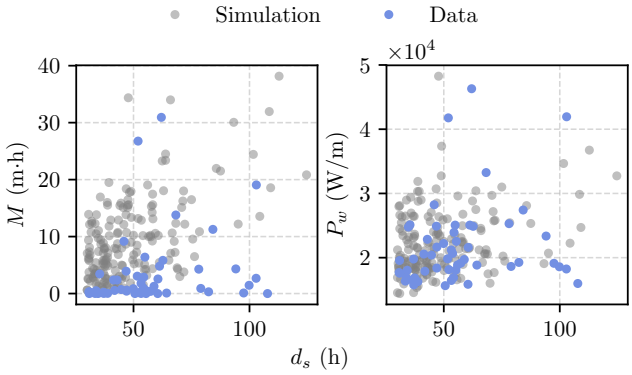

FIGURE 7.13: Scatter plots of historical (blue) and simulated (gray) data for M, P_w and d_s.

Figure 7.14 presents the monthly average storm frequency for the historical data and a simulation. It can be observed that the simulation methodology adequately reproduces the average number of storm events and the time dependent storminess characteristics.

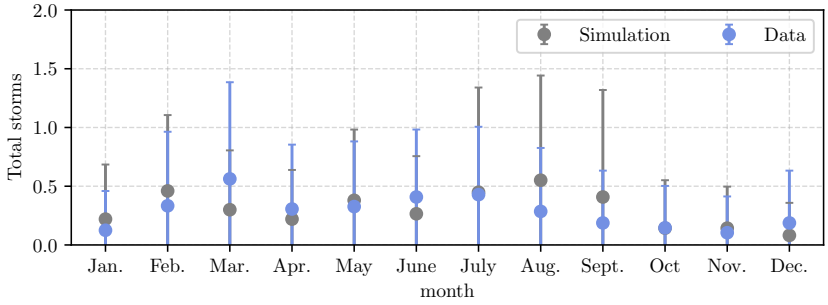

FIGURE 7.14: Monthly average storm frequency for historical (blue) and simulated (gray) data including confidence intervals.

Following this methodology, a total of 100 simulations of 50-year time series of storm events of H_s, T_p and θ_m were generated.

7.2 Safety margin and uncertainty assessment

A total of 100 simulations of 50-year time series of storm events were used as input for the analytical model with oblique wave incidence presented on Chapters 1 and 5 to obtain the time series of surface elevations and wave forces in the leeward and seaward regions.

Figure 7.15 presents the results of the simulations by means of the ECDF and theoretical fits of the maximum leeward-acting and seawards-acting forces, and the minimum safety margin for the case of $B = 5$ m and $d/h = 0.64$. The probability of failure is defined as the probability that $SM < 0$ given that the projected sea-state is exceeded at least once in the timeframe (useful life). In this case for a critical stress value of $F_c = 380$ kN/m, an approximate probability of failure of $SM \approx 0.2$ is obtained.

Therefore, this methodology can be used to efficiently project and design maritime studies by means of a simple analytical model and its application with simulation techniques to define the uncertainty of the structure's design.

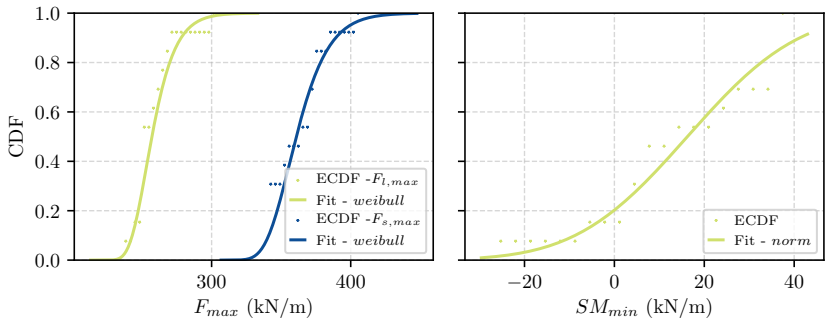

FIGURE 7.15: Empirical Cumulative Distribution Function (ECDF) and fit of maximum total forces and minimum safety margin at the plate ($x = 0$) for $B = 5$ m and $d/h = 0.64$.

7.3 Conclusions

The maritime data of SIMAR 2041080 is analyzed following the methodology presented on Chapter 3 and used as input data for the analytical model with oblique wave incidence described on Chapter 1.

The storm definition is given by a non-subjective method performing goodness-of-fit tests to obtain the optimal values of $H_{s,u}$, $d_{s,0}$ and δ_0. The main maritime

variables (H_s, T_p, θ) are fitted by univariate theoretical functions with the temporal dependence being analyzed by a VAR(q)-model. The storm duration d_s and interarrival time δ are jointly characterized by means of a copula model fitted by season.

The results show that the simulation model adequately reproduces the historical data including its seasonality and temporal evolution proving to be an efficient methodology for long-term simulation of storm events including its random natural and evolution.

Monte Carlo techniques were used to perform a number of equally likely simulations allowing to study the probability of failure and analyze the uncertainty, therefore reducing construction costs and proving to be a efficient tool for the predesign phase of a maritime structure towards the integral optimization of the system.

Conclusions and future research lines

Conclusions

This thesis addresses the design of maritime works at different time scales that go from the sea state to the useful life of the structure. A partially reflective maritime structure which can be designed to jointly control wave agitation in a harbor as well as to protect a wave energy converter is selected for the study. The structure is delimited by a semi-submerged plate and back wall. The work comprises its modeling by means of an analytical solution and the verification of its performance with numerical models results and experimental data obtained at the Atmosphere-Ocean Interaction Flume (CIAO).

The experimental tests at the CIAO were carried out under paddle-generated regular and irregular waves in combination with wind–sea waves for different wind speeds (wind tunnel) to account for the interaction of swell and sea waves and helped to gain knowledge on the effect of wind on a partially standing wave field. Unfortunately, during the experiments some of the instrumental devices failed as they were not suitable to be employed in a windy environment. The analyses of the experimental data are mainly descriptive due to the lack of sufficient data to extract information of a highly non-linear system.

A methodology to simulate multivariate long-term time series of extreme climate conditions is also proposed and used to analyze the structure under long-term time series of extreme events for real-world applications. Simulations were performed to assess the uncertainty of the results.

For the development of this thesis, different specific objectives were proposed: (i) set-up and validation of an analytical model for the optimization of maritime structures under regular and irregular waves forcings, (ii) analysis of the hydrodynamics of the interaction of swell and sea waves with partially reflective structures by laboratory experiments, (iii) study of the suitable and rigorous selection of the parameters that define extreme events, and (iv) development of a methodology for the analysis and simulation of multivariate long-term time series of extreme events for its application, e.g., in damage evolution models of maritime structures. Regarding the different methods used in this thesis, the following conclusions can be derived:

- The analytical model is a simple and efficient tool to analyze the hydrodynamic performance of the structure under obliquely incident irregular waves and presents a good performance when compared to the results of CFD models. It provides a simple and efficient engineering tool to search for an optimal design (trade-off between performance and structural design) towards the goals of (i) harbor tranquility in the far field region of the reflector, (ii) wave energy extraction in the inner chamber and (iii) structural safety analysis of the loads acting on the plate.

- A simplified configuration was selected for the analysis, however, the model can be easily be extended to a given chamber length (y-axis) by imposing appropriate matching conditions on the borders as well as with an inclined orientation.

- The analytical and experimental results present a good agreement for the reflection coefficient K_R and the maximum surface elevation in both the seaward and leeward regions.

- The storm definition is given by a non-subjective method performing goodness-of-fit tests to obtain the optimal values of $H_{s,u}$, $d_{s,0}$ and δ_0. The simulation model adequately reproduces the historical data including its seasonality and temporal evolution proving to be an efficient methodology for long-term simulation of storm events including its random natural and evolution.

- Monte Carlo techniques were used to perform a number of equally likely simulations allowing to study the probability of failure and analyze the uncertainty, therefore reducing construction costs and proving to be a efficient tool for the predesign phase of a maritime structure towards the integral optimization of the system.

Based on the results derived from each objective, the following conclusions are drawn:

- Due to the wave-structure interaction, the spectra in both regions contains nodal and antinodal frequencies depending on the geometrical configuration of the system, water depth and the incident swell and sea wave characteristics.

- At $x = 0$ the spectrum presents one peak outside the chamber and several peaks inside the chamber. The number of peaks and the distance between them depends on the geometric characteristics. In the seaward region far from the reflector the spectrum presents a nodal structure applicable for controlled harbor agitation.

- For increasing wave incidence, the behavior of the system varies with a periodicity at $B/L' = 0.5$ where $L' = L/\cos\theta$.
- Regarding the results involving only wind–sea waves (wind tunnel), these vary significantly when considering different temporal subsets of the complete time series as the waves are growing. he peak frequency decreases with an increase of wind speed varying from 2–4 Hz for $W2$ to 1–3 Hz for $W4$. Wind–sea waves have mean periods in the range of 0.2 to 0.4 s for the highest analyzed wind speed.
- For the experiments involving incident regular wave configuration with a wave period similar to the 1st natural period of the chamber, an amplification of wave energy in the seaward region is measured for a relative submergence of $d/h = 0.58$.
- Wind-driven waves have a high influence on the total wave period and symmetry of the waves. The influence of wind–sea waves is more noticeable for the experiments where $T_{z0}/T_1 \geq 1.5$, in which the short-crested waves proved to have a higher influence on the resulting wave periods and heights in the seaward region. Therefore, the influence of wind–sea waves on the behavior of the structure depends greatly on the period of the predominant periodic component (swell).
- The spectrum involving swell and sea waves presents different resonant peaks. At high frequencies the scenario is controlled by wind-driven waves and the resonant frequencies of the flume become less evident. Inside the chamber the peak frequencies in all sections correspond to the swell waves, closer in period to the natural period of the chamber. At higher frequencies the energy decreases with respect to the seaward side.

Future research lines

The results and conclusions of this thesis allow for the suggestions for future research:

- Extension of the analytical model for a given chamber length (y–axis), plate inclination and for an incident directional spectrum to better represent waves in nature and different geometrical configurations.
- Further analysis of the nonlinear interaction when between wind–sea waves, irregular swell waves and resonant waves controlled by the geometry of the system.

- Initially, the experimental design included the use of Particle Image Velocimetry (PIV) device to study the velocity field below the plate and pressure sensors to obtain the wave forces acting on the plate. Unfortunately, the data from both systems had to be discarded. Due to a technical error, the PIV data was not sufficient to analyze short crested waves while the pressure data was inconsistent as the instrument was not suitable to be employed in a windy environment. Therefore, a future research line is the acquisition of pressure sensors suited for both air and water and the repetition of the experiments to analyze the velocity field and the wave forces on both sides of the plate.
- Extension of the analytical model to include wind and wind–driven waves induced forces acting on the plate.
- Inclusion of climate change projections including sea level rise on the methodology for extreme events simulations in order to analyze future impacts on coastal structures.

Appendix A

Temporal evolution of swell and wind–sea waves

This appendix presents additional experimental results for the temporal evolution on swell and wind–sea waves. §A.1 presents the power spectrum for different temporal subsets of the wind–sea waves experiments. §A.2 presents the temporal evolution of statistical results and power spectrum of under swell and wind–sea waves.

A.1 Wind–sea waves

Power spectrum for different temporal subsets

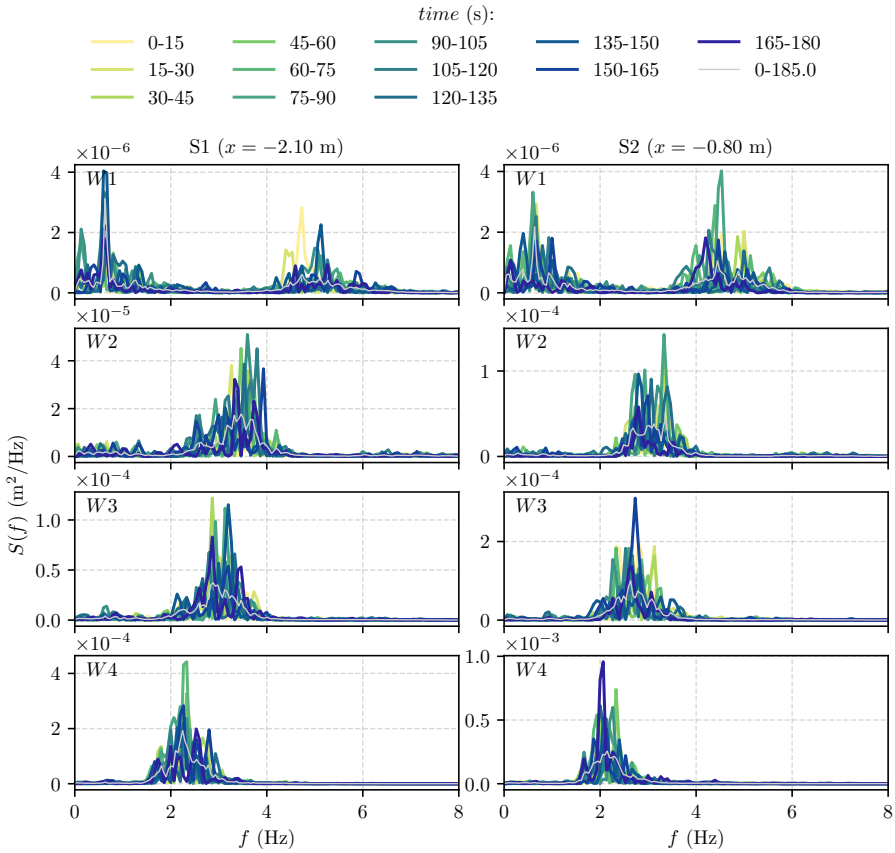

FIGURE A.1: Power spectrum (S) of η_1 for the wind–sea waves experiment *Wa*, different wind speeds and different temporal subsets.

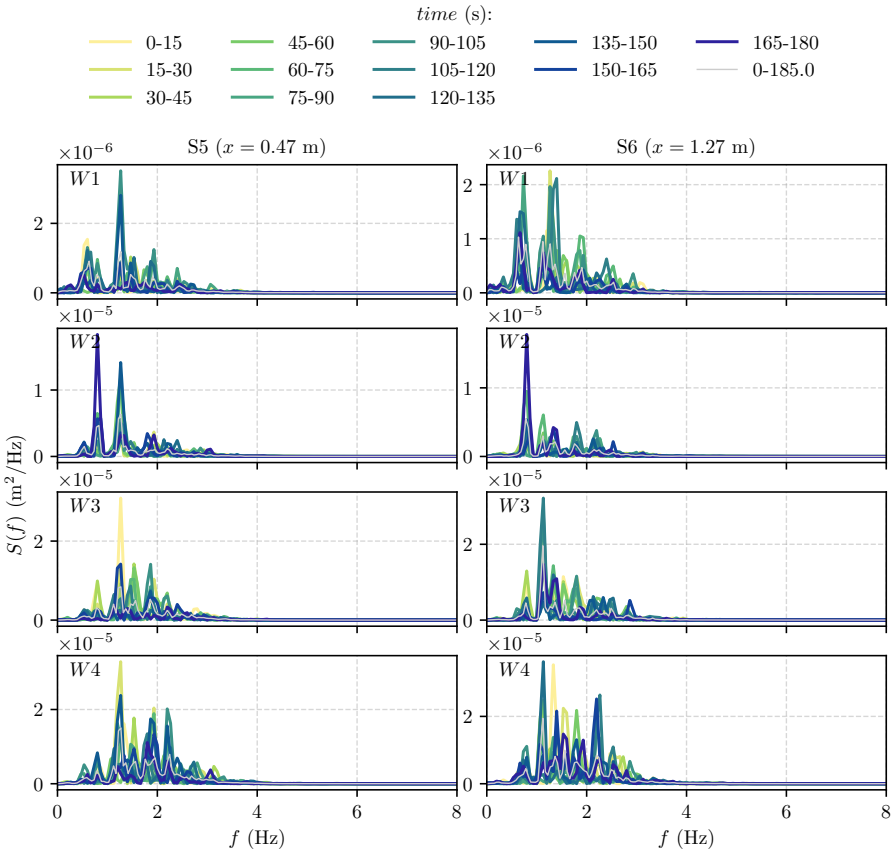

FIGURE A.2: Power spectrum (S) of η_2 for the wind–sea waves experiment *Wa*, different wind speeds and different temporal subsets.

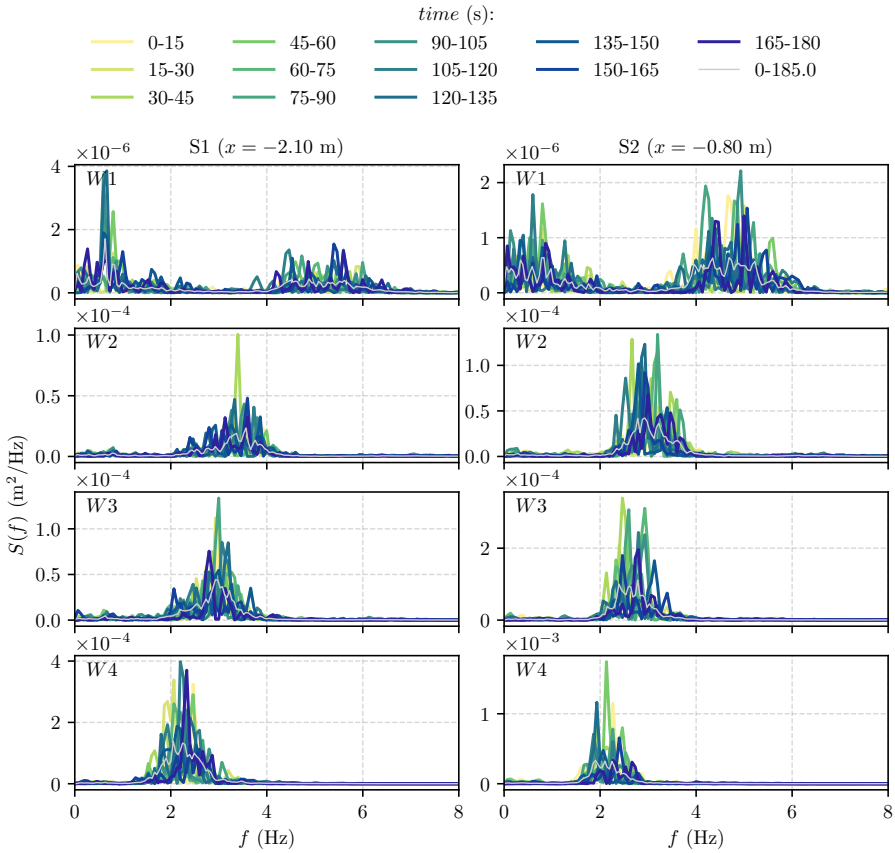

FIGURE A.3: Power spectrum (S) of η_1 for the wind–sea waves experiment *Wc*, different wind speeds and different temporal subsets.

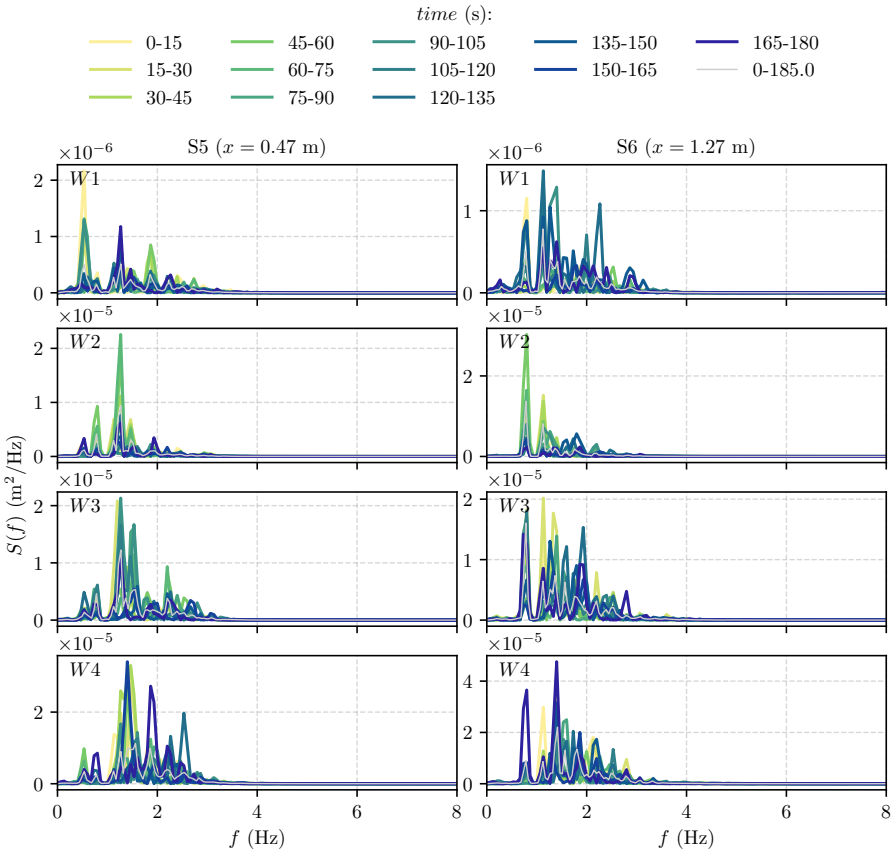

FIGURE A.4: Power spectrum (S) of η_2 for the wind–sea waves experiment *Wc*, different wind speeds and different temporal subsets.

A.2 Regular swell and wind–sea waves

Statistical parameters for different temporal subsets

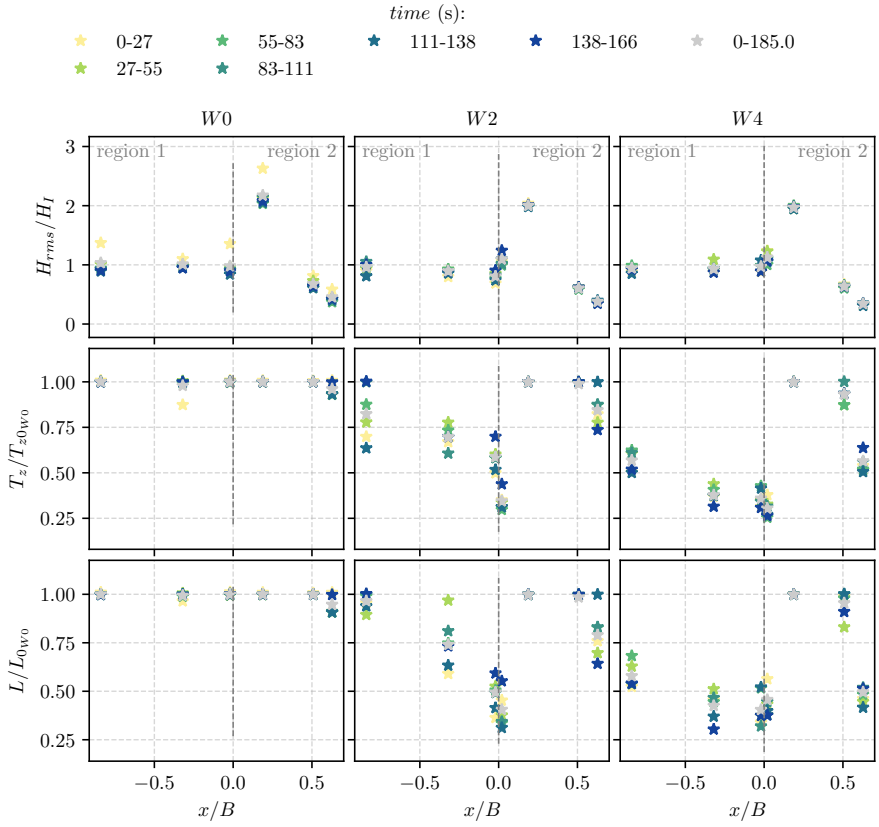

FIGURE A.5: Dimensionless statistical parameters for the regular wave experiment $R1a\_T1$ with respect to the wave gauges position x/B, different wind speeds (columns) and different temporal subsets (colors). The rows (top to bottom) depict the dimensionless r.m.s. wave height (H_{rms}/H_I), mean wave period ($T_z/T_{z0_{W0}}$) and mean wavelength $L/L_{0_{W0}}$).

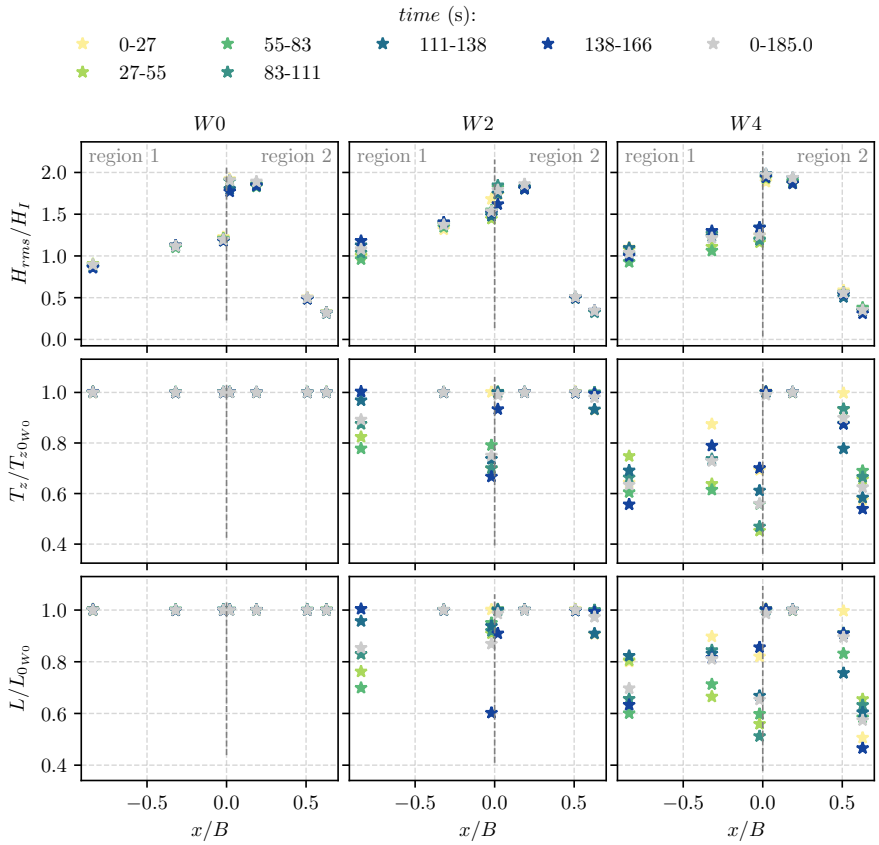

FIGURE A.6: Dimensionless statistical parameters for the regular wave experiment *R1b_T1* with respect to the wave gauges position x/B, different wind speeds and different temporal subsets. For an extended caption see Figure A.5.

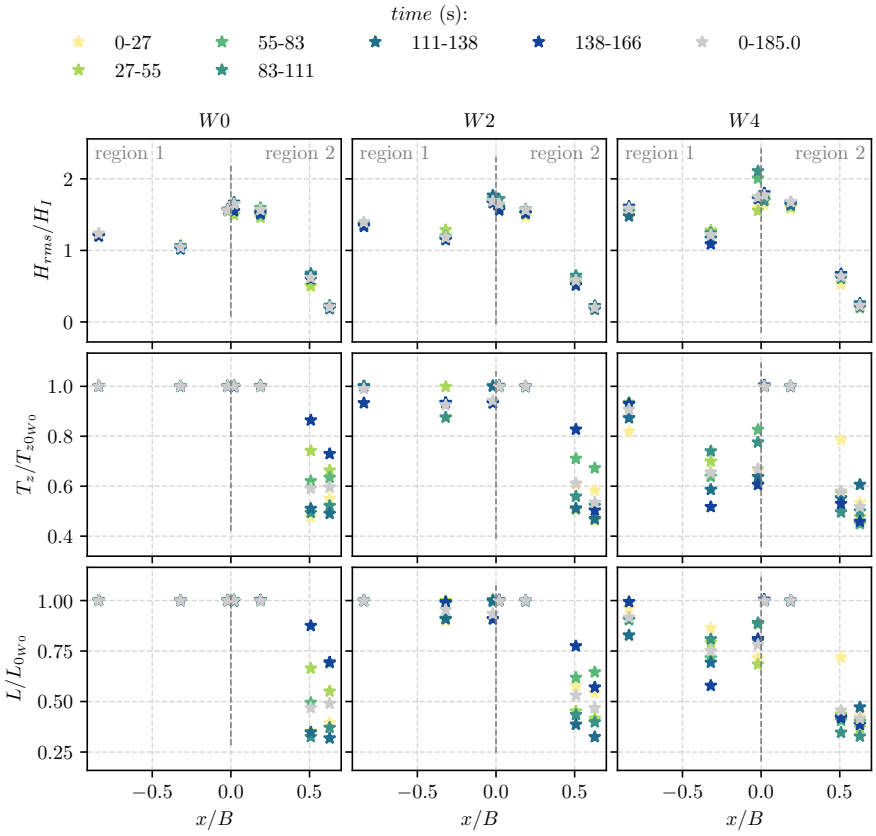

FIGURE A.7: Dimensionless statistical parameters for the regular wave experiment $R1c\_T1$ with respect to the wave gauges position x/B, different wind speeds and different temporal subsets. For an extended caption see Figure A.5.

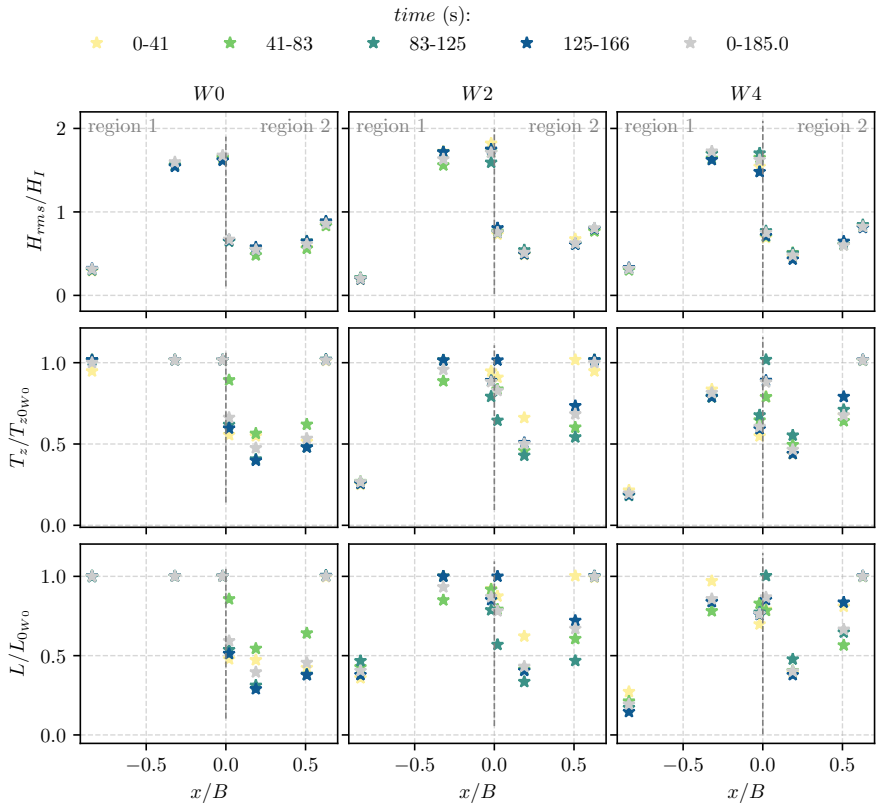

FIGURE A.8: Dimensionless statistical parameters for the regular wave experiment *R1b_T2* with respect to the wave gauges position x/B, different wind speeds and different temporal subsets. For an extended caption see Figure A.5.

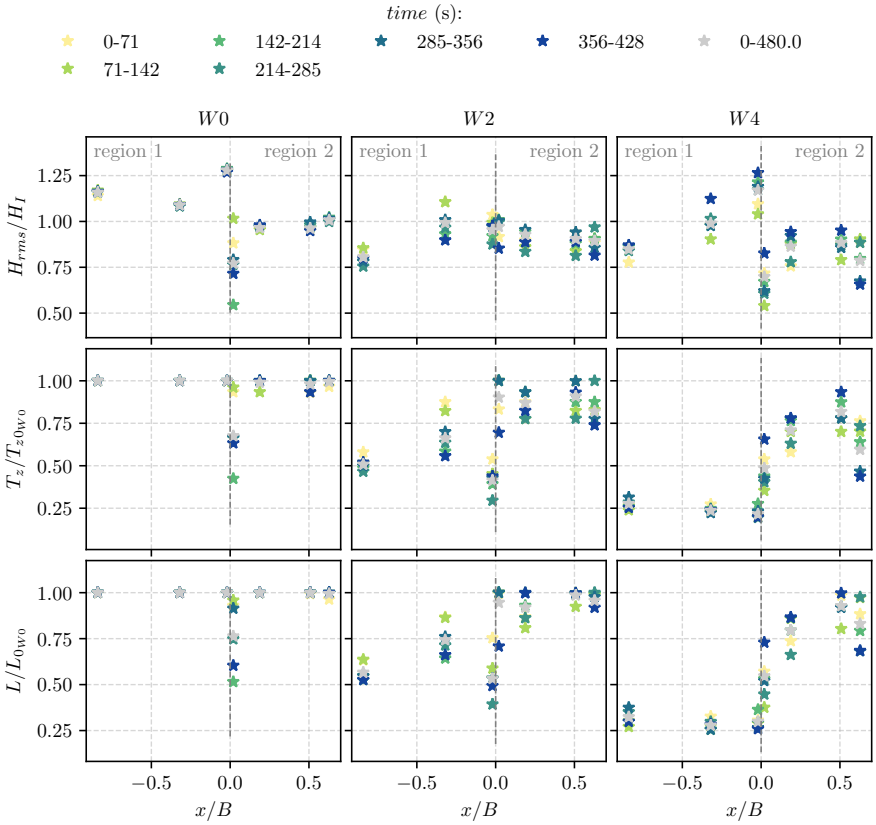

FIGURE A.9: Dimensionless statistical parameters for the regular wave experiment *R1b_T3* with respect to the wave gauges position x/B, different wind speeds and different temporal subsets. For an extended caption see Figure A.5.

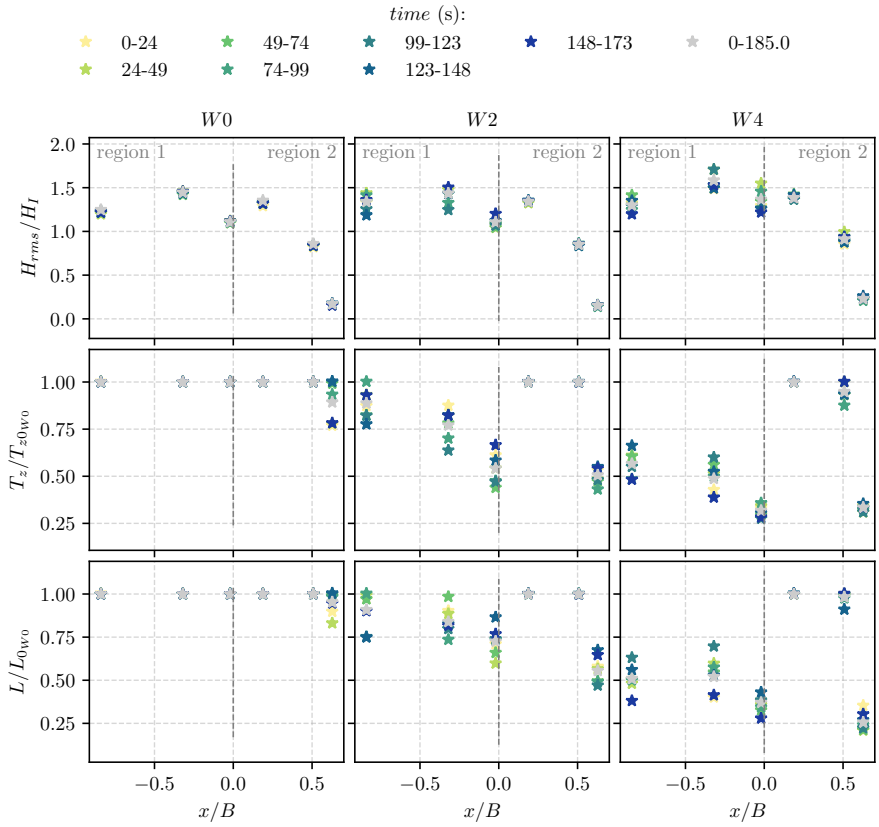

FIGURE A.10: Dimensionless statistical parameters for the regular wave experiment *R2a_T1* with respect to the wave gauges position x/B, different wind speeds (columns) and different temporal subsets (colors). The rows (top to bottom) depict the dimensionless r.m.s. wave height (H_{rms}/H_I), mean wave period ($T_z/T_{z0_{W0}}$) and mean wavelength $L/L_{0_{W0}}$).

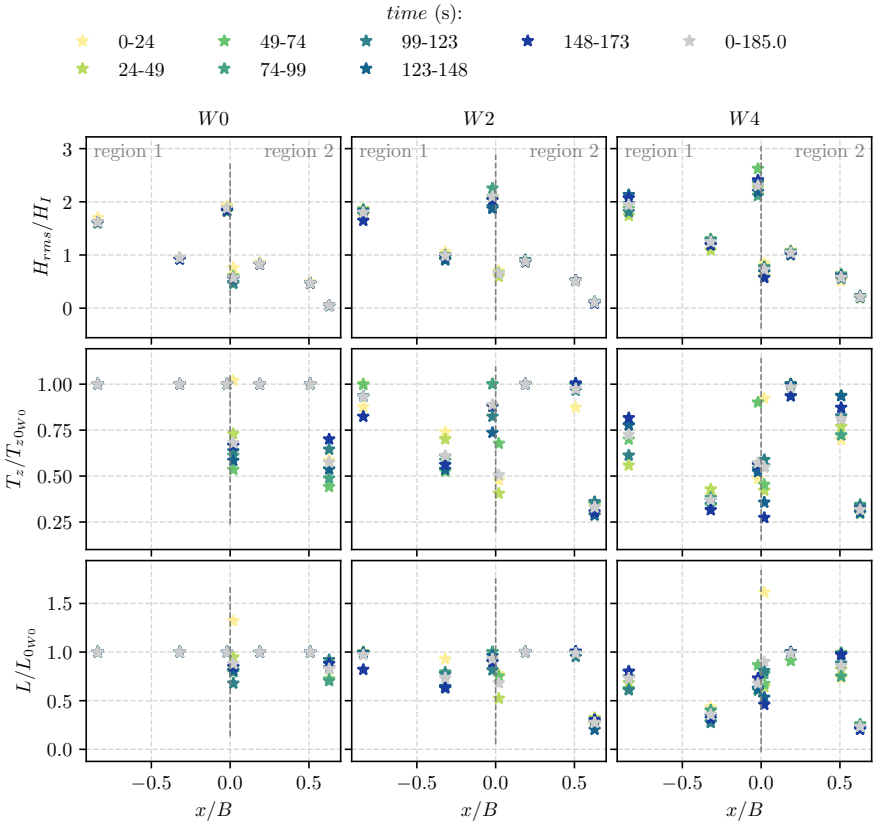

FIGURE A.11: Dimensionless statistical parameters for the regular wave experiment *R2b_T1* with respect to the wave gauges position x/B, different wind speeds and different temporal subsets. For an extended caption see Figure A.10.

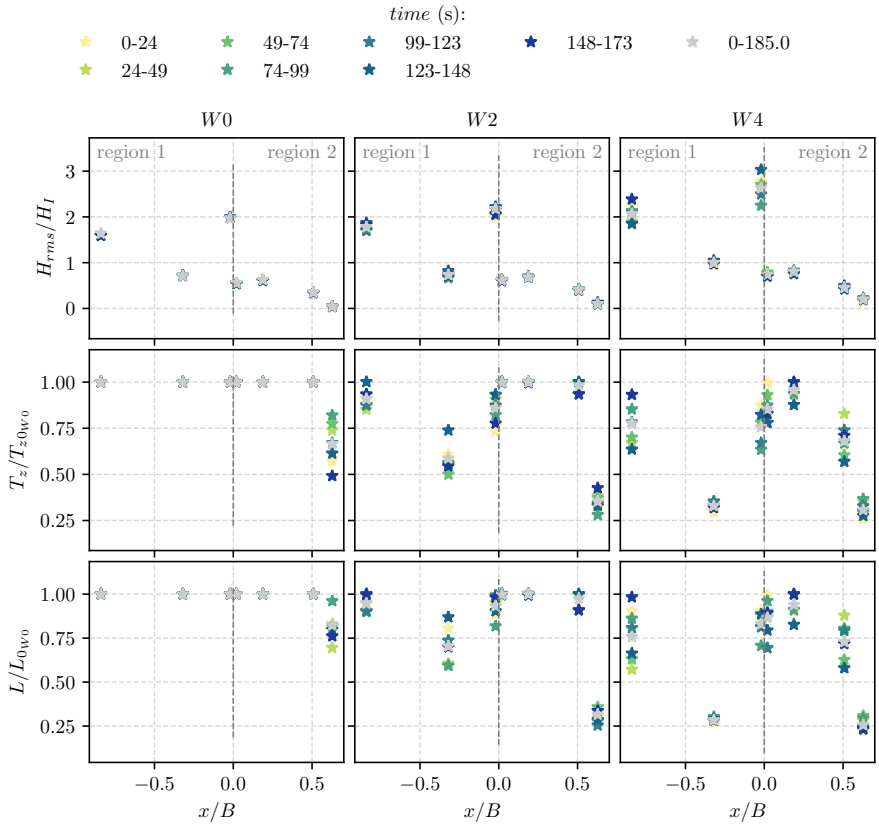

FIGURE A.12: Dimensionless statistical parameters for the regular wave experiment *R2c_T1* with respect to the wave gauges position x/B, different wind speeds and different temporal subsets. For an extended caption see Figure A.10.

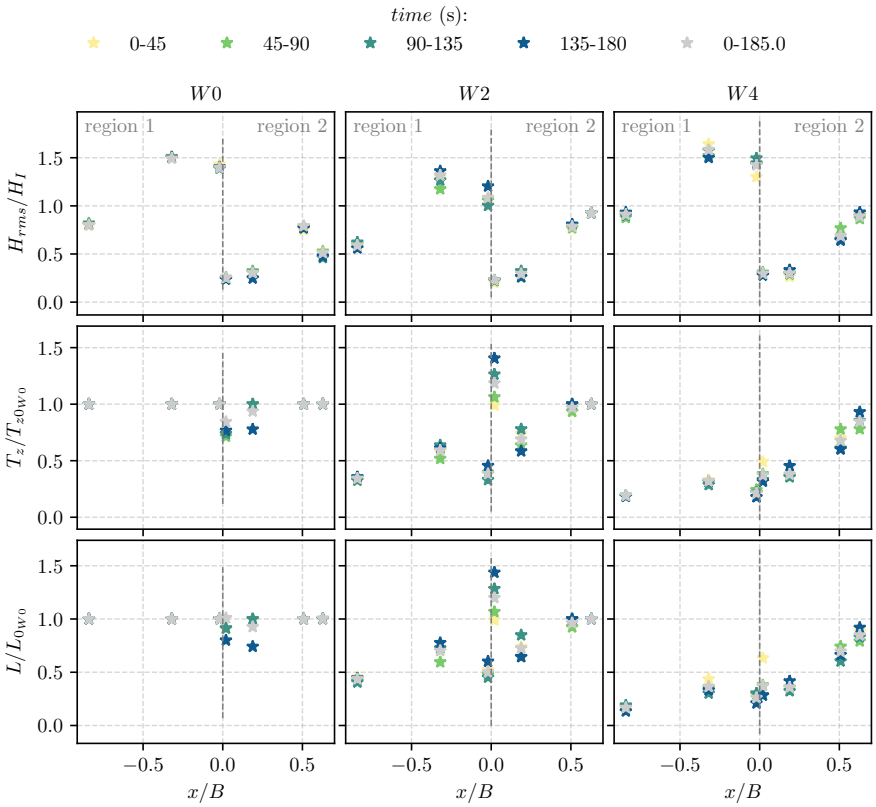

FIGURE A.13: Dimensionless statistical parameters for the regular wave experiment *R2b_T2* with respect to the wave gauges position x/B, different wind speeds and different temporal subsets. For an extended caption see Figure A.10.

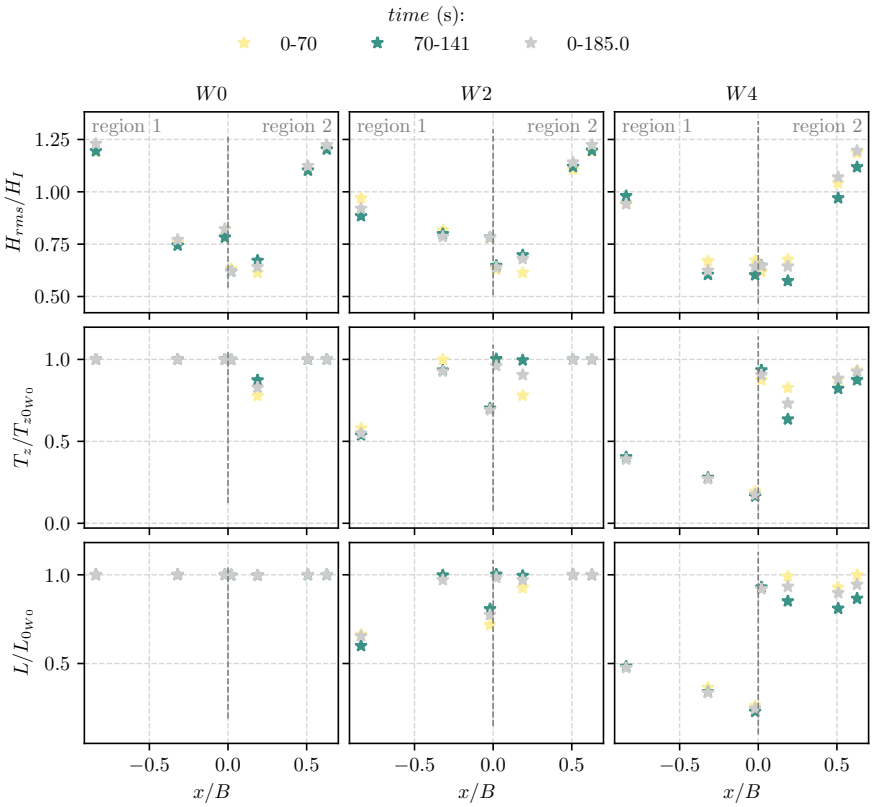

FIGURE A.14: Dimensionless statistical parameters for the regular wave experiment *R2b_T3* with respect to the wave gauges position x/B, different wind speeds and different temporal subsets. For an extended caption see Figure A.10.

Power spectrum for different temporal subsets

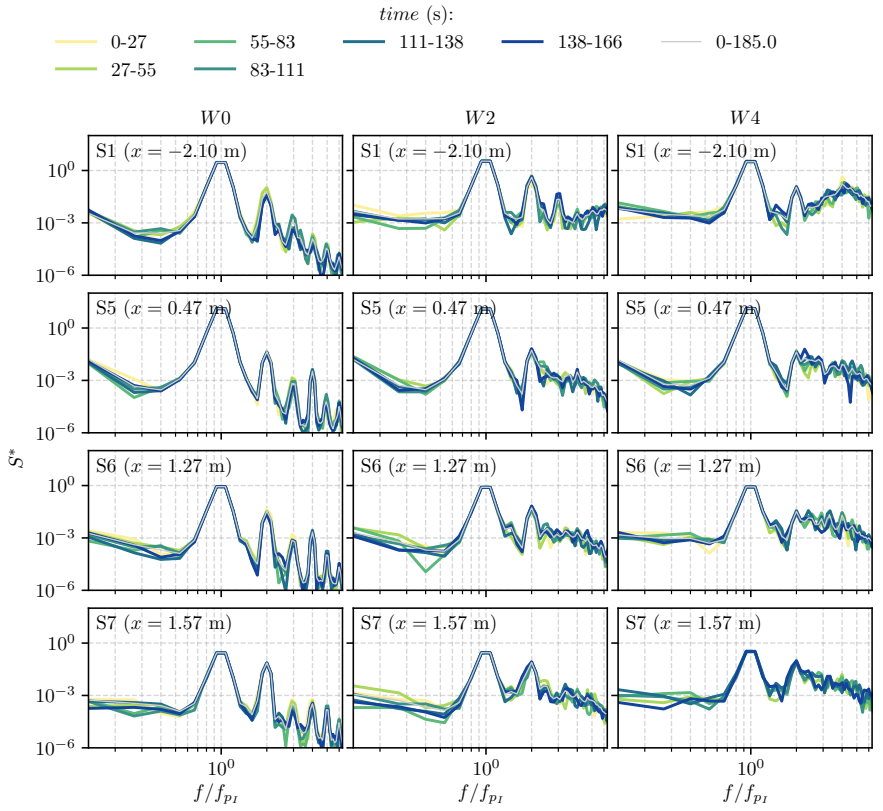

FIGURE A.15: Dimensionless power spectrum (S^*) of η for the regular wave experiment $R1b\_T1$–experiment, different wind speeds and different temporal subsets.

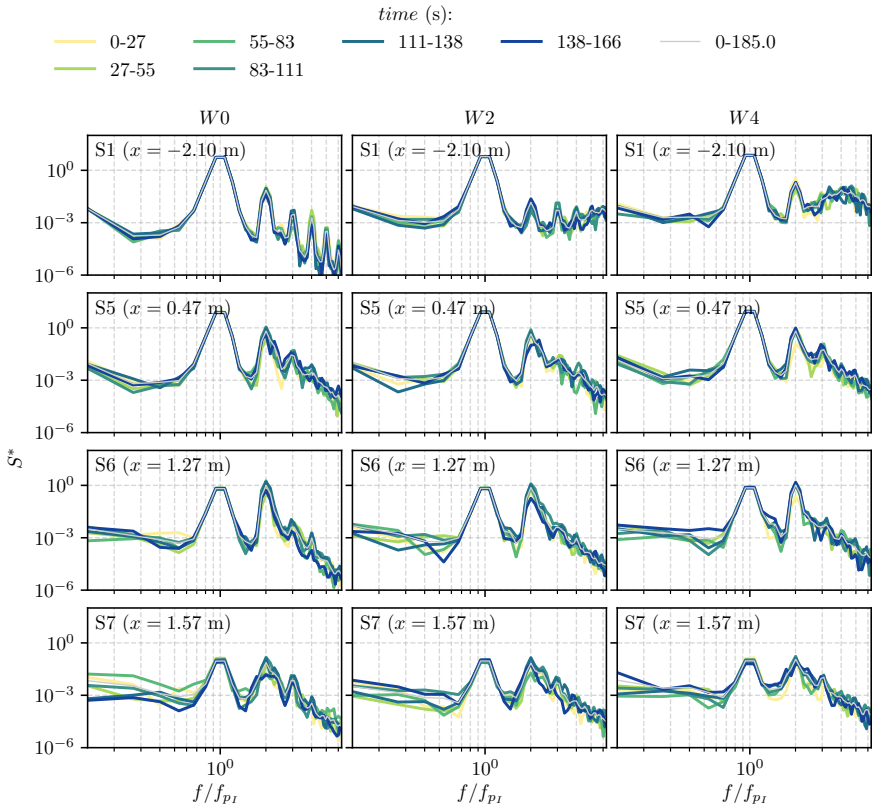

FIGURE A.16: Dimensionless power spectrum (S^*) of η for the regular wave experiment $R1c\_T1$, different wind speeds and different temporal subsets.

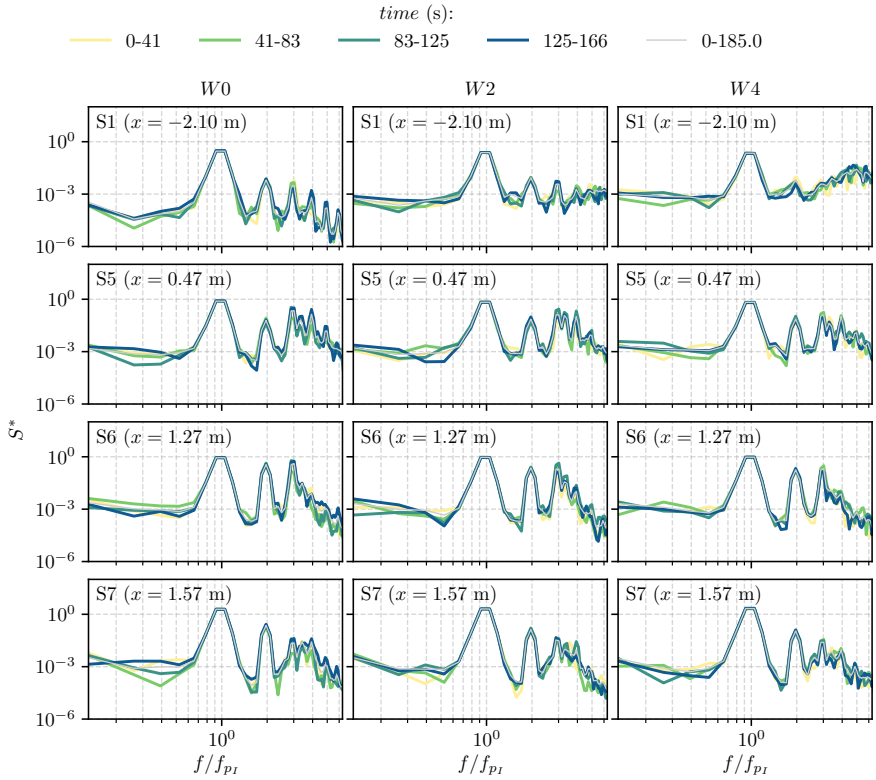

FIGURE A.17: Dimensionless power spectrum (S^*) of η for the regular wave experiment *R1b_T2*, different wind speeds and different temporal subsets.

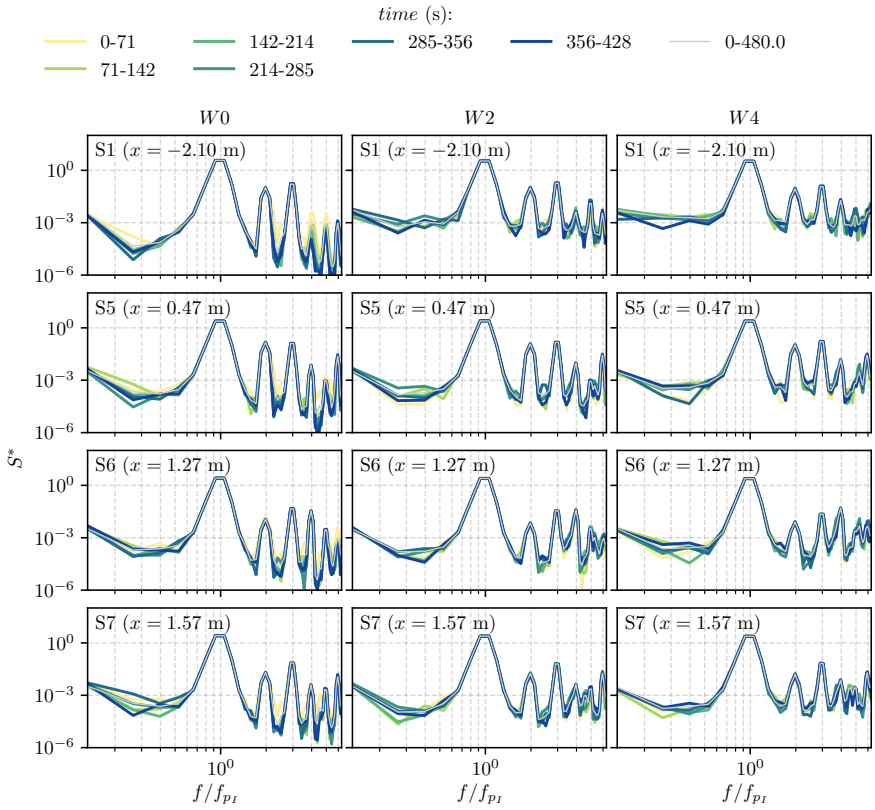

FIGURE A.18: Dimensionless power spectrum (S^*) of η for the regular wave experiment *R1b_T3*, different wind speeds and different temporal subsets.

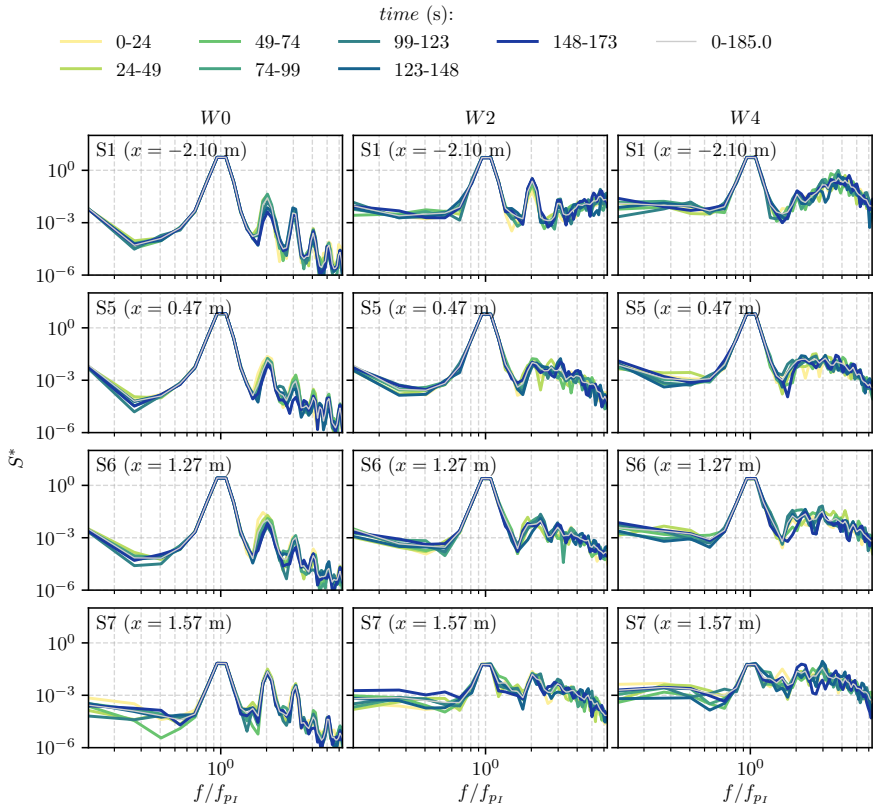

FIGURE A.19: Dimensionless power spectrum (S^*) of η for the regular wave experiment *R2a_T1*, different wind speeds and different temporal subsets.

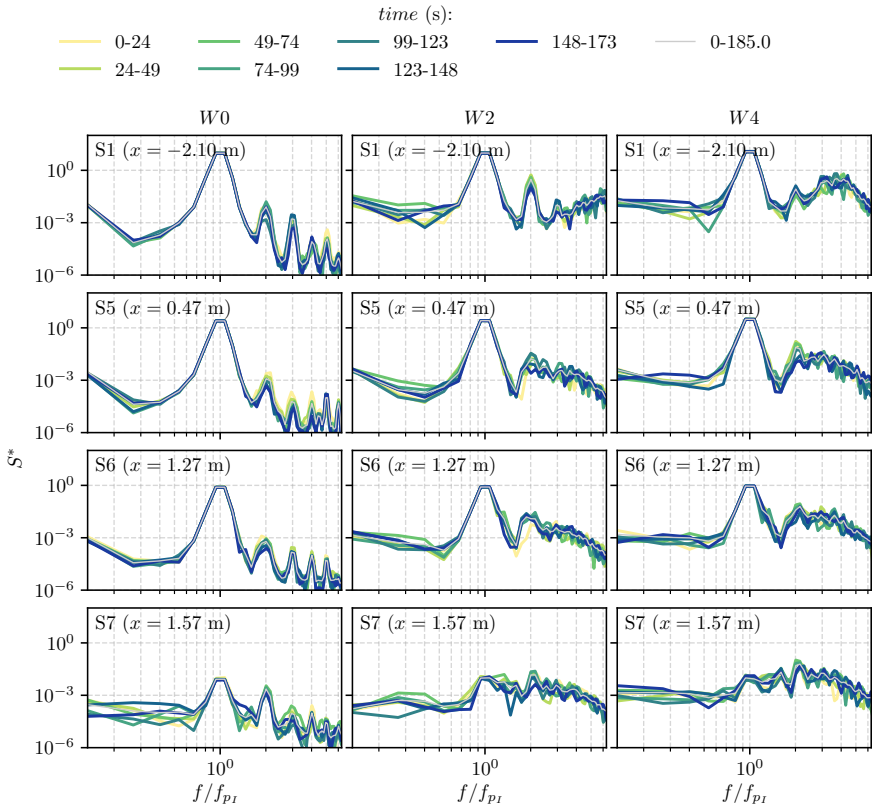

FIGURE A.20: Dimensionless power spectrum (S^*) of η for the regular wave experiment *R2b_T1*, different wind speeds and different temporal subsets.

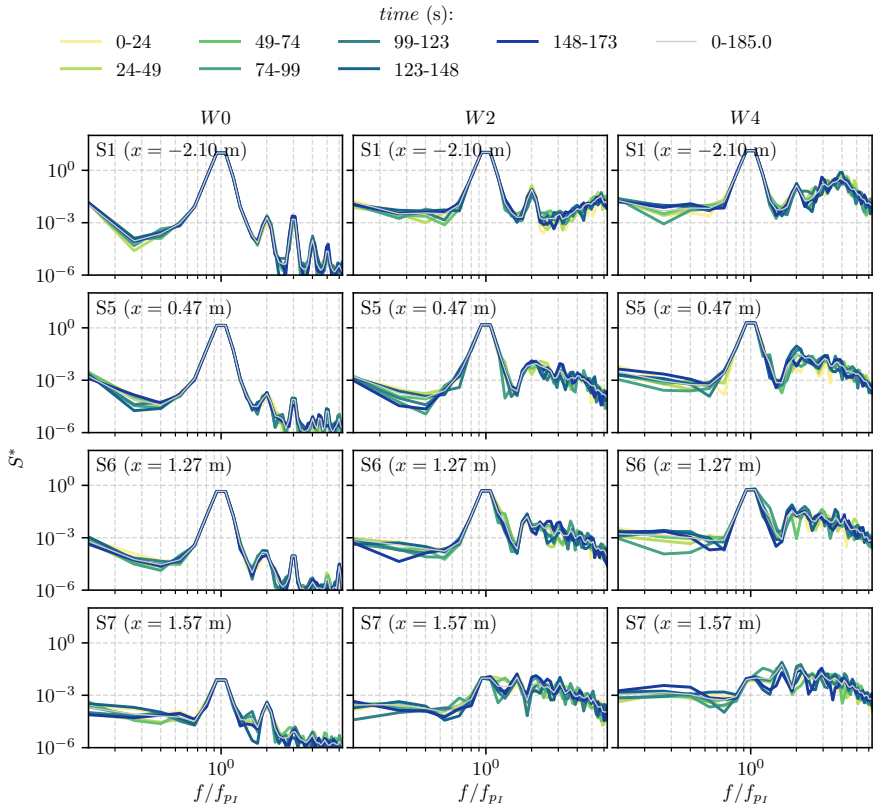

FIGURE A.21: Dimensionless power spectrum (S^*) of η for the regular wave experiment *R2c_T1*, different wind speeds and different temporal subsets.

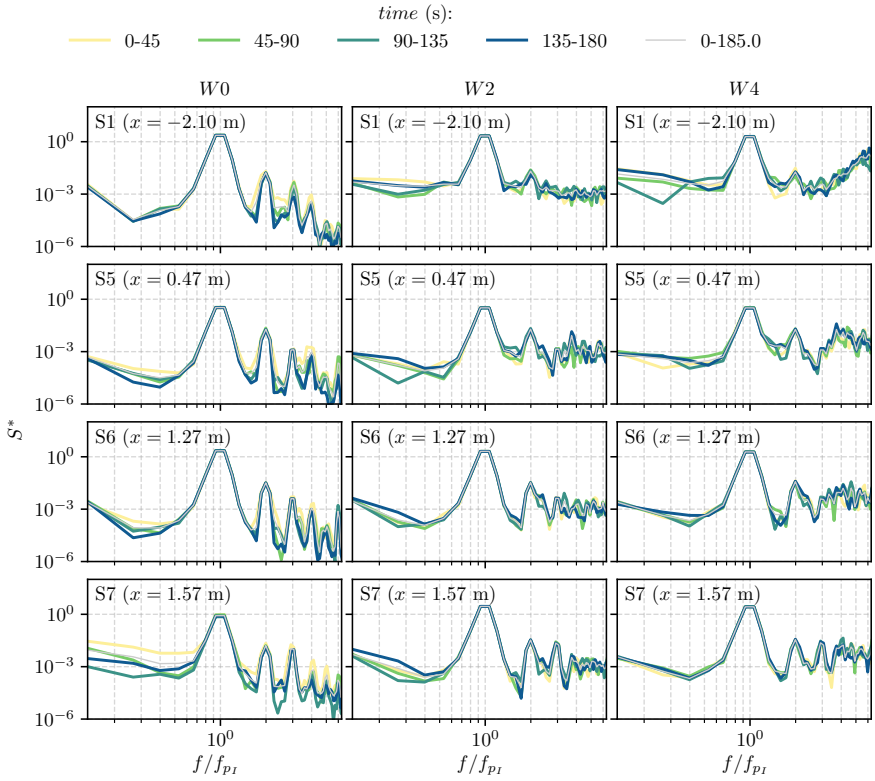

FIGURE A.22: Dimensionless power spectrum (S^*) of η for the regular wave experiment *R2b_T2*, different wind speeds and different temporal subsets.

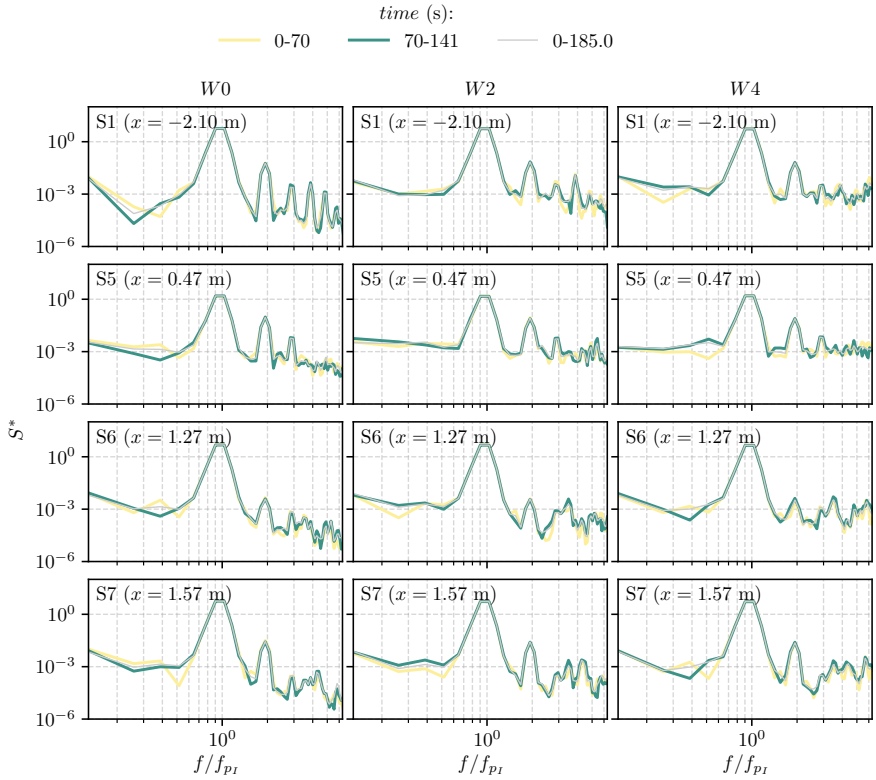

FIGURE A.23: Dimensionless power spectrum (S^*) of η for the regular wave experiment *R2b_T3*, different wind speeds and different temporal subsets.

A.3 Irregular swell and wind–sea waves

Power spectrum for different temporal subsets

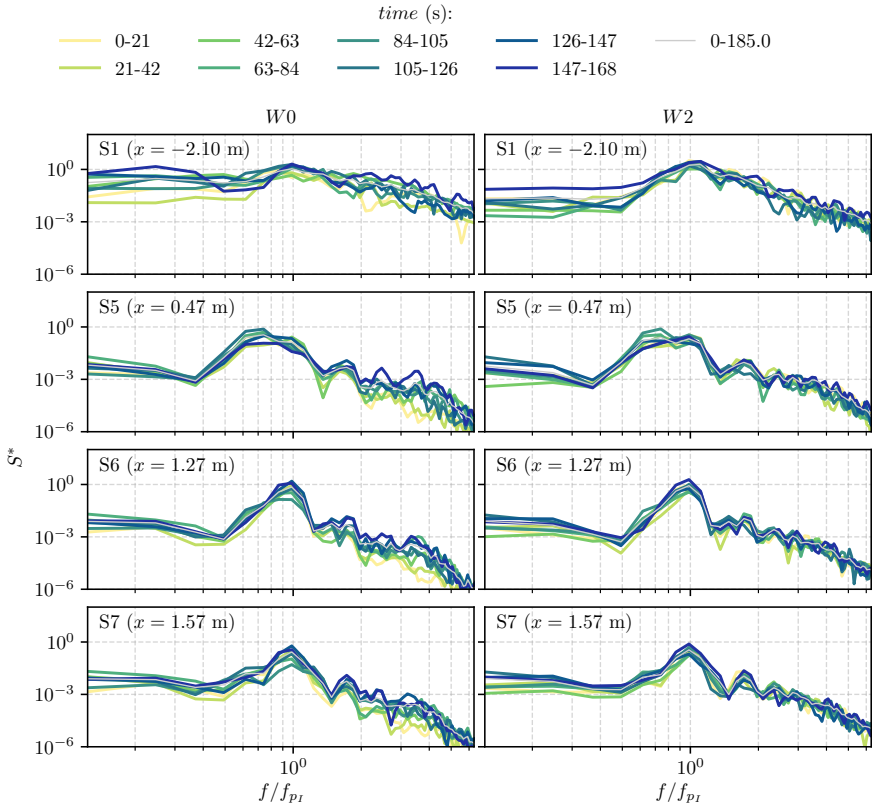

FIGURE A.24: Dimensionless power spectrum (S^*) of η for the Jonswap irregular wave wave experiment *JW1b_T1*, different wind speeds and different temporal subsets.

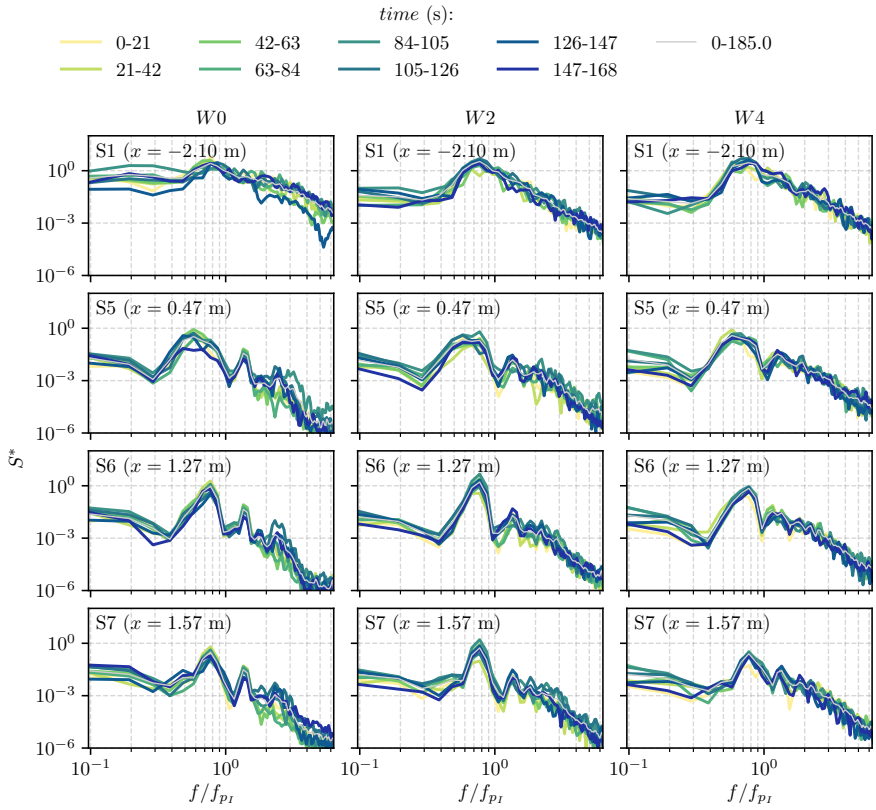

FIGURE A.25: Dimensionless power spectrum (S^*) of η for the Jonswap irregular wave wave experiment *JW1c_T1*, different wind speeds and different temporal subsets.

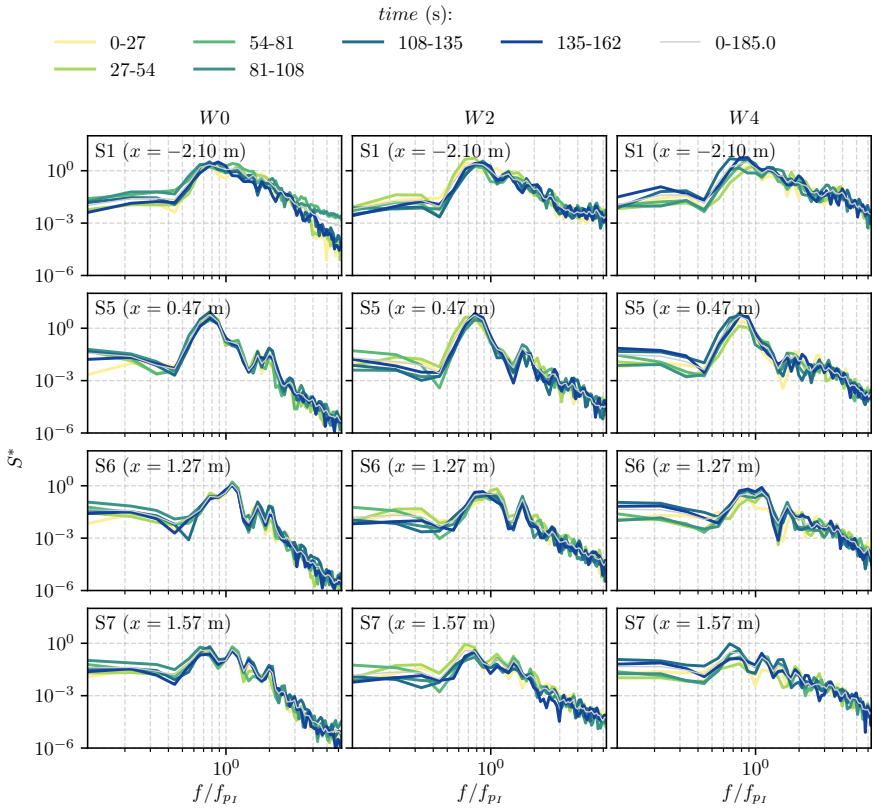

FIGURE A.26: Dimensionless power spectrum (S^*) of η for the Jonswap irregular wave wave experiment *JW1b_T2*, different wind speeds and different temporal subsets.

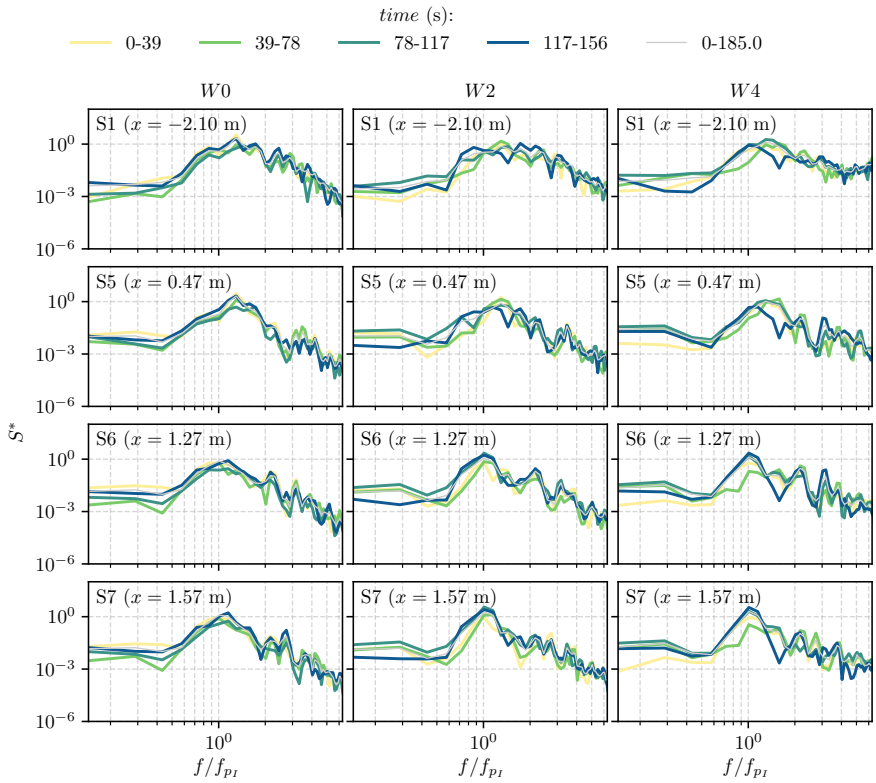

FIGURE A.27: Dimensionless power spectrum (S^*) of η for the Jonswap irregular wave wave experiment *JW1b_T3*, different wind speeds and different temporal subsets.

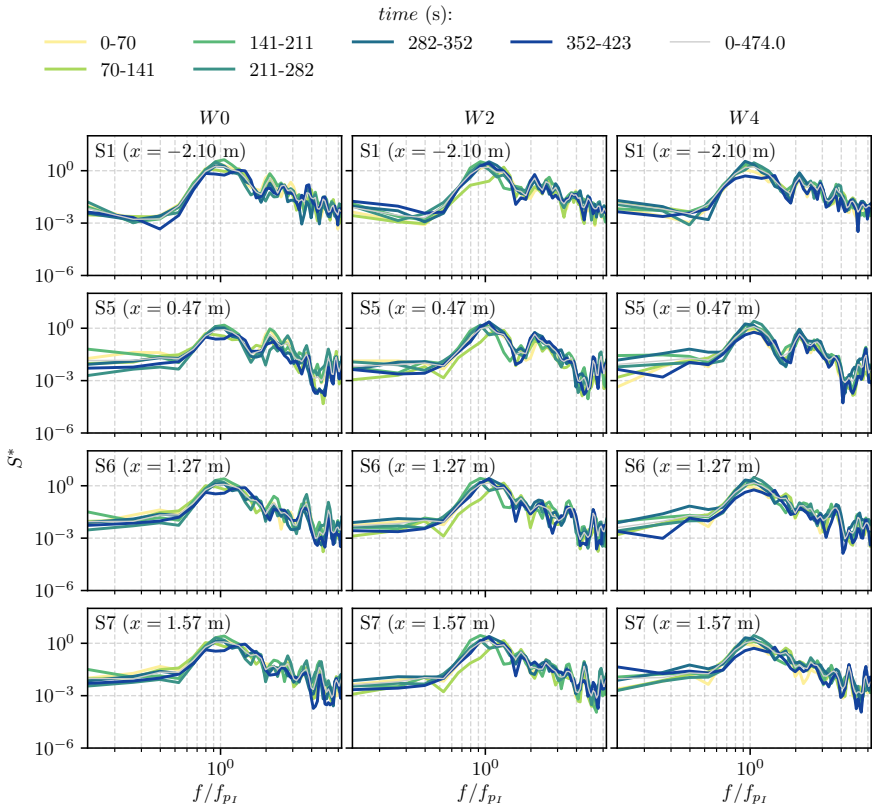

FIGURE A.28: Dimensionless power spectrum (S^*) of η for the Jonswap irregular wave wave experiment *JW1b_T4*, different wind speeds and different temporal subsets.

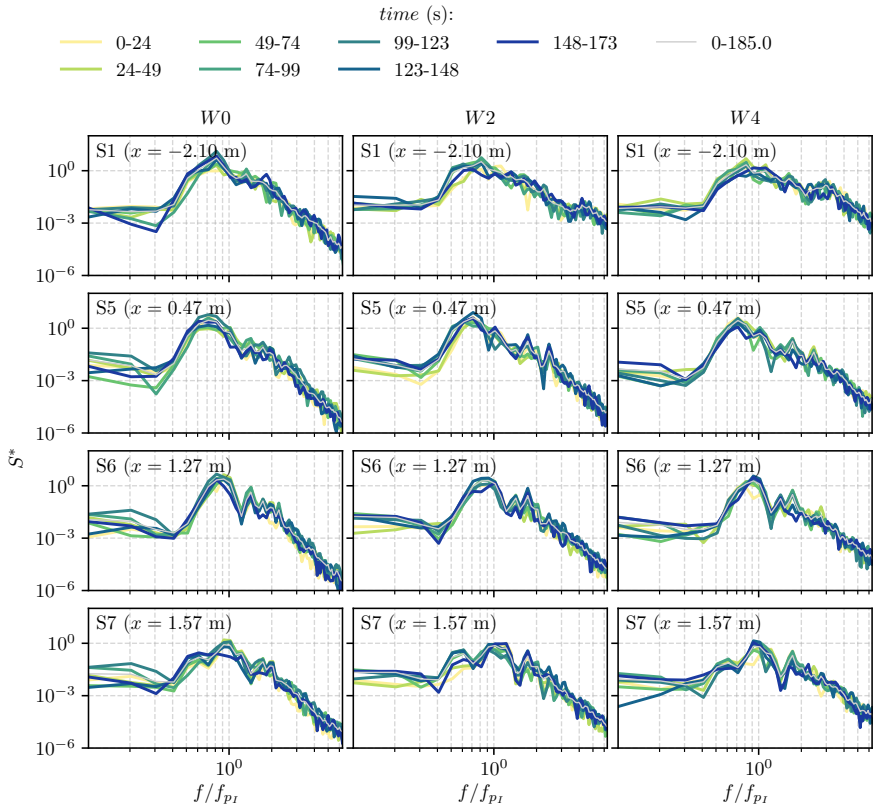

FIGURE A.29: Dimensionless power spectrum (S^*) of η for the Jonswap irregular wave wave experiment *JW2a_T1*, different wind speeds and different temporal subsets.

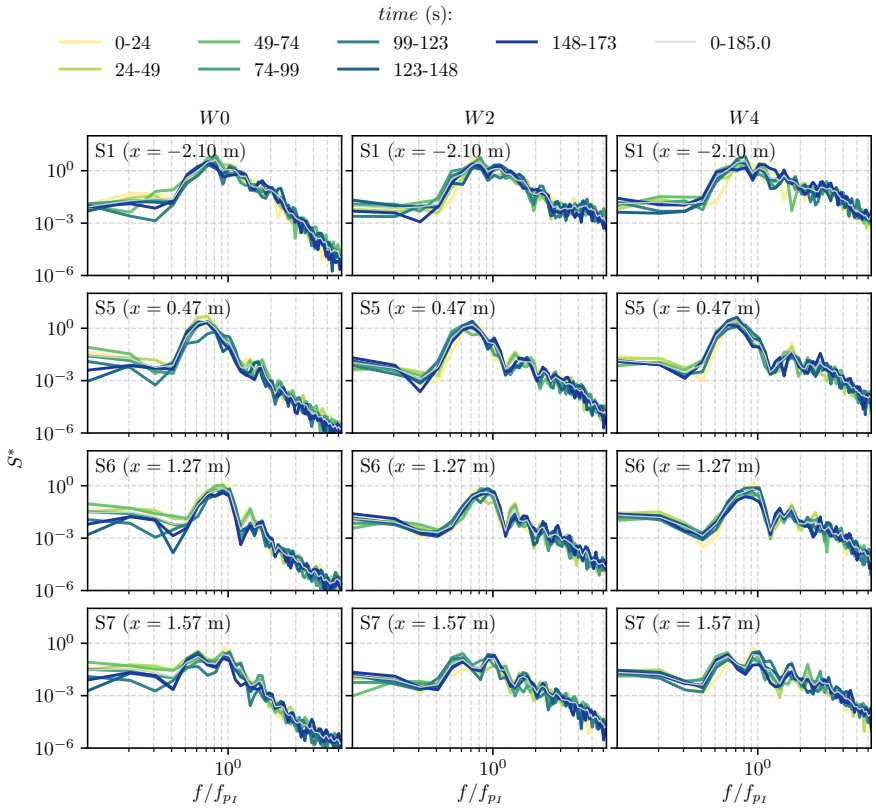

FIGURE A.30: Dimensionless power spectrum (S^*) of η for the Jonswap irregular wave wave experiment *JW2b_T1*, different wind speeds and different temporal subsets.

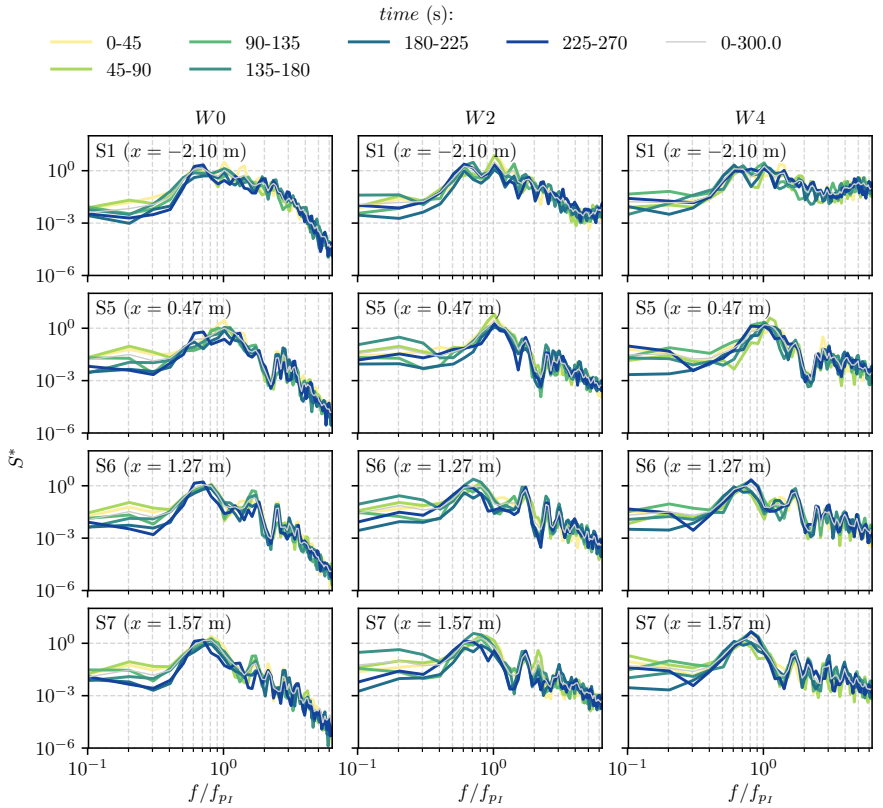

FIGURE A.31: Dimensionless power spectrum (S^*) of η for the Jonswap irregular wave wave experiment *JW2b_T2*, different wind speeds and different temporal subsets.

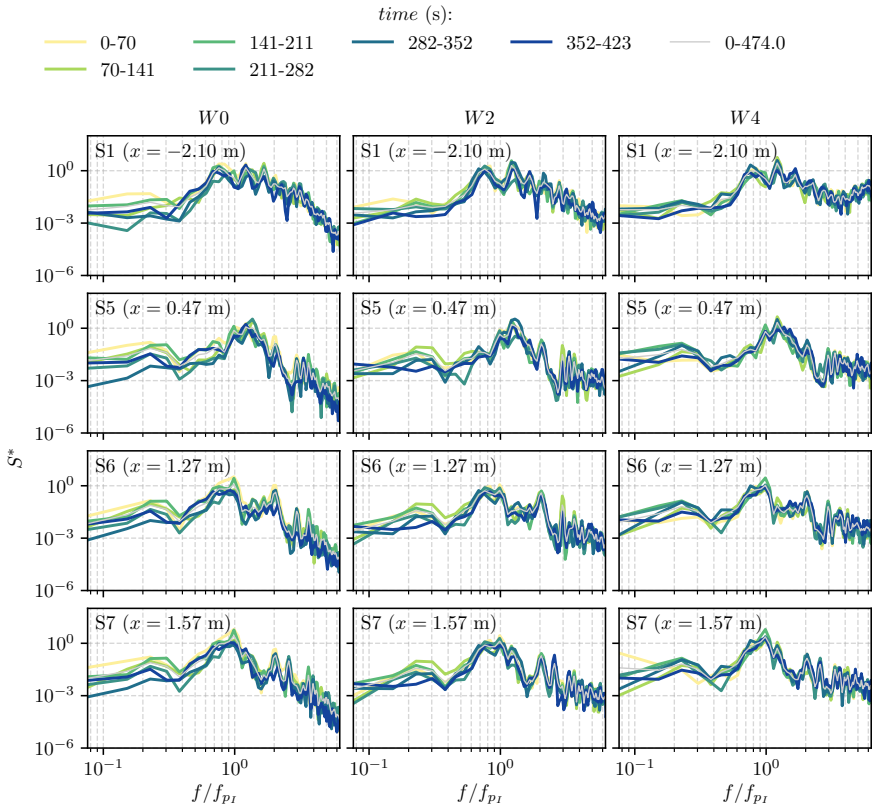

FIGURE A.32: Dimensionless power spectrum (S^*) of η for the Jonswap irregular wave wave experiment *JW2b_T3*, different wind speeds and different temporal subsets.

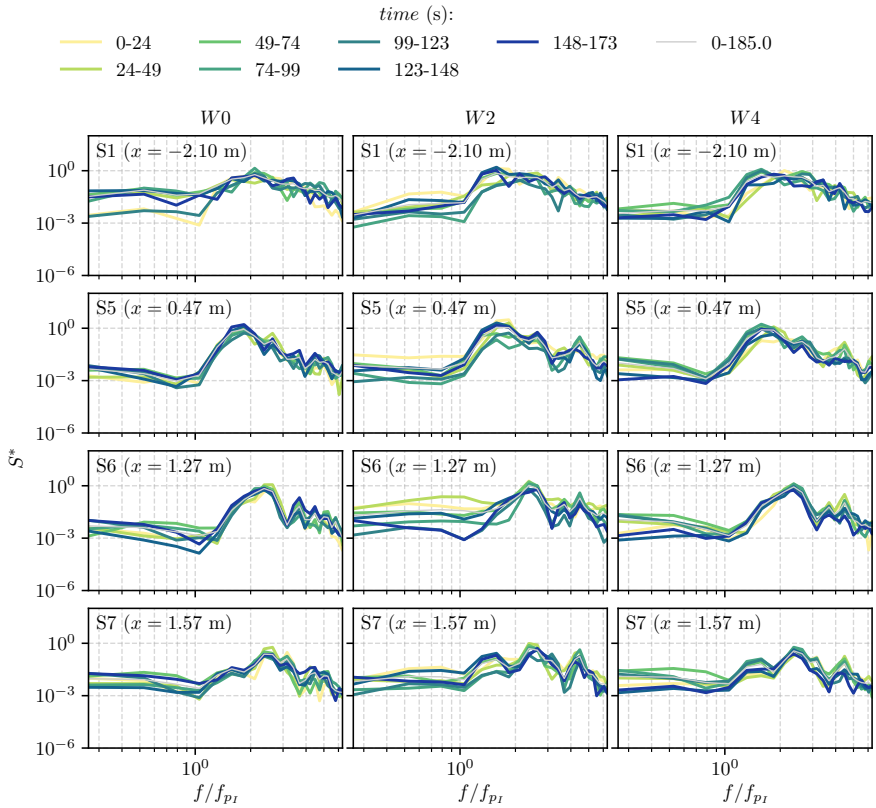

FIGURE A.33: Dimensionless power spectrum (S^*) of η for the Pierson-Moskowitz irregular wave wave experiment *PMa_T1*, different wind speeds and different temporal subsets.

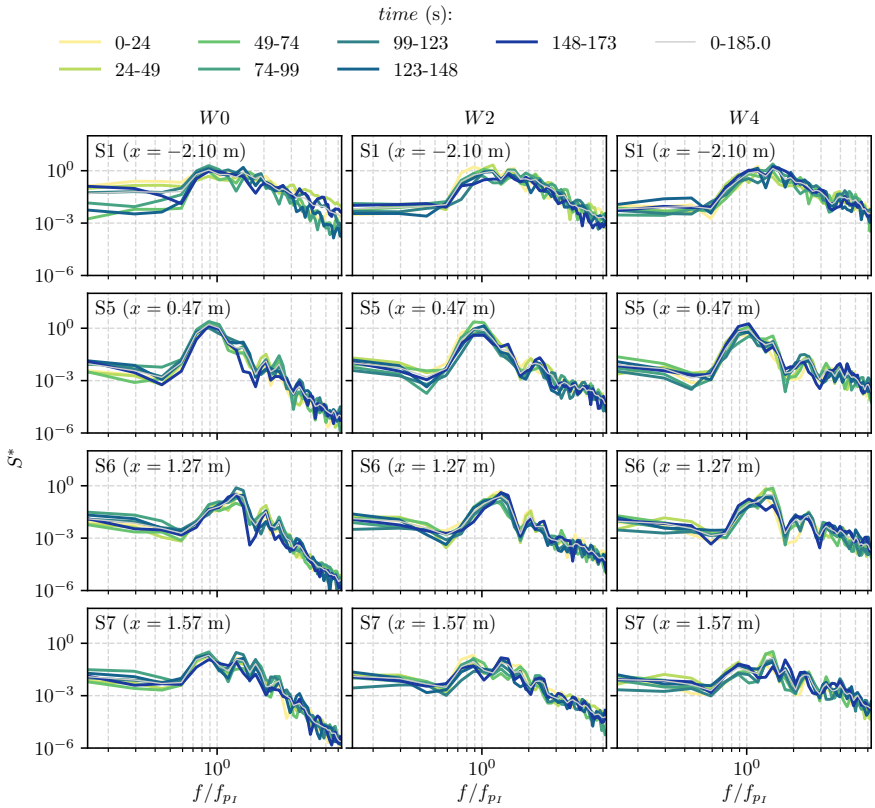

FIGURE A.34: Dimensionless power spectrum (S^*) of η for the Pierson-Moskowitz irregular wave wave experiment *PMb_T1*, different wind speeds and different temporal subsets.

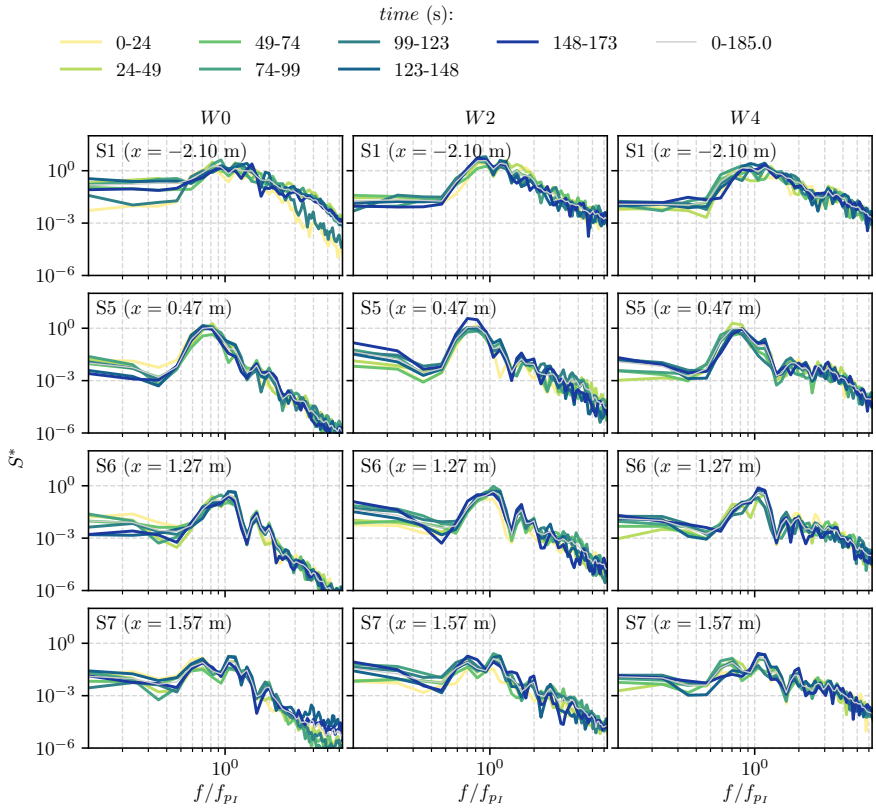

FIGURE A.35: Dimensionless power spectrum (S^*) of η for the Pierson-Moskowitz irregular wave wave experiment *PMc_T1*, different wind speeds and different temporal subsets.

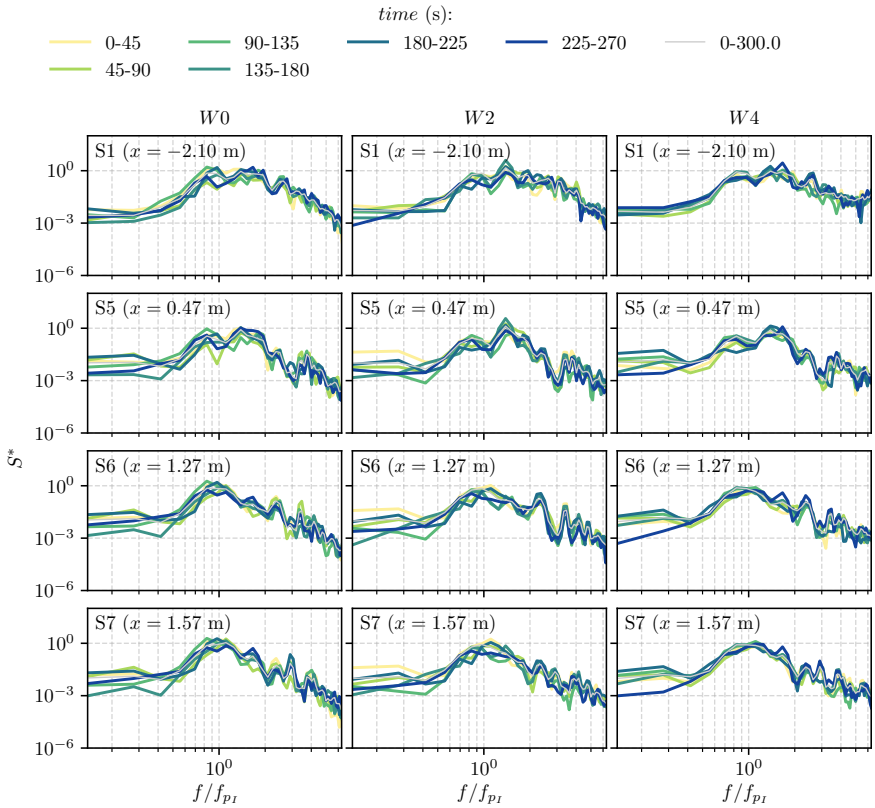

FIGURE A.36: Dimensionless power spectrum (S^*) of η for the Pierson-Moskowitz irregular wave wave experiment *PMb_T2*, different wind speeds and different temporal subsets.

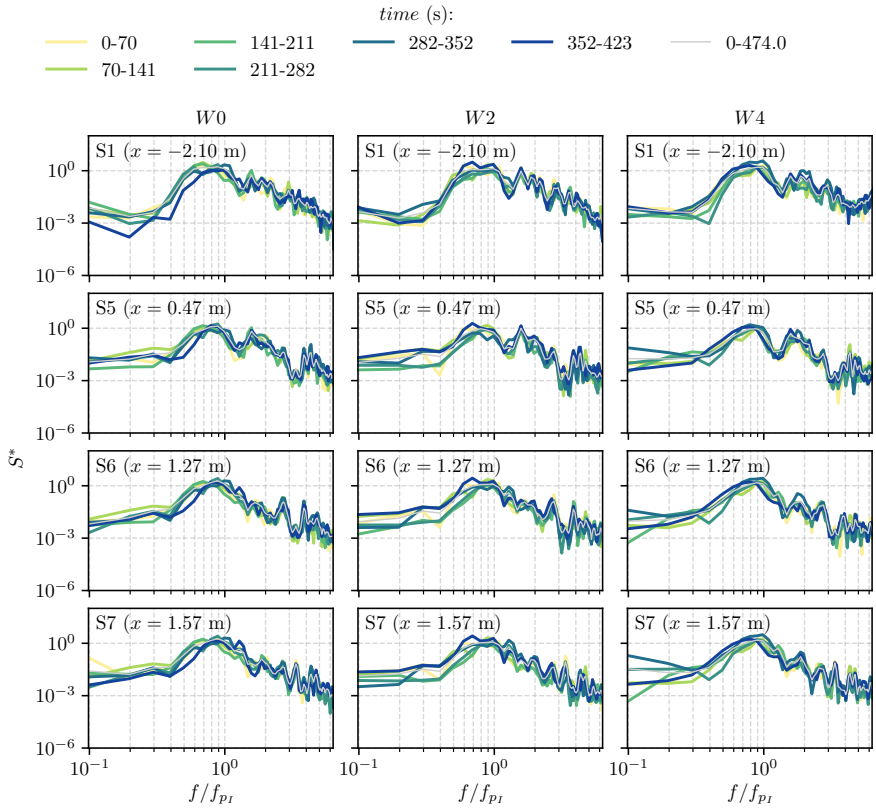

FIGURE A.37: Dimensionless power spectrum (S^*) of η for the Pierson-Moskowitz irregular wave wave experiment *PMb_T3*, different wind speeds and different temporal subsets.

Nomenclature

Roman Symbols

A	wave amplitude (m)
B	chamber width (m)
B/L	relative width
C_D	drag coefficient
C_l	complex amplitude of the propagating mode C_0 and a set of evanescent modes with coefficients C_l $(l > 0)$
d	submergence (m)
d/h	relative submergence
D_s	stochastic variable of storm duration
d_s	storm duration
$d_{s,0}$	minimum storm duration
e	error
f	frequency (Hz)
F_l	leeward-acting force ($\mathrm{N\,m^{-1}}$)
F_s	seaward-acting force ($\mathrm{N\,m^{-1}}$)
F_t	total force ($\mathrm{N\,m^{-1}}$)
F_{wall}	maximum force per unit width exerted by an incident wave train on a wall ($\mathrm{N\,m^{-1}}$)
G	piecewise function
H	wave height (m)
h	water depth (m)

H_s	significant wave height $H_{1/3}$ (m)
$H_{s,u}$	significant wave height threshold (m)
I	depth-dependent function ($\mathrm{m\,s^{-1}}$)
i	unit imaginary number $\sqrt{-1}$
k	wavenumber ($\mathrm{m^{-1}}$)
$\mathbb{K}_\mathbf{C}$	complex capture coefficient
K_C	modulus of the capture coefficient
$\mathbb{K}_\mathbb{R}$	complex reflection coefficient
K_R	modulus of the reflection coefficient
L	wavelength (m)
M	storm magnitude (m $\times$ h)
m_0	zeroth-order moment ($[...]^2$)
N	stochastic variable of annual number of storms
n	annual number of storms
N_l	number of evanescent modes
P	pressure (Pa)
p_Δ	p-value of the interarrival time goodness-of-fit test
p_N	p-value of the number of storms goodness-of-fit test
P_w	wave power ($\mathrm{W\,m^{-1}}$)
Q	amplification factor
S	energy spectrum ($[...]^2$s)
S^*	dimensionless energy spectrum
T	wave period (s)
t	time (s)
T_1	first natural period of the chamber (s)
T_2	second natural period of the chamber (s)

$\mathbb{TF}$ complex transfer function

TF modulus of the transfer function

T_{z0} incident mean wave period (S1–gauge data) (s)

$T_{z0_{W0}}$ incident mean wave period for the experiment without wind (S1–gauge data) (s)

u_* friction velocity ($\mathrm{m\,s^{-1}}$)

U_{ref} vertical mean wind speed ($\mathrm{m\,s^{-1}}$)

U_w wind speed ($\mathrm{m\,s^{-1}}$)

x longitudinal coordinate

y transversal coordinate

z vertical coordinate

z_0 roughness length (m)

Greek Symbols

α significance level

Δ stochastic variable of interarrival time

δ interarrival time

δ_0 minimum interarrival time

$\bar{\delta}$ mean interarrival time

ϵ relative aperture

η free surface elevation

Γ component in the x–direction of the wavenumber vector ($\mathrm{m^{-1}}$)

λ_N mean annual number of storms - parameter of Poisson distribution

ω angular frequency ($\mathrm{rad\,s^{-1}}$)

Φ velocity potential ($\mathrm{m^2\,s^{-1}}$)

ϕ velocity potential ($\mathrm{m^2\,s^{-1}}$)

φ_C phase of the capture coefficient ($^\circ$)

φ_R phase of the reflection coefficient (°)

Ψ phase lag (°)

φ phase (rad)

τ_K Kendall's tau - rank correlation coefficient

θ wave angle of incidence (°)

θ_c dependence parameter of the Clayton copula)

ξ friction coefficient

ζ_e equivalent friction coefficient

Superscripts

$input$ input values given to the wave generation software

Subscripts

0 incident conditions (propagating mode). S1–gauge data for experimental results.

I incident characteristics

j subscript index indicating the frequency component of the irregular sea state

l subscript index where $l = 0$ indicates the propagating mode and $l > 0$ indicate the evanescent modes

max maximum characteristics

n subscript index indicating the seaward and leeward regions ($n = 1, 2$)

p peak characteristics

I reflected characteristics

rms root mean square characteristics

z mean characteristics

Other Symbols

g gravitational constant (9.81 $\mathrm{m\,s^{-2}}$)

$\Im\{...\}$ imaginary part

π	$\simeq 3.14\ldots$
$\Re\{...\}$	real part
Re	Reynolds number
ρ_w	density of water (1027 kg m^{-3} - seawater)
$\{...\}'$	turbulent component
$\overline{\{...\}}$	mean component
$\widetilde{\{...\}}$	periodic component

Acronyms / Abbreviations

CDF	Cumulative Distribution Function
CIAO	Atmosphere Ocean Interaction Flume
ECDF	Empirical Cumulative Distribution Function
IISTA	Andalusian Institute for Earth System Research
JW	Tests with a JONSWAP incident wave spectrum
KS	Kolmogorov-Smirnov test
PM	Tests with a Pierson-Moskowitz incident wave spectrum
R	Tests with regular waves (paddle-generated)
W	Tests with wind-generated waves

Bibliography

Addona, F., A. Lira Loarca, L. Chiapponi, M.A. Losada, and S. Longo (2018). "The Reynolds wave shear stress in partially reflected waves". In: *Coastal Engineering* 138, 220 –226. ISSN: 0378-3839. DOI: https://doi.org/10.1016/j.coastaleng.2018.04.015.

Baquerizo, A. (1995). "Reflexión del oleaje en playas. Métodos de evaluación y de predicción". PhD thesis. Universidad de Cantabria.

Baquerizo, A., M.A. Losada, J.M. Smith, and N. Kobayashi (1997). "Cross-shore variation of wave reflection from beaches". In: *Journal of Waterway, Port, Coastal and Ocean Engineering* 123.5, 274–279.

Baquerizo, A., M.A. Losada, and I.J. Losada (2002). "Edge wave scattering by a coastal structure". In: *Fluid Dynamics Research* 31.4, 275–287.

Bennett, G.S., P. McIver, and J.V. Smallman (1992). "A mathematical model of a slotted wavescreen breakwater". In: *Coastal Engineering* 18.3, 231–249. DOI: 10.1016/0378-3839(92)90021-L.

Boccotti, P. (2000). *Wave mechanics for ocean engineering*. Vol. 64. Elsevier.

— (2012). "Design of breakwater for conversion of wave energy into electrical energy". In: *Ocean engineering* 51, 106–118.

Borgman, L. E. (1969). "Ocean Wave Simulation for Engineering Design". In: *Journal of the Waterways and Harbors Division* 95.4, 557–586.

Corbella, S and D.D. Stretch (Aug. 2012). "Multivariate return periods of sea storms for coastal erosion risk assessment". In: *Natural Hazards and Earth System Sciences* 12.8, 2699–2708.

Corbella, S. and D.D. Stretch (June 2013). "Simulating a multivariate sea storm using Archimedean copulas". In: *Coastal Engineering* 76, 68–78.

Dalrymple, R.A. and R.G. Dean (1991). *Water wave mechanics for engineers and scientists*. Prentice-Hall.

Dean, W.R. (1945). "On the reflexion of surface waves by a submerged plane barrier". In: *Mathematical Proceedings of the Cambridge Philosophical Society* 41.03, 231–238.

Falcão, A.F. de O. (2000). "The shoreline OWC wave power plant at the Azores". In: *Proceedings of the 4th European Wave Energy Conference*. Aalborg, Denmark.

Faraci, C., B. Cammaroto, L. Cavallaro, and E. Foti (2012). "Wave reflection generated by caissons with internal rubble mound of variable slope". In: *Proceedings of the 33rd International Conference on Coastal Engineering*. Santander, Spain.

Faraci, C., P. Scandura, and E. Foti (2015). "Reflection of Sea Waves by Combined Caissons". In: *Journal of Waterway, Port, Coastal, and Ocean Engineering* 141.2, 04014036. DOI: 10.1061/(ASCE)WW.1943-5460.0000275.

Folgueras, P., S. Solari, M. Mier-Torrecilla, M. Doblaré, and M.A. Losada (2016). "The extended Davenport peak factor as an extreme-value estimation method for linear combinations of correlated non-Gaussian random variables". In: *Journal of Wind Engineering and Industrial Aerodynamics* 157, 125–139.

Goda, Y. (2000). *Random seas and design of maritime structures*. World scientific.

Goring, D.G. and V.I. Nikora (2002). "Despiking Acoustic Doppler Velocimeter Data". In: *Journal of Hydraulic Engineering* 128.1, 117–126.

Huang, Z., Y. Li, and Y. Liu (2011). "Hydraulic performance and wave loadings of perforated/slotted coastal structures: a review". In: *Ocean Engineering* 38.10, 1031–1053. DOI: 10.1016/j.oceaneng.2011.03.002.

Isaacson, M., S. Premasiri, and G. Yang (1998). "Wave interactions with vertical slotted barrier". In: *Journal of Waterway, Port, Coastal, and Ocean Engineering* 124.3, 118–126.

Jäger, W.S., T. Nagler, C. Czado, and R.T. McCall (2018). "A statistical simulation method for joint time series of non-stationary hourly wave parameters". In: *Coastal Engineering*. ISSN: 0378-3839. DOI: https://doi.org/10.1016/j.coastaleng.2018.11.003.

Jalón, M.L. (2016). "Diseño Óptimo de un Sistema de Aprovechamiento de la Energía del Oleaje y Gestión Integral a Diferentes Escalas de Tiempo". PhD thesis. University of Granada.

Jarlan, G.E. (1961). "A perforated vertical wall breakwater". In: *The Dock and Harbour Authority* 41.486, 394–398.

Koutandos, E, P Prinos, and X Gironella (2005). "Floating breakwaters under regular and irregular wave forcing: reflection and transmission characteristics". In: *Journal of Hydraulic Research* 43.2, 174–188.

Kraus, E.B. and J.A. Businger (1995). *Atmosphere ocean interaction*. Oxford University Press.

Kriebel, D., C. Sollitt, and W. Gerken (1999). "Wave Forces on a Vertical Wave Barrier". In: *Proceedings in Coastal Engineering 1998*, pp. 2069–2081.

Li, F., P.H.A.J.M. van Gelder, R. Ranasinghe, D.P. Callaghan, and R.B. Jongejan (2014). "Probabilistic modelling of extreme storms along the Dutch coast". In: *Coastal Engineering* 86, 1–13.

Li, F., J. Zhou, and C. Liu (2018). "Statistical modelling of extreme storms using copulas: A comparison study". In: *Coastal Engineering* 142, 52 –61.

Lira-Loarca, A., M. Clavero, and M.A. Losada (2016). "Canal de Interacción Atmósfera Océano (CIAO)". In: *Proceedings of the I Jornadas de Investigadores en Formación*. Granada, España. ISBN: 978 - 84 - 16478 - 94 - 1.

Liu, P.L.F. and K. Al-Banaa (2004). "Solitary wave runup and force on a vertical barrier". In: *Journal of Fluid Mechanics* 505, 225–233.

Liu, Y. and C. Faraci (2014). "Analysis of orthogonal wave reflection by a caisson with open front chamber filled with sloping rubble mound". In: *Coastal Engineering* 91, 151–163.

Liu, Y. and H. Li (2013). "Wave reflection and transmission by porous breakwaters: A new analytical solution". In: *Coastal Engineering* 78, 46–52.

Liu, Y., Y. Li, and B. Teng (2007). "The reflection of oblique waves by an infinite number of partially perforated caissons". In: *Ocean engineering* 34.14, 1965–1976.

Liu, Y., Y. Li, B. Teng, J. Jiang, and B. Ma (2008). "Total horizontal and vertical forces of irregular waves on partially perforated caisson breakwaters". In: *Coastal Engineering* 55.6, 537–552.

Longo, S., L. Chiapponi, and D. Liang (2013). "Analytical study of the water surface fluctuations induced by grid-stirred turbulence". In: *Applied Mathematical Modelling* 37.12, 7206 –7222. ISSN: 0307-904X.

Losada, I.J., M.A. Losada, and A.J. Roldán (1992). "Propagation of oblique incident waves past rigid vertical thin barriers". In: *Applied Ocean Research* 14.3, 191–99.

Losada, I.J., M.A. Losada, and A. Baquerizo (1993a). "An analytical method to evaluate the efficiency of porous screens as wave dampers". In: *Applied Ocean Research* 15.4, 207–215.

Losada, I.J., M.A. Losada, and R. Losada (1994). "Wave spectrum scattering by vertical thin barriers". In: *Applied Ocean Research* 16.2, 123–128.

Losada, I.J., R. Silva, and M.A. Losada (Nov. 1997). "Effects of Reflective Vertical Structures Permeability on Random Wave Kinematics". In: *Journal of Waterway, Port, Coastal, and Ocean Engineering* 123.6, 347–353.

Losada, M.A., I.J. Losada, and A.J. Roldán (1993b). "Propagation of oblique incident modulated waves past rigid, vertical thin barriers". In: *Applied ocean research* 15.5, 305–310.

Lykke Andersen, T., M. Clavero, P. Frigaard, M.A. Losada, and J.I. Puyol (2016). "A new active absorption system and its performance to linear and non-linear waves". In: *Coastal Engineering* 114, 47 –60.

Lütkepohl, H. (2005). *New introduction to multiple time series analysis*. Berlin [u.a.]: Springer. 764 pp.

Mansard, E.P.D. and E.R. Funke (1980). "The Measurement of Incident and Reflected Spectra Using a Least Squares Method". In: *Proceedings of the International Conference on Coastal Engineering*. Sydney, Australia. DOI: 10.1061/9780872622647.008.

Martín-Soldevilla, M.J., M. Martín-Hidalgo, V. Negro, J.S. López-Gutiérrez, and P. Aberturas (2015). "Improvement of theoretical storm characterization for different climate conditions". In: *Coastal Engineering* 96, 71–80.

Massel, S.R. (1996). *Ocean Surface Waves: Their Physics and Prediction*. World Scientific. DOI: 10.1142/2285.

Mei, C.C. (1989). *The Applied Dynamics of Ocean Surface Waves*. Vol. 1. World scientific.

Mei, C.C., P.L.F. Liu, and A.T. Ippen (1974). "Quadratic loss and scattering of long waves". In: *Journal of the Waterways, Harbors and Coastal Engineering Division* 100.3, 217–239.

Mei, C.C., M. Stiassnie, and D.K.-P. Yue (2005). *Theory and Applications of Ocean Surface Waves: Nonlinear Aspects*. Vol. 23. World Scientific.

Méndez, F.J., M. Menéndez, A. Luceño, and I.J. Losada (July 2006). "Estimation of the long-term variability of extreme significant wave height using a time-dependent Peak Over Threshold (POT) model". In: *Journal of Geophysical Research: Oceans* 111.C7, 561.

Monk, K., Q. Zou, and D. Conley (2013). "An approximate solution for the wave energy shadow in the lee of an array of overtopping type wave energy converters". In: *Coastal Engineering* 73, 115–132.

Mori, N., T. Suzuki, and S. Kakuno (2007). "Noise of Acoustic Doppler Velocimeter Data in Bubbly Flows". In: *Journal of Engineering Mechanics* 133.1, 122–125.

Mustapa, M.A., O.B. Yaakob, Y.M. Ahmed, C. Rheem, K.K. Koh, and F.A. Adnan (2017). "Wave energy device and breakwater integration: A review". In: *Renewable and Sustainable Energy Reviews* 77, 43–58.

Nieto, S., A. Lira-Loarca, M. Clavero, and M.A. Losada (2015). "Canal de Interacción Atmósfera-Océano". In: *Proceedings of the XIII Jornadas Españolas de Ingeniería de Costas y Puertos*. Avilés, España. ISBN: 978 - 84 - 608 - 4359 - 7.

Ostermann, F., R. Woszidlo, S. Gaertlein, C. Nayeri, and C.O. Paschereit (Jan. 2014). "Phase-Averaging Methods for a Naturally Oscillating Flow Field". In: *Proceedings of the 52nd Aerospace Sciences Meeting*. Reston, Virginia: American Institute of Aeronautics and Astronautics, p. 4151955.

Pawitan, K.A., A.S. Dimakopoulos, D. Vicinanza, W. Allsop, and T. Bruce (2019). "A loading model for an OWC caisson based upon large-scale measurements". In: *Coastal Engineering* 145, 1–20.

Payo, A., A. Baquerizo, and M. Losada (Apr. 2008). "Uncertainty assessment: Application to the shoreline". In: *Journal of Hydraulic Research* 46.sup1, 96–104.

Phillips, 0.M. (1967). *The Dynamics of the Upper Ocean*. Cambridge University Press, p. 261.

Pires, Luciana Bassi Marinho, Igor Braga de Paula, Gilberto Fisch, Ralf Gielow, and Roberto da Mota Girardi (Sept. 2013). "Simulations of the Atmospheric Boundary Layer in a Wind Tunnel with Short Test Section". en. In: *Journal of Aerospace Technology and Management* 5, 305 –314. ISSN: 2175-9146.

Roldán, A.J. and Losada, M.A. and Losada, I.J. (1992). "Theoretical study of the wave attenuation in a channel with roughened sides". In: *Proceedings of the 23rd International Conference on Coastal Engineering*. Vol. 3. Venice, Italy, pp. 2786–2786.

ROM 0.0-01 (2001). *ROM 0.0. General Procedure and Requirements in the Design of Harbor and Maritime Structures*. Puertos del Estado, p. 218. ISBN: 84-88975-30-9.

ROM 1.0-09 (2009). *ROM 1.0. Recommendations for the Project Design and Construction of Breakwaters (Part I: Calculation and Project Factors. Climatic Agents)*. Puertos del Estado.

ROM 1.1-18 (2018). *ROM 1.1. Recomendaciones para el Proyecto de Construcción de Diques de Abrigo*. Puertos del Estado.

Sahoo, T., M.M. Lee, and A.T. Chwang (2000). "Trapping and generation of waves by vertical porous structures". In: *Journal of Engineering Mechanics* 126.10, 1074–1082.

Salvadori, G., C. De Michele, N.T. Kottegoda, and R. Rosso (2007). *Extremes in nature: an approach using copulas*. Vol. 56. Springer Science & Business Media.

Sawaragi, T. (1995). *Coastal engineering-waves, beaches, wave-structure interactions*. Vol. 78. Elsevier.

Solari, S. and P. van Gelder (2011). "On the use of Vector Autoregressive (VAR) and Regime Switching VAR models for the simulation of sea and wind state parameters". In: *Marine Technology and Engineering*.

Solari, S. and M.A. Losada (2014). "Statistical Methods for Risk Assessment of Harbor and Coastal Structures". In: *Design Of Coastal Structures And Sea Defenses*. Series On Coastal And Ocean Engineering Practice. World Scientific Publishing Company. ISBN: 9789814611022.

Solari, S., M. EgÃŒen, M.J. Polo, and M.A. Losada (Mar. 2017). "Peaks over threshold (POT): A methodology for automatic threshold estimation using goodness-of-fit p-value". In: *Water Resources Research*.

Sollitt, C.K. and R.H. Cross (1972). "Wave transmission through permeable breakwaters". In: *Proceedings of the 13th International Conference on Coastal Engineering*. Vancouver, Canada.

Sonnenberger, R., K. Graichen, and P. Erk (2000). "Fourier averaging: a phase-averaging method for periodic flow". In: *Experiments in Fluids* 28.3, 217–224.

Teixeira, P.R.F., D.P. Davyt, E. Didier, and R. Ramalhais (2013). "Numerical simulation of an oscillating water column device using a code based on Navier–Stokes equations". In: *Energy* 61, 513–30. DOI: 10.1016/j.energy.2013.08.062.

Torre-Enciso, Y., I. Ortubia, L.I. López de Aguileta, and J. Marqués (2009). "Mutriku Wave Power Plant: from the thinking out to the reality". In: *Proceedings of the 8th European Wave and Tidal Energy Conference*. Uppsala, Sweden, pp. 319–29.

Ursell, F and W R Dean (1947). "The effect of a fixed vertical barrier on surface waves in deep water". In: *Mathematical Proceedings of the Cambridge Philosophical Society* 43.03, 374–382.

Vílchez, M., M. Clavero, and M.A. Losada (2016). "Hydraulic performance of different non-overtopped breakwater types under 2D wave attack". In: *Coastal Engineering* 107, 34–52.

Yu, X. (1995). "Diffraction of water waves by porous breakwaters". In: *Journal of waterway, port, coastal, and ocean engineering* 121.6, 275–282.